

The Internal Kinematics of Intermediate Redshift Galaxies

by
Luc Simard
B.Sc. Queen's 1990

A Thesis Submitted in Partial Fulfillment of the
Requirements for the Degree of
DOCTOR OF PHILOSOPHY
in the Department of Physics and Astronomy

© Luc Simard, 1996,
University of Victoria.

*All rights reserved. Thesis may not be reproduced in whole or in part,
by mimeograph or other means, without the permission of the author.*



National Library
of Canada

Acquisitions and
Bibliographic Services

395 Wellington Street
Ottawa ON K1A 0N4
Canada

Bibliothèque nationale
du Canada

Acquisitions et
services bibliographiques

395, rue Wellington
Ottawa ON K1A 0N4
Canada

Your file Votre référence

Our file Notre référence

The author has granted a non-exclusive licence allowing the National Library of Canada to reproduce, loan, distribute or sell copies of this thesis in microform, paper or electronic formats.

The author retains ownership of the copyright in this thesis. Neither the thesis nor substantial extracts from it may be printed or otherwise reproduced without the author's permission.

L'auteur a accordé une licence non exclusive permettant à la Bibliothèque nationale du Canada de reproduire, prêter, distribuer ou vendre des copies de cette thèse sous la forme de microfiche/film, de reproduction sur papier ou sur format électronique.

L'auteur conserve la propriété du droit d'auteur qui protège cette thèse. Ni la thèse ni des extraits substantiels de celle-ci ne doivent être imprimés ou autrement reproduits sans son autorisation.

0-612-21948-8

Supervisor: Dr. C. J. Pritchett

Abstract

A dilemma is posed by studies of galaxy evolution at intermediate redshifts. If evolutionary effects are neglected, simple models predict number densities of faint galaxies which are $2\text{--}5\times$ lower than observed at $z \cong 0.4$. Yet the faint galaxy redshift distribution appears to be well modelled by the same no-evolution models. If low-mass starbursting galaxies are responsible for the excess, then the excess faint galaxy population should have rotation velocities lower than those of quiescent galaxies with the same luminosity.

This thesis describes the results of a limited survey of the internal kinematics of intermediate redshift ($z = 0.25\text{--}0.45$) field galaxies. The goal of this survey was to find the unmistakable kinematical signature of low-mass starbursting galaxies. Using the Canada-France-Hawaii Telescope, spatially-resolved spectra of the [O II] $\lambda\lambda$ 3726–3729 Å doublet emission line have been obtained for 22 galaxies. High-spatial resolution has made it possible to extract $V_{\text{rot}} \sin i$ and [O II] disk scale length from each galaxy spectrum using synthetic galaxy rotation curve fitting. It is found that about 25% of the galaxies in the sample have [OII] kinematics unrelated to rotation. [OII] emission is concentrated in the nucleus in these “kinematically anomalous” galaxies. A Doppler ellipse similar to those found in local dwarf irregular galaxies has been observed in a $z = 0.35$ galaxy.

An intermediate redshift Tully-Fisher (TF) relation defined by 12 kinematically normal galaxies shows that these galaxies have a systematically lower rotation velocity (i.e. mass) for their luminosity than expected from the local TF relation. These galaxies would have to fade by $\sim 1.5\text{--}2$ mag to lie on the local TF relation. This is consistent with starbursting dwarf galaxy models. Although the sample is small, there is also a hint that massive galaxies do not lie as far off the local TF relation as low-mass ones. However, as

shown using a large sample of local galaxies, the scatter in the local TF relation is large, especially for late-type galaxies. Selection effects, particularly [OII] emission strength, could be responsible for part of the observed TF shift if different star formation rates are responsible for the local TF scatter. A comparison with other works indicates that the luminosity-dependent luminosity evolution scenario neatly explains all the available internal kinematics and surface brightness data.

Contents

Abstract	ii
Contents	v
List of Tables	viii
List of Figures	ix
Acknowledgements	xii
1 Introduction	1
2 The Faint Galaxy Excess Problem	4
2.1 The Local Galaxy Luminosity Function	4
2.2 Number Counts	7
2.3 Redshift Distribution	10
2.4 Evolution of the Galaxy Luminosity Function	15
2.4.1 The Canada-France Redshift Survey	15
2.4.2 The Autofib Survey	19
2.5 Hubble Space Telescope Imaging	20
3 Models	24
3.1 Luminosity evolution	25
3.2 Merger model	27
4 Internal Kinematics of Distant Galaxies	29
4.1 A Critical Test	29
4.2 Previous Studies	30

4.3	Spatially-Resolved [OII] Internal Kinematics	33
4.3.1	Physics of the [OII] emission line doublet	33
4.3.2	An Internal Kinematics Survey at CFHT	35
5	Data	37
5.1	Sample Selection	37
5.2	Observations	41
5.2.1	MOS/SIS	41
5.2.2	SIS Observations	43
5.2.3	MOS Observations	45
5.3	Pre-Processing	45
6	Synthetic Rotation Curve Fitting	53
6.1	Fitting Model	54
6.1.1	Parameters	54
6.1.2	Surface Brightness Profile	54
6.1.3	Velocity Field	55
6.1.4	Spectra, PSF and Instrumental Profiles	56
6.2	Fitting Algorithm	57
6.2.1	An Example: The Suspicious Coin	61
6.3	ELFIT2D: 2D Emission Line Fitting	65
6.4	Simulations	69
6.4.1	Confidence Intervals	69
6.4.2	Parameter Recovery	70
7	Results	111
7.1	Broad-Band Light Profiles	111
7.2	Parameter Values and Probability Distributions	125
7.3	[OII] Morphologies	151
7.4	Intermediate Redshift Tully-Fisher Relation	163
8	Discussion	166
8.1	The Local Tully-Fisher Relation	166
8.2	Morphological Dependence of the Tully-Fisher Relation	170
8.3	Kinematical Evidence for Luminosity Evolution	178
8.4	Comparison with Other Works	186

<i>CONTENTS</i>	vii
9 Conclusion and Future Work	190
Bibliography	193
Glossary	199

List of Tables

5.1	Characteristics of Target Galaxies	49
5.2	MOS and SIS Instrumental Configurations	50
5.3	Characteristics of the CFHT LORAL3 CCD Detector	50
5.4	Observation Log – Part 1	51
5.5	Observation Log – Part 2	52
6.1	ELFIT2D Control Parameter Set - Part 1	66
6.2	ELFIT2D Control Parameter Set - Part 2	67
6.3	ELFIT2D results for 50 different noise realizations	70
6.4	ELFIT2D Simulation Test Sequences	85
6.5	ELFIT2D Simulation Sets	86
7.1	Parameter Value Search – Initial Conditions – Part 1	136
7.2	Parameter Value Search – Initial Conditions – Part 2	137
7.3	Best Parameter Values and Confidence Intervals	138
8.1	Luminosity Evolution from Absolute TF relation	180

List of Figures

2.1	B, I and K galaxy number counts	11
2.2	The LDSS Redshift Distribution	14
2.3	The CFRS galaxy luminosity as a function of redshift	17
6.1	Synthetic Rotation Curve Spectrum Flow Chart	58
6.2	The Suspicious Coin Posterior Probability Distributions	64
6.3	ELFIT2D median parameter values for fifty noise realizations	71
6.4	3 simulated posterior probability distributions	72
6.5	$z = 0.25$ ELFIT2D SIS test sequence 1.1	76
6.6	$z = 0.25$ ELFIT2D SIS test sequence 1.2	77
6.7	$z = 0.25$ ELFIT2D SIS test sequence 1.3	78
6.8	$z = 0.25$ ELFIT2D SIS test sequence 1.4	79
6.9	$z = 0.25$ ELFIT2D SIS test sequence 1.5	80
6.10	$z = 0.25$ ELFIT2D SIS test sequence 2.1	81
6.11	$z = 0.25$ ELFIT2D SIS test sequence 2.2	82
6.12	$z = 0.25$ ELFIT2D SIS test sequence 2.3	83
6.13	$z = 0.25$ ELFIT2D SIS test sequence 2.5	84
6.14	$z = 0.42$ ELFIT2D SIS test sequence 1.1	87
6.15	$z = 0.42$ ELFIT2D SIS test sequence 1.2	88
6.16	$z = 0.42$ ELFIT2D SIS test sequence 1.3	89
6.17	$z = 0.42$ ELFIT2D SIS test sequence 1.4	90
6.18	$z = 0.42$ ELFIT2D SIS test sequence 1.5	91
6.19	$z = 0.42$ ELFIT2D SIS test sequence 2.1	92
6.20	$z = 0.42$ ELFIT2D SIS test sequence 2.2	93
6.21	$z = 0.42$ ELFIT2D SIS test sequence 2.3	94
6.22	$z = 0.42$ ELFIT2D SIS test sequence 2.5	95
6.23	$z = 0.25$ ELFIT2D MOS test sequence 1	96
6.24	$z = 0.25$ ELFIT2D MOS test sequence 2	97

6.25	$z = 0.25$ ELFIT2D MOS test sequence 3	98
6.26	$z = 0.25$ ELFIT2D MOS test sequence 4	99
6.27	$z = 0.25$ ELFIT2D MOS test sequence 5	100
6.28	$z = 0.42$ ELFIT2D MOS test sequence 1	101
6.29	$z = 0.42$ ELFIT2D MOS test sequence 2	102
6.30	$z = 0.42$ ELFIT2D MOS test sequence 3	103
6.31	$z = 0.42$ ELFIT2D MOS test sequence 4	104
6.32	$z = 0.42$ ELFIT2D MOS test sequence 5	105
6.33	ELFIT2D MOS r_d and $V_{\text{rot}} \sin i$ tests - 1	106
6.34	ELFIT2D MOS r_d and $V_{\text{rot}} \sin i$ tests - 2	107
6.35	ELFIT2D MOS r_d and $V_{\text{rot}} \sin i$ tests - 3	108
6.36	ELFIT2D MOS r_d and $V_{\text{rot}} \sin i$ tests - 4	109
6.37	ELFIT2D MOS r_d and $V_{\text{rot}} \sin i$ tests - 5	110
7.1	CNOC MOS Gunn r galaxy luminosity profiles	114
7.2	CNOC MOS Gunn r galaxy luminosity profiles	115
7.3	CNOC MOS Gunn r galaxy luminosity profiles	116
7.4	CNOC MOS Gunn r galaxy luminosity profiles	117
7.5	CNOC MOS Gunn g galaxy luminosity profiles	118
7.6	CNOC MOS Gunn g galaxy luminosity profiles	119
7.7	CNOC MOS Gunn g galaxy luminosity profiles	120
7.8	CNOC MOS Gunn g galaxy luminosity profiles	121
7.9	SIS I band galaxy luminosity profiles	122
7.10	SIS I band galaxy luminosity profiles	123
7.11	SIS V and R band galaxy luminosity profiles	124
7.12	Parameter Probability Functions - A2390-101033	126
7.13	Parameter Probability Functions - A2390-100686	127
7.14	Parameter Probability Functions - A2390-350416	128
7.15	Parameter Probability Functions - A2390-350471	129
7.16	Parameter Probability Functions - E1512-301037A	130
7.17	Parameter Probability Functions - E1512-301037B	131
7.18	Parameter Probability Functions - E1512-101526	132
7.19	Parameter Probability Functions - E1512-201429	133
7.20	Parameter Probability Functions - E1621-100515	134
7.21	Parameter Probability Functions - A2390-100225	135
7.22	Parameter Probability Functions - A2390-101084	139
7.23	Parameter Probability Functions - A2390-200928	140

7.24	Parameter Probability Functions - A2390-200802	141
7.25	Parameter Probability Functions - A2390-200372	142
7.26	Parameter Probability Functions - E1512-201845	143
7.27	Parameter Probability Functions - A2390-201773	144
7.28	Parameter Probability Functions - E1512-200730	145
7.29	Parameter Probability Functions - E1512-200334	146
7.30	Parameter Probability Functions - E1512-200672	147
7.31	Parameter Probability Functions - E1512-201268	148
7.32	Parameter Probability Functions - E1512-202096	149
7.33	Parameter Probability Functions - E1512-201125	150
7.34	[OII] Nuclear Emission in $z = 0.25$ galaxy	152
7.35	[OII] Emission in kinematically normal galaxy at $z = 0.42$. .	153
7.36	Donut-shaped [OII] Emission in $z = 0.35$ galaxy	154
7.37	$V_{\text{rot}} \sin i$ versus rest-frame absolute B magnitude for kinematically normal galaxies	165
8.1	HI half-linewidth versus H_{α} rotation velocity for a sample of 204 nearby galaxies	169
8.2	The locus of the local H_{α} -I band Tully-Fisher relation and its dispersion	175
8.3	The locus of the local H_{α} -B band Tully-Fisher relation and its dispersion	176
8.4	The locus of the local H_{α} -B band Tully-Fisher relation for Hubble types Sb and Sc	177
8.5	The local H_{α} -B band Tully-Fisher relation and the CFHT internal kinematics data	183
8.6	Kinematical evidence for luminosity evolution - All type reference	184
8.7	Kinematical evidence for luminosity evolution - Late type reference	185

Acknowledgements

It is often said that red Smarties should be kept for last because they are the best. Although I have argued on many occasions that blue Smarties are much superior in taste and appearance to red ones, I cannot dispute the fact that acknowledgements are definitely the best part of writing a thesis. So, I wrote them last.

My years in Victoria were enriched by so many people. They helped me grow both as a person and as a scientist. My apologies for not mentioning everyone. I just did not want these acknowledgements to sound like Oscars' night.

I do not know how to thank my supervisor, Chris Pritchett. How can you thank someone for showing you what kind of scientist you want to be? Chris is an outstanding researcher, but he remained a "normal" person. His broad range of interests outside of astronomy has convinced me not to be afraid to follow my own interests. Chris was always there to answer my questions, and I will always keep fond memories of the discussions we have had together. I will not rest until I find out how he managed to break the law of momentum conservation every time we played pool at Hale Pohaku.

I would like to thank my parents, Lise and Pierre, for their constant

support and love. They always encouraged me to pursue my goals. They helped me with my first telescope, took me on tours, bought me a zillion books and always had time to satisfy their odd offspring's request to come and have "one more look at Saturn!". Their faith in me did not even falter when I started putting up weird structures in their backyard which I claimed would receive radio waves from the stars. They also managed to keep me down to earth. Good parents are one of life's true gifts. I am thankful that I have a chance to spend some time with them every summer in our little paradise deep in the woods of northern Québec.

A very special thank to Jim Hesser for that dinner on a dark, winter night which prevented me from making the biggest mistake in my life. Jim's love for astronomy radiates from everything he does. The astronomical community in Victoria is lucky. Thanks also go to Peter Stetson for saying: "Boy, that's stupid!" when I needed it. I hope the people at the Dominion Astrophysical Observatory on little Saanich Hill will never lose their gift of heartily welcoming students among them.

The various incarnations (softball, floor hockey, volleyball and soccer) of the Glorious Blue Stragglers have greatly contributed to my fight against keyboard insanity. Post-game analyses were particularly gripping. May the Blue Stragglers shine for gigayears to come.

Amusement was provided on many occasions by AHnold, StevoCop, RoboBob, SuperDave and Rookie who foolishly tried to defeat Rebel Scum. May they understand one day the hopelessness of their efforts. I ask my fellow graduate students for forgiveness. My habit of running `x_kinfit2d.e` on every single workstation probably generated some well-crafted curses.

Working on this project would not have been nearly as much fun without countless hours of musical accompaniment by Rush, Pink Floyd, the Tragically Hip, Sarah McLachlan, Loreena McKennitt and Enya. The last three are highly recommended for observing, but the first three would probably shatter the primary mirror. Special thanks to Baka Beyond for bringing far-away Africa to Elliott 404.

Random bits contribute significantly to the tapestry of life: sunset canoe paddles, Victor Hugo, 7-Eleven slurpies, noodles and sauce on a Whisperlite 600, the puzzling psychology of the slugs of the Gordon Head field, the view from the CFHT catwalk, la Rivière de la Misère et le Lac au Mirage, the Lucky Toaster, giant turtles and the blue ocean, Rock et Belles Oreilles, East Sooke Park Astro hikes, the past denizens of Nowhere in the Ghetto, shooting stars and the colorful northern lights, les Sentinelles de l'Air, les Grands Equipages de Lumière, frogs, late-night music on the radio, la tarte au sucre and Jésus de Montréal. Just to name a few.

This thesis has made use of data obtained at the Canada France Hawaii Telescope (CFHT), which is operated by the National Research Council of Canada, the Centre National de la Recherche Scientifique of France and the University of Hawaii. I would like to thank those agencies for funding such a wonderful instrument and allowing graduate students to use it. Many thanks to the people at CFHT for their assistance during many nights at 4200 meters.

By the time she gets here, my fiancé, Salome, will probably be asking herself why she should marry a goof that does not even include her in his acknowledgements. I kept her for last because she is the best part of my life.

ACKNOWLEDGEMENTS

xv

Every day, I am amazed by how much she has become a part of me. It will be a unique privilege to share the rest of my life with her, and I look forward to all our years together. Her parents have often assured me that my life with her would definitely not be boring. Guess what? I totally agree!

I hope this thesis will take you up to eleven. It certainly did for me.

Chapter 1

Introduction

At the turn of the century, astronomers started to chart our Galaxy, the Milky Way, by studying the distribution, kinematics, and chemical abundances of different types of stars. Our understanding of the Milky Way has its foundation in their pioneering work. Today, astronomers are faced with an equally daunting task: mapping the observable Universe. Their probes are not stars but galaxies. While it is true that 4-m class telescopes have been in existence for decades, the task of cataloging countless galaxies sprinkled like grains of sand across the Universe seemed nearly impossible to astronomers armed with photographic plates. Their dismay was easily understandable considering the fact that an *entire* night was required to collect enough light to determine the redshift of a *single*, relatively nearby galaxy.

Nowadays, astronomers can measure hundreds of redshifts in one night using the same telescopes. This tremendous gain in telescope efficiency comes from recent advances in sensitive digital detectors (known as charge-coupled devices or CCDs) and the advent of multi-object spectrographs. Equipped with these powerful “redshift machines”, astronomers set out to count galax-

ies and measure their spatial distribution. They had hoped to determine the values of fundamental cosmological constants linked to the topology of the Universe. It turned out otherwise. There were simply too many distant galaxies compared to what had been expected from studies of the neighborhood of the Milky Way. This puzzling observation became known as the faint galaxy excess problem. Though it has been the topic of extensive study in the astronomical literature, it has proven to be a particularly difficult problem to solve. Models proposed by astronomers to explain the distant Universe often had profound (and unforeseen) consequences on local galaxy properties – for example, the thickness of spiral disks, and the metallicity of dwarf galaxies, to name two.

Thanks to adaptive optics systems which can correct aberrations in astronomical images introduced by the Earth's atmosphere, it is now possible to study distant galaxies in greater detail and measure their masses directly from their internal velocity fields. Internal kinematics is a novel technique to tackle the faint galaxy excess problem – a technique that goes beyond redshift surveys. These surveys can provide information only on the global evolution of a galaxy population, whereas internal kinematics can be used to trace evolution in individual galaxies. The goal of this thesis is to use internal kinematics to probe the nature of distant galaxies and understand the manner in which they evolve into the local galaxy population. As the reader will see, the task is extremely challenging since it involves working at the limits of detection and spatial resolution of current telescopes.

This thesis is organized into nine chapters. Chapter 2 starts by showing how galaxy differential number counts $N(m)$ and galaxy redshift distributions

$N(z)$ led to the faint galaxy excess problem. Chapter 3 describes faint galaxy models based on luminosity evolution and mergers. These two chapters are intended to give the reader the background information needed to understand the motivation behind this thesis.

Chapter 4 explains how the internal kinematics of distant galaxies can be used to test faint galaxy models. Previous studies are discussed, and the goals of our survey, which was conducted at the Canada-France-Hawaii Telescope (CFHT), are given. Sample selection, observations and data pre-processing are explained in Chapter 5. Chapter 6 shows how synthetic rotation curves, a pattern-recognition method based on a parametric fitting model, can be used to optimally extract information on the internal kinematics of faint galaxies from very low signal-to-noise data. Topics covered in this chapter include the fitting model, the Metropolis algorithm used for finding parameter values, and the implementation of the synthetic rotation curve method within the IRAF environment.

Chapter 7 presents the results of the CFHT internal kinematics survey. Internal kinematics is compared to broad-band galaxy morphologies and surface brightness profiles, [OII] morphologies and rotation velocities expected on the basis of the local Tully-Fisher relation.

The results are discussed in Chapter 8. Kinematical evidence for luminosity evolution is presented. The effects of uncertainties in the local Tully-Fisher on this kinematical evidence are explained. A comparison with other works leads to the exciting conclusion that luminosity-dependent luminosity evolution is the cause of the faint galaxy excess problem.

Chapter 2

The Faint Galaxy Excess Problem

2.1 The Local Galaxy Luminosity Function

In order to talk about an excess, it is obviously important to define compared to what the excess is measured. The body of literature on the faint galaxy excess problem is considerable, but different studies have used different references and this has led to confusing claims of various amounts of evolution over the past half Hubble time. Galaxy luminosity functions (LFs) are usually expressed following Schechter (1976):

$$\phi(L)dL = \phi^* \left(\frac{L}{L^*}\right)^\alpha \exp\left(-\frac{L}{L^*}\right) \frac{dL}{L^*} \quad (2.1)$$

where L is the galaxy luminosity and $\phi(L) dL$ is the number of galaxies with luminosity between L and $L+dL$ per Mpc^3 . Equation 2.1 can be rewritten in absolute magnitude form as:

$$\phi(M)dM = \frac{2}{5} \phi^* (\ln 10) \left[10^{\frac{2}{5}(M^*-M)}\right]^{\alpha+1} \exp\left[-10^{\frac{2}{5}(M^*-M)}\right] dM \quad (2.2)$$

where M is the galaxy absolute magnitude and $\phi(M) dM$ is the number of galaxies with magnitude between M and $M + dM$ per Mpc^3 . The Schechter function has three free parameters which must be determined empirically: α , ϕ^* and M^* . The slope of the LF at the faint end is determined by α . A luminosity function with $\alpha = -1.0$ is said to be flat. M^* is called the characteristic Schechter luminosity, and ϕ^* is the number of galaxies per Mpc^3 per magnitude at the characteristic luminosity.

It turns out that there is considerable uncertainty in the local values of α and ϕ^* , and the root of this uncertainty is still not known. Part of the problem is that the parameters may be dependent upon galaxy morphological types, and the exact contribution of each galaxy type to the global LF is not well-known. The situation at higher redshifts is even worse as different galaxy types may evolve differently and selection effects may favor the detection of certain galaxy types over others.

The Stromlo-APM survey (Loveday et al., 1992) studied a local sample of 1769 galaxies complete down to a magnitude limit of $b_J = 17.15$. The sample was drawn at random from the APM Bright Galaxy Catalog. They found that the local luminosity function was well fitted over the magnitude range $-22 < M_{b_J} < -15$ by a Schechter function with parameters $M_{b_J}^* = -19.50$, $\alpha = -0.97$ and $\phi^* = 1.40 \times 10^{-2} \text{ Mpc}^{-3}$. Hence, the local luminosity function appeared to be flat.

The Las Campanas Redshift Survey (Lin et al., 1996) covered 18678 galaxies with an average redshift of $z = 0.1$. The LCRS luminosity function could be fitted by a Schechter luminosity function with $M^* = -20.29 + 5 \log h$ ($h \equiv H_0/100$), $\phi^* = 1.9 \times 10^{-2} \text{ Mpc}^{-3}$ and $\alpha = -0.7$ over the absolute

magnitude range $-23.0 < M - 5 \log h < -17.5$. Moreover, the LCRS found that emission ([OII] equivalent width $> 5 \text{ \AA}$) and non-emission galaxies had different luminosity functions, with emission galaxies dominating the faint end and non-emission galaxies prevailing at the bright end.

Both the Loveday *et al.* survey and the LCRS derived the same normalization ϕ^* for the local LF. However, when this normalization is used in models trying to reproduce faint number counts of galaxies, these models fall short by a factor of 2 at relatively bright magnitudes ($B \simeq 16-18$). Since it is believed that early-type galaxies are old, dynamically relaxed systems, it is hard to understand why half of them would have disappeared over the past 5-6 Gyrs. Therefore, many faint galaxy studies have normalized their number count models to the *observed* counts at $B \simeq 16-18$. Any excess observed at fainter magnitudes ($B \simeq 22-24$) is measured over observed bright counts and not over the local luminosity functions.

The CfA Redshift Survey (Marzke *et al.*, 1994b) covered 9063 galaxies with Zwicky m_Z magnitude < 15.5 to calculate the galaxy luminosity function over the range $-13 < M_Z < -22$. For galaxies with velocities $cz > 2500 \text{ km s}^{-1}$, the luminosity function was well-represented by a Schechter function with parameters $\phi^* = 4.0 \times 10^{-2} \text{ Mpc}^{-3}$, $M^* = -18.8$ and $\alpha = -1.0$. The normalization was a factor of 2 higher than found by the Stromlo-APM and LCRS surveys. When all galaxies with $cz > 500 \text{ km s}^{-1}$ were included, the number of galaxies in the range $-16 < M_Z < -13$ exceeded the extrapolation of the Schechter function by a factor of 3 – i.e. the LF rose steeply at magnitudes fainter than -16 . This steep faint end excess was dominated by Magellanic spirals and irregulars, and their LF had $M^* = -18.79$, $\alpha =$

-1.87 and $\phi^* = 0.6 \times 10^{-3} \text{ Mpc}^{-3}$ (Marzke et al., 1994a). This abundance of intrinsically faint, blue nearby galaxies will obviously affect the magnitude of the excess seen in faint number counts and could go a long way in reconciling no-evolution standard models with faint number counts. It is not known at the present time why the steep faint end of the CfA local LF has not been detected by the Stromlo-APM and LCRS surveys.

Given the uncertainty in the local LF, it is reassuring to know that, as explained later, internal kinematics studies will not rely on the local LF to calculate the amount of luminosity evolution in intermediate redshift galaxies. However, the choice of local LF should be explicitly stated in any comparison between luminosity evolution measured from luminosity functions and internal kinematics.

2.2 Number Counts

The simplest way to study galaxies is to count how many there are as a function of apparent magnitude per unit area (usually deg^2) on the sky. Number counts are usually denoted by $N(m)$. It was thought that $N(m)$ could be used to constrain cosmological models (Hubble and Tolman, 1935). For example, in an Euclidean universe uniformly populated by galaxies with the same intrinsic luminosity, the count slope $\gamma = d \log N(m) / dm$ should be equal to 0.6. It was soon realized that galaxy evolution could have at least as much of an effect on $N(m)$ as the geometry of the Universe. Also, number counts have a built-in weak point which makes their interpretation difficult: galaxies with a wide range of intrinsic luminosities are included in

each apparent magnitude bin. Number counts are the results of integrating over intrinsic luminosity and distance.

Early faint galaxy counts showed a marked number excess over standard models incorporating k -corrections but neglecting evolutionary effects, and an overall blueing trend. Shanks *et al.* (1984) obtained b_J and r_F galaxy number counts and colour distributions down to $B \sim 23$. At $b_J = 23$, they observed three times as many galaxies as predicted by a $q_0 = 0.02$ no-evolution model, but r_F counts were much closer to model counts. In the range $19.5 < r_F < 20.5$, galaxy colors appeared to be shifted towards the blue with respect to the data at brighter magnitudes, and with respect to the prediction of the no-evolution model. Koo (1986) presented UBVI counts and color distributions of ~ 10000 galaxies to $B \simeq 24$. He found that U counts rose rapidly with magnitude with $\gamma = 0.68$. Galaxies fainter than $B \simeq 20$ also had progressively more of an ultraviolet excess eventually exceeding that of Galactic subdwarfs. The fraction of field galaxies intrinsically bluer than $B-V = 0.7$ increased to $\sim 74\%$ by $z \simeq 0.4$ from the local value of ~ 0.4 . Tyson (1988) conducted a very deep multicolor imaging survey of 25000 galaxies that revealed strong evidence for color and luminosity evolution. Galaxy counts at $b_J = 25$ were a factor 5–15 above no-evolution models. The mean galaxy colours approached $b_J-R = 0$, $R-I = 0.8$ at the faint limit compared to $b_J-R \simeq 2.0$ at brighter magnitudes ($R = 21$).

More recent galaxy number counts confirmed the trends seen in earlier works. Metcalfe *et al.* (1991) determined B and R galaxy counts for $21 < B < 25$ and $19 < R < 23.5$. They also found that B counts were systematically higher than no-evolution model predictions. There was a factor of

three excess in the magnitude range $24.5 < B < 25$. The status of galaxy counts as of 1993 was neatly presented in Figure 1 of Lilly (1993) reproduced in Figure 2.1. Figure 2.1 shows galaxy counts in B, I and K plotted against various models. The lower solid curve and the dashed curve are no-evolution models with $q_0 = 0.5$ and $q_0 = 0$ respectively. The dot-dashed curve is a non-standard cosmological model with a non-zero cosmological constant ($\Omega_0 = 0.1$, $\lambda_0 = 0.9$). The upper solid curve represents an evolving model in which the luminosities of Irr galaxies have been arbitrarily increased by a factor of 41. Figure 2.1 clearly shows that the excess is more pronounced in B than in K. The K counts are almost fitted with a non-standard cosmology. The B counts cannot even be fitted with the extreme evolving model shown here. The color dependence of the excess is interpreted as increased star formation in faint galaxies. Different bandpasses look at different stellar populations within galaxies. The B bandpass looks at the young, star-forming component of galaxies whereas K looks at more long-lived, quiescent stellar populations. K band luminosities are therefore more representative of the masses of galaxies and are less affected by galaxy evolution.

Cowie *et al.* (1991) obtained redshifts and K-band magnitudes for 22 galaxies with B magnitudes down to 24. At $B = 23-24$, 30–80% of the galaxies were small, blue galaxies with median M_K , redshift and B–K color of -21.3 ($L = 0.01 L^*$), 0.24 and 3.4 respectively. To explain such a large fraction of low-luminosity galaxies, a steep rise in the Schechter function faint magnitudes was required. This population of low-luminosity objects contained as much K-band light as the normal galaxy population, which meant they contained as much baryonic matter as the normal galaxy population.

K-band counts over the range $10 < K < 23$ (Gardner et al., 1993) showed a change in slope at $K \simeq 17$ from $\gamma = 0.67$ to $\gamma = 0.26$. At $K \simeq 17$, the median B–K color as a function of K magnitude turned over, and galaxies fainter than $K = 17$ rapidly became bluer. Models with non-zero λ_0 did not appear to fit the counts: they overpredicted the faint end counts if evolution was added, and they underpredicted the bright end counts with no evolution. Gardner *et al.* expected their K magnitude-limited sample to be dominated by K^* elliptical (K^* is the K magnitude corresponding to the Schechter luminosity L^*) and Sa galaxies. Since a passively evolving K^* elliptical galaxy reaches $K = 17$ at $z \simeq 1$, their data indicated that the population of field galaxies had undergone an evolutionary changes by $z \simeq 1$ and that the colors were bluer than expected.

The Hubble Space Telescope (HST) has added a new dimension to number counts. As discussed in section 2.5, it is now possible with HST to determine galaxy number counts as a function of galaxy types and identify what population is responsible for the excess of faint galaxies.

2.3 Redshift Distribution

Redshift surveys are vastly superior to number count studies because the intrinsic luminosity of excess galaxies can be determined by using redshift as a distance indicator. Knowing their intrinsic luminosity helps in deciding what role selection effects may or may not play in the discrepancy between local and intermediate redshift samples. For example, galaxy surface brightness dimming goes as $(1+z)^4$ and such a strong function of redshift will work

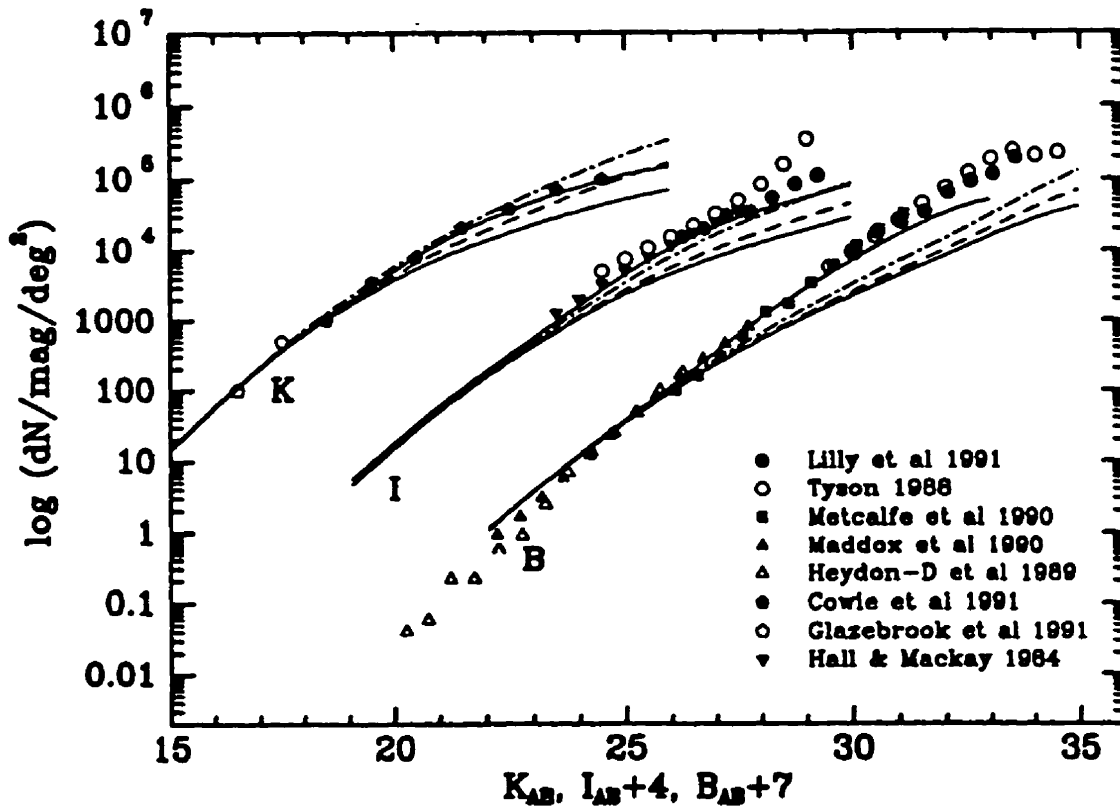


Figure 2.1: B, I and K galaxy number counts. Figure taken from Lilly (1993)

against high redshift galaxies. As discussed in Phillipps and Driver (1995) and references therein, there is also a local bias against low surface brightness galaxies. Distant galaxies are frequently surveyed with extremely low isophotal thresholds around $\mu_B = 25 \text{ mag/arcsec}^2$ corresponding to an intrinsic surface brightness $\mu_B \sim 27.5 \text{ mag/arcsec}^2$, but very little is known about local galaxies with surface brightness below $\mu_B \sim 25 \text{ mag/arcsec}^2$.

The heart of the faint galaxy problem lies with the fact that the same no-evolution models which fail to explain the number counts discussed in the previous section seem to fit the redshift distributions $N(z)$ of faint galaxies. The contradiction between $N(m)$ and $N(z)$ poses a basic problem to understanding intermediate redshift galaxy evolution.

The Durham/Anglo-Australian Telescope faint galaxy survey (Broadhurst et al., 1988) studied over 200 field galaxies selected in apparent magnitude slices in the range $20.0 < b_J < 21.5$ in five high Galactic latitude fields. The wavelength coverage sampled distinctive spectral features such as [OII] 3727 Å and Ca II H and K 3968,3933 Å over the redshift range $0 < z < 0.6$. The mean redshift was 0.25. No high redshift galaxies were found. All redshifts were below 0.47. This was a surprising result. Luminosity evolution in L^* galaxies should have made them visible at higher redshifts. Their no-evolution model based on the DARS results (Peterson et al., 1986) provided a good fit to $N(z)$ while falling short (by a factor of ~ 1.5 at $b_J = 21.5$) of reproducing blue number counts. The observed [OII] equivalent width distribution $N(W_\lambda)$ showed an excess of [OII] strong ($W_\lambda > 20 \text{ Å}$) objects. The slope of the counts γ changed as a function of W_λ , going from $\gamma = 0.18$ for $W_\lambda < 20 \text{ Å}$ to $\gamma = 0.61$ for $W_\lambda > 20 \text{ Å}$. This excess matched the count excess

at $b_J \sim 21-21.5$, and, since [OII] strong objects are usually very blue, they concluded that the excess population seen in the counts could be identified with the star-forming strong emission-line galaxies.

Better constraints were placed on the evolution of galaxies with luminosities greater than L^* by the LDSS survey (Colless et al., 1990; Colless et al., 1993). This survey looked at 149 objects with magnitudes in the range $21 \leq b_J \leq 22.5$. The LDSS redshift distribution is reproduced in Figure 2.2. The LDSS survey found that no more than 2% (90% confidence level) or 4% (99% confidence level) of galaxies brighter than $b_J = 22.5$ were at redshifts higher than 0.5. The 90% level upper limit on the number of high-redshift galaxies was not consistent with any evolution of the most luminous galaxies, and the 99% limit was consistent with no more than 1.0–1.2 magnitudes of brightening by $z = 1$. These limits led to the luminosity-dependent luminosity evolution hypothesis (discussed in section 3.1) to reconcile $N(m)$ and $N(z)$. The $b_J - r_F$ colors as a function of redshift in the LDSS survey spanned the full range of colors expected from the reddest spectral energy distributions of E/S0 and the spectral energy distribution of the bluest local galaxy, NGC 4449. In fact, some LDSS galaxies were *bluer* than NGC 4449 would appear at those redshifts.

The deepest B band redshift survey is the LDSS-2 (Glazebrook et al., 1995a). It produced 73 redshifts for objects in the magnitude range $22.5 < B < 24$. The median redshift was $z = 0.46$. The survey showed a large excess of galaxies at $z \sim 0.4$ with respect to luminosity evolution models of the form $L \propto (1 + bz)$ with $b=0$ being the no-evolution case. There was an increase in the space density of galaxies with $L \sim L_B^*(z = 0)$ which could arise

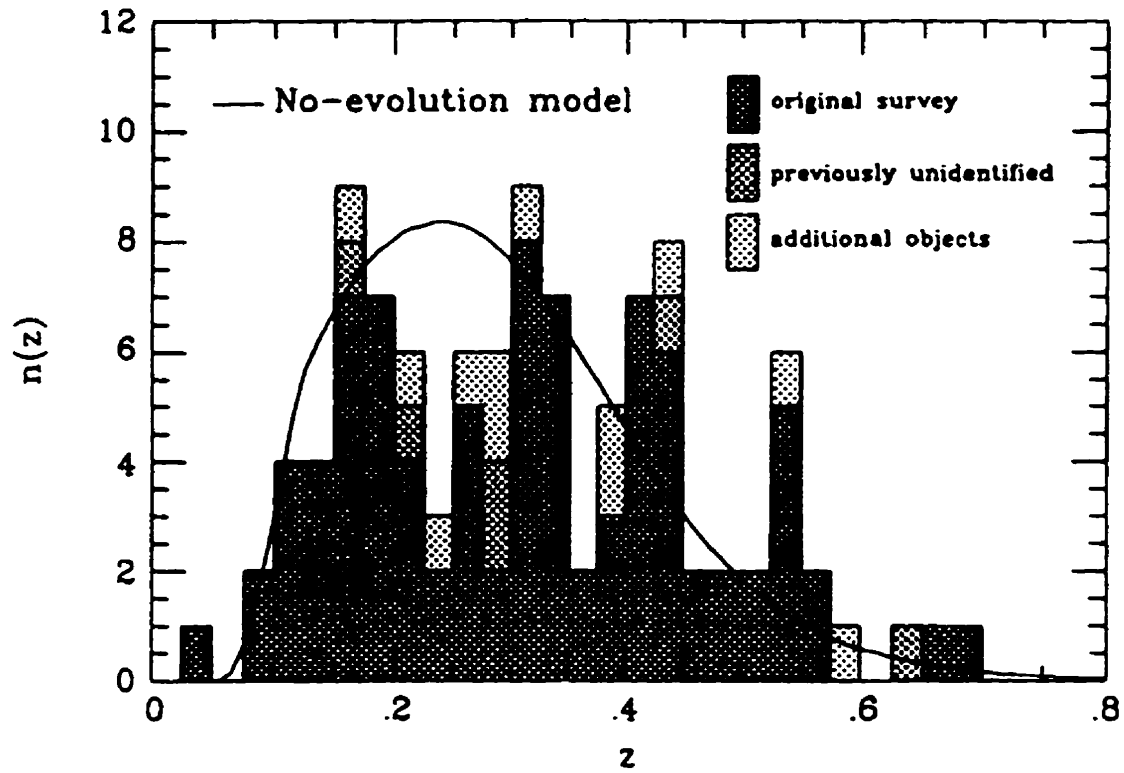


Figure 2.2: The LDSS Redshift Distribution taken from Colless *et al.* (1993). The solid curve is the shape of the distribution predicted for no evolution of the galaxy population.

through mergers or luminosity-dependent luminosity evolution. The survey also showed no trace of an excess of $z < 0.2$ galaxies predicted by models trying to explain number counts solely on the basis of a steep faint end to the local luminosity function.

A K-band selected redshift survey of 124 galaxies down to $K \simeq 17.3$ (Glazebrook et al., 1995c) showed no evidence for evolution of the K-band luminosity function below $z = 0.5$, but the luminosity function required a high normalization of $\phi^* = 0.026 \text{ h}^3 \text{ Mpc}^{-3}$. Beyond $z = 0.5$, M_K^* increased by 0.75 mag at $z = 1$. This result was opposite to expectations from simple merger-dominated models in which the masses of galaxies should decrease with redshift.

2.4 Evolution of the Galaxy Luminosity Function

Section 2.3 discussed what was known about $N(z)$ as of 1993. Two recent surveys have greatly contributed to the understanding of the evolution of the galaxy luminosity function with redshift: The CFRS and Autofib Surveys. Both deserve special attention as they provide an important framework for the interpretation of results from an internal kinematics survey.

2.4.1 The Canada-France Redshift Survey

The Canada-France Redshift Survey (CFRS) (Lilly *et al.* 1995, and references therein) consists of 591 galaxies with secure redshifts ($17.5 < I_{AB} < 22.5$, $0.02 < z < 1.2$). This long redshift baseline, a unique characteristic of

the CFRS, makes it possible to study the evolution of the galaxy luminosity function without relying on local samples. Figure 2.3 shows the CFRS galaxy luminosity function as a function of redshift with galaxies split according to color (blue \equiv bluer than Sbc). The local LF of Loveday *et al.* (1992) is plotted in all the panels as a reference keeping in mind that it has not been color-split the way the CFRS sample has been.

Figure 2.3 illustrates a number of important points. There is clear evidence for a population of faint galaxies ($M_{AB}(B) \sim -18$) in the lowest redshift bin with a significantly higher comoving number density than in the local LF of Loveday *et al.* (1992). There is no evidence for evolutionary changes in the galaxy population between the $0.05 < z < 0.2$ and $0.2 < z < 0.5$ redshift bins, but there are significant differences with the Loveday LF. However, uncertainties in the local luminosity function (see 2.1) make it hard to determine whether there is evolution back to $z \sim 0.2$. There is no change in the LF of redder galaxies over the entire CFRS redshift baseline. Therefore, there is no evidence for a substantial decrease with increasing redshift as expected if redder galaxies formed through mergers of massively star-forming sub-units, and the brightening is no more than a few tenths of magnitude as expected from the passive evolution of an old stellar population.

There is substantial evolution in the luminosity function of blue galaxies over the range $0.2 < z < 1.0$ which could be viewed either as a luminosity brightening with look-back time or as an increase in the galaxy comoving density. For example, the blue $0.50 < z < 0.70$ luminosity function could equally well be fitted by shifting the local LF to the left (luminosity brightening) or shifting the local LF upwards (number density increase). CFRS

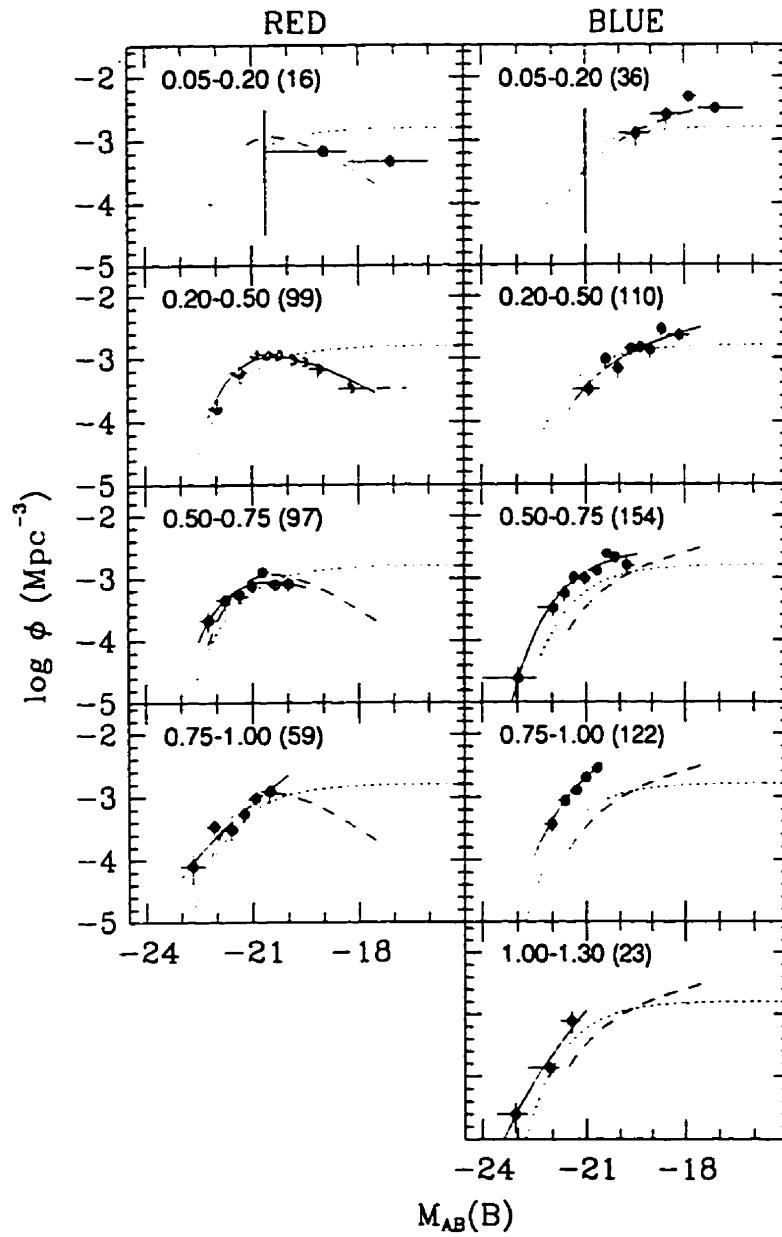


Figure 2.3: The CFRS galaxy luminosity as a function of redshift. Figure taken from Lilly *et al.* (1995).

cannot distinguish between the two. Between $0.2 < z < 0.5$ and $0.5 < z < 0.75$, the luminosity function brightens by about 1 magnitude. There is no change at the bright end when going to $0.75 < z < 1.0$, but there is an additional brightening of 1 mag around $M_{AB}(B) \sim -20$. It is important to note that this observed evolution does not depend on the local luminosity function at all.

Since the current [OII] kinematics survey covers blue galaxies with redshifts $0.25 < z < 0.45$ (see section 5.1), the blue CFRS $0.20 < z < 0.50$ redshift bin is of particular interest here. It is interesting to note that, in this redshift bin, the bright end of the CFRS LF ($M_{AB}(B) \sim -20.5$) is significantly below the Loveday LF whereas the faint end ($M > -19$) lies above it. Since the number of red and blue galaxies is nearly equal, it is reasonable to renormalize the Loveday LF by shifting it down by 0.3 dex. With this renormalization, the bright end of the CFRS LF now agrees with the Loveday LF. This renormalization also leads to much more evolution at $M_{AB}(B) \sim -19.5$ than suggested by the initial layout of Figure 2.3.

The shape of the blue CFRS LF's as a function of redshift is also interesting because it raises the question of whether it can be adequately described by a Schechter function (Schechter, 1976). The blue CFRS LF in the $0.05 < z < 0.2$ and $0.2 < z < 0.5$ redshift bins looks as though it could be fitted by a steep straight line, the $0.50 < z < 0.70$ LF looks more Schechter-like, and the $0.75 < z < 1.0$ LF again looks more like a steep straight line. This behavior is reflected in the values of α . In the $0.50 < z < 0.70$ redshift bin where the blue LF appears to be Schechter-like, α has a value of -1.07 which is close to the Loveday value. In the $0.2 < z < 0.5$ and $0.75 < z < 1.0$ redshift bins,

α has much steeper values of -1.34 and -1.56 . However, as stressed by the CFRS collaboration, there is a limited range of luminosities present in the survey at each epoch, and the parameter values of their Schechter segments were not intended as true determinations. If the luminosity function in the $0.2 < z < 0.5$ redshift bin truly has a steeper slope and a higher normalization than the Loveday LF, then there is room for considerable evolution at $M_{AB}(B) \sim -19$ to -18 at those redshifts.

2.4.2 The Autofib Survey

The Autofib Survey (Ellis et al., 1996) has used the Autofib fibre positioner on the Anglo-Australian Telescope to collect large numbers of redshifts. The collaboration has collected over 1700 redshifts for galaxies with apparent magnitude in the range $11.5 < b_J < 24.0$ to determine the rest-frame B-band galaxy luminosity function (LF) as a function of redshift and star-formation activity from $z = 0$ to $z \simeq 0.75$. The range of apparent magnitudes makes it possible to study the shape of the LF as a function of redshift. (The CFRS could only provide information on ‘‘Schechter segments’’ due to its narrower range of apparent magnitudes.) The Autofib survey used the [OII] emission line as a star-formation activity indicator, and the dividing line between quiescent and active galaxies was set at a rest-frame equivalent width W_λ of 20 \AA .

Locally ($z \leq 0.1$), the Autofib luminosity function is fitted with a Schechter faint end slope of $\alpha \simeq -1.1$ and Schechter normalization ϕ^* of $0.026 \text{ h}^3 \text{ Mpc}^{-3}$, which argues for a high normalization of the local LF. The luminosity function as a function of redshift shows strong evolution, especially for

galaxies with luminosities fainter than L^* . In the redshift ranges 0.15–0.35 and 0.35–0.75, the faint end steepens to $\alpha = -1.41$ and $\alpha = -1.45$. The picture is particularly revealing when the luminosity functions of quiescent and active galaxies are constructed separately. Although the faint end of both LF's is flat locally, the LF of galaxies with $W_\lambda > 20 \text{ \AA}$ steepens to $\alpha = -1.44$ beyond $z = 0.25$ whereas the LF of quiescent galaxies remains flat. The space density of star-forming galaxies decreased at all luminosities by almost a factor of 2 from $z \simeq 0.4$ to $z \simeq 0.15$. This decline corresponds to an *overall* fading of the star-forming population of 0.5 mag over this redshift range. As other redshift surveys, the Autofib survey cannot constrain the luminosity evolution of individual galaxies. The steepening of the overall LF with lookback time is of the form originally postulated by Broadhurst *et al.* (1988).

2.5 Hubble Space Telescope Imaging

The Hubble Space Telescope (HST) has a point-spread-function FWHM of $0''.05$. With this incredible spatial resolution, it is now possible to classify high-redshift galaxies according to the Hubble sequence, and, to quantify galaxy morphology with parameters such as central surface brightness, axial ratio, bulge-to-disk ratio, disk scale length and light profile models (point source, $r^{1/4}$, exponential). Although samples are still fairly small, very interesting results have been obtained, and HST imaging offers the exciting possibility of determining the morphology of the galaxies responsible for the faint galaxy excess.

Axial ratio is the simplest morphological parameter to measure. It appears that the axial ratio distribution of small (half-light radius $< 0''.7$), faint ($I \sim 20.5$) galaxies with exponential surface brightness profile has a marked excess at ratios around 0.7 (round = 1.0) over local samples of spiral galaxies (Im et al., 1995). The excess galaxies are similar to local dwarf galaxies: same axial ratio distribution and colors ($(B-V)_0 \simeq 0.4$, $(U-B)_0 \simeq 0.2$). These “Small Exponential Elliptical (SEE)” galaxies make up 21–25% of the population mix at $20 < I < 21$. Combined with irregular/peculiar galaxies, they could be responsible for up to 80% of the galaxy excess over model predictions. The presence of such large numbers of SEEs could be explained by a steep ($\alpha \simeq -1.4$ to -1.8) local luminosity function or a starburst stage around $z \sim 0.5$ caused by minor mergers.

Other studies (Driver et al., 1995; Glazebrook et al., 1995b) have produced deep ($I \simeq 24.2$ or $B \simeq 26$) morphological number counts based on light profiles, bulge-to-disk ratios and direct images. The counts showed that the galaxy mix at faint magnitudes differs from our local neighborhood. There was a steep rise in the number of late-type and irregular/peculiar galaxies. Sd/Irr galaxies made up 30–50% of the total population as opposed to 8–10% in the CfA survey (Marzke et al., 1994a). The number counts for early-types (E/S0, Sabc) were consistent with little or no evolution if number count models were normalized to the observed counts at $b_J = 18-20$. This normalization was twice as high as the ϕ^* value derived for local surveys (Loveday et al., 1992; Lin et al., 1996). The number counts of late-type/irregular galaxies were modelled in four different ways: (1) a no-evolution model based on the Loveday luminosity function for late-types,

(2) a no-evolution model based on the Marzke LF (Marzke et al., 1994a) for late-types, (3) an evolving model with a burst in the Sd/Irr population at $z = 0.5$, and (4) a dwarf-rich model with $\alpha = -1.8$ and a free normalization chosen to fit the counts. Models (1) and (2) under-predicted the number of observed late-types/Irrs. In model (3), the increase in luminosity required for the entire late-type population to match the counts with the Loveday et al. (1992) LF and with the Marzke et al. (1994a) LF were $\Delta m = 2.0$ magnitudes and $\Delta m = 1.3$ magnitudes respectively. The counts could also be matched with the Marzke et al. (1994a) LF and a $\Delta m = 2.0$ mag increase in luminosity in 20% of the late-type population. These increases in luminosity Δm are consistent with a 1 Gyr burst in a dwarf galaxy followed by an exponential fall-off (see Section 3.1). In model (4), a value of ϕ^* of 3.5×10^{-2} Mpc^{-3} was required to match the counts. This is *five times* the Loveday et al. (1992) normalization, and it is inconsistent with faint redshift surveys as it predicts too many low-redshift objects.

Three interesting results came from a quantitative study of a sample of 32 galaxies with magnitudes $17.5 < I_{AB} < 22.5$ and redshifts $0.5 < z < 1.2$ (Schade et al., 1995). First, galaxies at $z \sim 0.75$ exhibit the same range of morphological types as seen locally (ellipticals, spirals and irregulars). Second, 30% of the sample were so-called “blue nucleated galaxies”. They had asymmetric/peculiar structures and blue, compact components not always centered on the galaxies. Diagnostic line ratios ($[\text{OII}]/\text{H}\beta$ and $[\text{OIII}]/\text{H}\beta$) indicated that the compact components were sites of star formation. As shown later (section 7.3), these blue nucleated galaxies appear to be directly linked to the peculiar $[\text{OII}]$ kinematics observed in our survey even though it covers

a lower range of redshifts. Third, the central surface brightness of galaxies at $z \sim 0.7$ was $\mu_{AB}(B) = 20.2 \pm 0.25$ mag arcsec² – i.e. 1.2 mag brighter than the Freeman value found in local spiral galaxies. This increase in rest-frame surface brightness indicates that galactic disks undergo strong evolution at those redshifts, probably as a result of global star formation.

The work of Schade *et al.* (1995) has recently been extended with dramatic results (Schade *et al.*, 1996a; Schade *et al.*, 1996b). They studied the surface brightness of 351 cluster and field disk galaxies over the redshift range $0.1 < z < 0.6$, and 166 cluster and field early-type galaxies. Both samples were drawn from the CNOC galaxy cluster survey (Carlberg *et al.*, 1994; Yee *et al.*, 1996). Disk *and* early-type galaxies evolve significantly over that redshift range. Moreover, there was no significant difference in evolution in clusters *and* in the field. At redshifts of (0.23,0.43,0.55), the disk surface brightness in cluster and field late-type galaxies was higher in the B-band by $\Delta\mu_0(B) = (-0.58 \pm 0.12, -1.22 \pm 0.17, -0.97 \pm 0.2)$ mag respectively compared to the local Freeman law. For early-type galaxies, their surface brightness increased by $(-0.25 \pm 0.10, -0.55 \pm 0.12, -0.74 \pm 0.21)$ mag at redshifts of (0.23,0.43,0.55) compared to a local $z=0.06$ $M_{AB}(B)$ versus R_e relation. The amount of brightening was consistent with passive evolution of an old, single-burst population. The fact that galaxies evolved similarly in clusters and in the field was remarkable.

HST imaging has shown that late-type/irregular galaxies were responsible for the faint galaxy excess. The exact amount of luminosity evolution remains dependent upon uncertainties in the local luminosity function, but plausible models indicate that it must be at least one magnitude by $z = 0.5$.

Chapter 3

Models

To explain the faint galaxy excess, it is fair to say that there is also an excess in the number of models trying to explain it. When confronted with an excess of faint galaxies, the first step is to decide whether bright, distant galaxies or faint, nearby ones are responsible.

Models can be broadly divided into two scenarios: mergers and luminosity evolution. These scenarios are not mutually exclusive. For example, minor mergers could be triggering bursts of star formation at intermediate redshifts resulting in significant changes to the total luminosity of a galaxy. The two scenarios are simply divided inasmuch as they involve changes in different variables: number density and luminosity. Redshifts surveys have been unable to distinguish between the two since the evolution seen in luminosity functions as a function of redshift can either be fitted by an increase in the Schechter normalization ϕ^* (upward shift of the LF) or an increase in the Schechter luminosity L^* (leftward shift of the LF). This ambiguity is removed in internal kinematics studies since they are able to measure luminosity evolution in individual galaxies. Mergers and luminosity evolution

are discussed below to provide a framework for the interpretation of internal kinematics results.

3.1 Luminosity evolution

Locally, only dwarf galaxies have sufficiently high comoving density to be the counterparts of the faint blue galaxy population at intermediate redshifts; this fact led some to suggest that excess faint galaxies might be dwarf galaxies brightened by bursts of star formation (Broadhurst et al., 1988; Babul and Rees, 1992). The amount of star formation required by this scenario has important implications for metal abundance and gas loss in Irr galaxies (Lilly, 1993).

The Broadhurst *et al.* (1988) “starbursting dwarfs” model is based on the fact that gas content M_{HI} of a galaxy is related to its luminosity, L_g , via a simple relation of the form $L_g \propto M_{HI}^\beta$, and on the reasonable assumption that star-formation rates are proportional to the gas content during a burst. This model could be used to determine a relationship between star formation and galaxy luminosity. For the case $\beta = 1$ (late-type systems have $\beta > 1$), the burst strength is independent of absolute magnitude whereas a large value of β (> 4) produces a strong magnitude-dependence for the burst – i.e. evolution is much more important for lower luminosity galaxies. Dwarf galaxies are therefore selectively brightened up to L^* whereas galaxies now at L^* see their luminosity virtually unchanged. This luminosity-dependent luminosity evolution would explain the absence of a high redshift tail in the redshift distribution of faint blue galaxies and the low median of the redshift

distribution. A 0.1 Gyr burst converting 5 per cent of the galaxy mass into stars is sufficient to increase the B-band luminosity of the galaxy by 2.2 mag.

The amount of star formation produced by this model is limited by metal production considerations. A rough estimate of the far-ultraviolet (2500Å) luminosity of the faint blue galaxies population suggests that, over a timescale of $6 h_{50}^{-1}$ Gyr ($0.2 < z < 1$), a global metal density of approximately $10^{6.3} M_{\odot} \text{Mpc}^{-3}$ (independent of H_0 and q_0) will be produced. This is an order of magnitude larger than the metal density ($\sim 10^{5.0} h_{50} M_{\odot} \text{Mpc}^{-3}$) seen in the local Irr galaxies with comparable comoving density (Lilly, 1993). To avoid this metal enrichment problem, star-bursting galaxies would have had to remove 90% of their metal enriched gas. This is not ruled out by current gas loss models (Dekel and Silk, 1986), but the intergalactic medium would be considerably enriched.

Babul and Rees (1992) proposed a model in which faint blue galaxies were an entirely new population with a comoving density higher than any local population. In their model, faint blue galaxies were low-mass galaxies experiencing their starburst at $z \sim 1$. To explain the formation of faint blue galaxies, they used a generic hierarchical model in which mini-haloes ($M \sim 10^9 M_{\odot}$) condensed from the expanding background and virialized at a redshift of about 3. The onset of star formation was delayed by the UV intergalactic background radiation produced by quasars and/or by young galaxies. At $z=2$, this UV background was sufficiently intense to keep the gas trapped in the potential wells of the mini-haloes in a photoionized state. Thus, the gas could not concentrate towards the center to become gravitationally unstable and form stars. From $z=2$ and the present epoch, the UV background

strength fell sharply by a factor of about 100. It ceased to be able to photoionize a protogalaxy around $z = 1$, and star formation began at that epoch. A few million years thereafter, the first generation of supernovae began to explode. These explosions pumped enough energy in the interstellar medium to trigger a gas outflow. In low density regions where the pressure of the intergalactic medium (IGM) was low, all the gas was ejected from the galaxy. The loss of gas quenched star formation, and the galaxy faded away. In high density regions, the IGM stopped the escaping wind, and the gas then fell back on to the core where it was reprocessed in repeated bursts. These galaxies then evolved to become the present-day dwarf ellipticals seen within regions of high IGM density – i.e. around giant galaxies. It is interesting to note that the result of such an episodic star formation scenario may have been observed in the Carina dwarf spheroidal (Smecker-Hane et al., 1994).

3.2 Merger model

To circumvent the metal production problem and the absence of a high-redshift tail in redshift distributions, others (Rocca–Volmerange and Guiderdoni, 1990; Broadhurst et al., 1992) have suggested a high merger rate for the faint blue galaxies to reduce their $z \sim 0.4$ comoving density to the present-day value. A consequence of this strong merger model is that most metals would end up in L^* galaxies, where they are found today. However, this picture suffers from several problems.

Only roughly 15% by light of the galaxies at $z = 0.35$ can merge into ellipticals, otherwise there would be too much blue light in local elliptical galaxies

(Dalcanton, 1993). Only 4–15% by mass of the galaxies at $z=0.35$ can be removed by merging into spiral galaxies. More extensive merging could violate the constraints on the thinness of spiral disks (Tòth and Ostriker, 1992; Dalcanton, 1993). This constraint is based on the assumption that the energy deposited in disks by mergers goes into random motion (“disk heating”). However, if spiral disks are more resilient and the energy goes into exciting coherent modes in disks as suggested by others (Huang and Carlberg, 1996), then present-day galaxies could have accreted satellites with up to 25-30% of their mass without detectable thickening of their disks.

Faint galaxies are surprisingly weakly clustered (Efstathiou et al., 1991). Their clustering amplitude, a factor of 2 lower than local normal galaxies, is similar to that of local starbursting and HII galaxies (Infante and Pritchett, 1995). Merger rates required to remove the excess galaxies are uncomfortably large as a typical galaxy at $z = 0.3$ must merge with 15-30% of all its neighbors within $750 h_{100}^{-1}$ kpc (Bernstein et al., 1994). In other, milder merger scenarios (Carlberg and Charlot, 1992), galaxies undergo extensive merging between $z = 1$ and $z = 0.5$. At $z = 1$, the characteristic galaxy mass is 25% of the $z = 0$ value. Interactions at $z < 0.5$ mainly brighten and blue galaxies with little change in comoving density.

Chapter 4

Internal Kinematics of Distant Galaxies

4.1 A Critical Test

Internal kinematics directly measures a fundamental property of galaxies: mass. It can therefore be a powerful probe of the nature of intermediate redshift galaxies. The idea is simple: if intermediate redshift galaxies are as massive as “normal” spirals such as the Milky Way (instead of being dwarf galaxies), we would observe rotation velocities of ~ 200 km/s. On the other hand, if they are really lower mass objects that have been boosted in luminosity by $\sim 10\times$ as suggested in the luminosity-dependent luminosity evolution scenario, then the TF relation predicts that their rotation velocities will be ~ 100 km/s. This approach is direct. It is not affected by uncertainties in models based on local luminosity functions. Also, whereas luminosity functions derived from redshift surveys show the evolution of a population as a whole, the present approach can measure luminosity boosting in individual galaxies and can thus tie luminosity boosting directly to other galaxy properties on

a *galaxy by galaxy* basis.

Luminosity evolution will shift the Tully-Fisher relation to brighter magnitudes at intermediate redshifts. If merging has been a significant process in the evolution of galaxies over the last 5–6 Gyrs, galaxies should be less massive at $z \sim 0.4$. This would shift the Tully-Fisher relation to lower rotation velocities. It would seem at first glance that the two effects cannot be disentangled. However, significant mergers would certainly modify the structure (e.g. disk scale length) of galaxies as a function of time. Therefore, pure luminosity changes can be isolated by comparing the luminosity of intermediate redshift galaxies with the luminosity of local galaxies with the same size and rotation velocity.

4.2 Previous Studies

Most previous kinematical studies (Franx, 1993; Vogt et al., 1993; Colless, 1994; Koo et al., 1995; Forbes et al., 1995) have either suffered from small samples or the lack of spatial information, but they have shown that current telescopes can tackle the task of measuring the internal kinematics of intermediate redshift galaxies. In cases where spatial information was available, galaxies were typically at low redshifts and had relatively large intrinsic sizes.

Two studies had spatial information. Franx (1993) used the Multiple-Mirror Telescope (MMT) to measure the rotation curve of an E+A galaxy in Abell 665 at $z = 0.18$. The galaxy had an exponential disk scale length of $6.5 h_{50}^{-1}$ kpc, and its circular velocity was estimated at $\simeq 270$ km/s. The galaxy was offset by -2.2 mag from the Faber-Jackson relation and by -0.3

mag from the Tully-Fisher relation. Vogt *et al.* (1993) used the Hale 5-m telescope to observe the [OII] doublet ($\lambda\lambda 3726, 3729$) and the [OIII] line pair ($\lambda\lambda 4959, 5007$) in four galaxies at redshifts between 0.20 and 0.38. These galaxies were large intrinsically and had unusually strong [OII] emission. Two galaxies had [OII] emission concentrated in the nucleus. The other two galaxies had rotation velocities of 166 and 253 km/s which corresponded to offsets from the Tully-Fisher relation of -3.1 and -0.9 mag respectively.

Colless (1994) observed 54 galaxies with the Autofib fibre spectrograph on the AAT. The galaxies had redshifts in the range 0.15–0.35, [OII] equivalent widths $> 20 \text{ \AA}$, $b_J - r_F$ colors < 1.2 and b_J magnitude in the range 21.25–22.0. Twenty-four galaxies had detectable [OII] emission. Of the 24 detections, 9 had $\sigma < 70$ km/s and 15 had σ in the range 70–200 km/s (11 had $\sigma > 100$ km/s). The preliminary conclusion of this work was that although some galaxies at $z = 0.15$ –0.35 may be dwarfs, the majority had velocities typical of normal present-day galaxies.

Koo *et al.* (1995) measured line widths in a sample of 17 galaxies at $z \sim 0.1$ –0.7 with the Keck telescope. Twelve of these galaxies were compact (stellar-like), narrow emission line galaxies (CNELGSs), and five were more extended objects with colors and emission lines similar to CNELGSs. The galaxies were all luminous with $M_B \sim -21$. Measured velocity widths were between 28 and 157 km/s instead of $\sigma \sim 200$ km/s expected for nearby spiral galaxies of similar luminosity. Objects with $\sigma < 65$ km/s followed the same correlations between σ and both blue and H_β luminosities as those of nearby HII galaxies (Telles and Terlevich, 1993).

Forbes *et al.* (1995) measured velocity line widths in 18 faint field galax-

ies with $19 < I < 22$ and $0.2 < z < 0.4$. Their sample showed a brightening of ~ 1 mag in the luminosity-disk size and luminosity-internal velocity relations. However, their determination of brightening in the luminosity-internal velocity relation appears to have been measured with respect to the Rubin *et al.* (1985) relations. The slopes of these relations are incorrect as shown in Figure 8.4, and lead to an underestimate of the luminosity brightening.

A recent internal kinematics study (Vogt *et al.*, 1996) presented a beautiful set of rotation curves for nine faint field galaxies in the redshift range $0.1 \leq z \leq 1$ observed with the Keck Telescope. The rotation curves appeared similar to those of local galaxies in both form and amplitude. The galaxies in this Keck sample were all brighter than $M_B = -20.7$ except for two galaxies with $M_B = -19.3$ and $M_B = -19.8$. Their sample therefore was a full magnitude brighter in absolute magnitude than the CFHT sample presented in Section 5.1. Owing to limited spatial resolution, the galaxies in the Keck sample were intrinsically big. Their disk scale lengths were all greater than 3.0 kpc except for one galaxy with a scale length of 1.8 kpc. These intrinsic sizes were much larger than the typical size of the objects studied in this thesis. Clearly, the two samples occupy different niches, and this has very interesting consequences as discussed in Section 8.4. The Keck study showed that at least some massive disks were in place at $z \sim 1$. The kinematics of the Keck galaxies showed evidence for only a modest increase in luminosity ($\Delta M_B \leq 0.6$ mag) compared to the local Tully-Fisher relation of Pierce and Tully (1992). This is not surprising considering that all the galaxies are bright and massive. One would *not* expect to see any brightening in these galaxies based on a luminosity-dependent luminosity evolution

scenario. This issue is further discussed in Section 8.4.

4.3 Spatially-Resolved [OII] Internal Kinematics

4.3.1 Physics of the [OII] emission line doublet

Young, bright stars are usually embedded in clouds of gas which are photoionized by energetic photons from these stars. The $H\alpha$ Balmer line of hydrogen at 6562.8 \AA is the best tracer of star formation because in ionization-bounded HII regions, the Balmer emission line luminosities scale directly with the ionizing fluxes of the embedded stars. The $H\alpha$ line can therefore be used to derive quantitative star formation rates in galaxies. However, beyond redshifts of $z=0.2-0.3$, $H\alpha$ becomes redshifted to the near infrared where many strong sky emission lines are present.

UV radiation produced by young, massive stars shortward of 730 \AA is sufficient to photoionize heavier elements such as neutral oxygen. The [OII] $\lambda\lambda 3726-3729 \text{ \AA}$ doublet is the strongest feature after $H\alpha$. [OII] equivalent widths are well correlated with $H\alpha$, but [OII] has on average half the flux as $H\alpha$. The [OII] doublet is the most prominent feature in the spectra of faint galaxies in the blue, and it is a prime candidate for tracing the internal kinematics of the ionized gas. The ${}^2D_{3/2} \rightarrow {}^4S_{3/2}$ and ${}^2D_{5/2} \rightarrow {}^4S_{3/2}$ transitions give rise to the 3726.1 \AA and 3728.8 \AA emission lines respectively.

At temperatures typical of star-forming regions ($T \sim 10000-20000 \text{ K}$), the excitation energy between the two upper 2D levels and the lower ${}^4S_{3/2}$ level is of the order of the thermal electron energy kT . The [OII] doublet is

therefore closely linked to collisional excitations and de-excitations – i.e. to the electronic density N_e (Osterbrock, 1974). Since the two 2D levels have nearly the same excitation energy, the relative excitation rates of the two levels depend only on the ratio of collision strengths. In the low-density limit $N_e \rightarrow 0$, every collisional excitation will be followed by the emission of a photon since the radiative transition A coefficient will dominate the decay probability to the lower level. The relative excitation rates of the ${}^2D_{5/2}$ and ${}^2D_{3/2}$ levels are proportional to their statistical weights. Since the z-axis components of the total angular momenta J_z of the ${}^2D_{5/2}$ and ${}^2D_{3/2}$ levels have a six-fold and four-fold degeneracy respectively, the ratio of strengths of the two lines in this low-density limit is $j_{\lambda 3729}/j_{\lambda 3726} = 1.5$. In the high density limit $N_e \rightarrow \infty$, collisional excitation and de-excitations dominate and set up a Boltzmann population ratio. The relative populations of the two levels ${}^2D_{5/2}$ and ${}^2D_{3/2}$ are in the ratio of their statistical weights, and the relative strengths of the two lines are in the ratio

$$\frac{j_{\lambda 3729}}{j_{\lambda 3726}} = \frac{N_{2D_{5/2}} A_{\lambda 3729}}{N_{2D_{3/2}} A_{\lambda 3726}} = \frac{3 \cdot 4.2 \times 10^{-5}}{2 \cdot 1.8 \times 10^{-4}} = 0.35 \quad (4.1)$$

$A_{\lambda 3726}$ and $A_{\lambda 3729}$ are the ${}^2D_{3/2} \rightarrow {}^4S_{3/2}$ and ${}^2D_{5/2} \rightarrow {}^4S_{5/2}$ radiative transition probabilities (Osterbrock, 1974). The [OII] intensity ratio measures the electron density best in the neighborhood of $N_e \simeq 10^3 \text{ cm}^{-3}$, and it could be used to measure electron density as function of position within intermediate redshift galaxies.

4.3.2 An Internal Kinematics Survey at CFHT

Spatial information is crucial in studies of the internal kinematics of intermediate redshift galaxies. The line emission must be spatially-resolved to ascertain that the [OII] kinematics is actually coupled to the rotation (i.e. mass) of galaxies. It may not always be the case. For example, the nucleus of a galaxy could be undergoing massive star formation, and the [OII] emission could all be concentrated in the nucleus. Winds from a few giant HII regions could dominate the [OII] line widths making them unusable as virial measurements of galaxy mass. Rotation can be readily seen in spectra with good spatial information as a “S-shaped” or “tilted” line emission. The use of the Tully-Fisher relation as a comparison will only be valid for galaxies in which a rotational component has been identified and isolated from other types of motion (random, radial, etc.) which may be present.

Low-order, “tip/tilt” image stabilization systems have been in operation at the Canada-France-Hawaii Telescope (CFHT) for a few years now. The Subarcsecond Imaging Spectrograph (SIS) is the latest example of such a system (see section 5.2.1). These systems improve the seeing FWHM by 0'2-0'3 and routinely deliver images with 0'5 FWHM seeing. It was thus possible to obtain spatially resolved spectra of relatively compact (effective radius $\sim 1''$) intermediate redshift galaxies. CFHT was ideally suited for a survey of the internal kinematics of field galaxies with redshifts in the range 0.25–0.45 using the [O II] $\lambda\lambda 3726\text{--}3729$ Å emission line doublet as a kinematical tracer. The availability of the CNOC cluster survey database (see section 5.1) which contained information on a large number of galaxy

candidates suitable for internal kinematics observations greatly facilitated target selection.

The survey was aimed at answering a number of questions: (1) What kind of kinematics do intermediate redshift galaxies have?, (2) What are the masses of intermediate redshift galaxies?, (3) Is there a systematic shift in the intermediate redshift Tully-Fisher relation as described in section 4.1?, (4) Is the TF slope the same as the local one or equivalently, is the shift from the local TF mass-dependent? and (5) Do galaxies with the same mass undergo different amounts of luminosity boosting? If yes, what is (are) the other underlying parameter(s)?

The answer to question 1 may not be as obvious as one might think at first sight. Very little was known about [OII] kinematics in intermediate redshift galaxies at the time this survey was started, and yet Question (1) lay at the heart of any proposal to use internal kinematics to study galaxy evolution. A wide range of [OII] kinematics would indicate that a number of processes are responsible for the star formation activity seen at intermediate redshifts. Questions (3) and (4) address what kind of evolution excess galaxies might be undergoing. Luminosity-dependent luminosity evolution predicts that some L^* galaxies should be low-mass galaxies significantly shifted from the local TF relation whereas other L^* galaxies should be massive galaxies with little or no deviation from the local TF relation. A systematic TF shift preserving the slope of the local relation would rule out luminosity-dependent luminosity evolution. An answer to Question (5) may elude the present survey as a larger sample will probably be required to explore the dependence of luminosity boosting on various galaxy properties.

Chapter 5

Data

5.1 Sample Selection

The Canadian Network for Observational Cosmology (CNOC) cluster survey (Carlberg et al., 1994; Yee et al., 1996) mapped 16 intermediate redshift galaxy clusters selected by X-ray luminosity with the goal of determining cluster mass profiles and the cosmological density parameter Ω . The survey data base contains direct Gunn r and g MOS images, 2D spectra and extracted 1D spectra for thousands of galaxies. Position, Gunn r total magnitude, Gunn $g - r$ color, and redshift were determined by the CNOC collaboration for each galaxy. In order to provide field contamination estimates, 1/3 to 2/3 of the galaxies in a typical CNOC field were field galaxies unassociated with the clusters. This large subset of field galaxies with known properties was ideal for the preparation of efficient multi-object spectroscopy runs.

Four CNOC clusters (EMSS1512, EMSS1621, Abell 2390 and EMSS0015), which were visible at the time the observations were scheduled (July-August

1994), were selected. Using the CNOC spectral classification index S_{cl} assigned to each galaxy, the catalog files went through a first pass to pick out all objects with $S_{cl} = 5$ (emission line). The S_{cl} index is based on the template giving the best cross-correlation peak. A second pass through the catalog files identified field galaxies. In order for a galaxy to be identified as part of the field, its redshift had to be in the range 0.25–0.45 and at least 0.02 above or below the mean CNOC cluster redshift. A $1' \times 1'$ area was extracted around each field emission line object on both the Gunn r and g images. These postage stamp images were used to calculate galaxy position angles. The position angle of each object was determined in both colors by fitting galaxy isophotes with ellipses using the task ELLIPSE in the IRAF/STSDAS package ISOPHOTE. The position angles were used at the telescope to align slitlets with the major axis of the primary target galaxy (see section 5.2).

The major limiting factor of internal kinematics studies on a 4-m class telescope is flux. [OII] strong objects were selected according to their [OII] equivalent widths. Equivalent widths were measured from the CNOC 1D extracted spectra by fitting a Gaussian to the [OII] line using SPLOT in the IRAF/NOAO package ONEDSPEC. The observed equivalent widths were corrected to their rest-frame value by dividing them by $(1+z)$. Objects with equivalent widths in the range 20–50 Å were selected as targets. This inevitable selection criterion complicates the task of tying intermediate redshift samples with the diverse (and often poorly known) local galaxy population. Although such [OII] strong objects could be locally regarded as extreme, they are representative of the excess galaxy population at intermediate redshifts (Broadhurst et al., 1988; Broadhurst et al., 1992; Kennicutt, 1992).

Locally, there is a dependence of [OII] equivalent width on galaxy type. The target galaxies may be [OII] strong relative to early-type (Sb and earlier) spirals which have [OII] equivalent width not exceeding 20\AA , but they have the same [OII] equivalent widths as many late-type (Sc and later) galaxies (Kennicutt, 1992) which have equivalent widths between 20 and 60\AA . The claim made in many studies that local galaxies have [OII] equivalent widths lower than 20\AA is incorrect.

To summarize the target selection process, target galaxies had to be emission-line objects in the field with redshifts in the range 0.25–0.45 and [OII] equivalent widths greater than 20\AA . No selection was made on the basis of size or color. The next step consisted of maximizing the number of galaxies that could potentially be observed with a multi-object spectrograph. A group was formed around each target galaxy by drawing a square the size of the SIS field ($3' \times 3'$) with the same position angle as the galaxy's major axis and counting the neighboring galaxies falling within the square. A number of considerations dictated the choice of the best target fields: total number in group, [OII] strength, elongated galaxy images, and a usable guide star for SIS adaptive optics corrections (see section 5.2).

The characteristics of the target galaxies are shown in Table 5.1. Column 1 is the galaxy identification (ID). The first part of a galaxy ID is the name of the CNOC cluster around which the field was observed, and the second part is the PPP number identifying a galaxy in the CNOC catalog file. Columns 2-4 are the galaxy redshift, CNOC Gunn r magnitude and $g - r$ color. Columns 5-6 are the Johnson B band apparent magnitude and the rest-frame Johnson B absolute magnitude described below. Target

galaxies span a wide range of absolute B magnitudes ranging from -21.7 to -18.2 . Column 7 is the rest-frame [OII] equivalent widths determined from the CNOC 1D extracted spectra, and column 8 is the expected H_α rotation velocity corresponding to M_{B_0} according to the absolute calibration of the local B band Tully-Fisher relation (see Section 8.1). Column 9 is the exponential disk scale length measured from fits to the luminosity profiles of the target galaxies (see section 7.1).

Rest-frame absolute B band magnitudes are key quantities in the present study. They were calculated from the CNOC Gunn r magnitudes and $g-r$ colors as follows. M_{B_0} is given by

$$M_{B_0} = r_{obs} + (B - r) - k_B - 5 \log d_L + 5 \quad (5.1)$$

where r_{obs} is the observed Gunn r apparent magnitude, $(B-r)$ is the color index necessary to convert r to B at the redshift of the galaxy, k_B is the so-called B k-correction, and d_L is the luminosity distance computed in a $H_0 = 75 \text{ km s}^{-1} \text{ Mpc}^{-1}$ and $q_0 = 0.5$ universe. The k-correction is needed to account for the fact that a filter with a fixed bandpass will “see” different regions of a galaxy’s spectral energy distribution with increasing redshift and that the energy seen by a filter decreases by a factor of $(1+z)$ due to wavelength stretching by the cosmological expansion. The k-correction is thus defined as

$$k(z) = 2.5 \log \frac{\int F(\lambda) S(\lambda) d\lambda}{\int F[\lambda/(1+z)] S(\lambda) d\lambda} + 2.5 \log(1+z) \quad (5.2)$$

where $F(\lambda)$ is the galaxy spectral energy distribution (SED), and $S(\lambda)$ is

the filter response function (King and Ellis, 1985). Frei and Gunn (1994) computed tables of galaxy colors (including $B-r$) and B k-corrections for galaxy types E, Sbc, Scd and Im. The $(B-r)$ color and the B k-correction k_B in equation 5.1 were computed by interpolating the Frei and Gunn (1994) tables to obtain two bivariate functions f and h such that $B-r = f(g-r, z)$ and $k_B = h(g-r, z)$. The functions f and h were both calculated with the IRAF SURFIT and two third-order interpolation schemes (Legendre and polynomial) as a consistency check. The observed Gunn $g-r$ color was used as an indicator of galaxy type. M_{B_0} values obtained with the Frei and Gunn (1994) tables were double-checked against those obtained in a much indirect way from the filter transformations and k-corrections given in King and Ellis (1985), Windhorst *et al.* (1991) and Metcalfe *et al.* (1991). The systematic discrepancy between the two methods did not exceed 0.1 mag although the difference in M_{B_0} could reach 0.3 mag for some galaxies. The M_{B_0} values based on the Frei and Gunn (1994) tables were adopted as the true values because they were computed in a more direct way using more recent work.

5.2 Observations

5.2.1 MOS/SIS

Observations were obtained with the Multi-Object Spectrograph (MOS) and the Subarcsecond Imaging Spectrograph (SIS) (LeFèvre *et al.*, 1994) at the Canada-France-Hawaii 3.6-m Telescope (CFHT) on Mauna Kea, a dormant volcano on the Big Island of Hawaii. MOS and SIS are two distinct spectrographs sharing a common interface behind the telescope bonnette.

MOS is optimized for multi-object observations over a large ($10' \times 10'$) field with a spatial sampling of $0''.315/\text{pixel}$ for $15 \mu\text{m}$ pixels. SIS is designed for high spatial resolution observations over a smaller field of view ($3' \times 3'$) with a better pixel sampling of $0''.0866/\text{pixel}$ for $15 \mu\text{m}$ pixels. The MOS/SIS interface is mounted at the F/8 Cassegrain focus.

One of the characteristics of SIS is a fast moving mirror providing tip/tilt image stabilization. The point-spread-function (PSF) is the image of an unresolved source produced by the telescope, and it is often approximated by a Gaussian function. The atmosphere distorts the planar wavefront coming from distant objects. Wavefront distortions are introduced on all scales. On the largest scales, these distortions called tip and tilt shift the centroid of the PSF around on timescales of 0.25 seconds. These are the distortions corrected by SIS's fast-moving mirror. Wavefront distortions on smaller scales increase the width of the PSF, and they must be corrected with faster, higher order systems such as the CFHT AO Bonnette.

SIS requires a relatively bright ($V \sim 18$) guide star. The tip/tilt corrections are measured using a quadrant detector mounted on a moving guide probe. The probe can be moved anywhere in the SIS field of view, but, in practice, the guide star must lie near the corner of the field. Otherwise, the probe mount can occult close to $1/3$ of the field of view. SIS fast guiding yields typical resolution improvements of $0''.2-0''.3$ and routinely delivers images with $0''.5$ seeing. A seeing FWHM of $0''.5$ corresponds to scales $< 1.5h_{100}^{-1}$ kpc at $z = 0.35$ ($q_0 = 0.5$).

5.2.2 SIS Observations

SIS observations were scheduled for July 3-6, 1994 (3 nights, spectroscopy) and August 6-8, 1994 (2 nights, deep B and I imaging). The instrumental configuration consisted of the B600 grism and a LORAL 2048×2048 CCD detector (“LORAL3”). Slit widths were 0'6 and 0'8. The CCD detector was binned by 2 in both the spatial and dispersion directions for improved signal-to-noise ratios. The SIS instrumental configuration is described in Table 5.2, and the characteristics of the LORAL CCD are given in Table 5.3.

SIS observing involved a complex procedure which required up to 20 minutes of set-up overhead per field for an experienced observer. The first step was to rotate the telescope's Cassegrain bonnette to the position angle of the major axis of the primary target and to move the telescope to the target field. Once the telescope was in position, a direct, short exposure image was taken to determine the exact pixel coordinates of the primary target and the guide star. The guide probe was then moved to the guide star coordinates, and SIS guiding was initiated. The telescope position was then fine-tuned with a series of SIS-offsets such that all the target objects were centered on their respective slitlets. SIS-offsets moved the telescope while maintaining the guide probe locked on the guide star. The final telescope position was checked by taking a direct (no filter, no grism) image through the multi-object mask. Multi-object masks were created by laser cutting slitlets at the positions of the targets measured on a direct image.

The SIS observation log is shown in Table 5.4. Typical total integration time per galaxy was 7200 seconds. For each galaxy, the total exposure time

was split between 2–3 exposures to identify and flag pixels hit by cosmic rays (see section 5.3). In July, 3/4 of the first night was lost to very poor seeing conditions ($\text{FWHM} > 1''.6$), and mediocre quality images were obtained without SIS fast guiding. Towards the end of the night, it was possible to take direct images for mask making. The first half of the second night was lost due to clouds, and a conflict between SIS guiding and the Telescope Control System (TCS). The telescope kept losing its position lock whenever SIS guiding was turned on.

The first multi-object spectroscopy exposure taken after solving the tracking problem revealed that something was terribly wrong with the mask alignment. There was a small rotation between the multi-object mask and the direct image used to create it. The positions of slitlets far from the center of the field were completely off their intended targets. The problem remained unsolved until after the second SIS run in August. It was traced back to lateral screw adjustments in the SIS mask holders which had never been adjusted since the commissioning of SIS. Each of the four SIS mask holders suffered from different amounts of rotation. Therefore, SIS had to be used in long-slit mode for the remainder of the July run and all of the August run, and the number of targets actually observed was considerably lower than expected. Three objects were successfully observed during the third night of the July run.

Weather conditions during the August run were good with a typical seeing of $0''.6$. Only two hours were lost when the CCD warmed up unexpectedly. Unfortunately, the seeing during these two hours went down to $0''.4$! Two objects were observed on the first night. Observations of a third object were

ruined by high CCD temperature. Four objects were observed on the second night.

5.2.3 MOS Observations

MOS observations were conducted as a secondary observing program during 1.5 nights of engineering/discretionary time on July 27-28, 1994. The first half-night was plagued by high humidity, but one field was successfully observed. Weather was good on the second night except for high altitude cirrus clouds towards the end. Two fields were observed. The bonnette angle had to remain fixed for the needs of the primary observing program. Slitlets in these multi-object MOS observations were aligned along the major axis of a galaxy only when the galaxy position angle corresponded to the bonnette angle of the telescope. Misalignments between the position angle of the major axis of a target galaxy and the position angle of the slitlet artificially decrease the magnitude of $V_{\text{rot}} \sin i$. The velocity error depends on slit width, seeing, and the rotation curve in the central regions of the target galaxies.

5.3 Pre-Processing

In this section, the pre-processing steps needed to convert raw data frames to 2D spectra suitable for analysis by ELFIT2D are described. The first steps were the overscan and bias corrections. Each CCD pixel value starts from a different initial value. These pixel-to-pixel zero-point differences seen in zero second exposures called bias frames are usually described by the sum of a mean zero-point level and a bias structure. The bias structure has zero

mean as it gives only the fluctuations about the mean zero-point level. The bias structure usually does not change from frame to frame, but temperature variations in the CCD electronics environment introduce changes in the mean zero-point level. These changes are removed by subtracting the overscan value row by row from each frame including bias frames. Each frame has a section which is continuously clocked during an exposure. The overscan value of a given row is the mean value of the same row in the overscan region. The overscan-subtracted bias frames give the bias structure. Eleven bias frames were taken every night and were “average combined” after overscan subtraction using the IRAF task IMCOMBINE. The highest and lowest pixel were rejected at each pixel location before the average was computed. The resulting bias structure frame was subtracted from all overscan-subtracted data frames taken on the same night.

In addition to pixel-to-pixel zero-point variations, CCD detectors have pixel-to-pixel variations in sensitivity which introduce an extra variance in the noise proportional to the flux received during the exposure. There may also be large scale sensitivity variations across the CCD chip. These sensitivity variations are removed by dividing data frames by uniformly illuminated images (dome lights or twilight sky) called flat fields. Flat field images were taken on nights when direct images were taken. The flat field images for each night were scaled by their mode and average combined with a $3\text{-}\sigma$ clipping to remove bad pixel values. Data frames were then divided by the combined flat image to produce flat fielded images. This flat fielding successfully removed “rings” on the direct images caused by dust particles on the CCD dewar window. Spectroscopic data were not flat-fielded for the following reasons:

(1) Every time a correction is applied to a data frame, there is degradation of the original signal-to-noise ratio. Since flat field noise is proportional to flux and flux levels were very low, flat field noise was not significant. (2) spatially-resolved emission lines are very small in extent compared to the total area of the detector. Large scale variations in sensitivity do not affect velocity and size measurements, but they do preclude direct comparisons of the measured emission-line fluxes.

Since the spectroscopic data frames were read-out noise limited, it was important to limit the number of exposures on a given object. In many cases, only 2 long exposures were taken. The passage of cosmic ray secondaries or radioactive decay products through CCD detectors can produce hundreds of spikes of charge on the images. Each spike is usually confined to a few pixels. The cosmic ray rates at a high altitude site such as Mauna Kea is much larger than at sea level. Having a small number of exposures complicates cosmic ray removal. Hubble Space Telescope images are particularly affected by cosmic rays, and the number of exposures is also typically small. Cosmic ray removal on HST data is performed by comparing the difference in pixel values in consecutive images taken at the same telescope position to the background noise of the images. Pixels with values differing by more than 10σ , say, have probably been hit by a cosmic ray (Windhorst et al., 1994). The same approach was adopted for the present data. Series of consecutive data frames were summed together using an IRAF/SPP task called REMCOS. Pixels with consecutive values differing by more than 10σ were flagged by a large negative value (-9999.99). The spatially-resolved emission-line analysis program ELFIT2D recognizes this large negative value as a cosmic

ray pixel and does not include these pixels in its synthetic rotation curve fits (see chapter 6). Such a high rejection threshold should not bias pixel values in the final summed frames. Indeed, image statistics and pixel value histograms of the final frames were the same as those of the individual images before summation.

In order to isolate the emission line flux, it was necessary to perform two background subtractions: sky (rows) and continuum (columns). Sky subtraction was performed on the 2D spectra using the IRAF/LONGSLIT task BACKGROUND. BACKGROUND was used to fit the 2D spectra *row-by-row* with a second order Legendre function with one 2.5σ rejection iteration. The continuum was removed by fitting the 2D spectra *column-by-column* in two continuum windows, one on each side of the emission line. The result of these background subtractions was a 2D image of the emission line flux. For each galaxy, it was important to find the center of the [OII] emission. In most galaxies, the continuum was used to define the x-coordinate (i.e. the position along the slit) of the center, and the y-coordinate of the center was taken to be the point where the [OII] emission crossed the continuum. In the absence of a continuum, an [OII] intensity-weighted centroid was used to define the [OII] center. Finally, a small image section was extracted with IRAF/IMCOPY around each spatially-resolved line for synthetic rotation curve analysis (see chapter 6). The final sample was made up of 22 spatially-resolved [OII] spectra.

Table 5.1: Characteristics of Target Galaxies

ID	z	Gunn r_{obs}	Gunn $(g-r)_{obs}$	B	M_{B_0}	[OII] EW ₀ (Å)	V_{rot}^{TF} (km/s)	$r_d^{optical}$ (h_{100}^{-1} kpc)
A2390-101033	0.2460	18.90	0.70	19.8	-20.3	55	208	2.4 ± 0.2
A2390-100686	0.3822	21.22	0.67	21.7	-19.4	21	155	1.2 ± 0.3
A2390-350416	0.2558	20.14	0.27	20.7	-19.5	35	160	1.7 ± 0.3
A2390-350471	0.2559	19.40	0.28	19.9	-20.3	21	208	1.4 ± 0.2
E1512-301037A	0.3457	21.41	0.19	21.8	-19.1	41	140	3.8 ± 0.2
E1512-301037B	0.3457	21.41	0.19	21.8	-19.1	41	140	3.8 ± 0.2
E1512-101526	0.4026	20.36	1.12	21.0	-20.2	48	202	3.1 ± 0.1
E1512-201429	0.4231	20.44	0.56	20.9	-20.4	26	215	1.8 ± 0.2
E1621-100515	0.3455	20.00	0.42	20.6	-20.3	22	208	1.5 ± 0.2
A2390-100225	0.3829	21.65	0.89	22.2	-18.9	26	131	1.2 ± 0.1
A2390-101084	0.2302	17.31	0.68	18.2	-21.7	110	327	2.8 ± 0.4
A2390-200928	0.2645	21.51	0.22	22.0	-18.2	40	103	1.0 ± 0.2
A2390-200802	0.3208	21.16	0.37	21.6	-19.1	25	140	1.2 ± 0.1
A2390-200372	0.3485	20.15	0.65	20.7	-20.2	16	202	1.7 ± 0.3
E1512-201845	0.3387	19.60	0.82	20.3	-20.5	36	222	4.8 ± 0.3
E1512-201773	0.3383	20.06	0.35	20.5	-20.3	26	208	1.5 ± 0.3
E1512-200730	0.4266	21.35	0.58	21.8	-19.5	32	160	1.5 ± 0.2
E1512-200334	0.4142	21.81	0.70	22.3	-19.0	36	136	1.5 ± 0.4
E1512-200672	0.4152	21.85	0.43	22.2	-19.1	29	140	1.3 ± 0.2
E1512-201268	0.3412	21.77	0.39	22.2	-18.6	29	119	1.2 ± 0.2
E1512-202096	0.4252	20.33	0.66	20.8	-20.5	23	222	1.8 ± 0.3
E1512-201125	0.3823	21.69	0.74	22.2	-18.9	15	131	1.4 ± 0.2

Table 5.2: MOS and SIS Instrumental Configurations

	MOS	SIS
Grism	B600	B600
Dispersion ($\text{\AA}/\text{pix}$)	1.58	0.88
Slit width (")	1.0	0.6 and 0.8
Spectral Resolution (\AA)	5.0	3.0 and 4.0
Image Scale ("/pix)	0.315	0.173
Typical Seeing (")	1.0–1.2	0.6

Table 5.3: Characteristics of the CFHT LORAL3 CCD Detector

Characteristic	Description
Manufacturer	Loral
Size	2048 \times 2048
Pixel size	15 μm
Nominal gain	1.9 e^-/DU
Read noise	8.0 e^-
Nominal bias	1000 DU
Full well	> 80000 e^-
Dark current	0.25 $e^-/\text{min}/\text{pixel}$
Nonlinearity	< 0.5%

Table 5.4: Observation Log – Part 1

ID	Date	RA DEC (1950.0)	MOS/ SIS	Exposure Time (seconds)	Slit Width (")	Seeing FWHM (")
A2390-101033	06/07/94	21:51:10 17:27:18	SIS	3×2400	0.6	0.56
A2390-100686	06/08/94	21:51:04 17:26:15	SIS	2×3600	0.8	0.60
A2390-350416	07/08/94	21:50:24 17:25:59	SIS	2×3600	0.8	0.65
A2390-350471	07/08/94	21:50:22 17:26:18	SIS	3600+1800	0.8	0.65
E1512-301037A	05/07/94	15:11:42 36:47:38	SIS	3×2400	0.8	0.77
E1512-301037B	05/07/94	15:11:42 36:47:38	SIS	3×2400	0.8	0.77
E1512-101526	05/07/94	15:12:33 36:48:32	SIS	2×1800	0.8	0.62
E1512-201429	06/08/94	15:13:07 36:48:52	SIS	2×2400	0.8	0.60
E1621-515	07/08/94	16:21:24 26:38:58	SIS	2×2400	0.8	0.60
A2390-100225	27/07/94	21:51:06 17:24:37	MOS	2×2400	1.0	1.11
A2390-101084	27/07/94	21:51:15 17:27:26	MOS	2×2400	1.0	1.11

Table 5.5: Observation Log – Part 2

ID	Date	RA DEC (1950.0)	MOS/ SIS	Exposure Time (seconds)	Slit Width (")	Seeing FWHM (")
A2390-200928	28/07/94	21:51:51 17:28:32	MOS	3×2400	1.0	1.0
A2390-200802	28/07/94	21:51:50 17:27:47	MOS	3×2400	1.0	1.0
A2390-200372	28/07/94	21:51:50 17:25:28	MOS	3×2400	1.0	1.0
E1512-201845	28/07/94	15:13:22 36:50:23	MOS	3×2400	1.0	1.2
E1512-201773	28/07/94	15:13:12 36:50:09	MOS	3×2400	1.0	1.2
E1512-200730	28/07/94	15:13:07 36:46:32	MOS	3×2400	1.0	1.2
E1512-200334	28/07/94	15:13:09 35:45:06	MOS	3×2400	1.0	1.2
E1512-200672	28/07/94	15:12:58 36:46:18	MOS	3×2400	1.0	1.2
E1512-201268	28/07/94	15:13:20 36:48:23	MOS	3×2400	1.0	1.2
E1512-202096	28/07/94	15:13:12 36:51:16	MOS	3×2400	1.0	1.2
E1512-201125	28/07/94	15:13:18 36:47:52	MOS	3×2400	1.0	1.2

Chapter 6

Synthetic Rotation Curve Fitting

Low flux levels have been a major obstacle to overcome in this project. At redshifts of 0.25–0.45, the [O II] $\lambda\lambda 3726\text{--}3729$ Å emission line doublet is observed in the blue between 4659 Å and 5400 Å. Until very recently, CCD detectors have been plagued by poor blue quantum efficiency (15-25%). The LORAL3 CCD at CFHT is no exception with a quantum efficiency of 23% at 4500 Å, but new CCDs with high blue quantum efficiency (80% at 5000 Å) will greatly alleviate this problem in the future. Due to the very low [O II] flux levels (typical S/N ratio *per pixel* $\sim 2\text{--}3$), it was important to choose a method which used all the pixels simultaneously to statistically find the best parameter values and their respective uncertainties. The synthetic rotation curve fitting method described below can be used to extract internal kinematics from faint, spatially-resolved emission line spectra.

6.1 Fitting Model

6.1.1 Parameters

The parameters of the fitting model were the projected rotation velocity $V_{\text{rot}} \sin i$ of the galaxian disk in km/s (slit spectra cannot be used to disentangle V_{rot} and $\sin i$), the [OII] exponential disk scale length in h_{100}^{-1} kpc, the [OII] total line flux in DU and the dimensionless [OII] doublet intensity ratio $I(3726 \text{ \AA})/I(3729 \text{ \AA})$. It was necessary to include the doublet intensity ratio in the model to deal with the broadening of the observed [OII] profile resulting from the effect of the $(1+z)$ spectral stretching on the doublet separation. The rest-frame separation of the doublet components is 2.7 \AA . The observed separation can only be resolved at redshifts of $z \sim 0.4-0.5$ ($\Delta\lambda = 3.9 \text{ \AA}$) with the MOS/SIS spectral resolutions of $3-5 \text{ \AA}$. Even though the signal-to-noise ratios and the spectral resolution may not been adequate to measure a precise value for the [OII] ratio, the additional degree of freedom was needed to properly model the observed line profile.

6.1.2 Surface Brightness Profile

The synthetic rotation curves used a thin exponential disk model for the [OII] surface brightness distribution. In this model, the surface brightness Σ as a function of radius from the center of a galaxy is given by the simple equation:

$$\Sigma(r) = \Sigma_0 e^{-r/r_d} \quad (6.1)$$

where Σ_0 and r_d are the central surface brightness and scale length of the

disk respectively. Equation 6.1 provides a good fit to the light profiles of spiral disk galaxies. The central surface brightness Σ_0 of an exponential disk is related to the total luminosity L_{tot} of the disk by:

$$L_{tot} = 2\pi r_d^2 \Sigma_0 \quad (6.2)$$

Equation 6.2 is obtained by simply integrating equation 6.1 from zero to infinity. In real disk galaxies, surface brightness profiles are influenced by complex internal absorption by dust lanes. Internal absorption by dust lanes was not taken into account in the fitting model since dust distributions vary from galaxy to galaxy, and they can only be mapped with HST's high spatial resolution at intermediate redshifts. Every point in the simulated disk was given an observed intensity $I(r)$ following equation 6.1.

6.1.3 Velocity Field

The differential rotation of spiral disks possesses a peculiar characteristic: the rotation velocity $V(r)$ is a constant except in the innermost regions. This behavior persists at the largest radii sampled by the best rotation curves which means that the edge of the mass distribution in spiral galaxies has not yet been reached. The rotation curves of spiral galaxies are said to be *flat*. For intermediate redshift galaxies, the rise of the rotation curve in the innermost regions cannot be resolved. Therefore, the simplest velocity field reproducing a flat rotation curve in this case is one in which $V(r)$ is constant everywhere, $V(r=0)$ is zero, and the direction of rotation is specified by the sign of the projected velocity $V_{rot} \sin i$.

6.1.4 Spectra, PSF and Instrumental Profiles

Slit spectra are said to be two-dimensional (2D). The abscissa of slit spectra (also called the spatial axis) is the position along the slit. The ordinate is wavelength, and the wavelength interval per pixel is called the dispersion. The intensity as a function of position along the spatial axis is the flux integrated over the slit width at each position. All spatial information perpendicular to the spatial axis is thus lost. The simulated spectra were built wavelength interval by wavelength interval. The k^{th} pixel along the dispersion axis is bounded by two wavelengths, $\lambda_{\text{min},k}$ and $\lambda_{\text{max},k}$, corresponding to two velocities, $V_{\text{min},k}$ and $V_{\text{max},k}$. This velocity window was used to build a narrow-band image of the simulated disks from [OII] fluxes at locations with projected velocities between $V_{\text{min},k}$ and $V_{\text{max},k}$.

The k^{th} narrow-band image was then convolved with the point-spread-function (PSF) of the telescope. The PSF is the image of an unresolved source produced by the telescope. Although it has been traditionally approximated by a Gaussian function, it is common practice to determine this function empirically from direct images to take into account instrumental aberrations. This was especially important for MOS observations as the MOS PSF varied considerably over the field of view. Bright stars as near as possible to slitlet position on direct images taken before and after spectroscopy on each object were used as PSF's. The volume under each PSF was normalized to unity to preserve the flux in each narrow-band image. The seeing convolved image was produced by Fourier transforming the product of the Fourier transforms of the PSF and initial images. After PSF convolution, the result of placing a slit

in front of the convolved image was calculated by integrating the flux across the width of the slit at each position along the spatial axis. The resulting intensity profile was then placed in the k^{th} row of the simulated spectrum image. A 2D spectrum image of the simulated disk with infinite spectral resolution is obtained after repeating the above steps for each wavelength interval.

To take into account the finite spectral resolution, instrumental profiles were calculated from bright emission lines in comparison arc images. For a given galaxy, the arc emission line was chosen to be as close in wavelength as possible to the observed [OII] wavelength. The central columns of the arc line were summed together to produce a 1D instrumental profile. Each column of the 2D spectrum image was then convolved with that instrumental profile to produce the final synthetic spectrum image. Figure 6.1 summarizes the steps in the construction of synthetic galaxy rotation curves from a trial set of parameter values.

6.2 Fitting Algorithm

Non-linear model fitting can be approached in two ways. One involves a gradient method such as the Levenberg-Marquardt method which uses the gradient and a second derivative matrix to quickly find the *local* minimum nearest to the starting point. The other involves searching for the absolute minimum by taking steps with Monte-Carlo generated sizes and directions through parameter space. A variant of this approach called the Metropolis algorithm (Press et al., 1986; Saha and Williams, 1994) was used. It

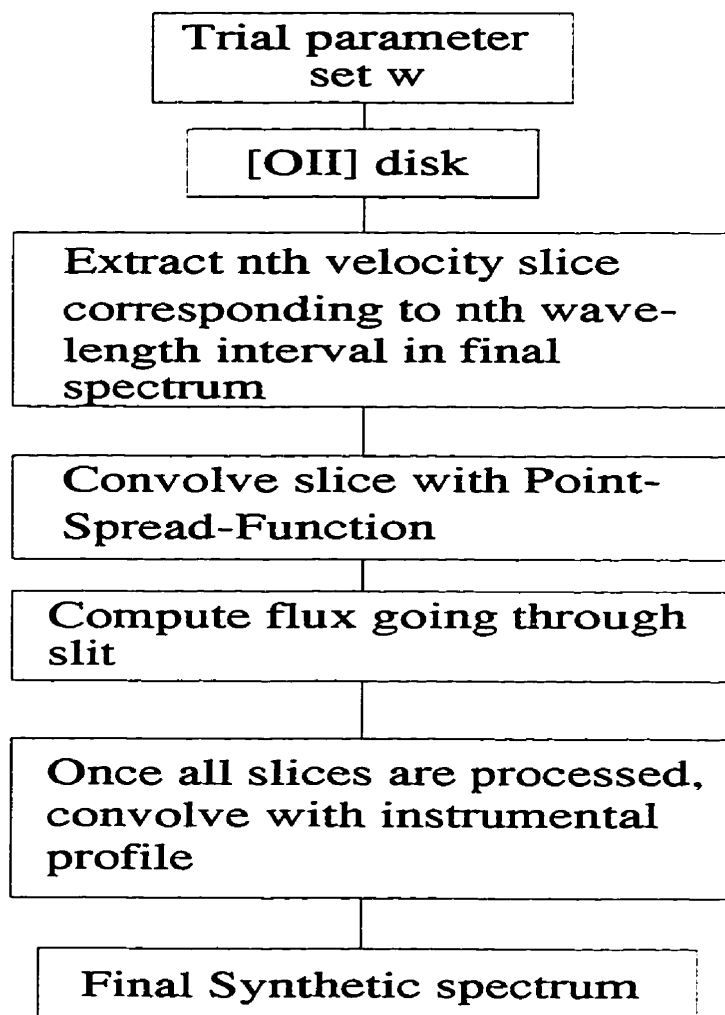


Figure 6.1: Synthetic Rotation Curve Spectrum Flow Chart. This chart outlines the construction of a synthetic galaxy rotation curve spectrum from a trial set of parameter values.

Monte–Carlo samples parameter space with a sampling density proportional to the likelihood. It has less chances of getting trapped in the first local minimum it encounters. Confidence intervals can be directly calculated as the same time the algorithm is looking for the best parameter values.

Let $P(D|\omega, M)$ be the probability distribution that a set of data D will be collected given a model M with a set of parameter values ω . $P(D|\omega, M)$ is not in itself interesting because the parameter values are not known. Using Bayes' theorem, it is possible to invert $P(D|\omega, M)$ to get $P(\omega|D, M)$, the probability distribution that ω will be observed given a model and a set of data. This distribution may be used to define best parameter values and suitable confidence intervals on those values. Bayes' theorem here can be expressed as:

$$P(\omega|D, M) = \frac{P(D|\omega, M)P(\omega|M)}{P(D|M)} \quad (6.3)$$

$P(\omega|M)$ is called the prior probability of the parameters, and it represents whatever is known (if anything is) about parameter values before taking any data. $P(D|\omega, M)$ is called the likelihood, $P(\omega|D, M)$ is called the posterior probability distribution and $P(D|M)$ is just a normalizing factor called the global likelihood. Equation 6.3 simply states that $P(\omega|D, M)$ is proportional to the likelihood. For Gaussian noise, the likelihood that N measurements X_i are consistent with pure noise is given by

$$P(D|\omega, M) \propto \prod_{i=1}^N \frac{1}{\sqrt{2\pi}\sigma_i} e^{-\frac{(x_i - x_i^M)^2}{2\sigma_i^2}} \quad (6.4)$$

The X_i^M 's are the predictions of the model M for the set of parameter

values ω . Carrying out the product in equation 6.4, $P(D|\omega, M)$ becomes

$$P(D|\omega, M) \propto \frac{1}{\sqrt{2\pi} \prod_{i=1}^N \sigma_i} e^{-\sum_{i=1}^N \frac{(x_i - x_i^M)^2}{2\sigma_i^2}} \propto \frac{1}{\sqrt{2\pi} \prod_{i=1}^N \sigma_i} e^{-\frac{1}{2}x^2} \quad (6.5)$$

In read-out and sky noise limited CCD images, the photon noise due to the galaxy signal is negligible, and the σ_i 's are all equal to the background noise σ_{bkg} , so $P(D|\omega, M) \propto e^{-\frac{1}{2}x^2}$. The background noise σ_{bkg} was determined for each spectrum by computing image statistics in four regions at the corners of the spectrum.

The Metropolis algorithm starts with some set of parameter values ω and the associated $P(\omega|D, M)$. It then picks a possible change $\delta\omega$ in the parameters and computes $P(\omega + \delta\omega|D, M)$. If $P(\omega + \delta\omega|D, M) > P(\omega|D, M)$, then the change $\delta\omega$ is accepted. If $P(\omega + \delta\omega|D, M) < P(\omega|D, M)$, then the change $\delta\omega$ is accepted only some fraction $P(\omega + \delta\omega|D, M)/P(\omega|D, M)$ of the time. After hundreds of such iterations, the distribution of accepted values of ω will converge to $P(\omega|D, M)$ provided that all possible ω are eventually accessible. Parameter space is thus sampled with a density proportional to the likelihood. The trial changes $\delta\omega$ are chosen at random. If they are too small (i.e. the parameter search is too "cold"), then all iterations will accept changes. On the other hand, if the search is too "hot", then none of the iterations will accept changes. It is usual to regulate the size of the steps (i.e. the temperature of the search) so that half the iterations accept changes.

Temperature control is thus an important element of the Metropolis. The temperature control scheme must allow the search to sample the largest volume in parameter space with the lowest possible number of steps. In

the current implementation of the Metropolis, it starts with a n -dimensional volume centered on ω_0 given by $V_0 = \prod_{i=1}^n T_{i_0}$ where T_{i_0} is the initial temperature on the i^{th} parameter. Parameter values are generated using $\omega = \omega_0 + \alpha T_{i_0}$ where α is a random number between -1 and 1 . If the first lower χ^2 value is found N_{iter} iterations after the beginning of the search, then one would expect that this region would have a characteristic size $V = V_0/N_{\text{iter}}$. In order to match the search temperature to the size of that lower χ^2 region, the temperature of each parameter is then reduced according to $T_i = T_{i_0} \sqrt[n]{\frac{1}{N_{\text{iter}}}}$. After this initial cooling, the search continues. The ratio of the number of accepted ω over the number of trial ω is computed after every ten trials. If less than half the changes have been accepted, then the parameter temperatures are all decreased by 30%. If not, then the parameter temperatures are all increased by 30%.

The best parameter values were chosen to be the median ω 's of $P(\omega|D, M)$. These median values were obtained by simply sorting out the N_{acc} accepted ω values and taking the $\frac{1}{2}N_{\text{acc}}^{\text{th}}$ value. The $0.16 N_{\text{acc}}^{\text{th}}$ and $0.84 N_{\text{acc}}^{\text{th}}$ values were used as the lower and upper bounds of the 68% confidence intervals.

6.2.1 An Example: The Suspicious Coin

The suspicious coin experiment is a particularly illustrative of the Bayesian approach adopted here. Consider a suspicious coin which has been tampered with so that the probabilities of getting heads or tails are not equal to 0.5 anymore. Let p_{true} be the true probability of getting heads, and let it be equal to 0.5 without, of course, telling the experimenter. For N tosses, the posterior probability distribution is given by

$$P(p|N, n) = p^n(1 - p)^{N-n} \quad (6.6)$$

where n is the numbers of heads obtained after N tosses. In the extreme case of $N = 1$, there are obviously two possible outcomes: $n = 0$ and $n = 1$. Given only one of these outcomes, the ($N = 1, n = 1$) case say, the experimenter might be tempted to conclude that $p = 1.0$. However, according to equation 6.6, $P(p|1, 1)$ is equal to p , and its median value is $1/\sqrt{2}$. This median value is already closer to p_{true} than the experimenter's first instinctive guess of 1.0. The information in $P(p|1, 1)$ is still very limited, but *it is the best one can do with the current data.*

In order to improve his estimate of p_{true} , the experimenter must increase the signal-to-ratio of his data by increasing the number of tosses. Consider the $N = 4$ case of which three possible outcomes ($n = 1, n = 2, n = 3$) are shown in Figure 6.2. Only one outcome (i.e. one galaxy spectrum!) is accessible to the experimenter. $P(p|4, 1)$ and $P(p|4, 3)$ are wide and asymmetric with maximum at $p = 0.25$ and $p = 0.75$ respectively. The location of the maxima is not surprising. The posterior probability distributions are simply saying that a "good bet" for the true value of p is n/N although it does not offer any guarantee that it is the best one. In both cases, the median values are closer to p_{true} than the "good bet" values are. The median values are less biased by noise than the "good bet" values. It is important to emphasize that these "good bet" values are picked by algorithms (such as least-squares fitting) trying to find the parameter value which minimizes χ^2 without taking the topology of parameter space into account. Therefore, at low signal-to-

noise ratios, the Bayesian parameter estimates will differ from least-squares estimates. Moreover, many least-squares routines give Gaussian errors based on a curvature matrix computed around the χ^2 minimum. These Gaussian errors cannot accurately represent asymmetric posterior probability distributions.

Since $P(p|4, 2)$ is symmetric about $p = 0.5$, $P(p|4, 1)$ is positively skewed (towards p_{true}), and $P(p|4, 3)$ is negatively skewed (also towards p_{true}), it might seem possible at first glance to cheat and tell in which direction p_{true} lies with respect to the median value of the posterior probability distribution. This is not so. $P(p|4, 1)$ remains the same whether $p_{true} = 0.5$ or 0.25 . The ($N = 4, n = 1$) case is consistent with both values of p_{true} . Larger N 's are needed to distinguish between $p_{true} = 0.5$ and $p_{true} = 0.25$.

As N becomes really large (high signal-to-noise ratios), n will be very close to $p_{true}N$. All posterior probability distributions will be symmetric and narrow. The suspicious coin experiment illustrates two important points. First, posterior probability distributions are not symmetric at low S/N . As a matter of fact, many real parameter posterior probability distributions in section 7.2 are not symmetric. The errors quoted on parameter value estimates cannot be considered to be Gaussian. Second, least-squares fitting is the high S/N special case of the current approach, and least-squares is not as robust at low S/N .

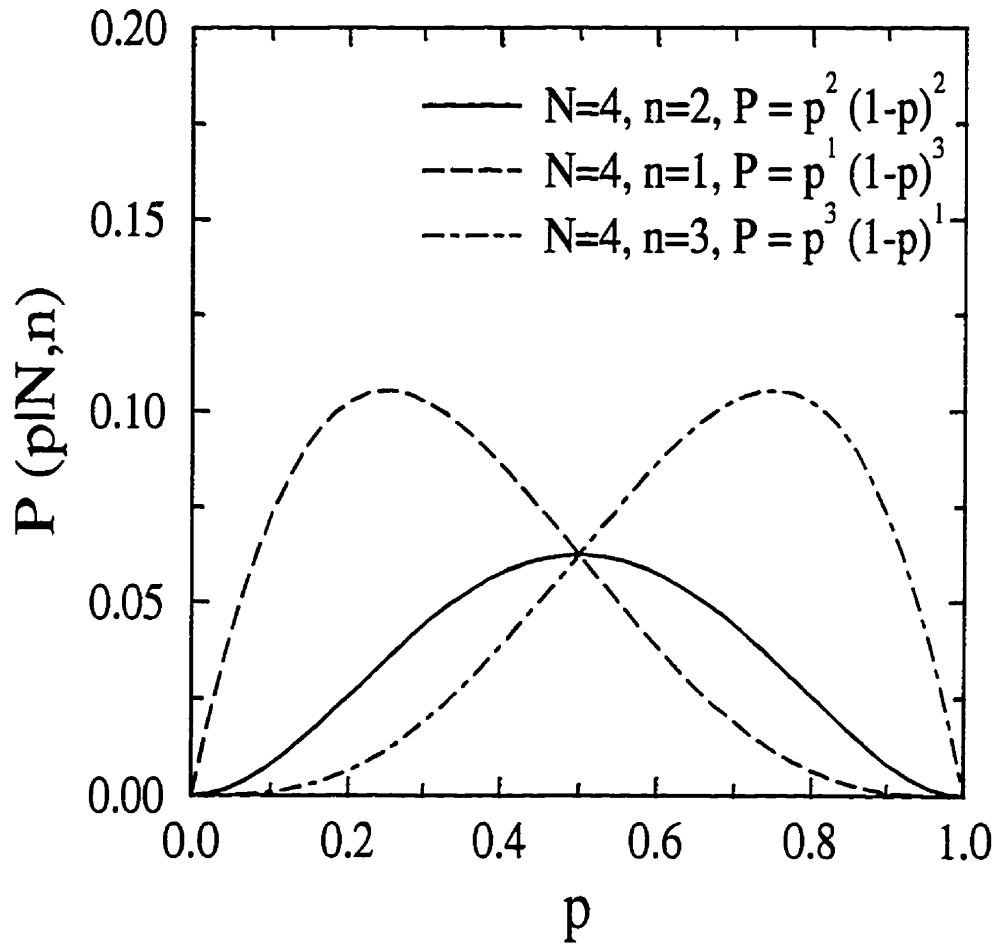


Figure 6.2: The Suspicious Coin posterior probability distributions for three $N=4$ outcomes.

6.3 ELFIT2D: 2D Emission Line Fitting

This section describes the ELFIT2D program used to analyze low S/N spatially-resolved spectra of intermediate redshift galaxies. ELFIT2D was written by the author in the Subset Pre-Processor (SPP) language. SPP is the native language of IRAF. This choice was motivated by the flexibility in parameter management and image manipulations offered by SPP within the IRAF environment. ELFIT2D is used in the same way as any other IRAF tasks. It has a set of control parameters shown in Tables 6.1 and 6.2.

In_image is the name of an input 2D postage image of a spatially-resolved emission spectrum obtained following Section 5.3. *Out_image* is the name of an image of a synthetic rotation curve created by ELFIT2D from the median values of the parameter values. *Out_image* can be subtracted from *In_image* to study fit residuals. ELFIT2D sends all the information on accepted Metropolis iterations and final median parameter values to *logfile*.

ELFIT2D starts up by creating a square grid (with dimensions given by *mesh*) which oversamples the spatial scale of input 2D spectrum by a factor of 64 (8×8). The scale of this grid (kiloparsecs/pixel) is computed from the input spectrum image scale *imscale* and the galaxy redshift using the standard angular distance relation for $q_0 = 0.5$. There are two choices for the telescope's point-spread-function (PSF): Gaussian and empirical. For a Gaussian PSF, the FWHM is specified by *seeing*. For an empirical PSF, *in_psf* specifies the name of a "postage stamp" image of the PSF derived from stars on direct images. In both cases, the PSF is mapped onto a 128×128 grid, and so are the slit dimensions *slitx* and *slity*. The PSF is then normalized to a

Table 6.1: ELFIT2D Control Parameter Set - Part 1

Parameter name	Typical Value	Short Description
in_image	A100686.el	Name of input image
out_image	A100686.fit	Name of output best-fit image
logfile	A100686.log	Name of log file
mesh	512	Mesh size of nearby image (pixels)
imscale	0.315	Image scale (arcsecond/pixel)
slitx	20.	X-dimension of slit (arcseconds)
slity	1.	Y-dimension of slit (arcseconds)
seeing	1.1	Seeing FWHM (arcseconds)
psftype	empirical	PSF type (empirical/gaussian)
in_psf	E27_npsf.1	Name of empirical PSF image
init_rd	2.	Initial disk scale length (kpc)
rdmin	0.	Minimum possible disk scale length (kpc)
rdmax	4.	Maximum possible disk scale length (kpc)
rdtemp	4.	Scale length initial temperature
init_vsi	200.	Initial disk $V \sin i$ (km/s)
vsimin	0.	Minimum possible disk $V \sin i$ (km/s)
vsimax	400.	Maximum possible disk $V \sin i$ (km/s)
vsitemp	400.	$V \sin i$ initial temperature
init_I	1000.	Initial total line flux (DU)
Imin	1.	Minimum possible total line flux (DU)

unit volume and Fourier transformed in preparation for seeing convolutions later on. Synthetic rotation curves are created over a $mesh \times mesh$ grid as described in Section 6.1. The flux is integrated to rebin the $mesh \times mesh$ grid to the 128×128 grid. Since values of $mesh$ used are always multiples of 128, no flux interpolation is needed, and potential flux errors are avoided. The seeing convolution of each velocity slice (see Section 6.1.4) was performed using the Fourier Convolution Theorem over the 128×128 grid to speed up

Table 6.2: ELFIT2D Control Parameter Set - Part 2

Parameter name	Typical Value	Short Description
<i>lmax</i>	2000.	Maximum possible total line flux (DU)
<i>ltemp</i>	2000.	Total line flux initial temperature
<i>init_o2r</i>	1.	Initial [OII] doublet intensity ratio
<i>o2rmin</i>	0.	Minimum possible doublet intensity ratio
<i>o2rmax</i>	2.	Maximum possible doublet intensity ratio
<i>o2rtemp</i>	2.	Doublet intensity ratio initial temperature
<i>init_bk</i>	0.	Initial background level (DU)
<i>bkmin</i>	-5.	Minimum background level (DU)
<i>bkmax</i>	5.	Maximum background level (DU)
<i>bktemp</i>	10.	Background level temperature
<i>nsamp</i>	500	Number of 5D parameter space samples
<i>dispersion</i>	1.58	Dispersion (Å/pixel)
<i>instprof</i>	empirical	Instrumental profile (empirical/gaussian/box)
<i>in_eiprof</i>	mos_ip_e27	Name of instrumental profile image
<i>specres</i>	5.	Spectral resolution (Å)
<i>sosamp</i>	1	Spectral Oversampling
<i>redshift</i>	0.3412	Redshift of galaxy
<i>bksig</i>	8.1	Background sigma (DU)
<i>metseed</i>	11441	Metropolis seed
<i>mode</i>	q	

calculations.

For each of the 5 synthetic rotation curve parameters, ELFIT2D has 4 control parameters. For example, *init_vs*, *vsimin*, *vsimax* and *vsitemp* control what steps will be taken by the Metropolis algorithm. Initially, trial values will be uniformly generated between $init_vs - 0.5 \times vsitemp$ and $init_vs + 0.5 \times vsitemp$. As the Metropolis algorithm proceeds, both the temperature and the location around which steps are generated change, but trial values

are never allowed outside the range defined by *vsimin* and *vsimax*. The value of a given parameter can be held fixed throughout a Metropolis search by simply setting its initial temperature to zero.

The Metropolis search stops after it has accepted *nsamp* iterations. The parameter *dispersion* gives the number of Angstroms per pixel in the input spectrum. The dispersion is set by the grism used during the observations. There are three choices for the instrumental profile of the spectrograph: gaussian, box and empirical. Obviously, the last choice is the best one to use when an instrumental profile is available. The parameter *in_eiprof* is the name of an 1D image containing an instrumental profile which can be derived from comparison arc lines for example (see Section 6.1.4 for details). Each column of the simulated 2D spectra was convolved with this 1D instrumental profile using the Fourier Convolution Theorem. End effects were avoided with zero-padding. The parameters *specres* and *sosamp* are only used for the gaussian and box instrumental profiles.

Finally, *bkgsig* is the standard deviation of background pixel values measured by performing image statistics in background sections of the input spectrum images, and *metseed* is a large odd integer number needed to seed the random generator used for the Metropolis trial values. The use of ELFIT2D is not restricted to the [OII] doublet emission line. Other emission lines can be easily analyzed by changing the emission line rest wavelength(s) specified in the first lines of the source code.

The performance of ELFIT2D is analyzed in the next section.

6.4 Simulations

6.4.1 Confidence Intervals

The validity of the confidence intervals returned by the Bayesian approach in ELFIT2D can be tested by running ELFIT2D on a number of noise realizations of the *same* galaxy rotation curve spectrum. A simulation of a typical SIS/LORAL3 spectrum ($t = 2 \times 3600 \text{sec}$, $N_R = 8 \text{ e}^-$) of a $z = 0.35$ galaxy with $V_{\text{rot}} \sin i = 130 \text{ km/s}$, disk scale length of $2.0 h^{-1} \text{ kpc}$, [OII] ratio of 1.0, total [OII] flux of 1053 DU and background level of 0 DU was created. Random noise was added to this galaxy spectrum using the IRAF task MKNOISE in the ARTDATA package. Fifty galaxy spectra were created using a different seed for the noise each time. ELFIT2D was run with the same initial conditions on all fifty spectra. The results are given in Table 6.3 and shown in Figure 6.3.

Columns 2-5 in Table 6.3 show that the measured median values are scattered in an unbiased way around the true parameter values. Column 8 gives for each parameter the fraction f of spectra in which the true parameter value was within the 68% confidence interval derived by ELFIT2D from the posterior probability distribution $P(\omega|D, M)$. These confidence intervals include the true value between 0.56 and 0.72 of the time according to the f values. The expected value of 0.68 for f corresponds to 34 spectra out of 50, and the $\sigma = 5.8$ Poisson error can account for the fluctuations seen in f . Therefore, the confidence intervals given by ELFIT2D are valid. Figure 6.4 shows $P(V_{\text{rot}} \sin i | D, M)$ for three noise realizations. It is interesting to note that the skewness of the distributions exhibits the same behavior as

$P(p|N, n)$ in the suspicious coin experiment (see Figure 6.2).

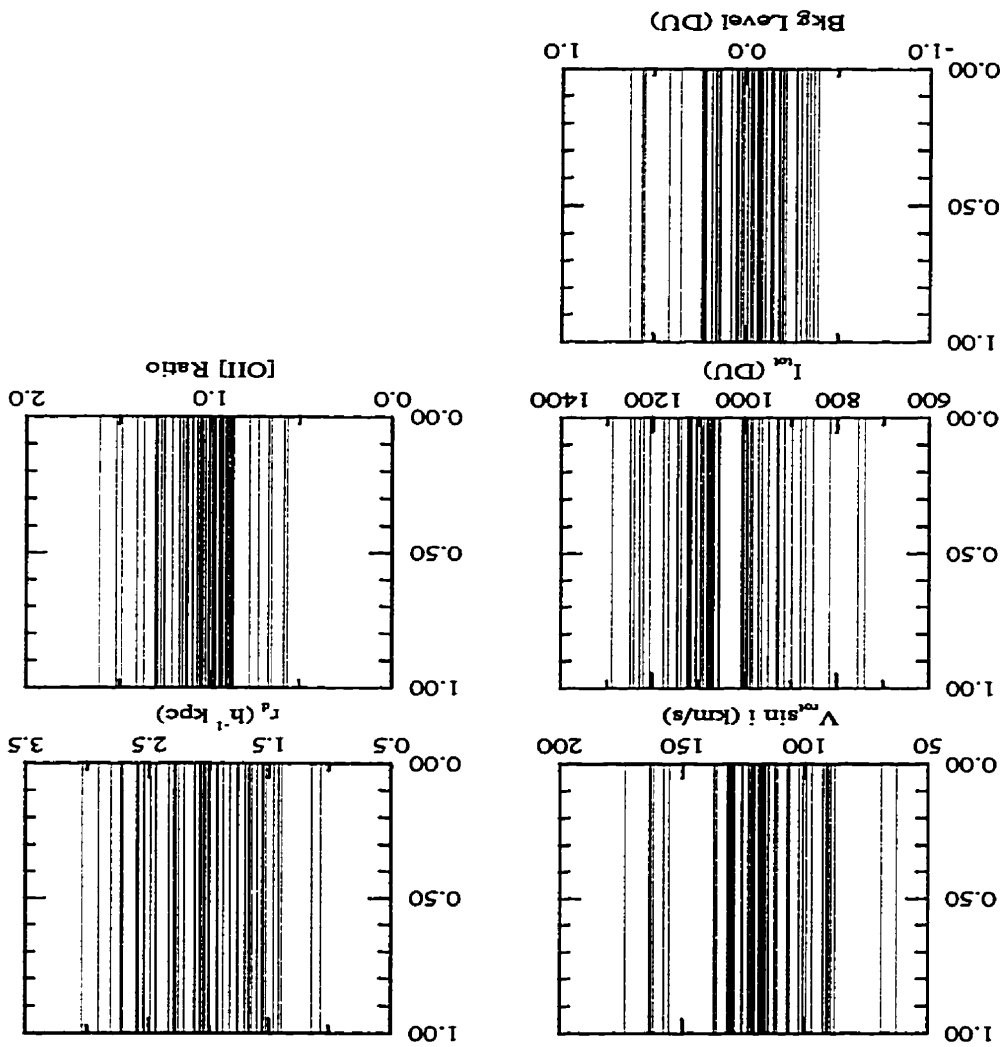
Table 6.3: ELFIT2D results for 50 different noise realizations of the same galaxy rotation curve.

Parameter (1)	Input value (2)	Mean (3)	σ (4)	Median (5)	Min. (6)	Max. (7)	f (8)
$V_{\text{rot}} \sin i$ (km/s)	130	120	23	120	63	173	0.64
r_d (h^{-1} kpc)	2.0	2.1	0.5	2.0	1.1	3.0	0.56
I_{tot} (DU)	1053	1046	124	1069	742	1290	0.62
[OII] ratio	1.0	1.0	0.2	1.0	0.57	1.61	0.72
Bkg Level (DU)	0.0	0.01	0.2	0.10	-0.39	0.63	0.68

6.4.2 Parameter Recovery

At a fixed total observed emission line flux, the signal-to-noise (S/N) ratio in spatially-resolved spectra depends on the apparent size and $V_{\text{rot}} \sin i$ of the target galaxies. In read-out and sky photon noise limited spectra, the rotation curve of small, slow rotating galaxies have higher S/N ratios because the emission line flux is spread over a smaller area on the CCD detector. The complex interplay between flux, intrinsic size, rotation velocity and redshift yielding the final S/N values can only be thoroughly modelled through simulations. ELFIT2D was tested on a set of simulations spanning a wide range of parameter values and hence, a wide range of S/N ratios to look for systematic biases and parameter covariances. A total of 342 rotation

Figure 6.3: ELFIT2D median parameter values for fifty noise realizations of the same galaxy rotation curve. Each panel shows 50 vertical lines corresponding to the median parameter values returned by ELFIT2D for the 50 different noise realizations. The parameter values used in the simulations are $V_{\text{rot}} \sin i = 130$ km/s, disk scale length = $2.0 h^{-1}$ kpc, [OII] ratio = 1.0, total [OII] flux = 1053 DU and background level = 0 DU.



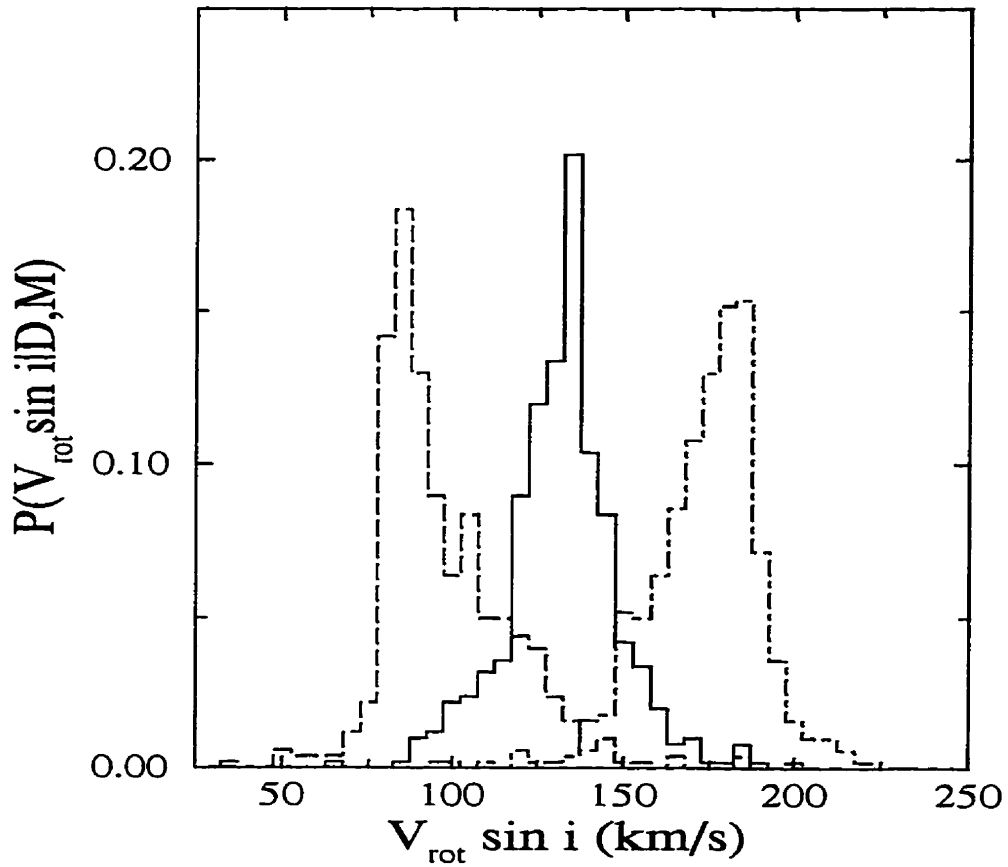


Figure 6.4: 3 simulated posterior probability distributions $P(V_{\text{rot}} \sin i | D, M)$ with median $V_{\text{rot}} \sin i$ of 89, 130 and 173 km/s respectively. The true $V_{\text{rot}} \sin i$ value is 130 km/s. These distributions should be compared with those of the suspicious coin experiment shown in Figure 6.2.

curve simulations were analyzed with ELFIT2D.

The simulated rotation curves were created using an IRAF/SPP task called GO2DBLT which produced simulated spectra of the [OII] doublet following the description of synthetic rotation curves given in section 6.1. Photon and read-out noise was added using the IRAF task MKNOISE in the ARTDATA package. Each simulated rotation curve was the sum of two 3600s exposures and was analyzed with ELFIT2D as if it were a real observed spectrum. Canonical parameter values were $V_{\text{rot}} \sin i = 130$ km/s, disk scale length of $2.0h^{-1}$ kpc, [OII] ratio of 1.0, total [OII] flux of 1053 DU and background level of 0 DU. With these values, the S/N ratios in simulations were typically worse than the S/N ratios of observed spectra. For example, most target galaxies had disk scale length less than $2.0 h^{-1}$ kpc (see Table 7.3), and only 4 out of 13 observed MOS spectra had total [OII] fluxes lower than 1053 DU. On the other hand, only 2 out of 9 SIS spectra had total [OII] fluxes higher than 1053 DU, so another set of simulations with total [OII] flux of 526 DU was generated. All observed SIS spectra had total [OII] fluxes higher than this lower flux limit.

Two main sets of simulations were created: one for SIS and one for MOS. Each set was further subdivided in low and high redshift subsets ($z=0.25$ and $z=0.42$), and each of these subsets comprised 5 sequences with each sequence exploring a range of values for a given parameter. The parameter values used in the five simulation sequences are given in Table 6.4. The independent variables in sequences 1, 2, 4 and 5 were disk scale length, $V_{\text{rot}} \sin i$, total [OII] flux and [OII] ratio respectively. Sequence 3 was made up of random combinations of parameter values. Note that the parameters for

the sequences 1.3 and 2.3 are given in order – i.e. the first simulation had $r_d = 2.5 \text{ h}^{-1} \text{ kpc}$, $V_{\text{rot}} \sin i = 130 \text{ km/s}$ and a [OII] ratio of 0.3, the second simulation had $r_d = 1.0 \text{ h}^{-1} \text{ kpc}$, $V_{\text{rot}} \sin i = 173 \text{ km/s}$ and a [OII] ratio of 1.5, and so on. The total [OII] flux in all 1.x sequences was 1052 DU, and the total [OII] flux in the 2.x simulation sequences generated for SIS was 526 DU. A five-panel figure showing parameter variations measured by ELFIT2D as a function of input values of the independent variable was plotted for each sequence. The identification numbers labelling all these figures are given in Table 6.5. Table 6.5 gives Figure ID for sequences 1.1 through 1.5 and 2.1 through 2.5 generated for MOS and SIS at low ($z=0.25$) and high ($z=0.42$) redshifts.

For the simulated SIS rotation curves, ELFIT2D did a remarkable job at recovering the input parameter values even in the 2.x sequences which had very low total [OII] fluxes. For MOS, Figures 6.25 and 6.30 show that ELFIT2D does well at recovering parameter values (except for the [OII] ratio as expected from the spectral resolution of MOS), but worrisome biases are seen in other figures. In particular, Figure 6.24 shows that, for MOS data, the scale lengths measured by ELFIT2D are consistently too low and the measured $V_{\text{rot}} \sin i$'s are consistently too low for input $V_{\text{rot}} \sin i$ values greater than 150 km/s. The total [OII] flux also appears to be systematically underestimated. These biases are what would be expected from spectra with S/N ratios that are too low. These biases are particularly worrisome because they affect two important variables. Disk scale length is used to determine whether [OII] is concentrated in the nuclei of galaxies, and $V_{\text{rot}} \sin i$ is used to look for changes in luminosity. Figure 6.24 shows very low S/N ratios

introduce systematic errors which could be interpreted as anomalous [OII] kinematics and/or luminosity boosting.

One of the limitations of the body of simulations described so far is its set of canonical parameter values. Ideally, simulations should all be re-run for 22 different sets of canonical parameter values, one per observed spectrum. It would be the best way to test the performance of ELFIT2D on each spectrum. However, this would require generating close to 7500 simulations which could only be analyzed in a reasonable time with faster computers. Are the biases seen in the MOS simulations simply due to the fact that MOS simulations had lower S/N ratios than the observations? To answer this question, additional MOS simulations were generated. Sequence 2 was generated for each galaxy observed with MOS. The broad-band disk scale length taken from Table 5.1 was used for the [OII] scale length. The total [OII] flux of the galaxy was taken to be its observed flux (Table 7.3). It is important to keep mind that the observed total [OII] flux could be an underestimate in some cases as suggested by Figure 6.24. The redshift of the simulations of a given galaxy was the redshift given in Table 5.1 for that galaxy. Figures 6.33 to 6.37 show ELFIT2D measured disk scale length and $V_{\text{rot}} \sin i$ as a function of input $V_{\text{rot}} \sin i$ for each galaxy observed with MOS. These figures are discussed galaxy by galaxy in Section 7.3.

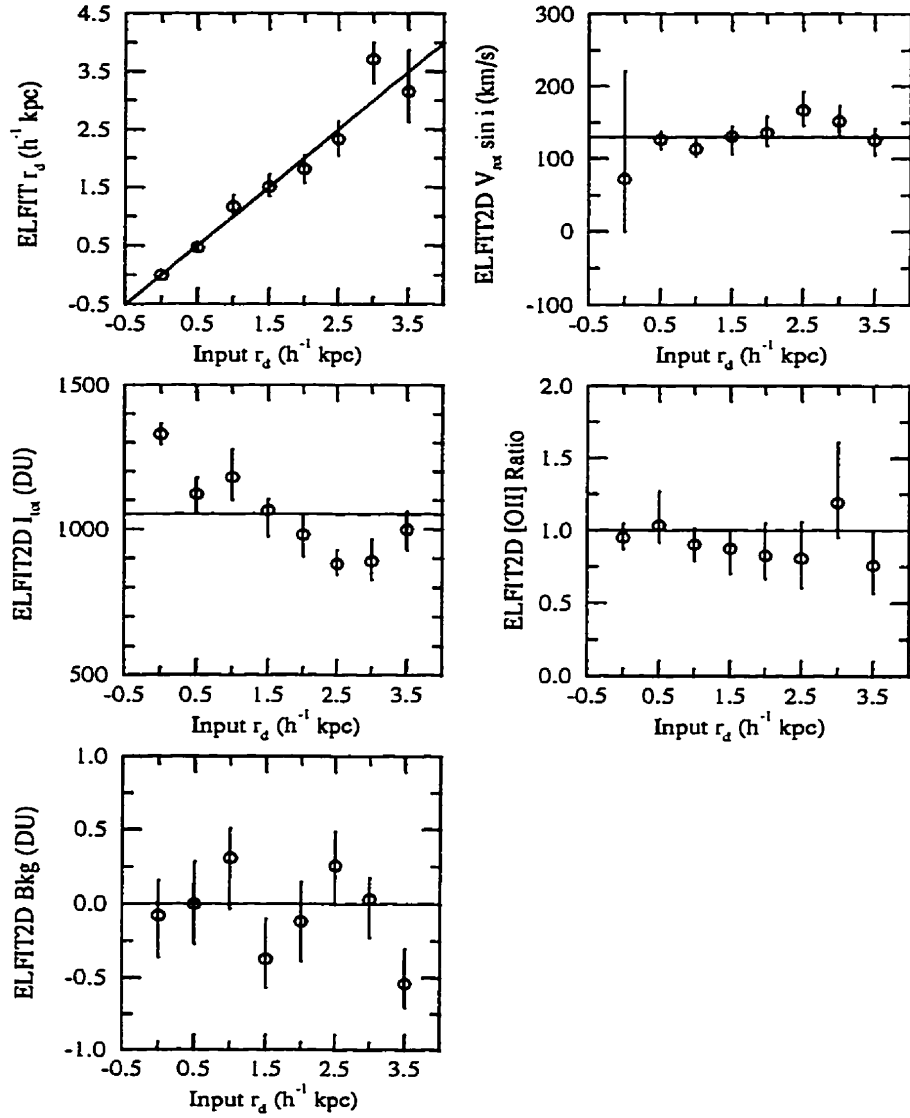


Figure 6.5: $z = 0.25$ ELFIT2D SIS test sequence 1.1

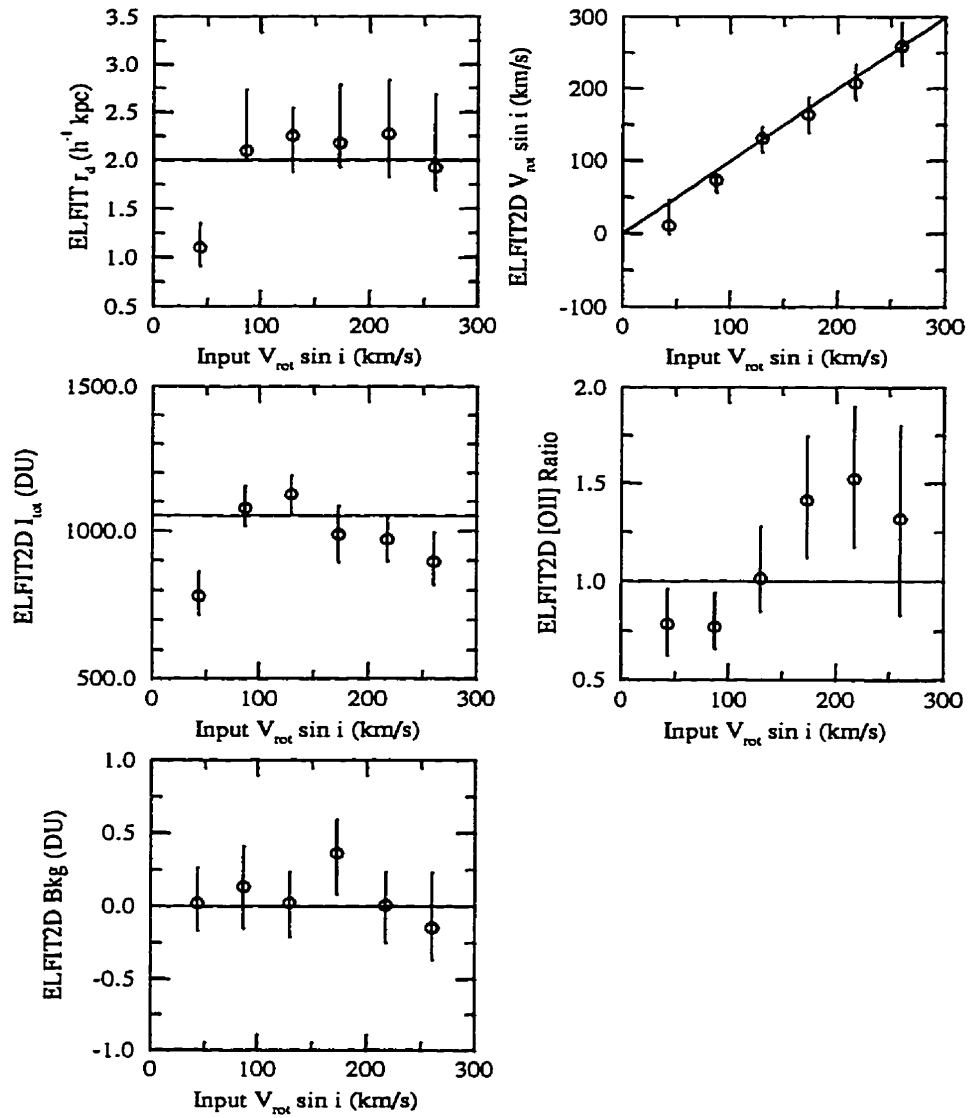


Figure 6.6: $z = 0.25$ ELFIT2D SIS test sequence 1.2

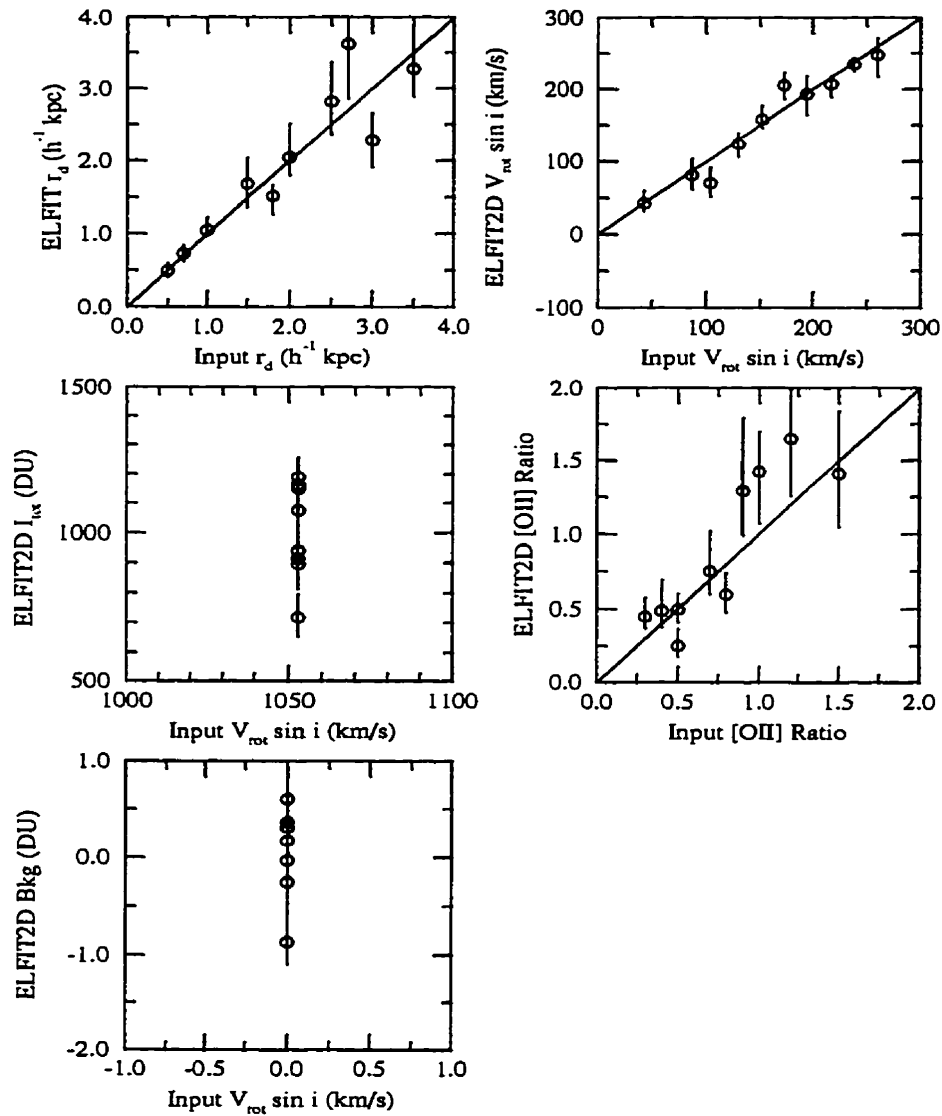


Figure 6.7: $z = 0.25$ ELFIT2D SIS test sequence 1.3

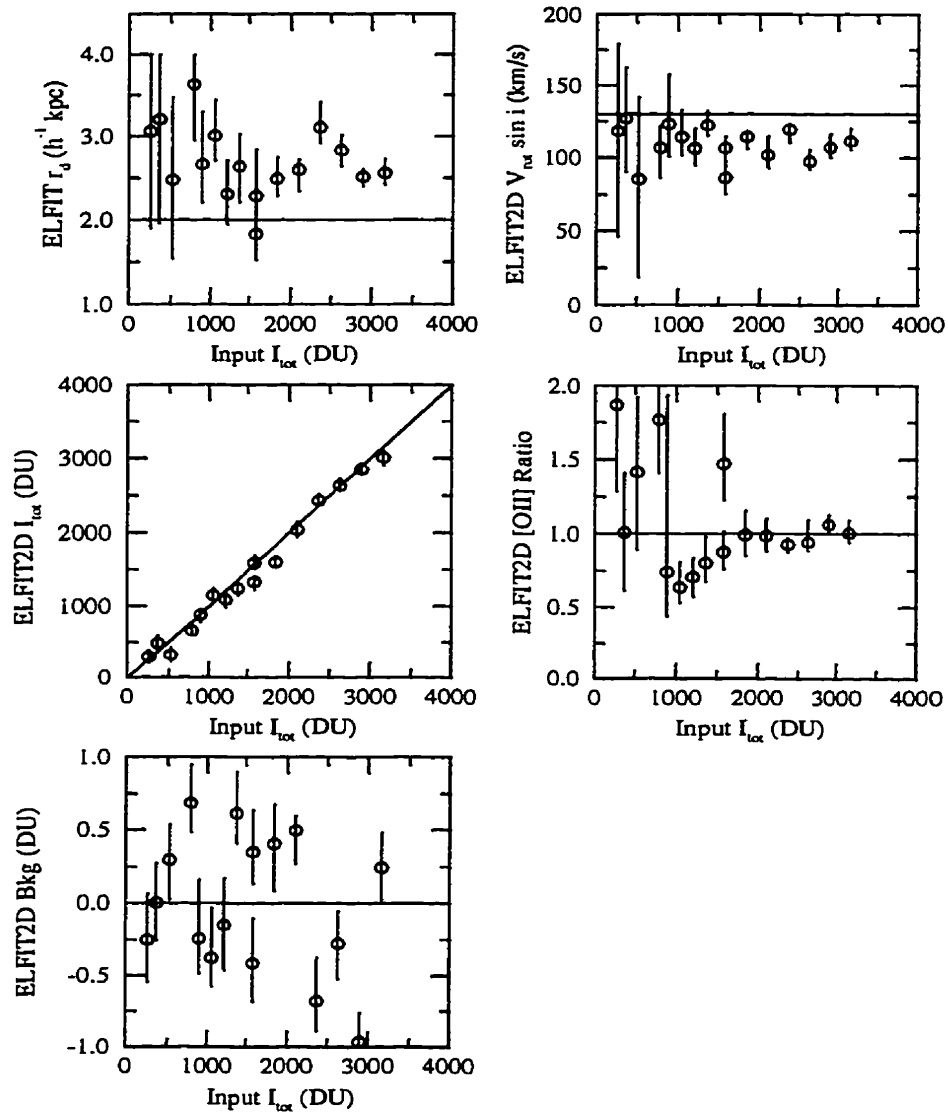


Figure 6.8: $z = 0.25$ ELFIT2D SIS test sequence 1.4

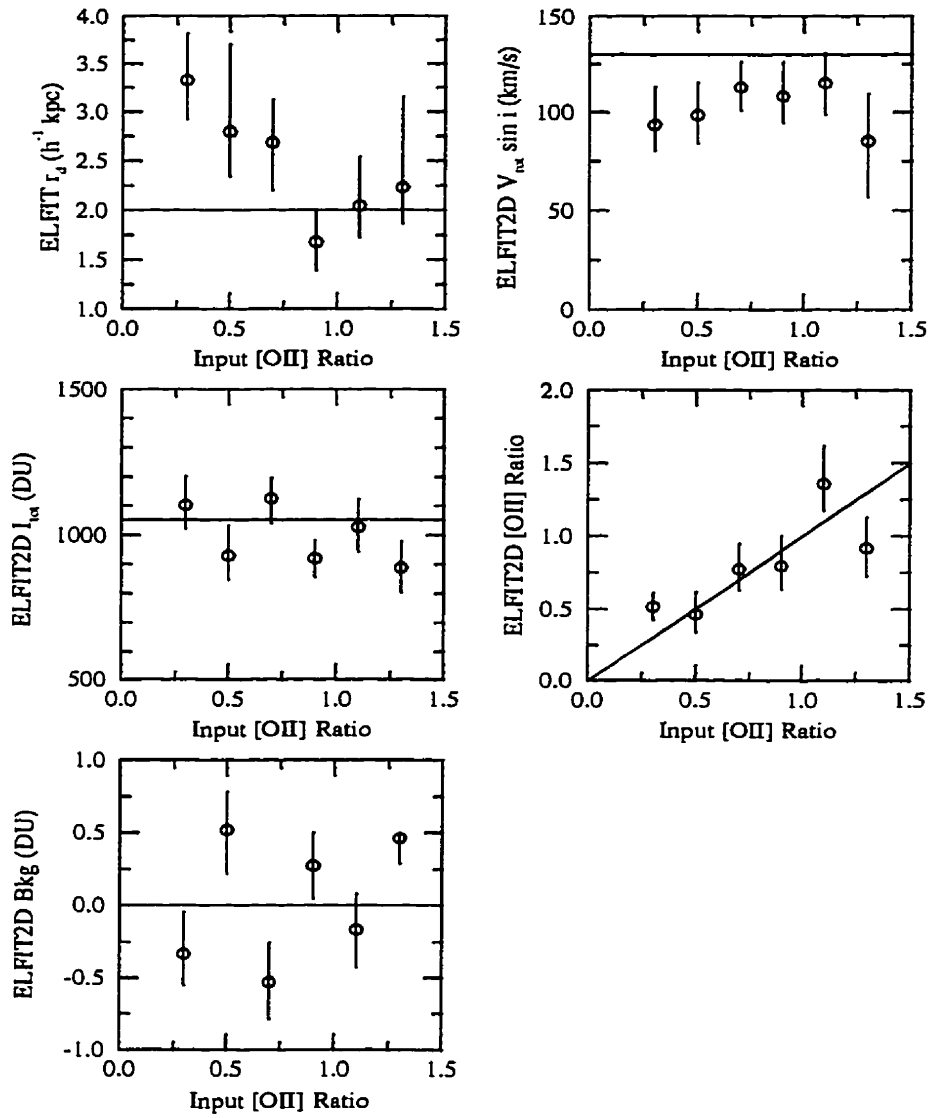


Figure 6.9: $z = 0.25$ ELFIT2D SIS test sequence 1.5

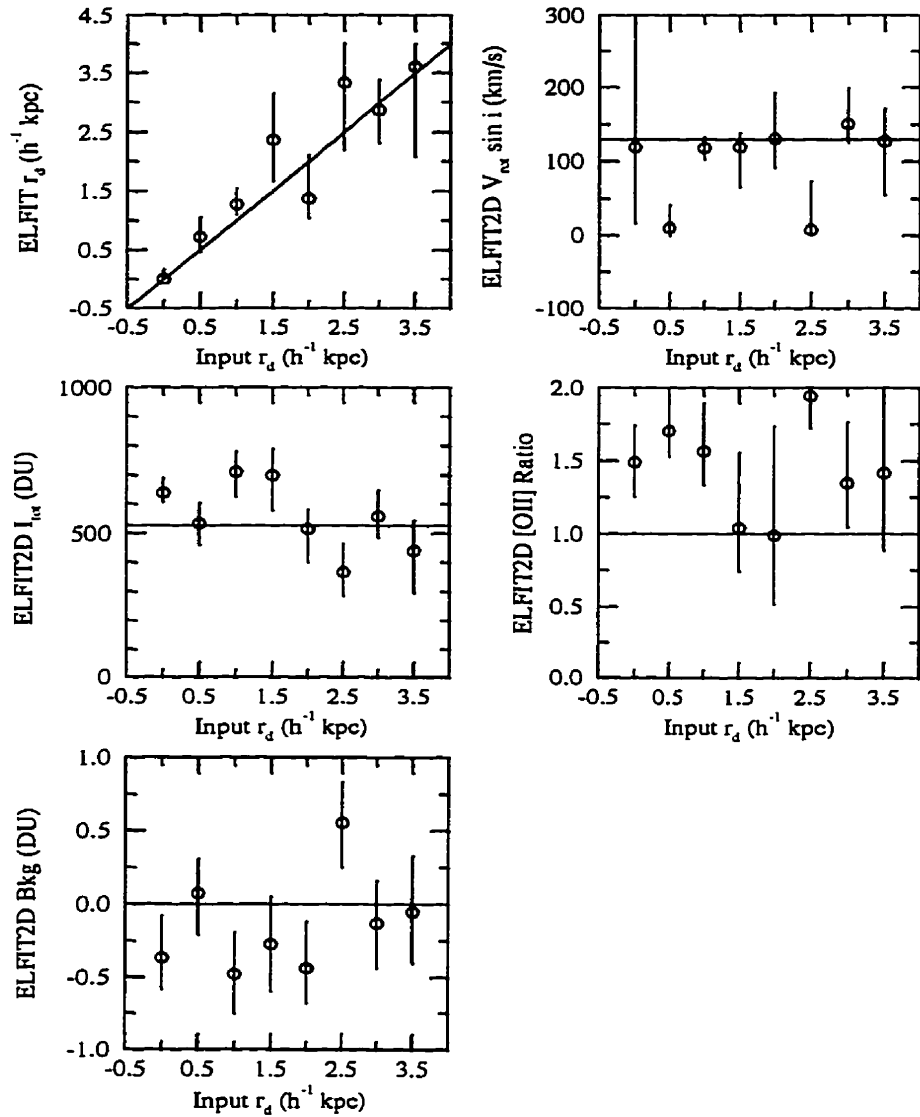


Figure 6.10: $z = 0.25$ ELFIT2D SIS test sequence 2.1

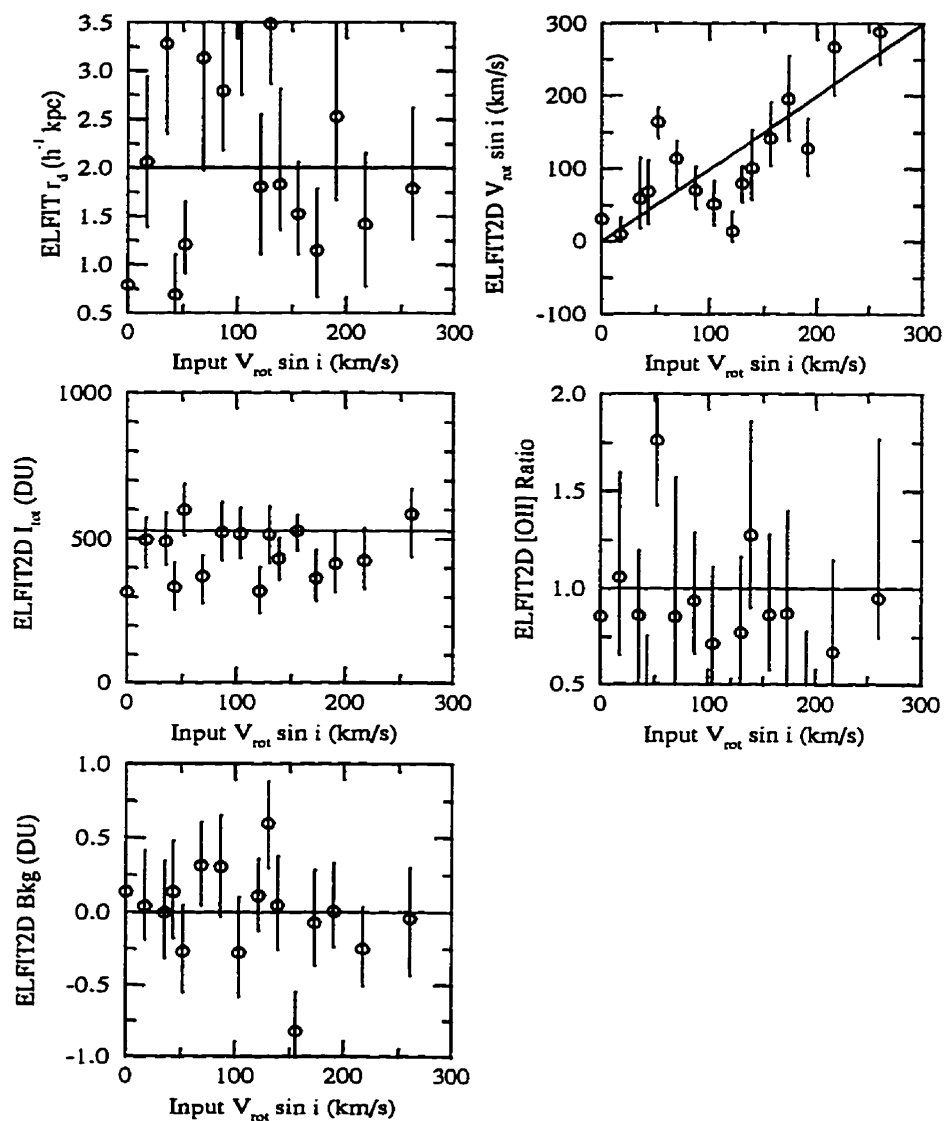


Figure 6.11: $z = 0.25$ ELFIT2D SIS test sequence 2.2

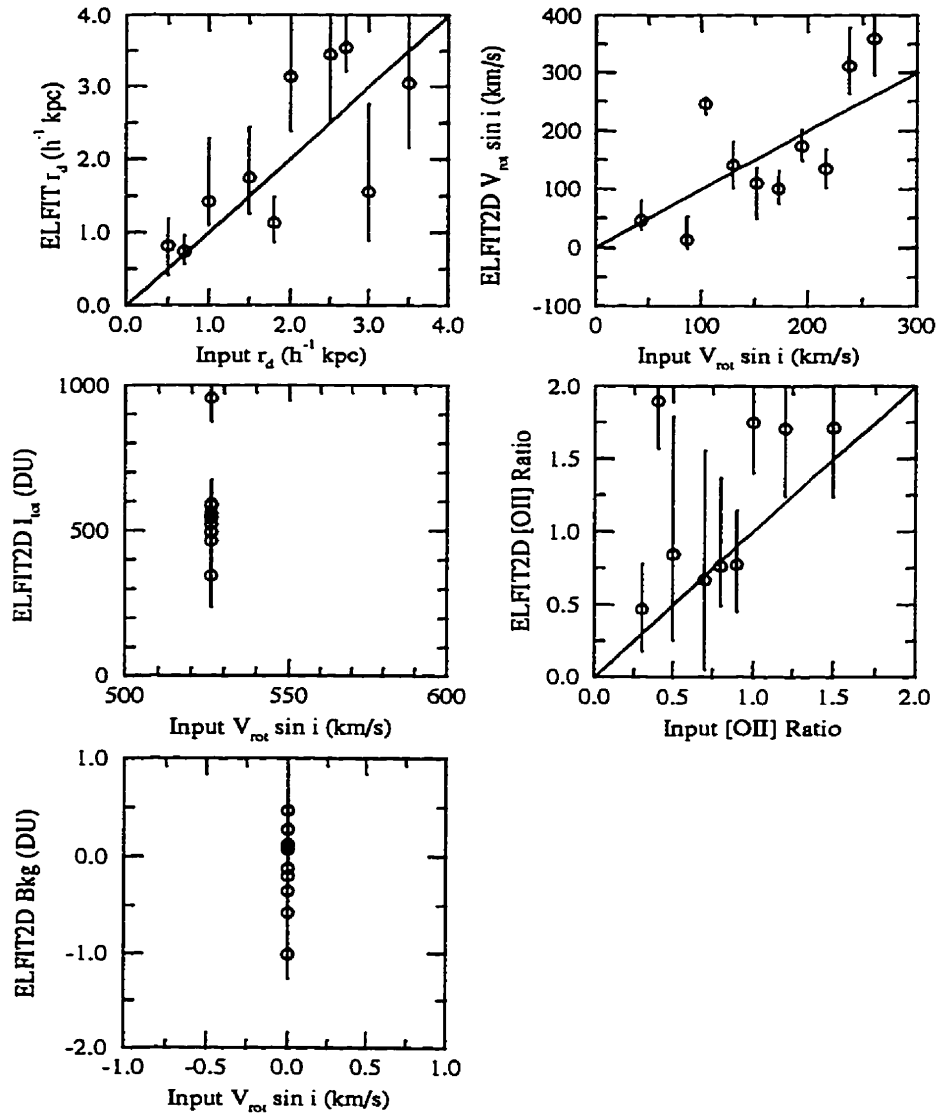


Figure 6.12: $z = 0.25$ ELFIT2D SIS test sequence 2.3

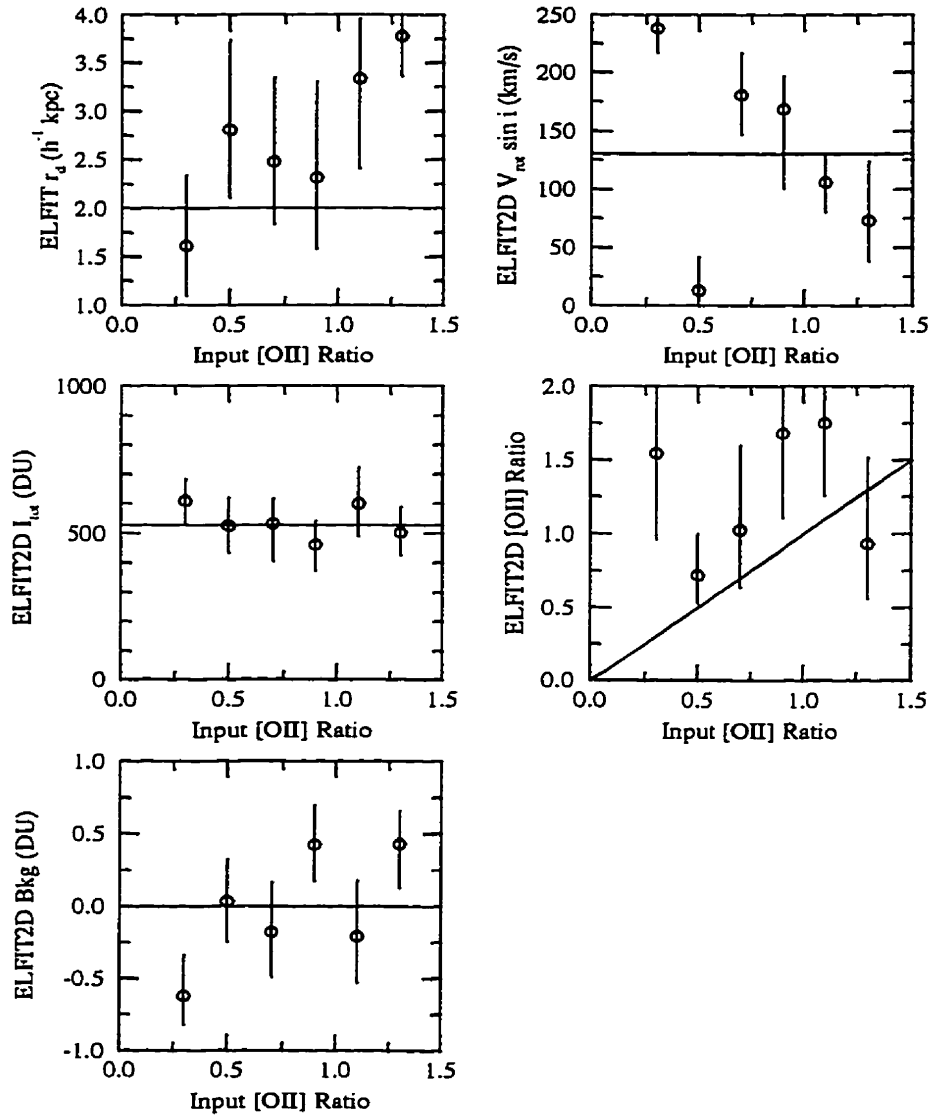


Figure 6.13: $z = 0.25$ ELFIT2D SIS test sequence 2.5

Table 6.4: ELFIT2D Simulation Test Sequences

ID	r_d (h_{100}^{-1} kpc)	$V_{rot} \sin i$ (km/s)	I_{tot} (DU)	[OII] Ratio	Bkg (DU)
1.1	0.0 0.5 1.0 1.5 2.0 2.5 3.0 3.5	130	1052	1.0	0.0
1.2	2.0	43 87 130 173 216 260	1052	1.0	0.0
1.3	2.5 1.0 3.0 1.5 0.5 3.5 2.0 0.7 1.8 2.7	130 173 260 238 216 87 43 152 195 104	1052	0.3 1.5 0.7 0.5 1.0 0.9 0.5 0.8 1.2 0.4	0.0
1.4	2.0	130	250 350 500 750 850 1000 1150 1300 1500 1500 1750 2000 2250 2500 2750 3000	1.0	0.0
1.5	2.0	130	1052	0.3 0.5 0.7 0.9 1.1 1.3	0.0
2.1	0.0 0.5 1.0 1.5 2.0 2.5 3.0 3.5	130	526	1.0	0.0
2.2	2.0	0 17 35 43 52 69 87 104 121 130 139 156 173 190 216 260	526	1.0	0.0
2.3	2.5 1.0 3.0 1.5 0.5 3.5 2.0 0.7 1.8 2.7	130 173 260 238 216 87 43 152 195 104	526	0.3 1.5 0.7 0.5 1.0 0.9 0.5 0.8 1.2 0.4	0.0
2.5	2.0	130	526	0.3 0.5 0.7 0.9 1.1 1.3	0.0

Table 6.5: ELFIT2D Simulation Sets

MOS/ SIS	z	Figure ID									
		1.1	1.2	1.3	1.4	1.5	2.1	2.2	2.3	2.4	2.5
SIS	0.25	6.5	6.6	6.7	6.8	6.9	6.10	6.11	6.12	—	6.13
	0.42	6.14	6.15	6.16	6.17	6.18	6.19	6.20	6.21	—	6.22
MOS	0.25	6.23	6.24	6.25	6.26	6.27	—	—	—	—	—
	0.42	6.28	6.29	6.30	6.31	6.32	—	—	—	—	—

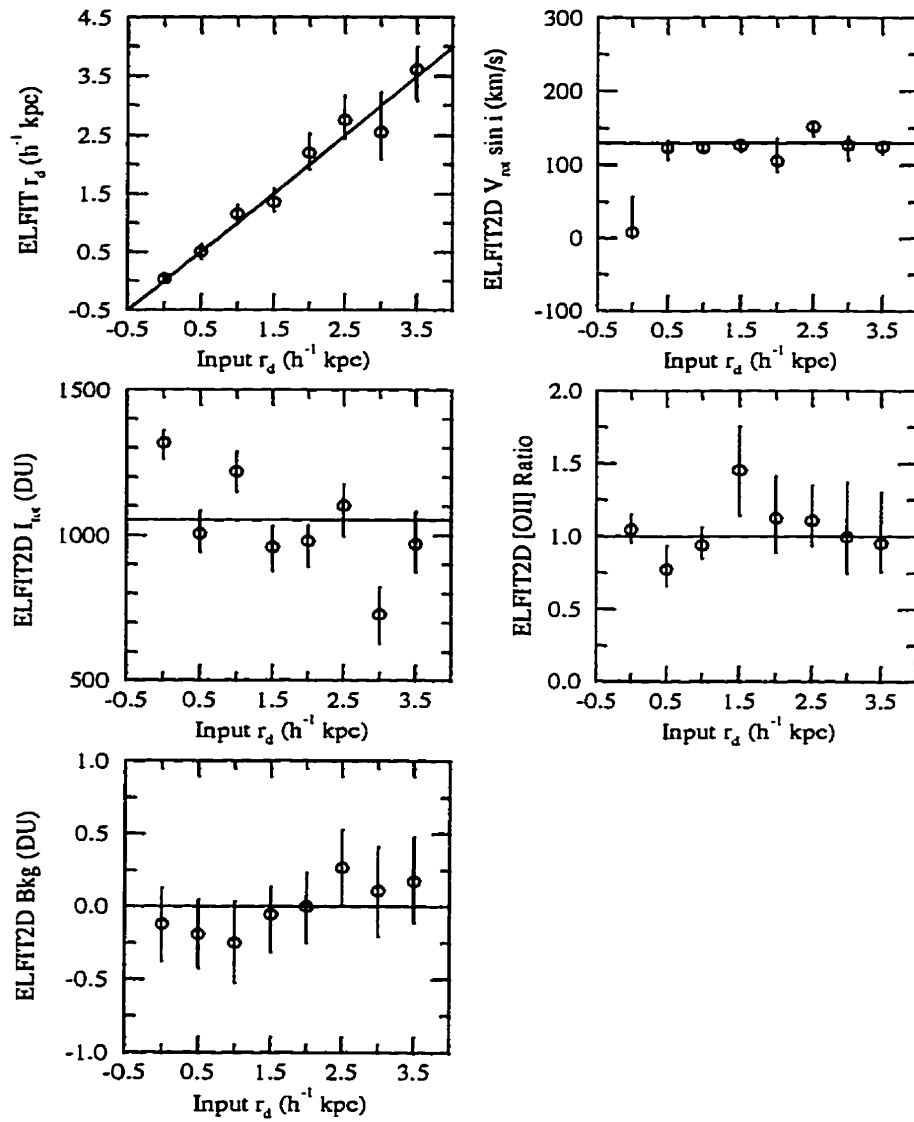


Figure 6.14: $z = 0.42$ ELFIT2D SIS test sequence 1.1

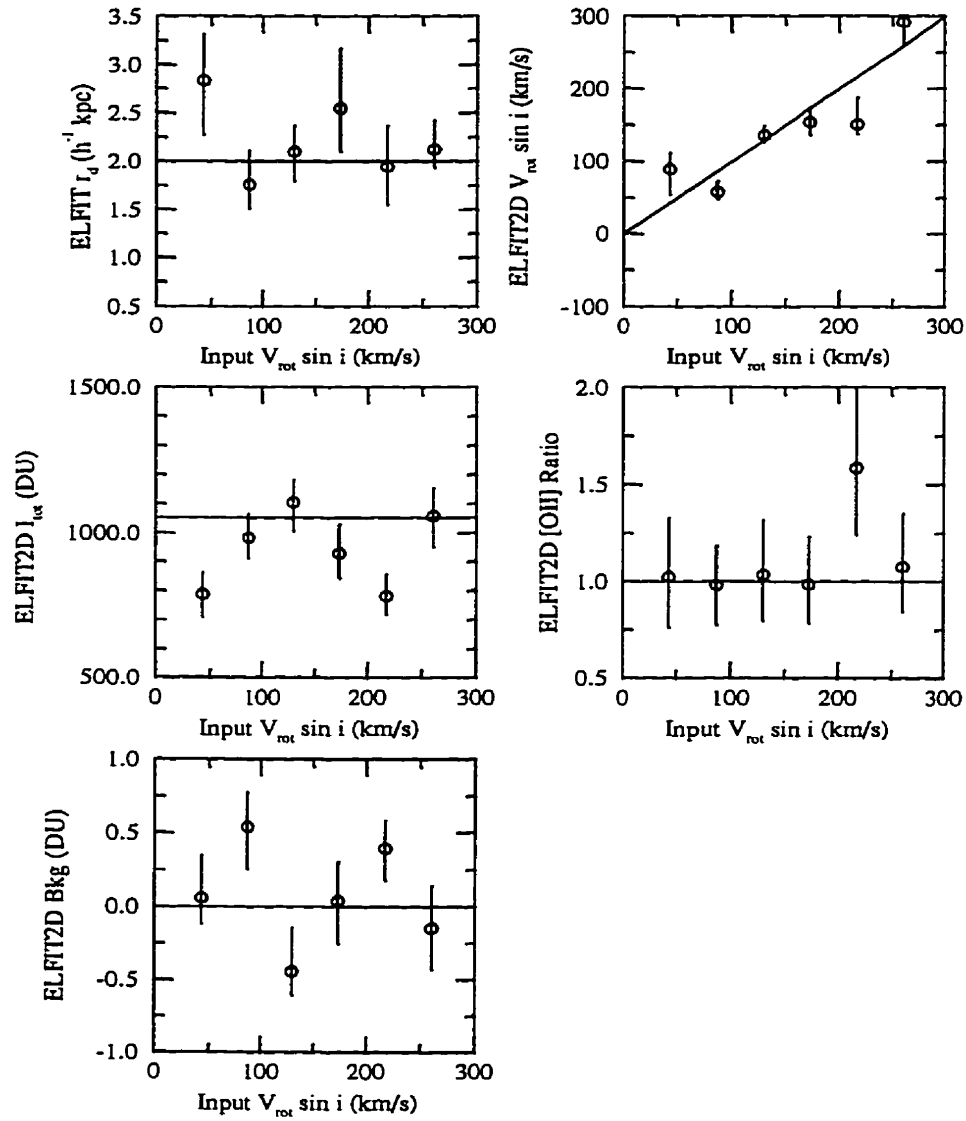


Figure 6.15: $z = 0.42$ ELFIT2D SIS test sequence 1.2

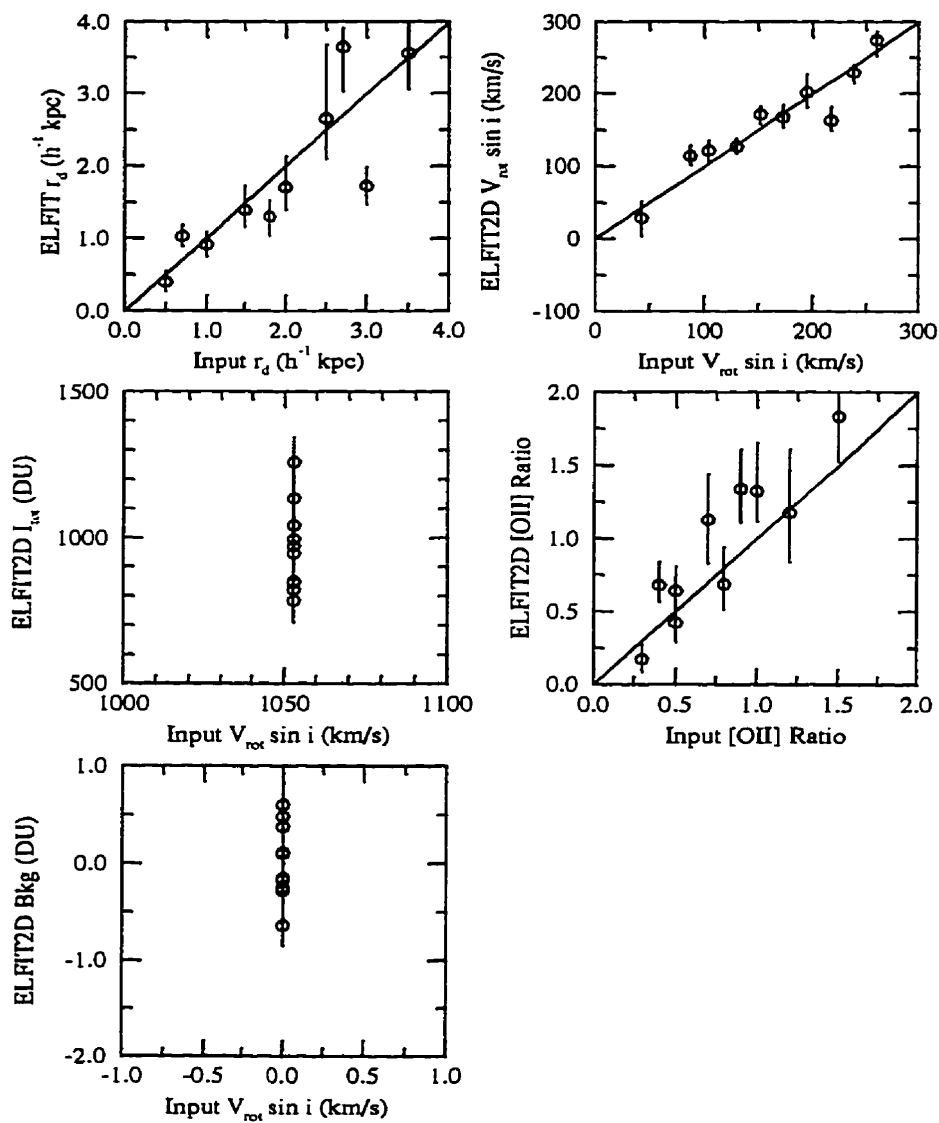


Figure 6.16: $z = 0.42$ ELFIT2D SIS test sequence 1.3

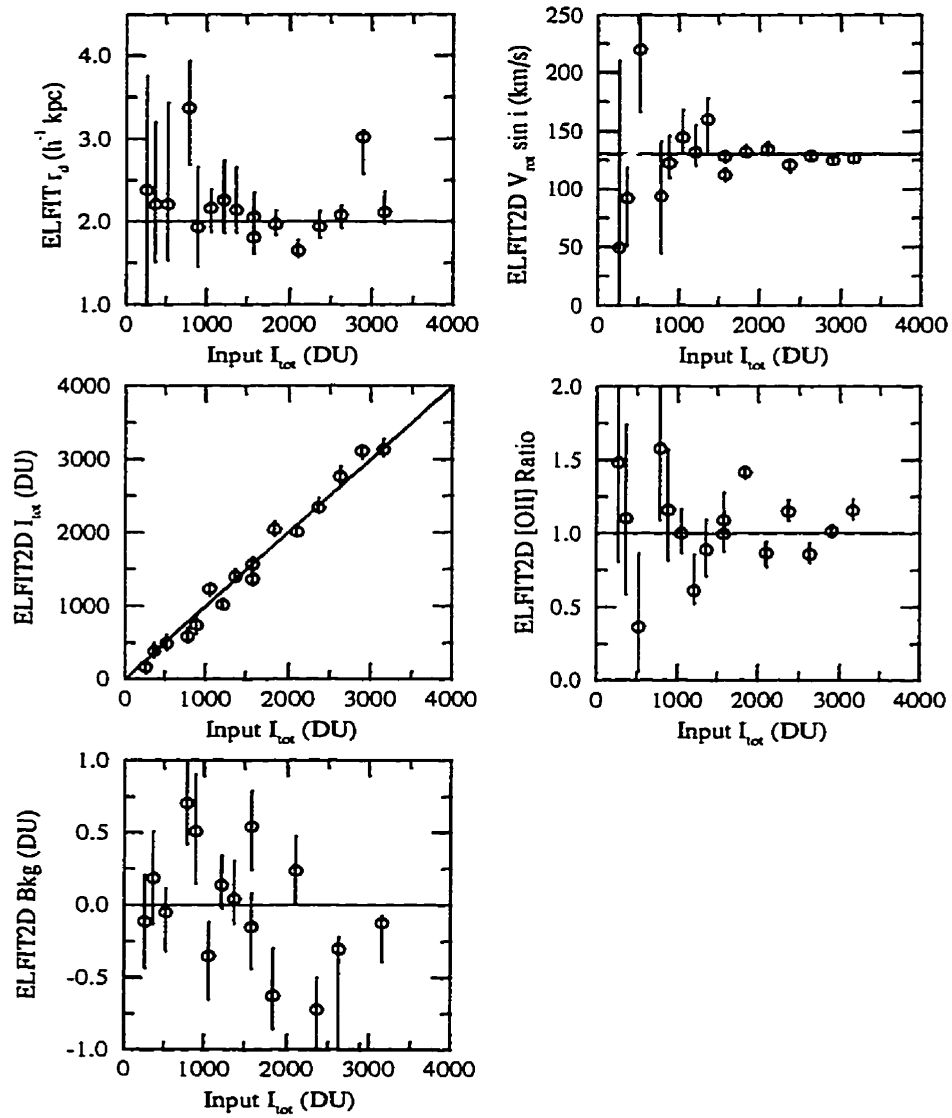


Figure 6.17: $z = 0.42$ ELFIT2D SIS test sequence 1.4

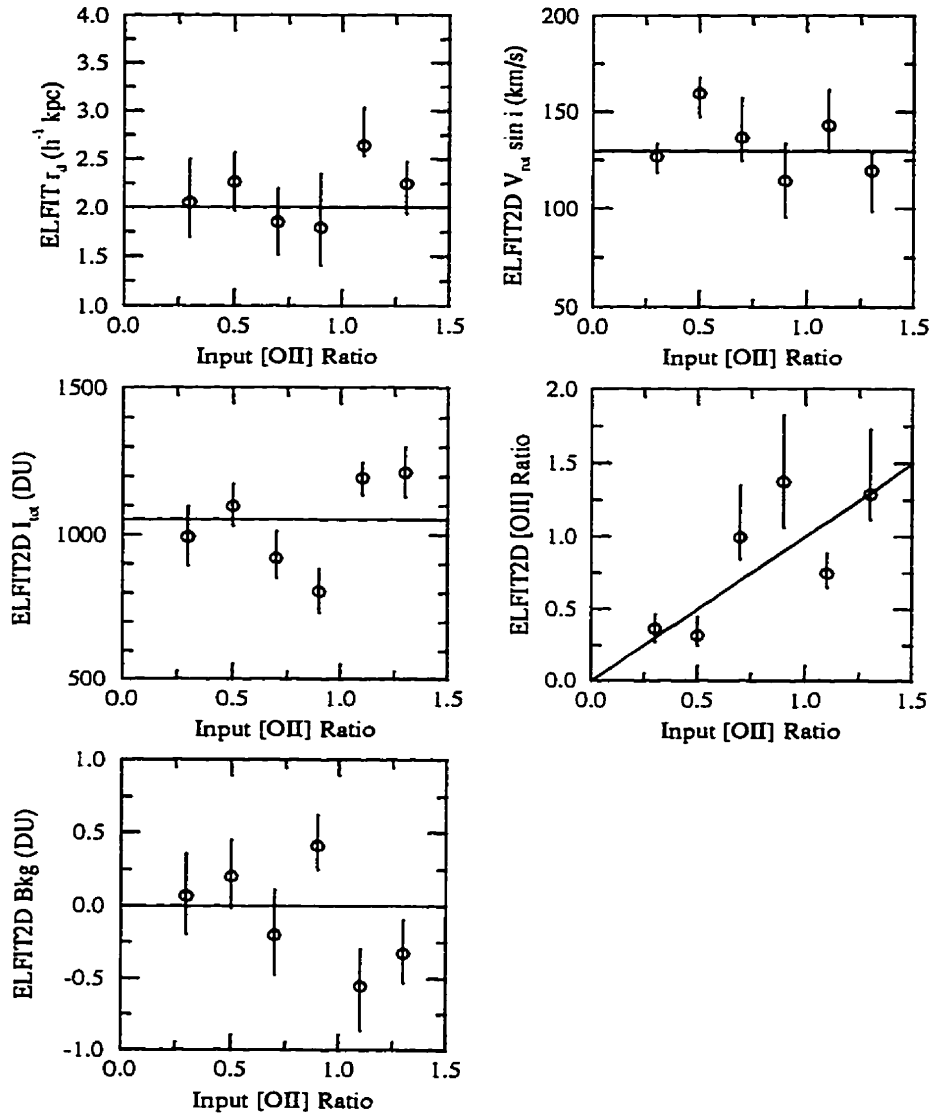


Figure 6.18: $z = 0.42$ ELFIT2D SIS test sequence 1.5

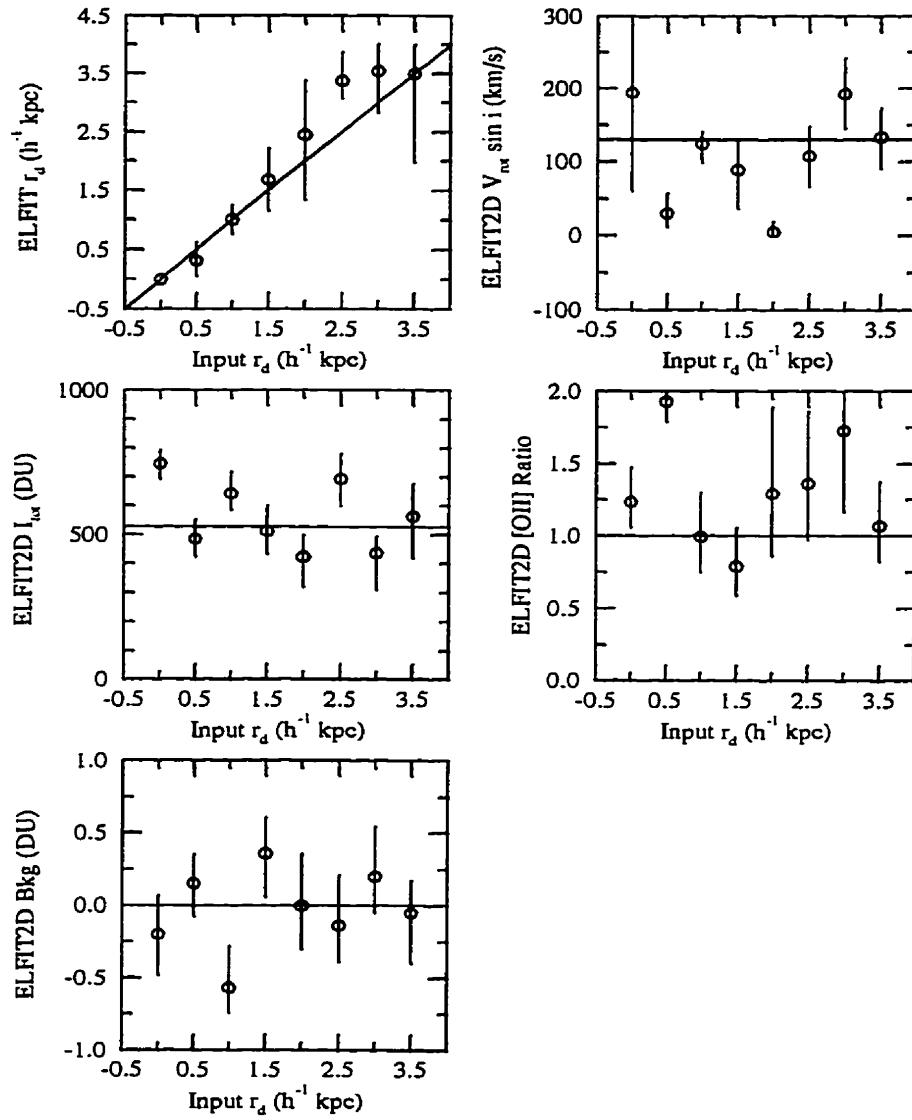


Figure 6.19: $z = 0.42$ ELFIT2D SIS test sequence 2.1

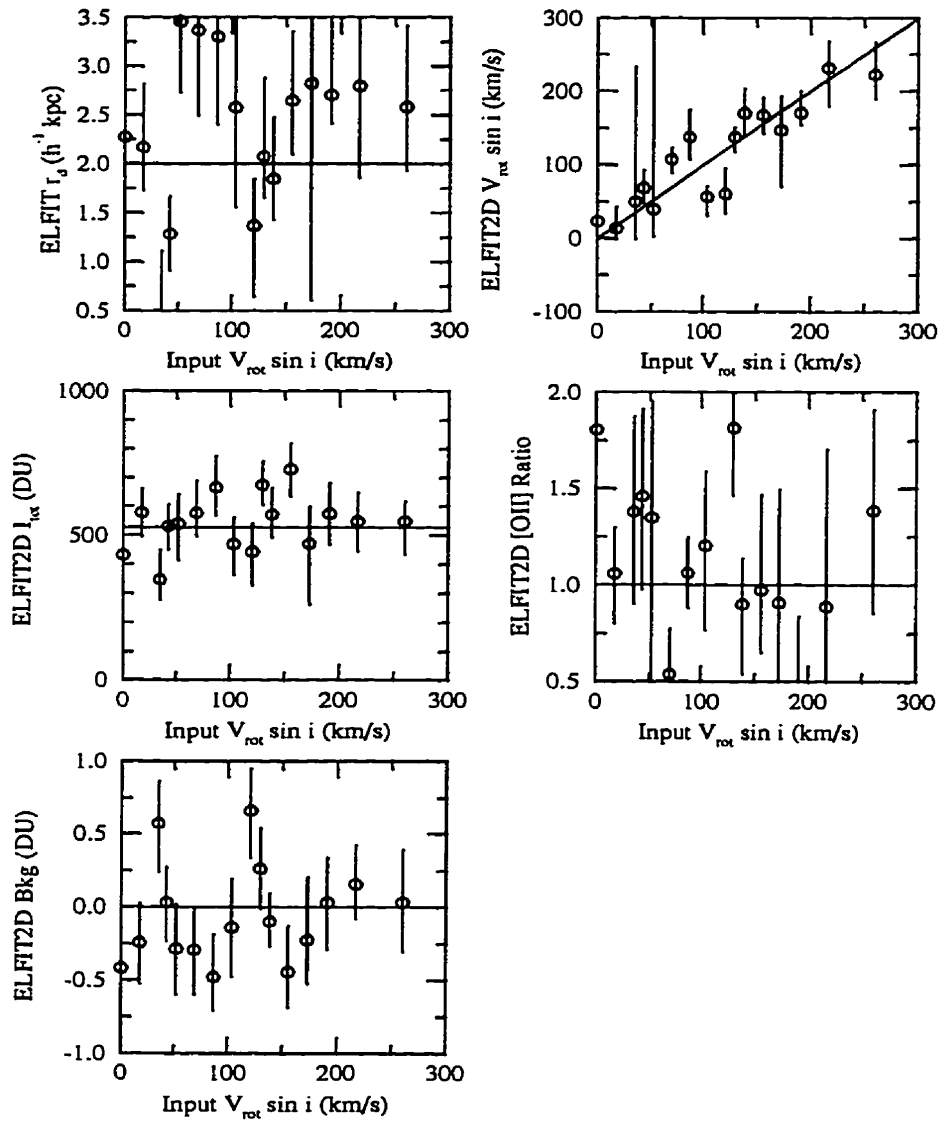


Figure 6.20: $z = 0.42$ ELFIT2D SIS test sequence 2.2

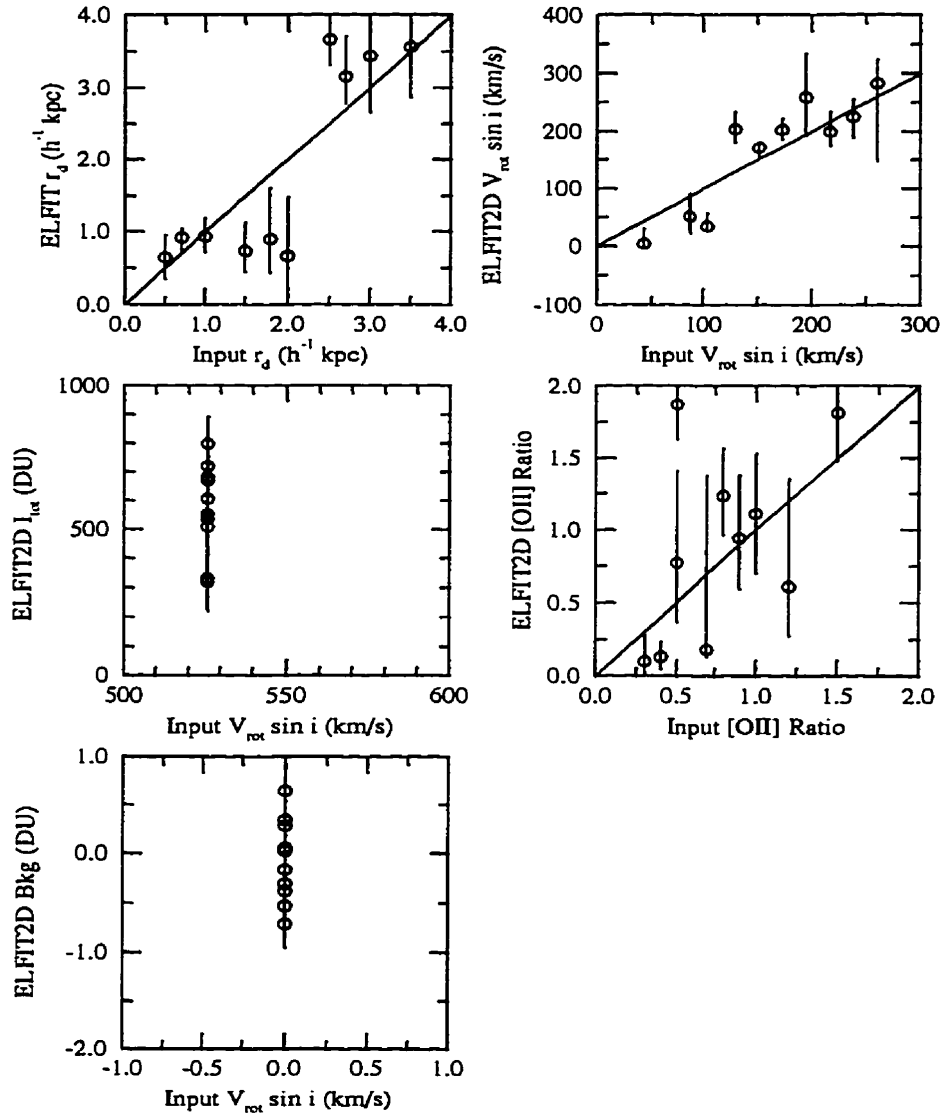


Figure 6.21: $z = 0.42$ ELFIT2D SIS test sequence 2.3

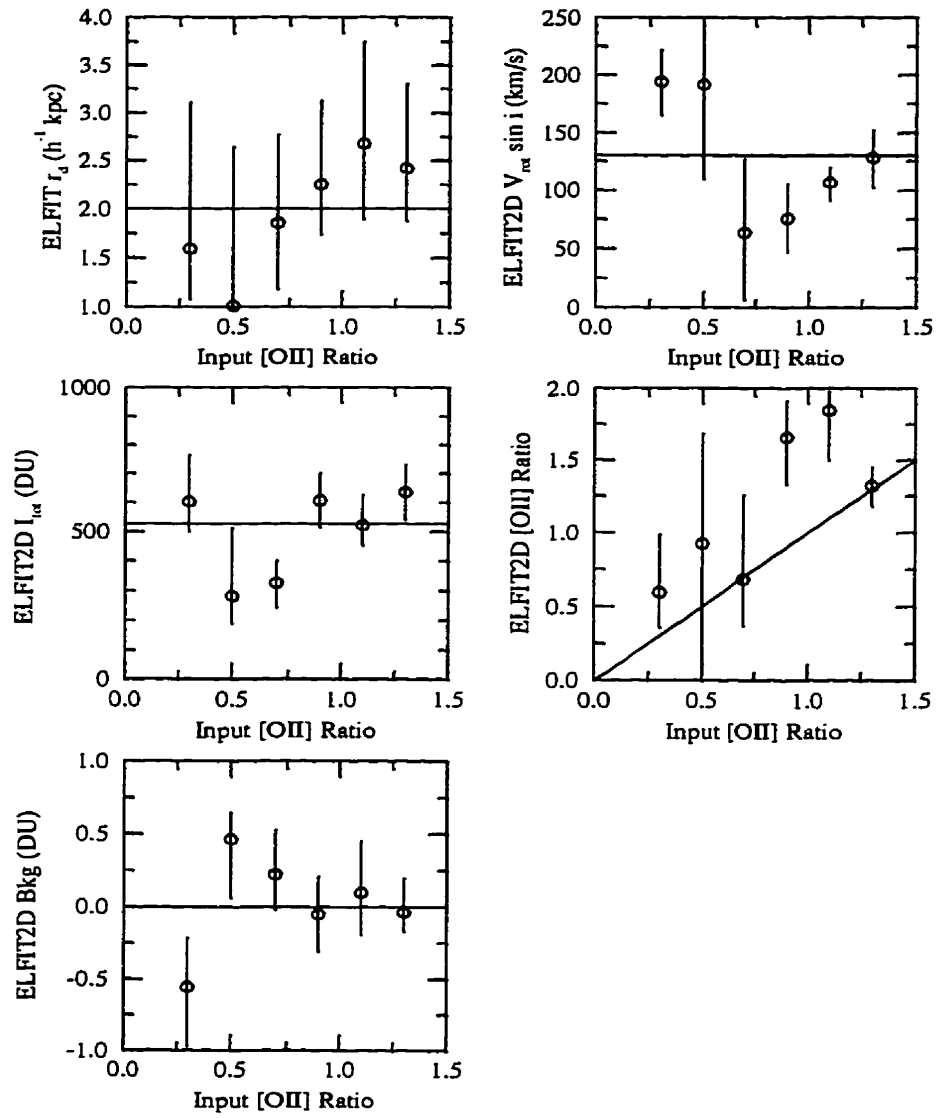


Figure 6.22: $z = 0.42$ ELFIT2D SIS test sequence 2.5

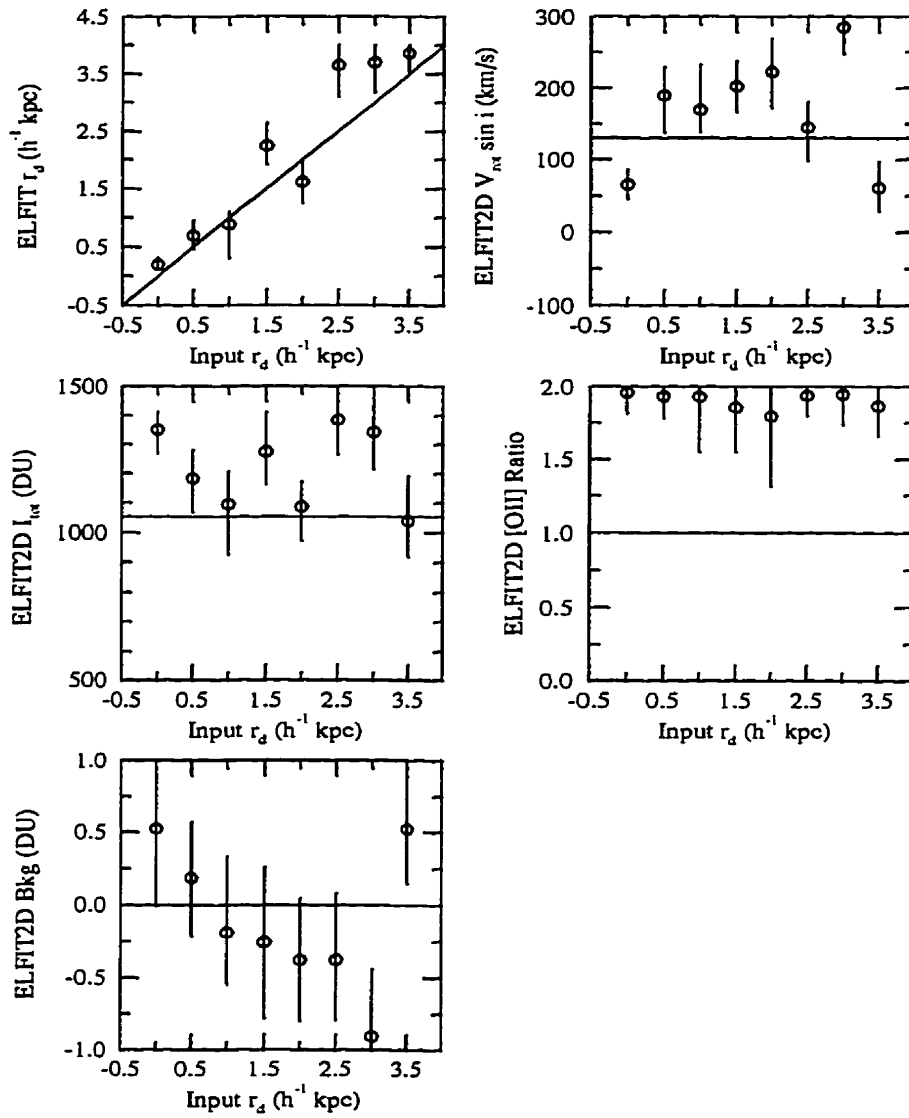


Figure 6.23: $z = 0.25$ ELFIT2D MOS test sequence 1

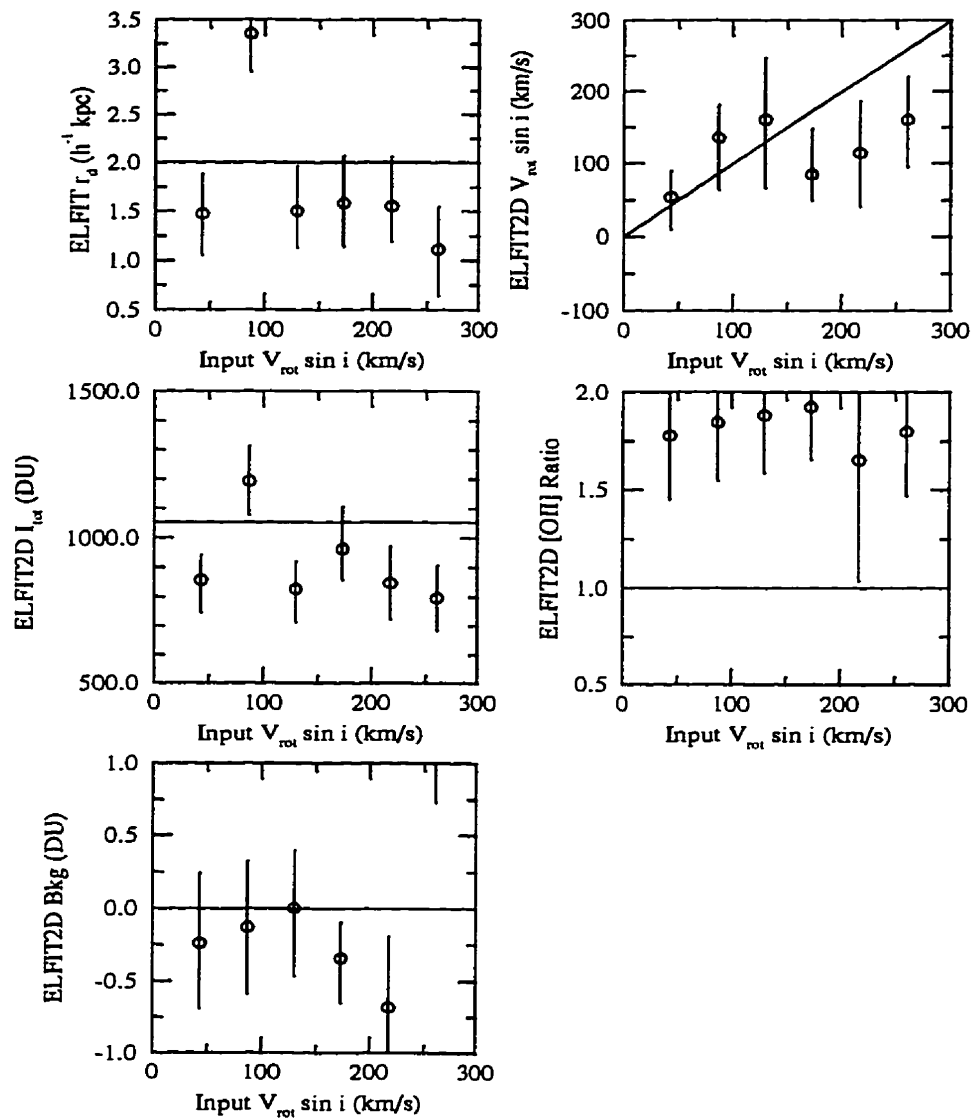


Figure 6.24: $z = 0.25$ ELFIT2D MOS test sequence 2

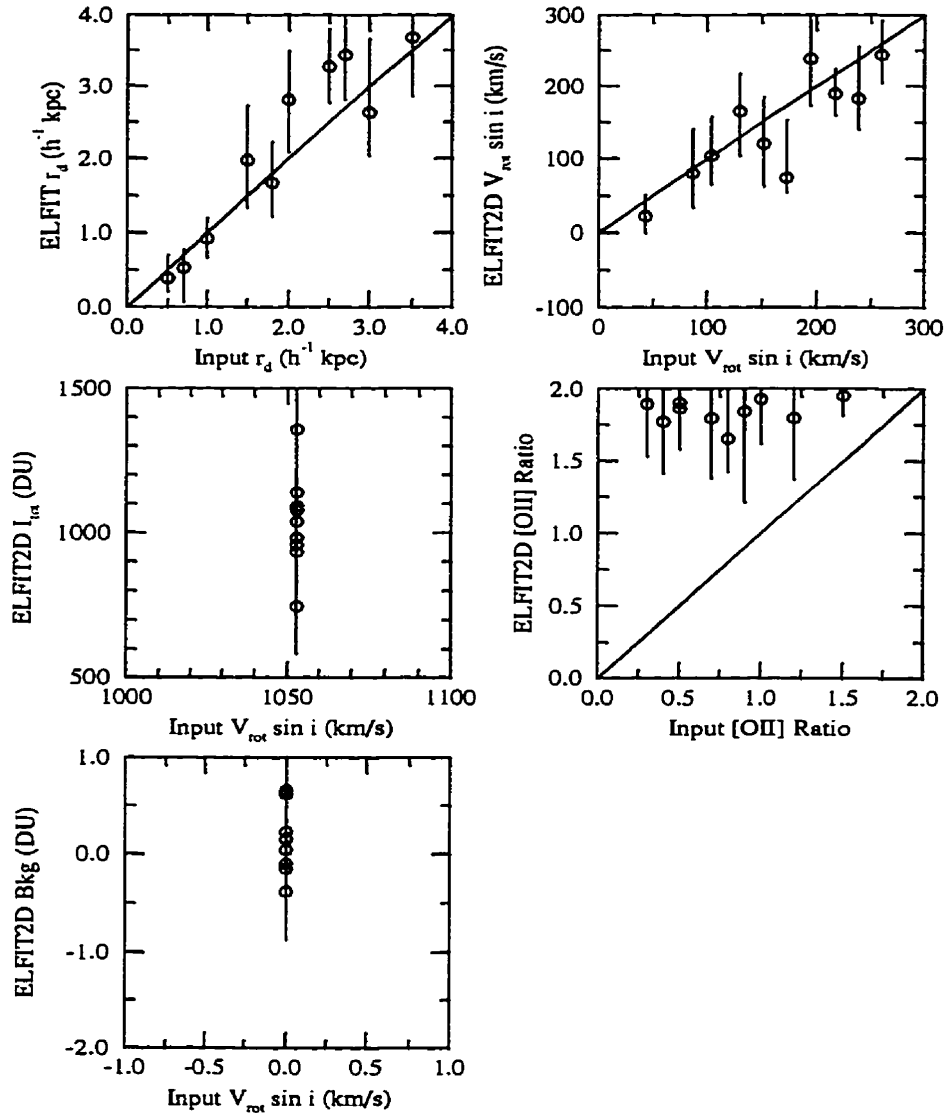


Figure 6.25: $z = 0.25$ ELFIT2D MOS test sequence 3

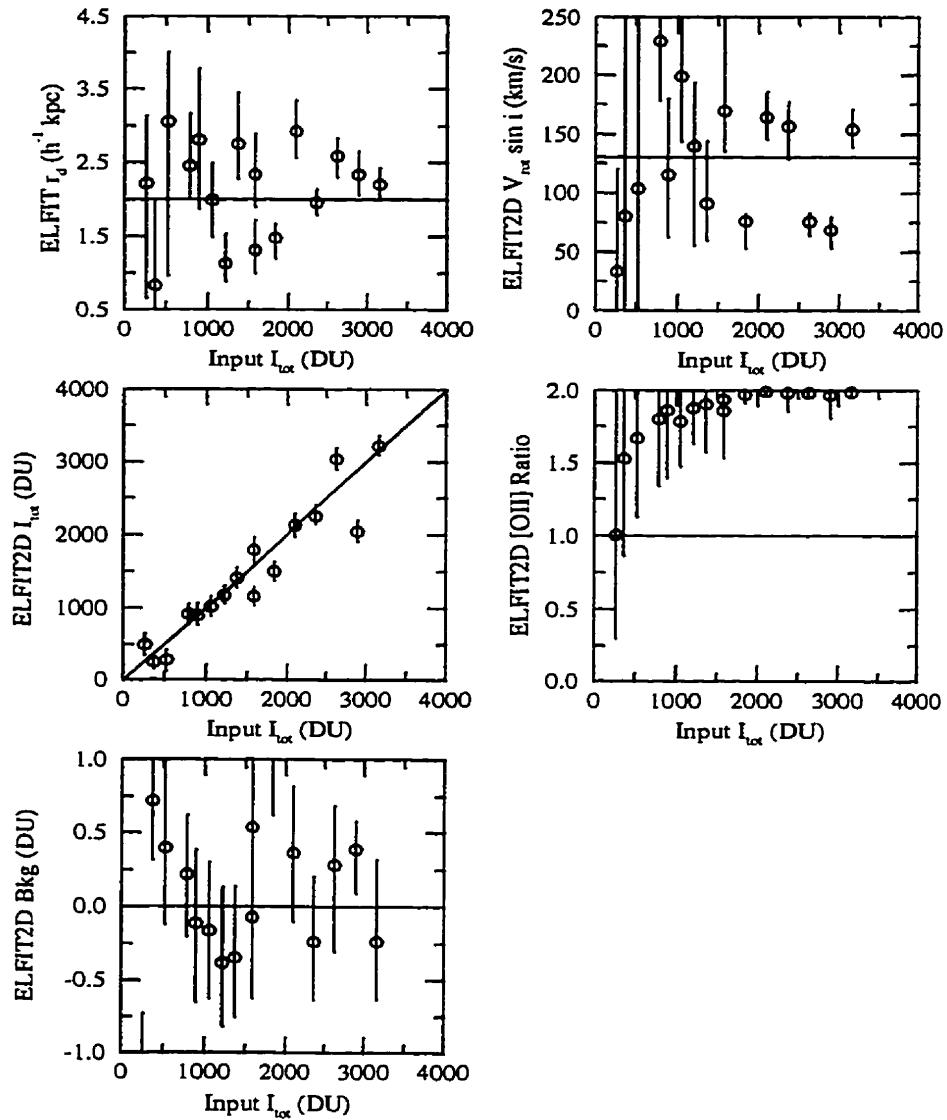


Figure 6.26: $z = 0.25$ ELFIT2D MOS test sequence 4

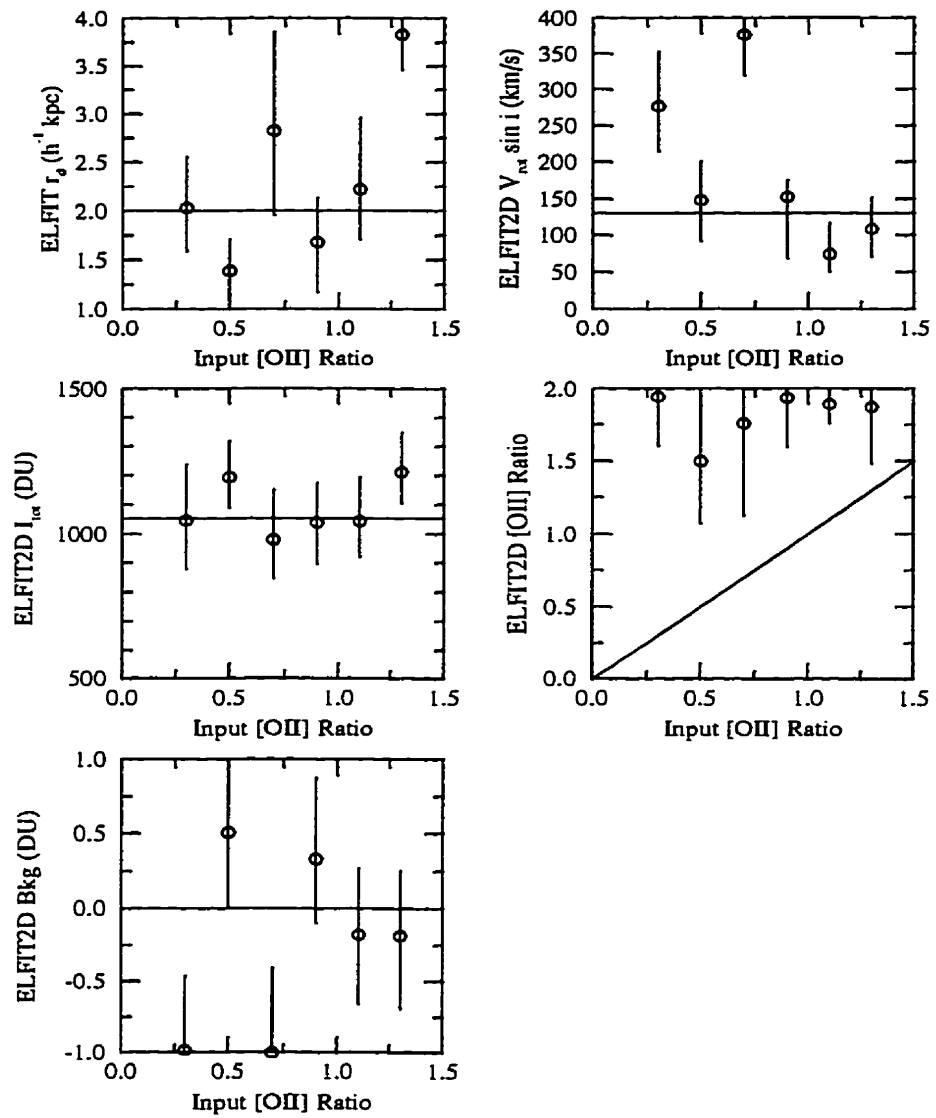


Figure 6.27: $z = 0.25$ ELFIT2D MOS test sequence 5

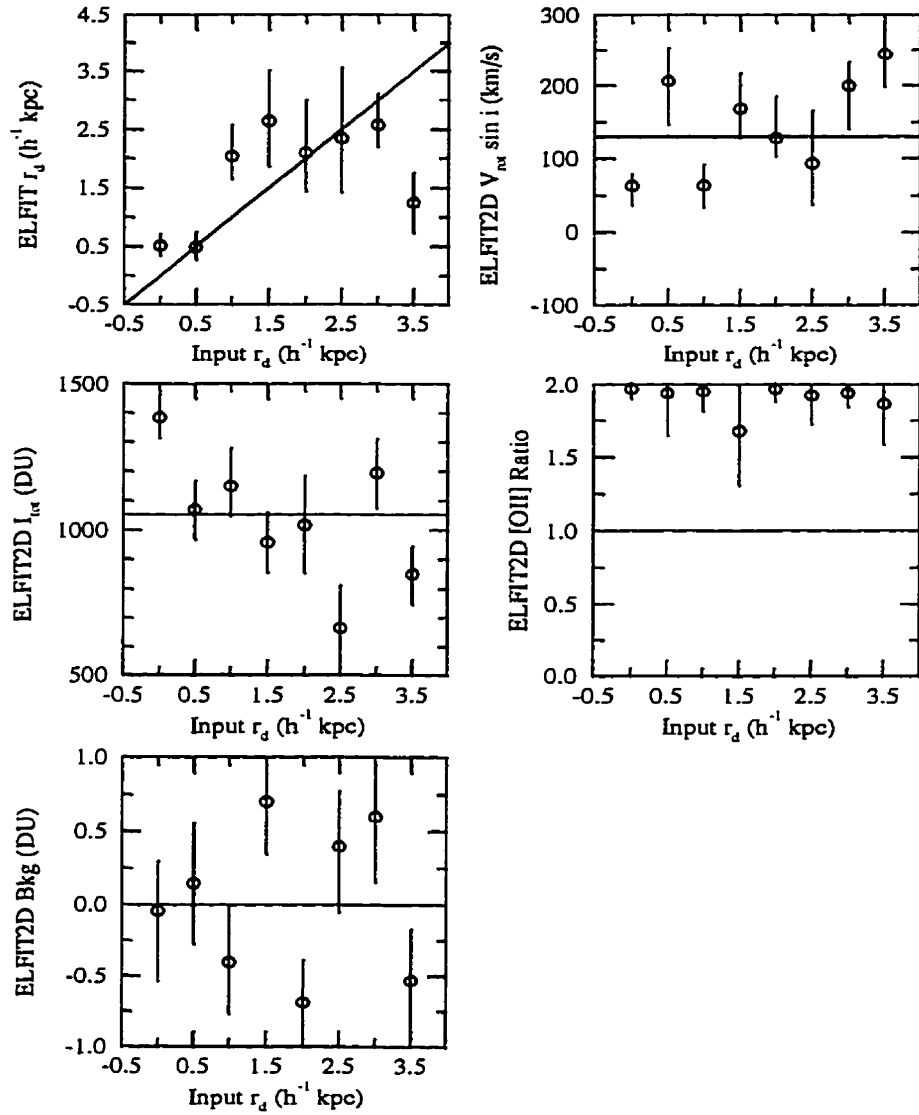


Figure 6.28: $z = 0.42$ ELFIT2D MOS test sequence 1

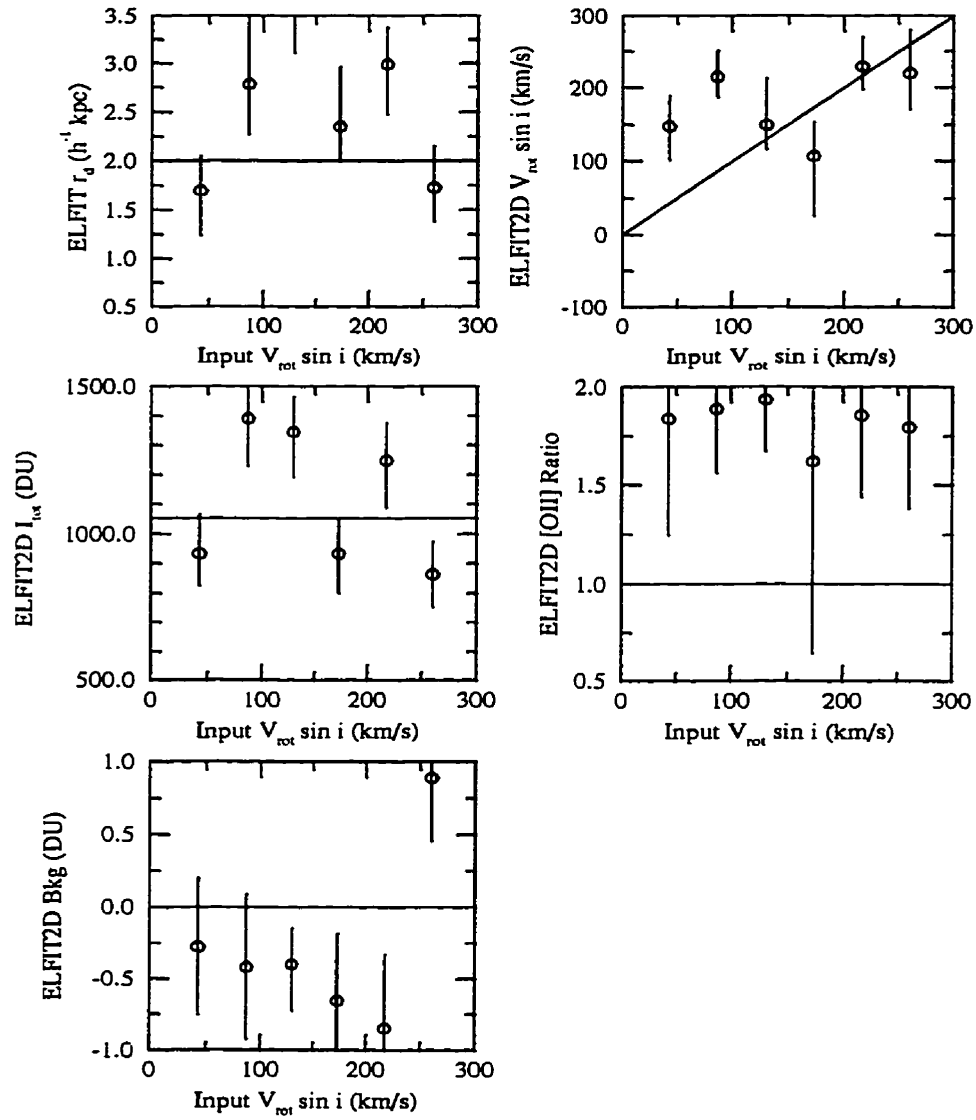


Figure 6.29: $z = 0.42$ ELFIT2D MOS test sequence 2

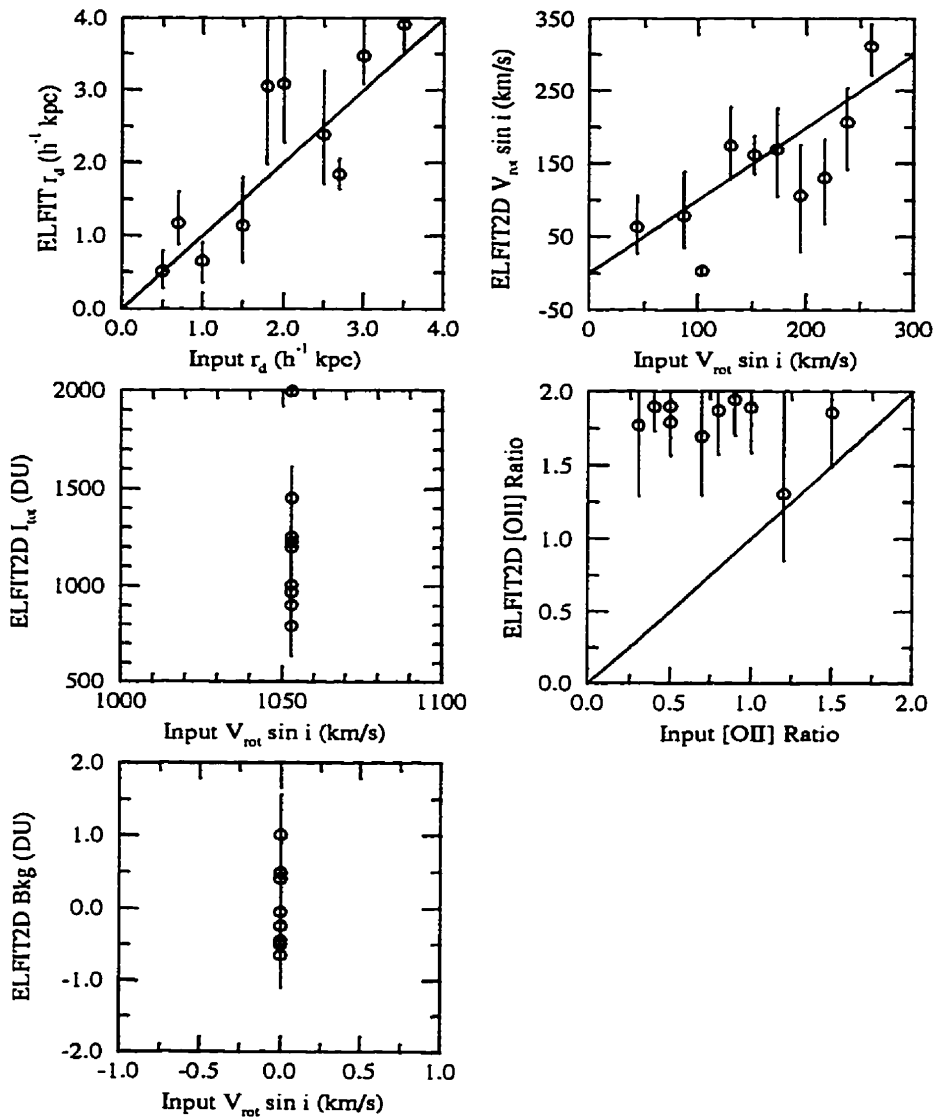


Figure 6.30: $z = 0.42$ ELFIT2D MOS test sequence 3

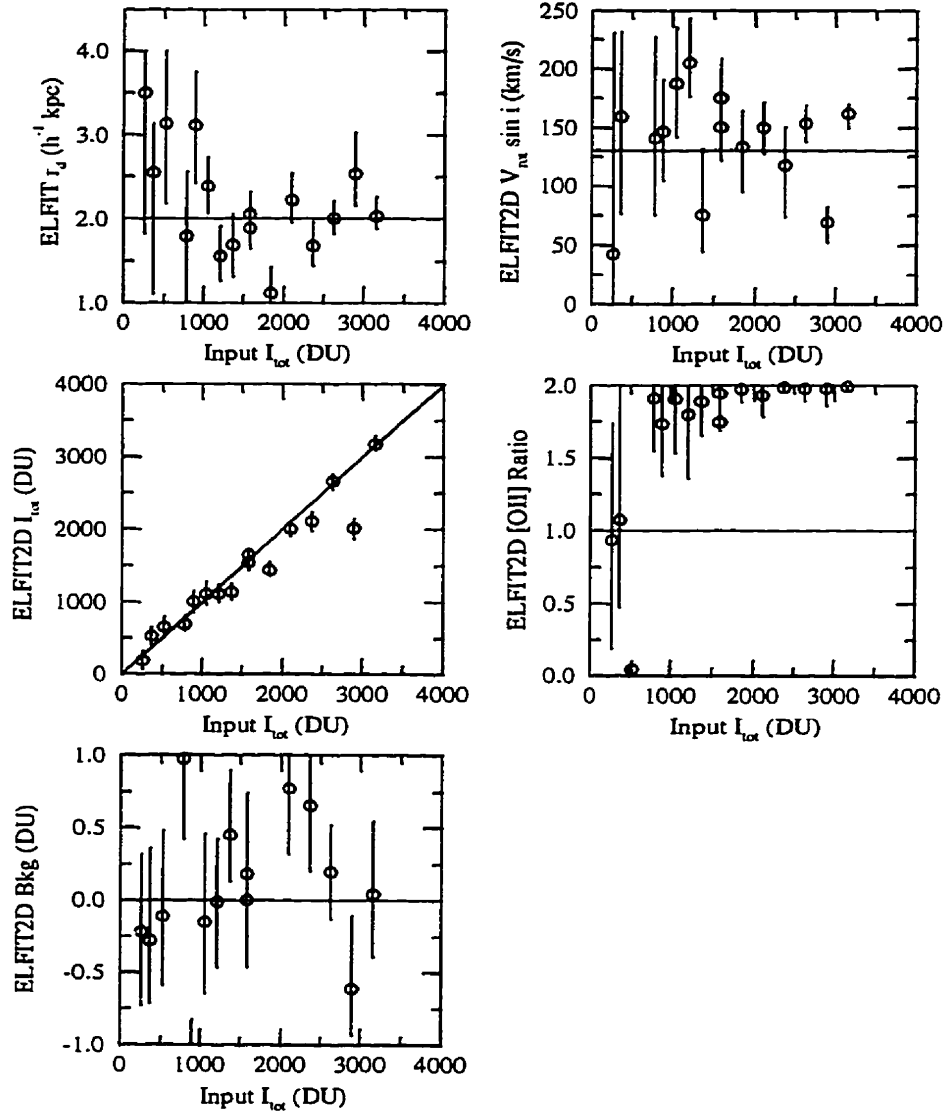


Figure 6.31: $z = 0.42$ ELFIT2D MOS test sequence 4

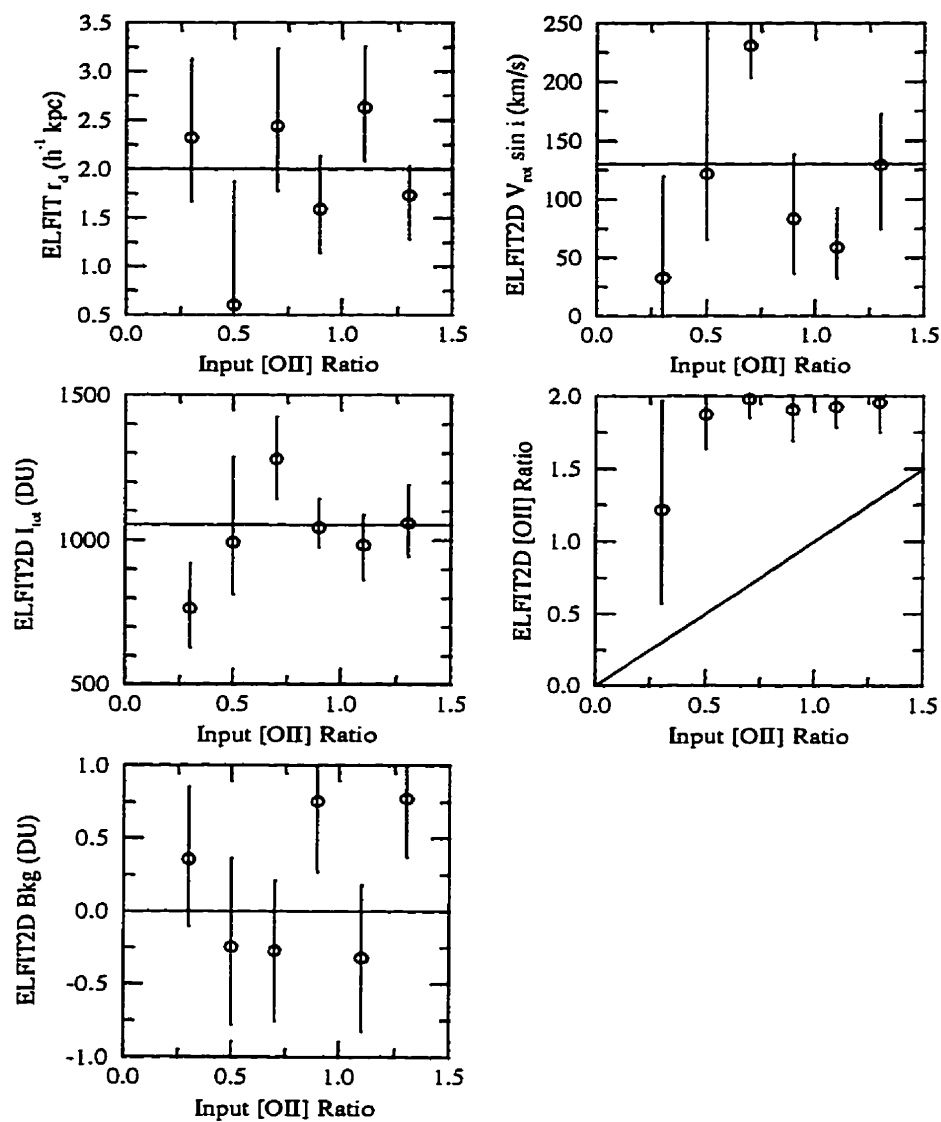


Figure 6.32: $z = 0.42$ ELFIT2D MOS test sequence 5

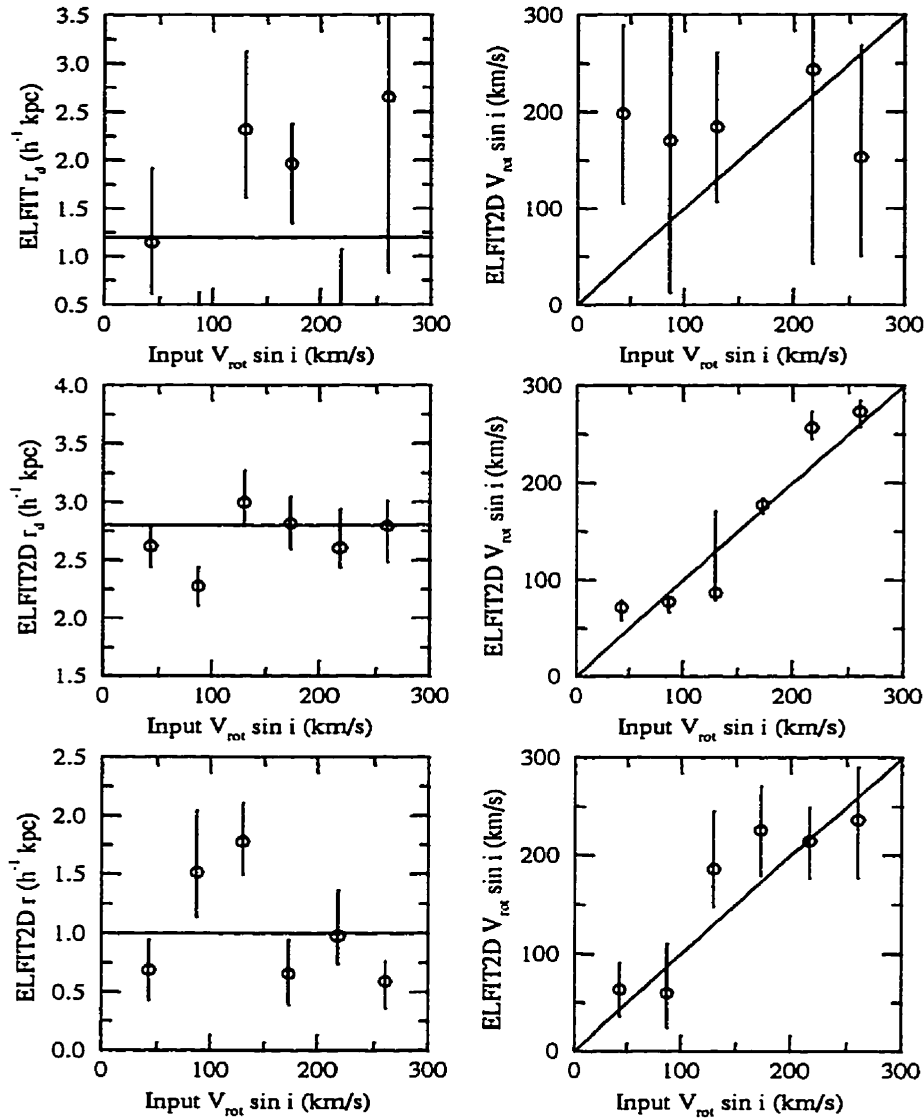


Figure 6.33: ELFIT2D MOS scale length and $V_{\text{rot}} \sin i$ tests - 1. From top to bottom: A2390-100225, A2390-101084 and A2390-200928. The solid lines show the input values as a function of $V_{\text{rot}} \sin i$.

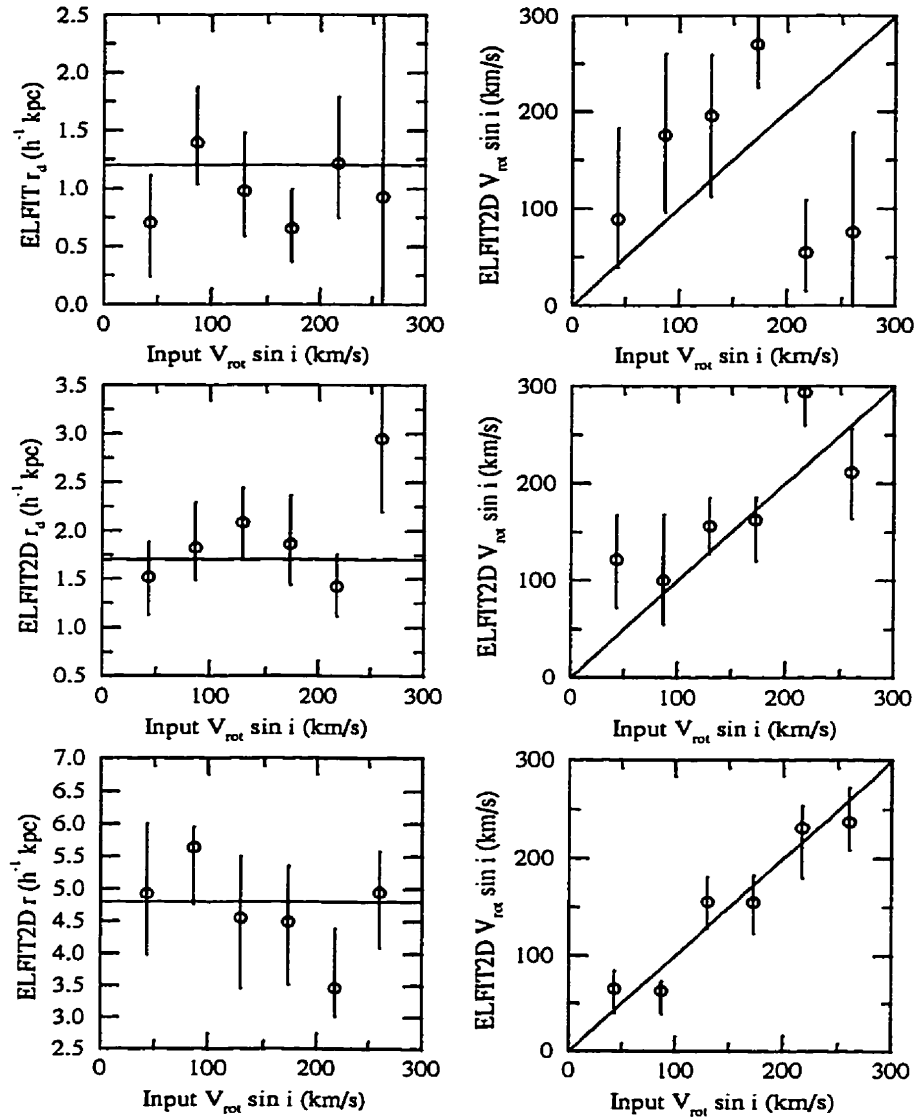


Figure 6.34: ELFIT2D MOS scale length and $V_{\text{rot}} \sin i$ tests - 2. From top to bottom: A2390-200802, A2390-200372 and E1512-201845. The solid lines show the input values as a function of $V_{\text{rot}} \sin i$.

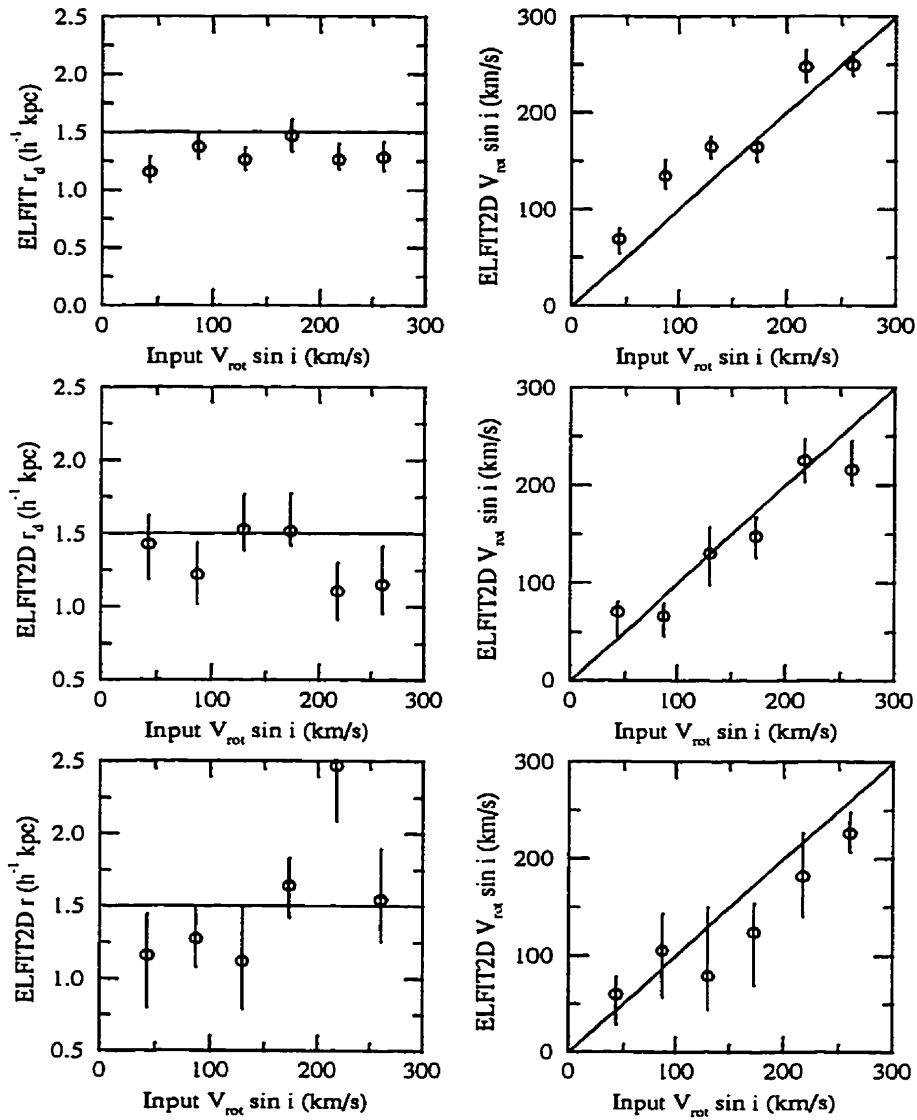


Figure 6.35: ELFIT2D MOS scale length and $V_{\text{rot}} \sin i$ tests - 3. From top to bottom: E1512-201773, E1512-200730 and E1512-200334. The solid lines show the input values as a function of $V_{\text{rot}} \sin i$.

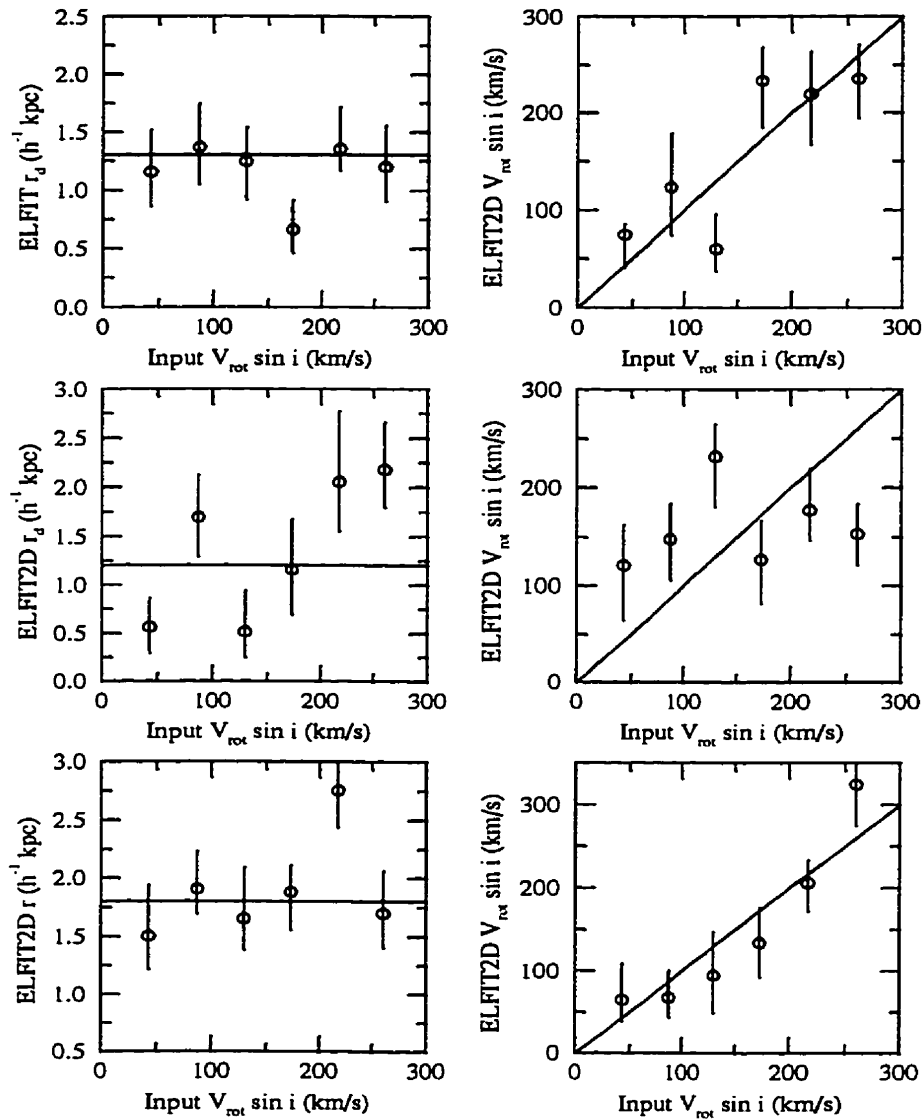


Figure 6.36: ELFIT2D MOS scale length and $V_{\text{rot}} \sin i$ tests - 4. From top to bottom: E1512-200672, E1512-201268 and E1512-202096. The solid lines show the input values as a function of $V_{\text{rot}} \sin i$.

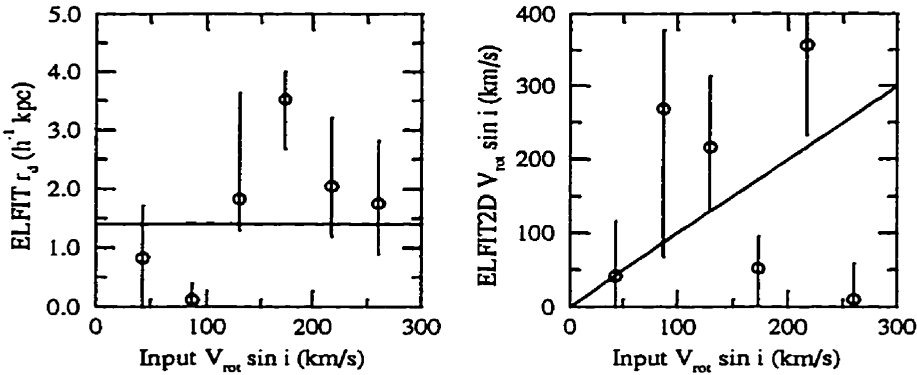


Figure 6.37: ELFIT2D MOS scale length and $V_{\text{rot}} \sin i$ tests - 5. At the top: E1512-201125. The solid lines show the input values as a function of $V_{\text{rot}} \sin i$.

Chapter 7

Results

7.1 Broad-Band Light Profiles

Galaxy luminosity profiles show the surface brightness of galaxies $\Sigma(r)$ as a function of galactocentric radius r . They fall into two broad categories: exponential and de Vaucouleurs profiles. The exponential profile is given by

$$\Sigma(r) = \Sigma_0 e^{-r/r_d} \quad (7.1)$$

where Σ_0 and r_d are the central surface brightness and scale length of the disk respectively. Disks are best fitted by an exponential profile. The de Vaucouleurs profile (also known as the $r^{1/4}$ law) is given by

$$\Sigma(r) = \Sigma_e e^{-7.67[(r/r_e)^{1/4} - 1]} \quad (7.2)$$

where Σ_e and r_e are known as the effective surface brightness and radius respectively. The de Vaucouleurs profile is a purely empirical fit to the profiles of elliptical galaxies and bulges. It is relatively easy to qualitatively determine whether a given galaxy profile is exponential or de Vaucouleurs by

plotting $\log \Sigma$ as function of r or $r^{1/4}$. In the $\log \Sigma - r$ plane, an exponential profile will simply look like a straight line whereas a de Vaucouleurs will look “concave up”. Similarly, in the $\log \Sigma - r^{1/4}$ plane, a de Vaucouleurs profile will be a straight line whereas the exponential profile will look “concave down”.

The initial plan was to perform deep SIS imaging on all target galaxies during the August 1994 observing run. However, technical problems and bad weather in July made it necessary to devote most of the August run to spectroscopic observations. Consequently (and unfortunately), the imaging data set is quite heterogeneous: Gunn r and g MOS images taken by the CNOC cluster surveys for all target galaxies, I band SIS images obtained for 9 galaxies during the July and August runs, and deep V and R images of two galaxies obtained during a third run in September 1994 unrelated to the current project.

Galaxy luminosity profiles were measured using the task ELLIPSE in the STSDAS/ISOPHOTE package. ELLIPSE fits the galaxy luminosity profiles with isophotal ellipses following Jedrzejewski (1987). The fits were made with four degrees of freedom: x and y coordinates of galaxy center, ellipticity and position angle of the semi-major axis. Starting from user-specified values for the semi-major axis, x and y axis center, ellipticity and position angle, ELLIPSE samples the image along a first-guess elliptical path to produce a 1-dimensional intensity distribution as a function of the ellipse eccentric anomaly. The harmonic content of this distribution is analyzed by least-squares fitting, and the changes to the initial parameter values are given by the harmonic amplitudes. Once convergence has been achieved, ELLIPSE

proceeds outwards to the next radius until the profile gradient is less than a user-specified fraction of the RMS intensity residuals along the isophotal path. Parameter values are frozen beyond this point to determine the intensity levels of the outwardmost isophotes.

Gunn r and g luminosity profiles measured from CNOC MOS images are shown in Figures 7.1- 7.4 and Figures 7.5- 7.8. SIS I band profiles are shown in Figures 7.9 and 7.10. SIS V and R profiles are shown in Figure 7.11. The solid lines are exponential profile fits with the scale length shown for each galaxy. The galactocentric radius in kiloparsecs was computed from the apparent size in arcseconds and the galaxy redshift using the angular distance relation for $q_0 = 0.5$. Discussion of these broad-band galaxy luminosity profiles is deferred to section 7.3 where they are compared to [OII] morphologies.

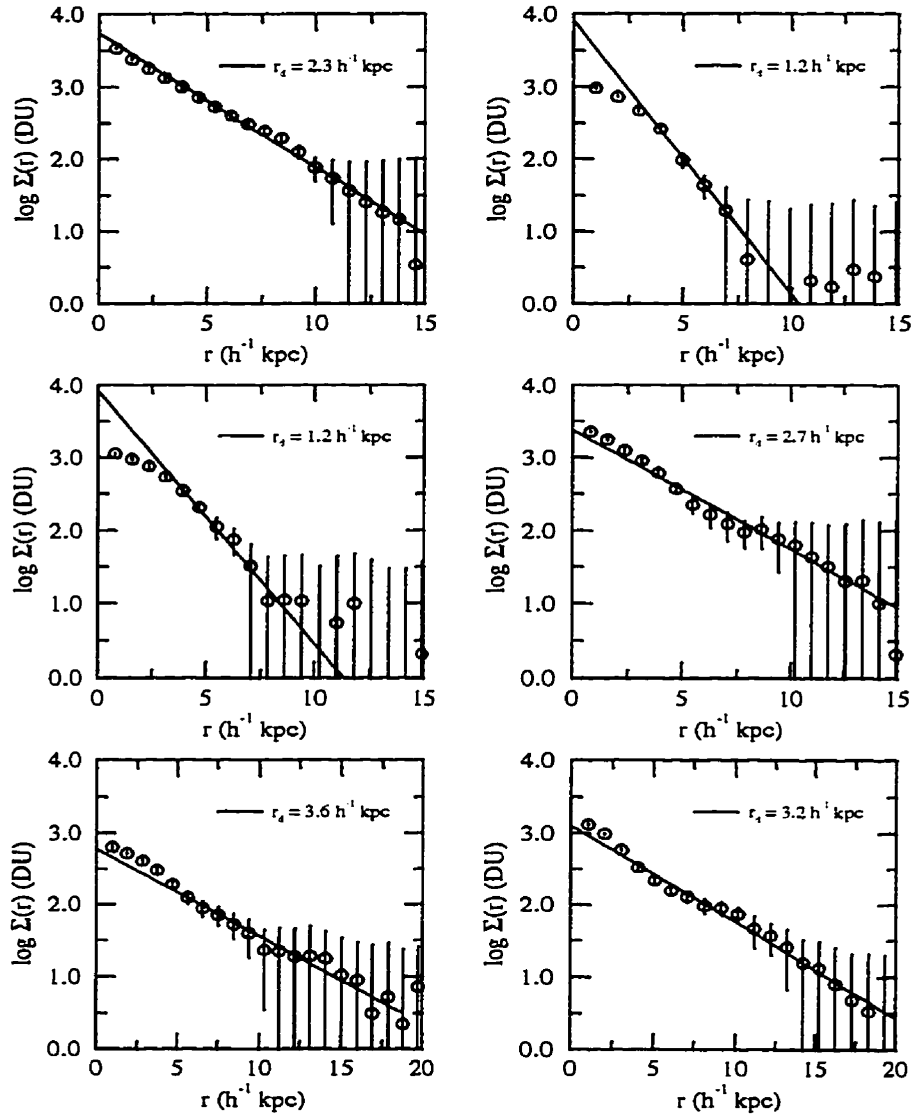


Figure 7.1: CNOC MOS Gunn r galaxy luminosity profiles determined with ELLIPSE. Row-by-row and starting from the top: A2390-101033 and A2390-100686, A2390-350416 and A2390-350471, E1512-301037 and E1512-101526. The solid lines are exponential disk fits with the scale length shown for each galaxy. The physical distance on the x-axis was calculated from the redshift of the galaxy and the angular distance relation for $q_0 = 0.5$.

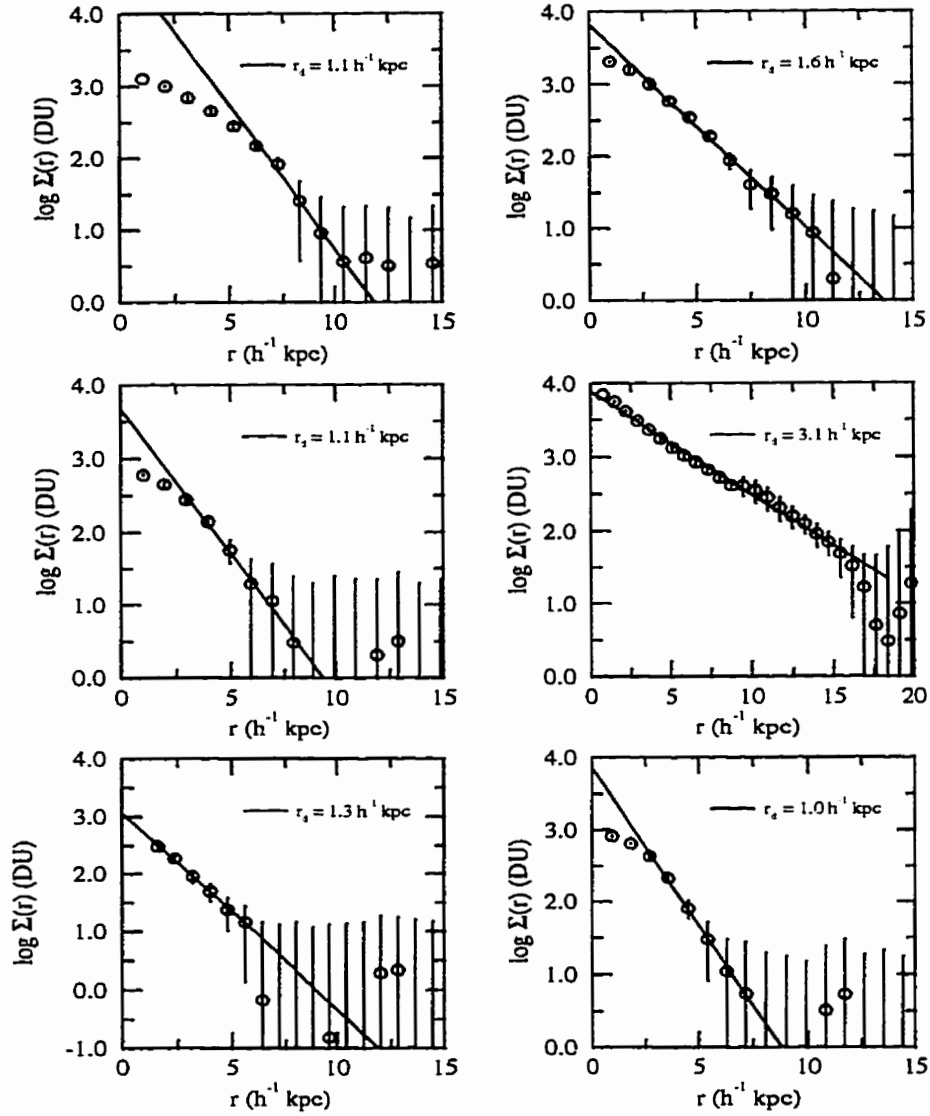


Figure 7.2: CNOC MOS Gunn r galaxy luminosity profiles determined with ELLIPSE. Row-by-row and starting from the top: E1512-201429 and E1621-100515, A2390-100225 and A2390-101084, A2390-200928 and A2390-200802. The solid lines are exponential disk fits with the scale length shown for each galaxy. The physical distance on the x-axis was calculated from the redshift of the galaxy and the angular distance relation for $q_0 = 0.5$.

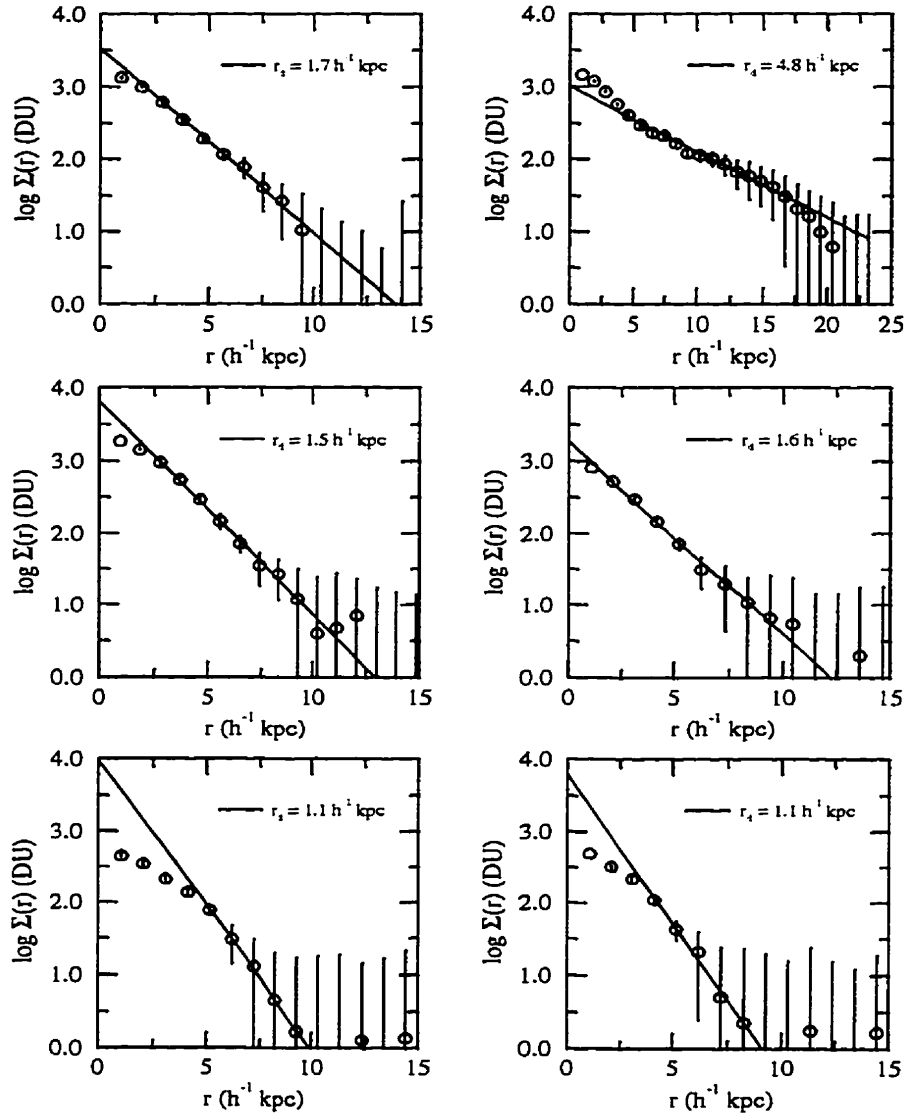


Figure 7.3: CNOC MOS Gunn r galaxy luminosity profiles determined with ELLIPSE. Row-by-row and starting from the top: A2390-200372 and E1512-201845, E1512-201773 and E1512-200730, E1512-200334 and E1512-200672. The solid lines are exponential disk fits with the scale length shown for each galaxy. The physical distance on the x-axis was calculated from the redshift of the galaxy and the angular distance relation for $q_0 = 0.5$.

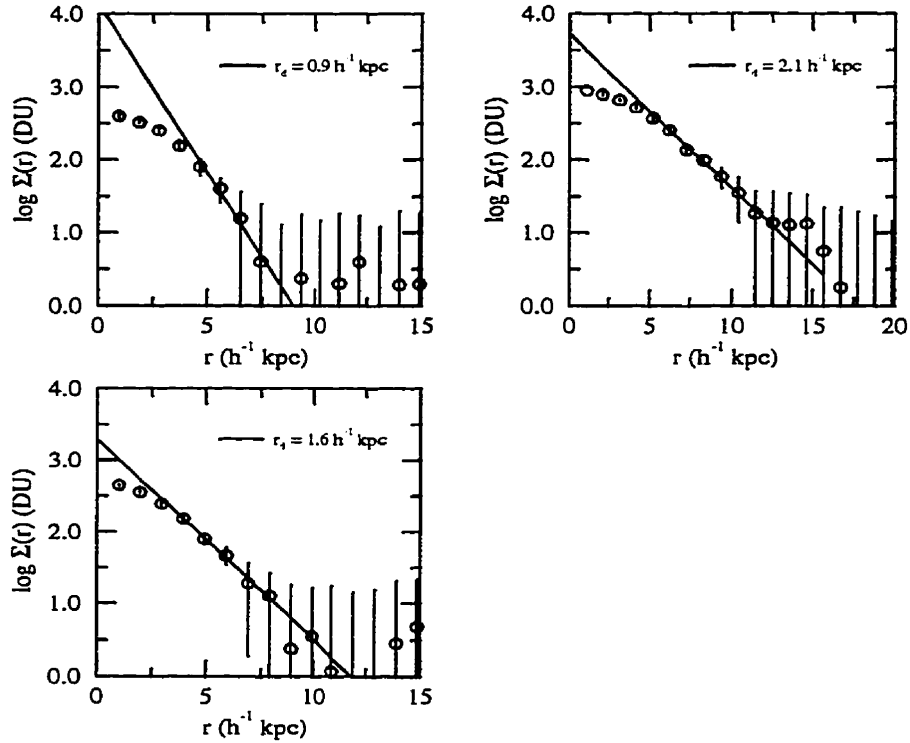


Figure 7.4: CNOC MOS Gunn r galaxy luminosity profiles determined with ELLIPSE. Row-by-row and starting from the top: E1512-201268 and E1512-202096, E1512-201125. The solid lines are exponential disk fits with the scale length shown for each galaxy. The physical distance on the x-axis was calculated from the redshift of the galaxy and the angular distance relation for $q_0 = 0.5$.

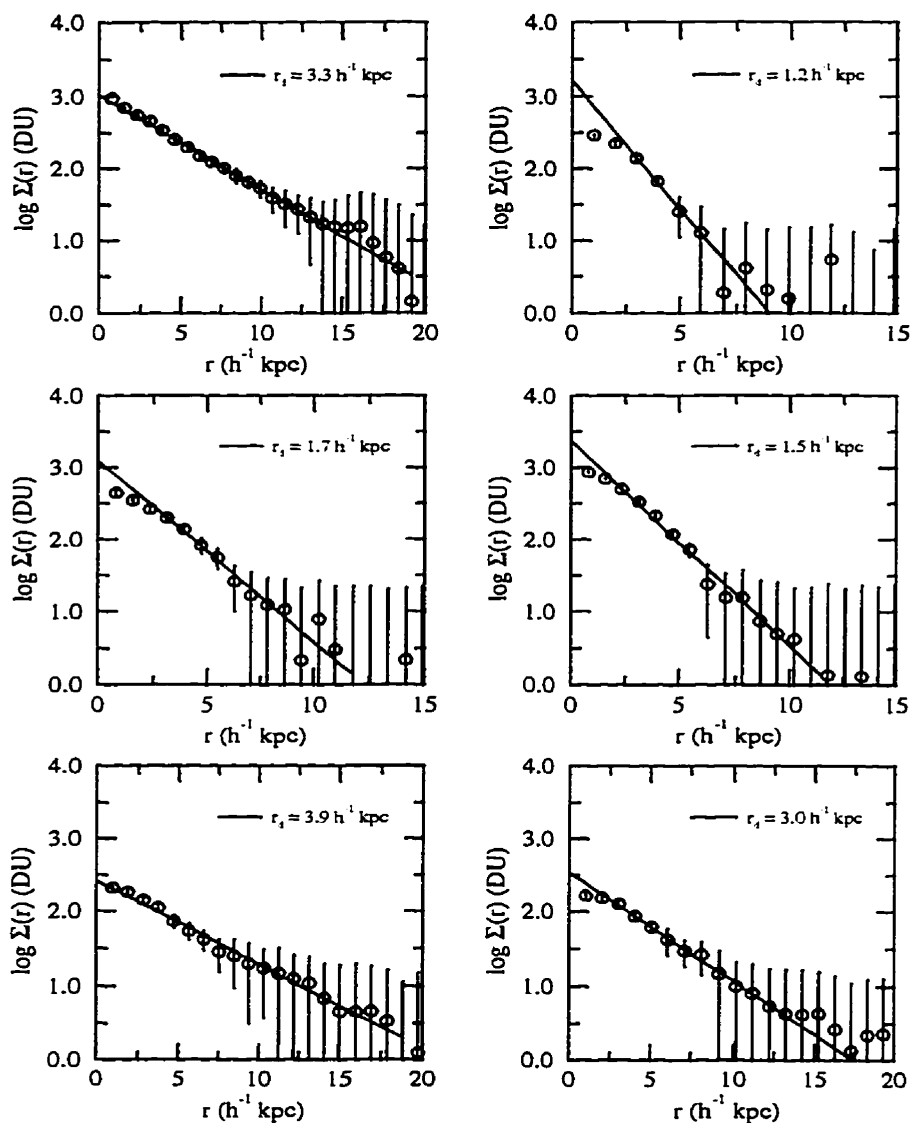


Figure 7.5: CNOC MOS Gunn g galaxy luminosity profiles determined with ELLIPSE. Row-by-row and starting from the top: A2390-101033 and A2390-100686, A2390-350416 and A2390-350471, E1512-301037 and E1512-101526. The solid lines are exponential disk fits with the scale length shown for each galaxy. The physical distance on the x-axis was calculated from the redshift of the galaxy and the angular distance relation for $q_0 = 0.5$.

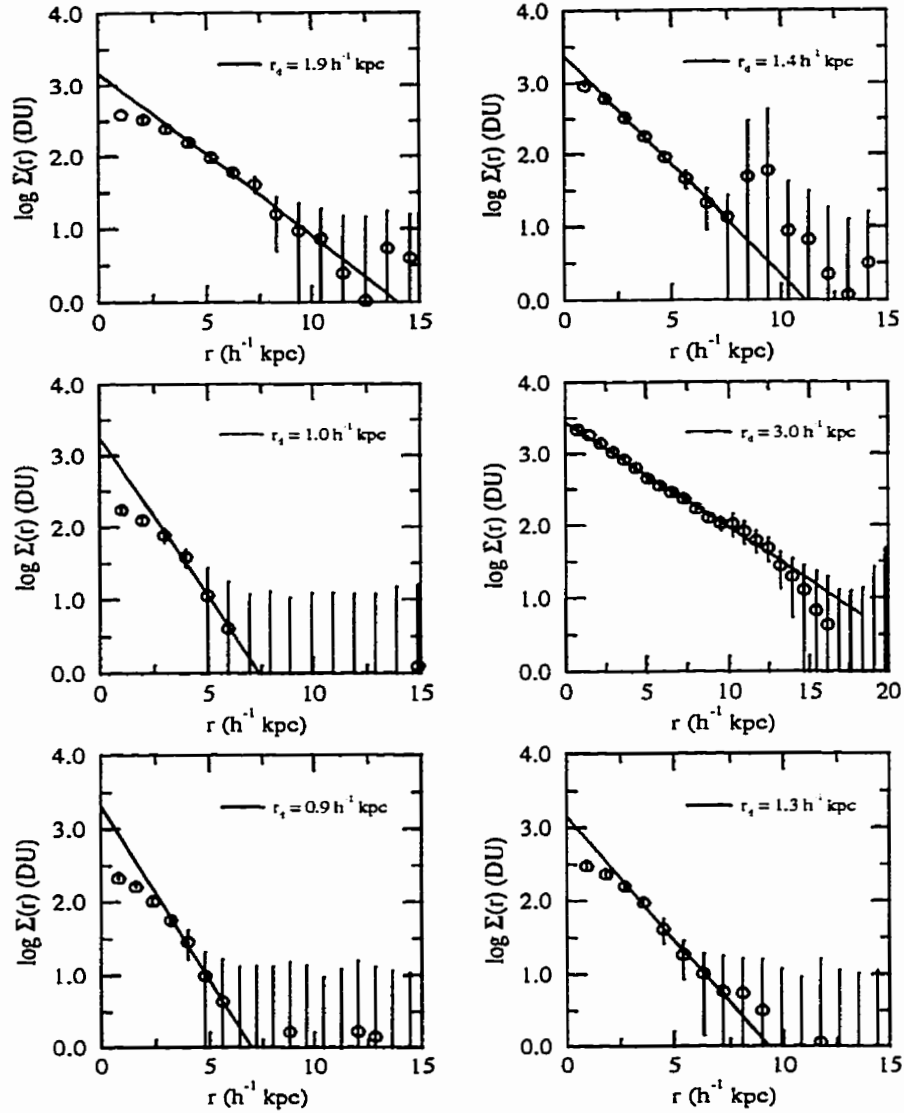


Figure 7.6: CNOC MOS Gunn g galaxy luminosity profiles determined with ELLIPSE. Row-by-row and starting from the top: E1512-201429 and E1621-100515, A2390-100225 and A2390-101084, A2390-200928 and A2390-200802. The solid lines are exponential disk fits with the scale length shown for each galaxy. The physical distance on the x-axis was calculated from the redshift of the galaxy and the angular distance relation for $q_0 = 0.5$.

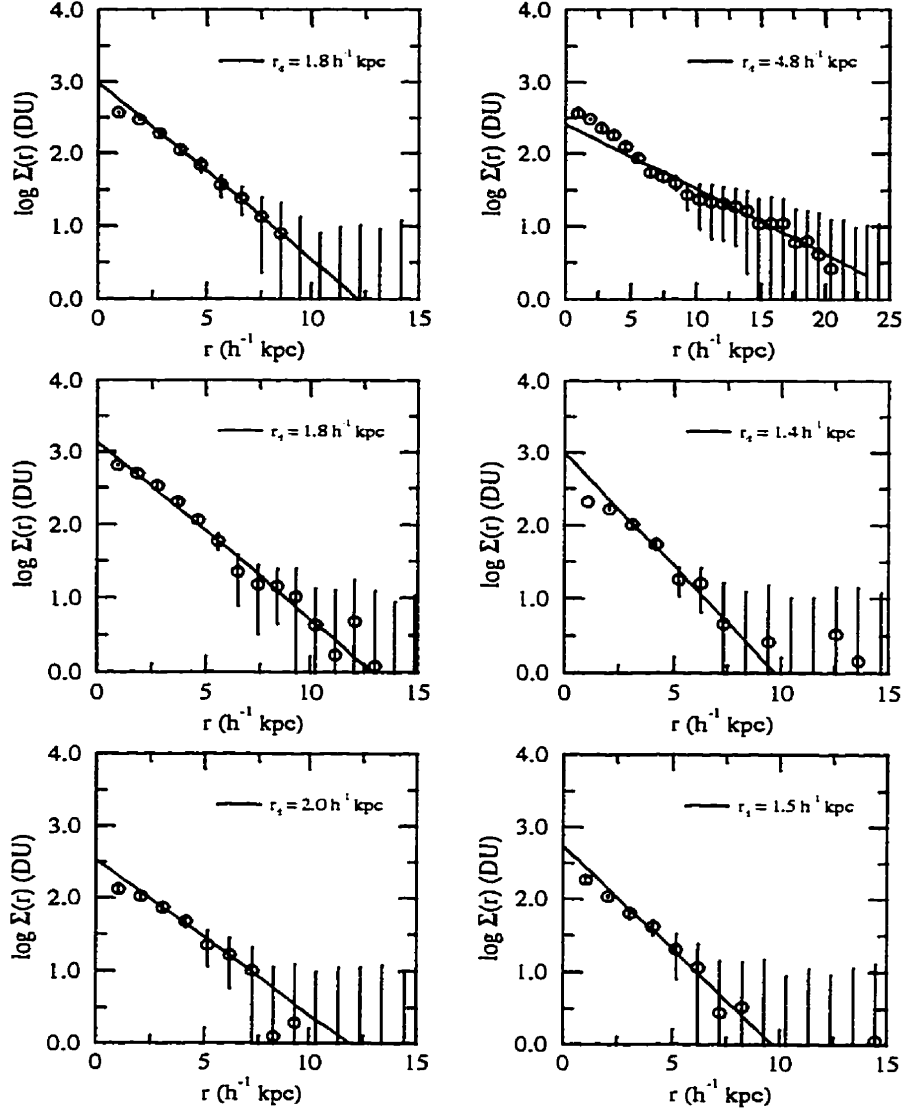


Figure 7.7: CNOC MOS Gunn g galaxy luminosity profiles determined with ELLIPSE. Row-by-row and starting from the top: A2390-200372 and E1512-201845, E1512-201773 and E1512-200730, E1512-200334 and E1512-200672. The solid lines are exponential disk fits with the scale length shown for each galaxy. The physical distance on the x-axis was calculated from the redshift of the galaxy and the angular distance relation for $q_0 = 0.5$.

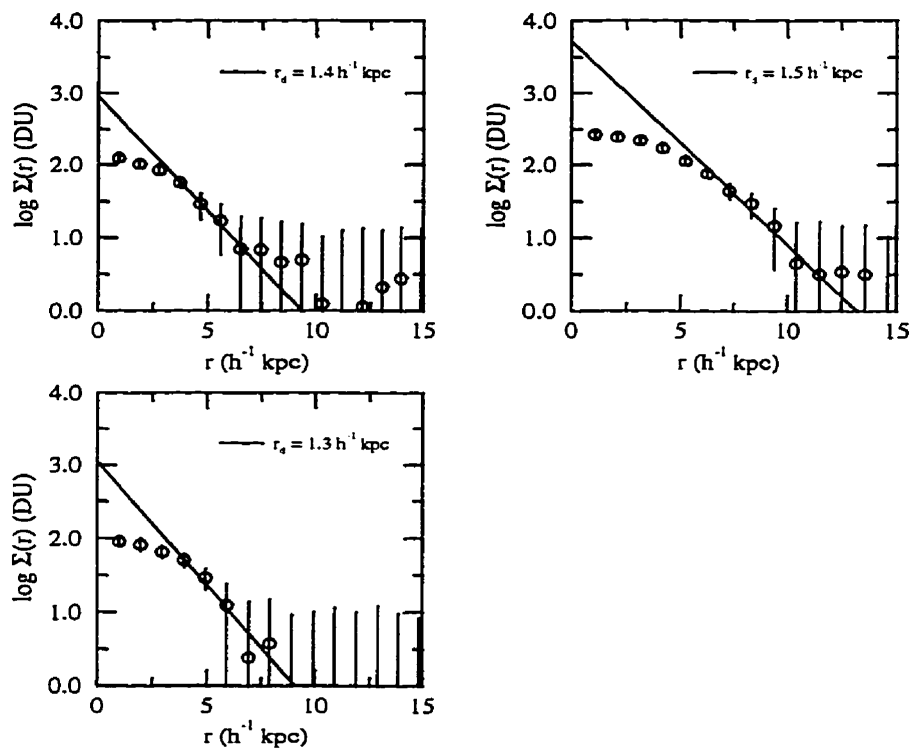


Figure 7.8: CNOC MOS Gunn g galaxy luminosity profiles determined with ELLIPSE. Row-by-row and starting from the top: E1512-201268 and E1512-202096, E1512-201125. The solid lines are exponential disk fits with the scale length shown for each galaxy. The physical distance on the x-axis was calculated from the redshift of the galaxy and the angular distance relation for $q_0 = 0.5$.

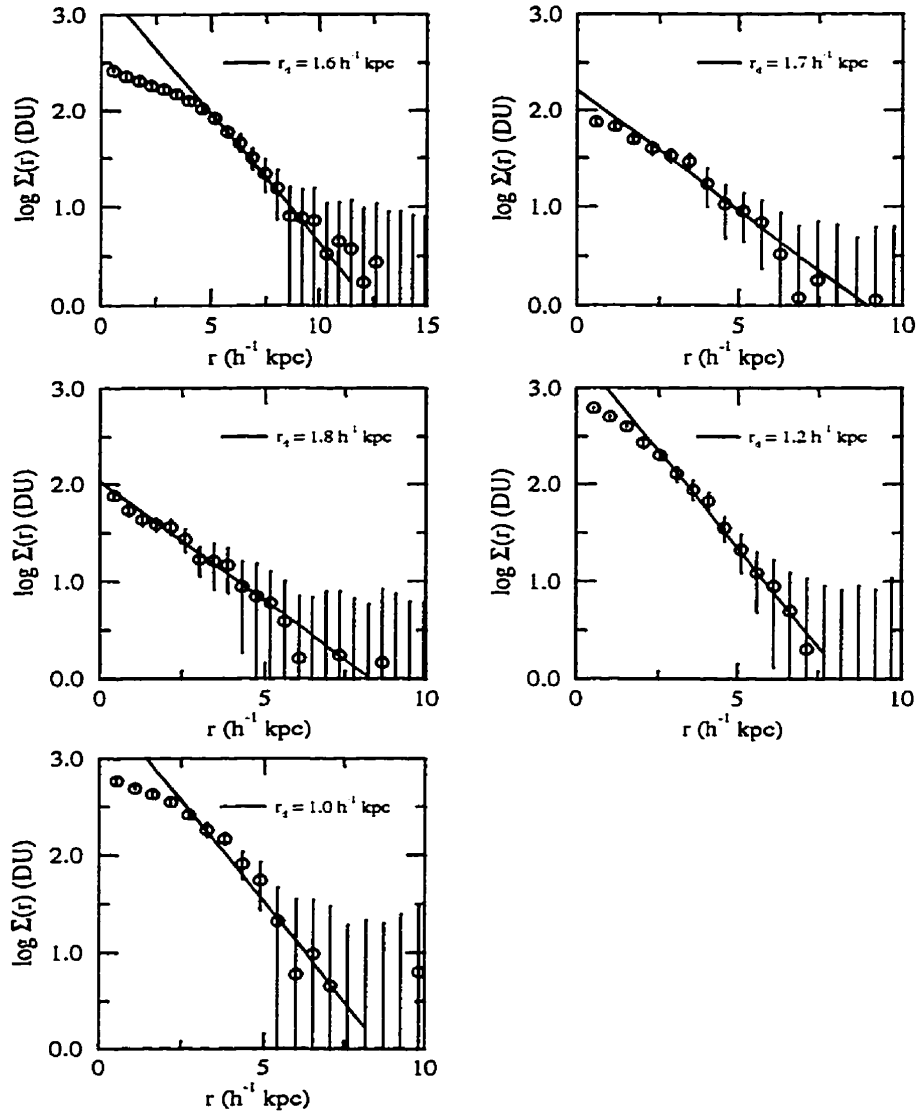


Figure 7.9: SIS I band galaxy luminosity profiles determined with ELLIPSE. Row-by-row and starting from the top: E1512-202096 and E1512-201429, A2390-350416 and E1512-201773, A2390-100686. The solid lines are exponential disk fits with the scale length shown for each galaxy. The physical distance on the x-axis was calculated from the redshift of the galaxy and the angular distance relation for $q_0 = 0.5$.

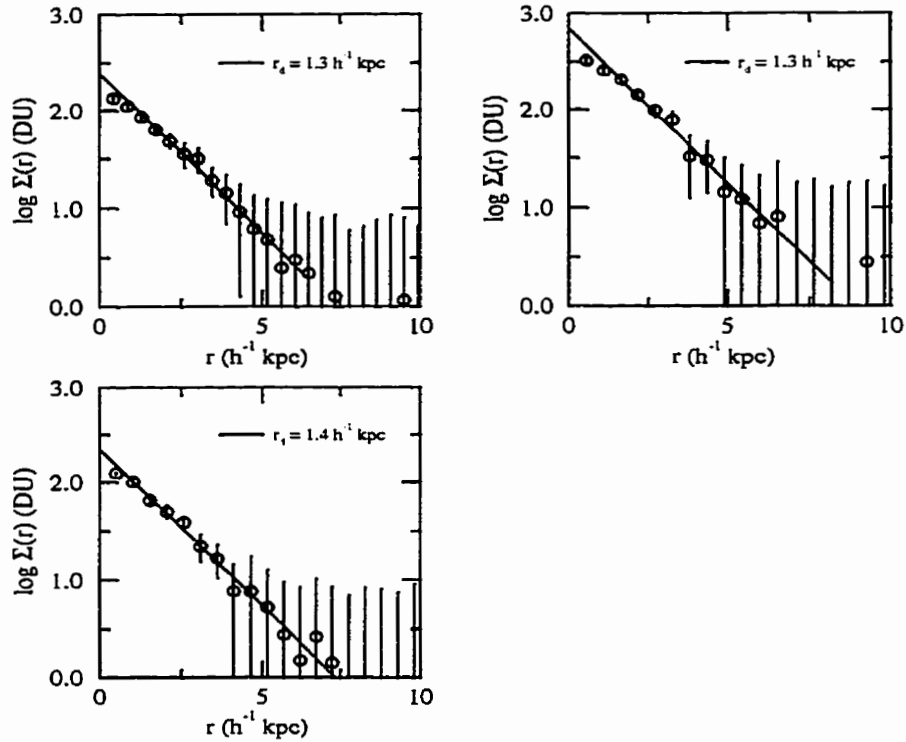


Figure 7.10: SIS I band galaxy luminosity profiles determined with ELLIPSE. Row-by-row and starting from the top: A2390-350471 and A2390-100225, E1621-100515. The solid lines are exponential disk fits with the scale length shown for each galaxy. The physical distance on the x-axis was calculated from the redshift of the galaxy and the angular distance relation for $q_0 = 0.5$.

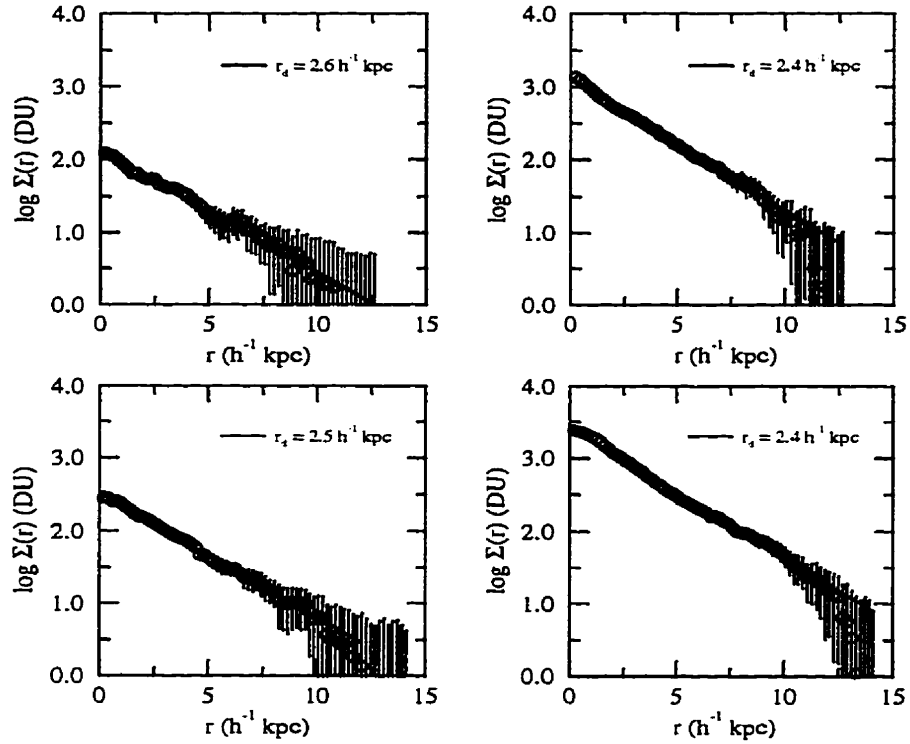


Figure 7.11: SIS V and R band galaxy luminosity profiles determined with ELLIPSE. Row-by-row and starting from the top: A2390-101033 in V and R, A2390-101084 in V and R. The solid lines are exponential disk fits with the scale length shown for each galaxy. The physical distance on the x-axis was calculated from the redshift of the galaxy and the angular distance relation for $q_0 = 0.5$.

7.2 Parameter Values and Probability Distributions

Results of the ELFIT2D analysis are presented in this section. Tables 7.1 and 7.2 show the initial conditions of the ELFIT2D parameter searches. Initial values and temperatures are given for each parameter. The physically allowed range for ELFIT2D [OII] ratio values is 0.6 to 2.9 as discussed in section 4.3.1. Table 7.3 gives the best parameters values and their 68% confidence interval as defined in section 6.2. Kinematically anomalous galaxies (see Section 7.3) are identified by the superscript *n*, cluster galaxies are identified by the superscript *c*, and kinematically normal galaxies are identified by a dagger (†). Figures 7.12 to 7.33 show the five parameter posterior probability distributions for each galaxy. The median value as well as the lower and upper bounds of the 68% confidence interval are marked by vertical dotted lines.

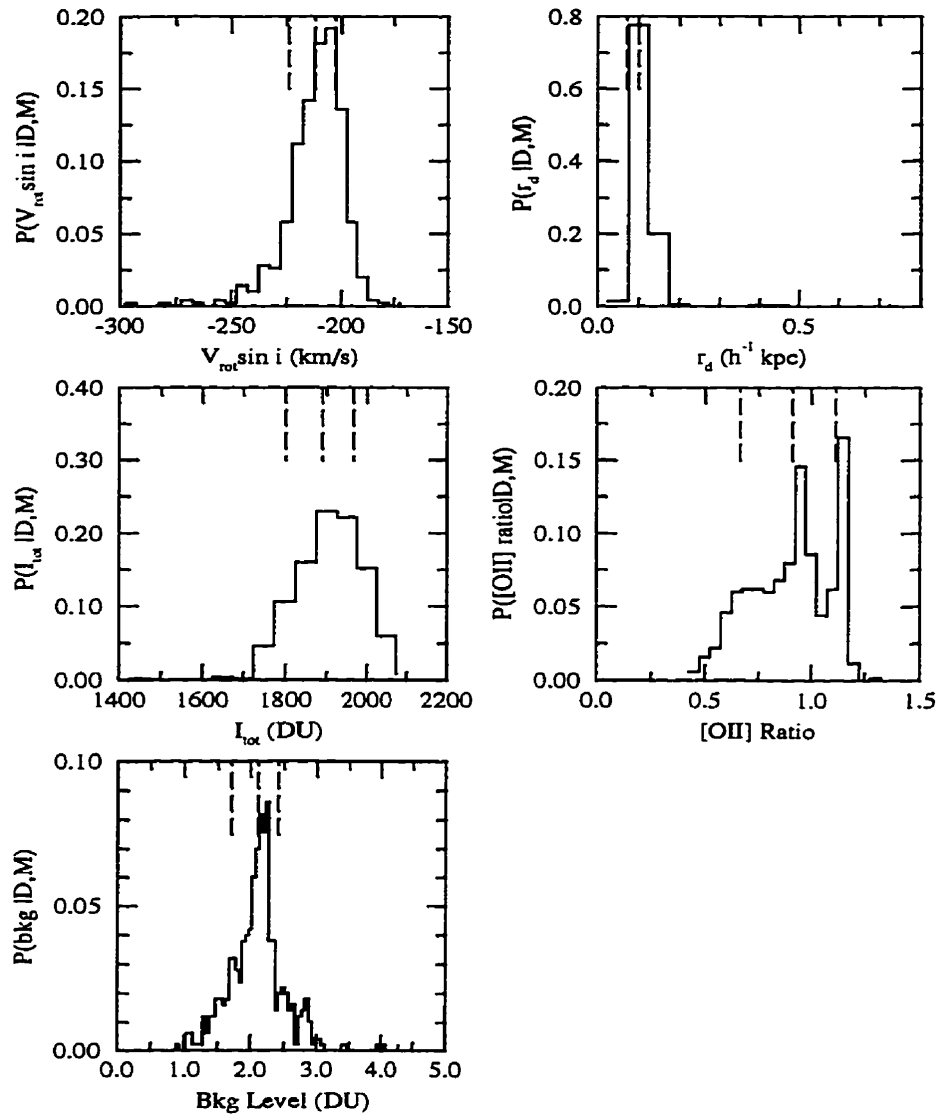


Figure 7.12: Parameter Probability Functions - A2390-101033. Each distribution is made up of 500 Metropolis selected points. Bin sizes are: $\Delta V \sin i = 5$ km/s, $\Delta r_d = 0.05 h^{-1}$ kpc, $\Delta I = 50$ DU, $\Delta[\text{OII}]$ ratio = 0.05 and $\Delta \text{bkg} = 0.05$ DU. The median value as well as the lower and upper bounds of the 68% confidence interval are marked by vertical dashed lines

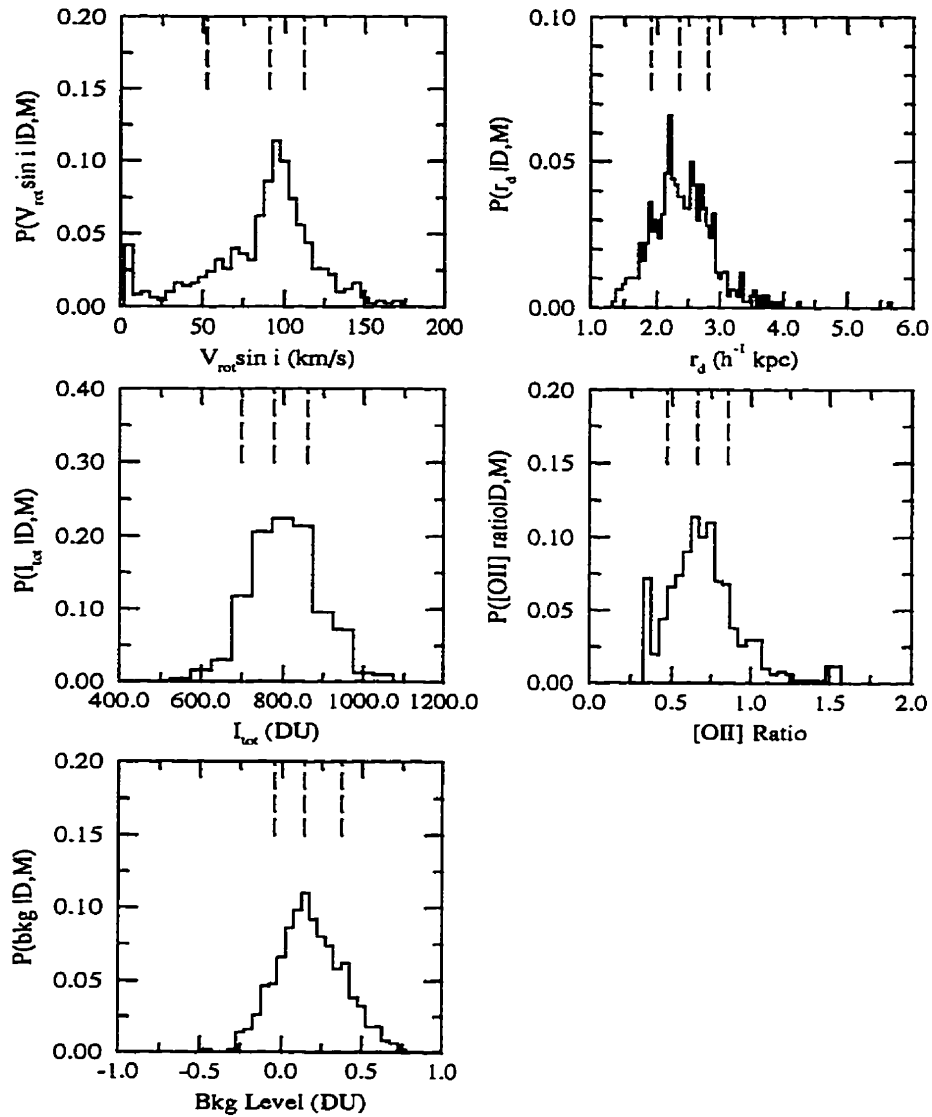


Figure 7.13: Parameter Probability Functions - A2390-100686. Each distribution is made up of 500 Metropolis selected points. Bin sizes are: $\Delta V \sin i \approx 5$ km/s, $\Delta r_d = 0.05 h^{-1}$ kpc, $\Delta I = 50$ DU, $\Delta [\text{OII}] \text{ ratio} = 0.05$ and $\Delta \text{bkg} = 0.05$ DU. The median value as well as the lower and upper bounds of the 68% confidence interval are marked by vertical dashed lines

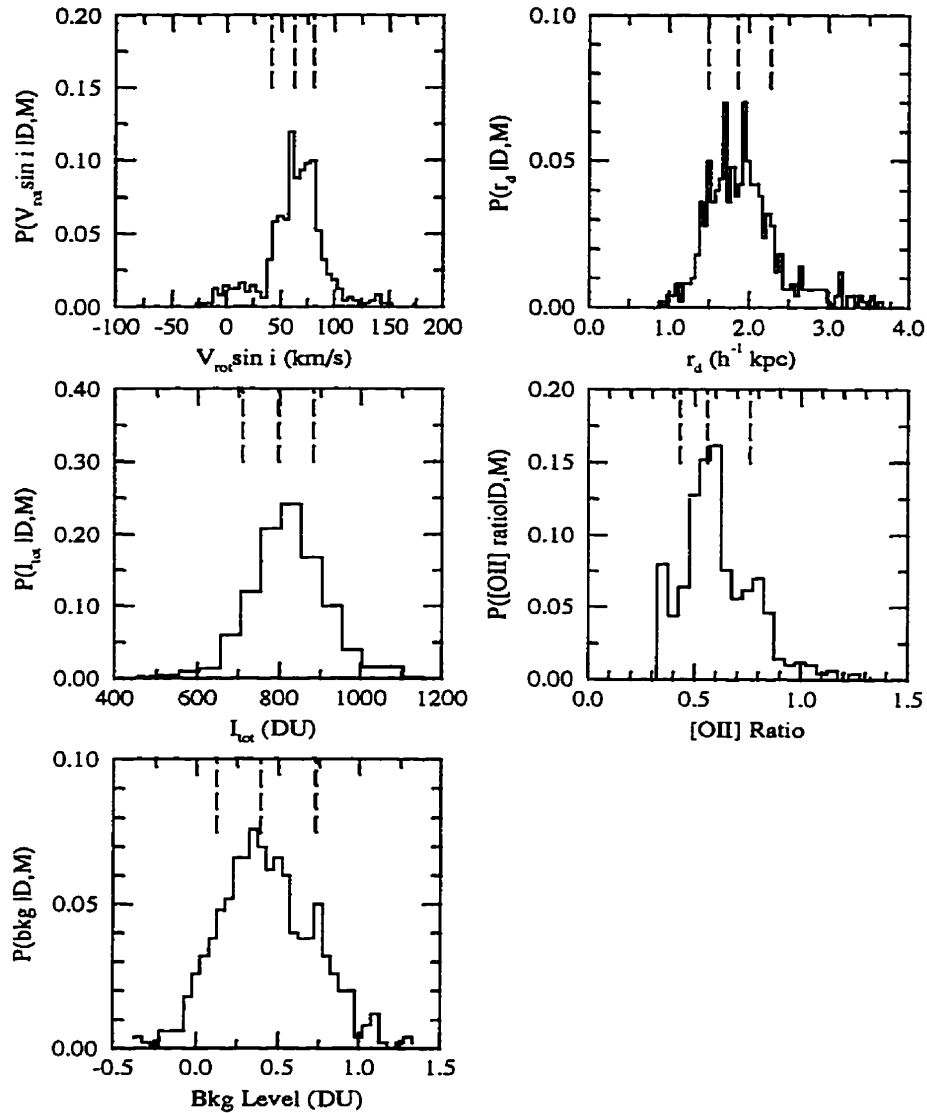


Figure 7.14: Parameter Probability Functions - A2390-350416. Each distribution is made up of 500 Metropolis selected points. Bin sizes are: $\Delta V_{\text{rot}} \sin i = 5$ km/s, $\Delta r_d = 0.05$ h^{-1} kpc, $\Delta I = 50$ DU, $\Delta [\text{OII}] \text{ ratio} = 0.05$ and $\Delta \text{bkg} = 0.05$ DU. The median value as well as the lower and upper bounds of the 68% confidence interval are marked by vertical dashed lines

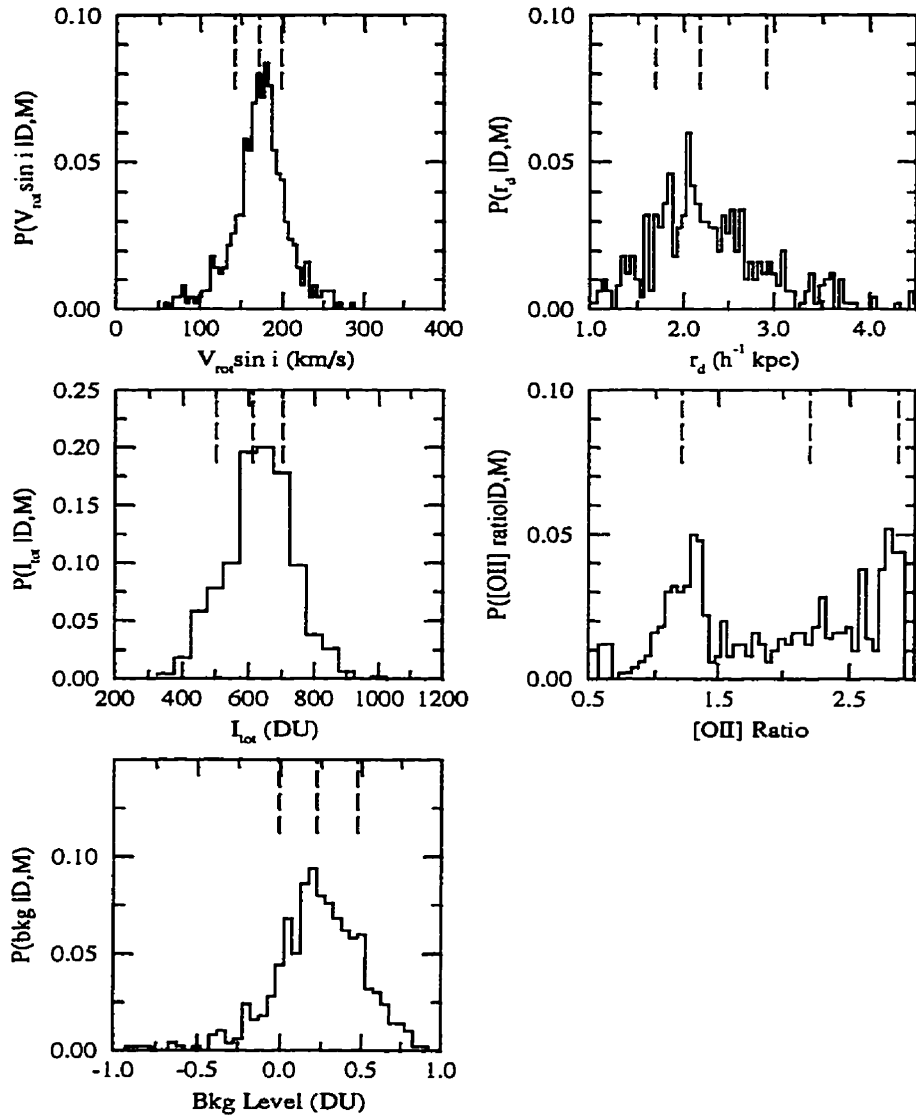


Figure 7.15: Parameter Probability Functions - A2390-350471. Each distribution is made up of 500 Metropolis selected points. Bin sizes are: $\Delta V \sin i = 5$ km/s, $\Delta r_d = 0.05 h^{-1}$ kpc, $\Delta I = 50$ DU, $\Delta[\text{OII}] \text{ ratio} = 0.05$ and $\Delta \text{bkg} = 0.05$ DU. The median value as well as the lower and upper bounds of the 68% confidence interval are marked by vertical dashed lines

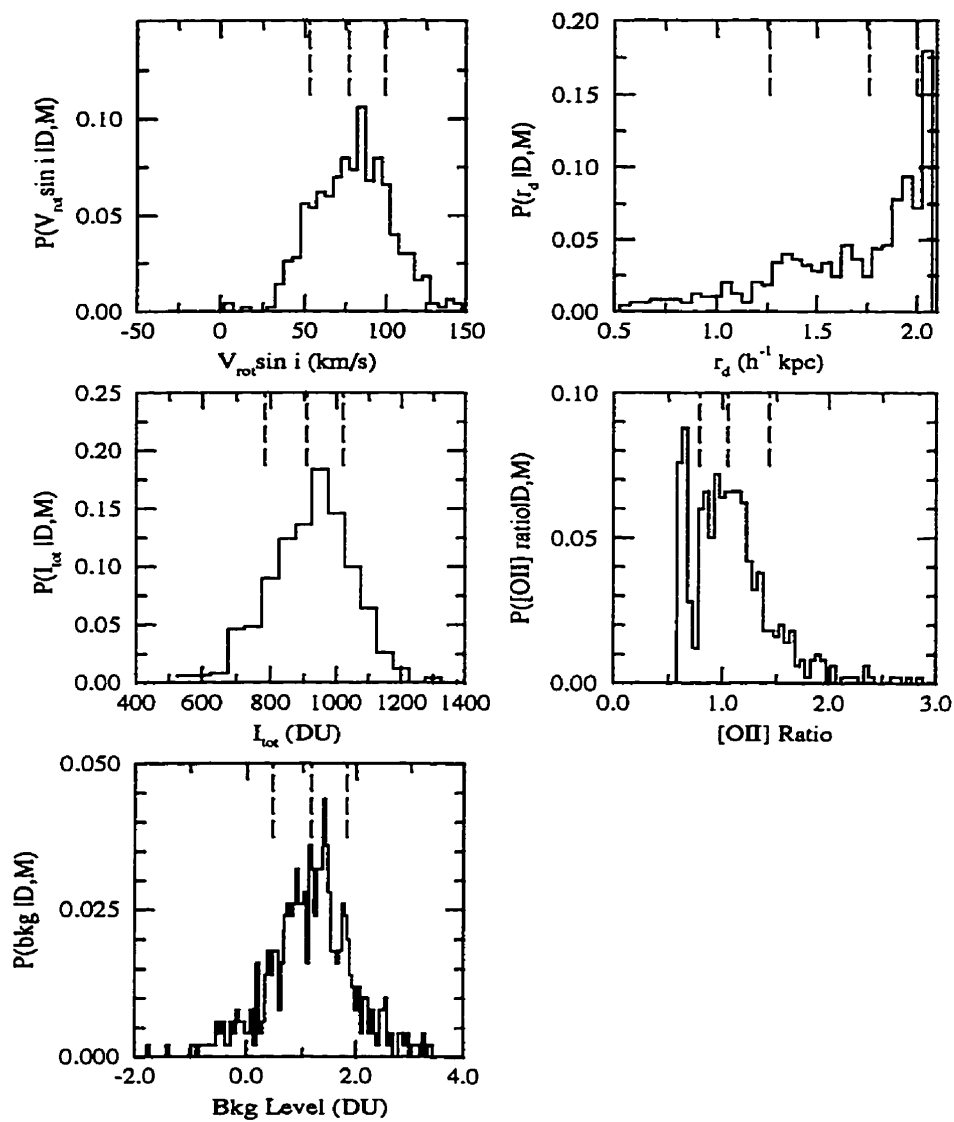


Figure 7.16: Parameter Probability Functions - E1512-301037A. Each distribution is made up of 500 Metropolis selected points. Bin sizes are: $\Delta V \sin i = 5$ km/s, $\Delta r_d = 0.05 h^{-1}$ kpc, $\Delta I = 50$ DU, $\Delta[\text{OII}]$ ratio = 0.05 and $\Delta \text{bkg} = 0.05$ DU. The median value as well as the lower and upper bounds of the 68% confidence interval are marked by vertical dashed lines

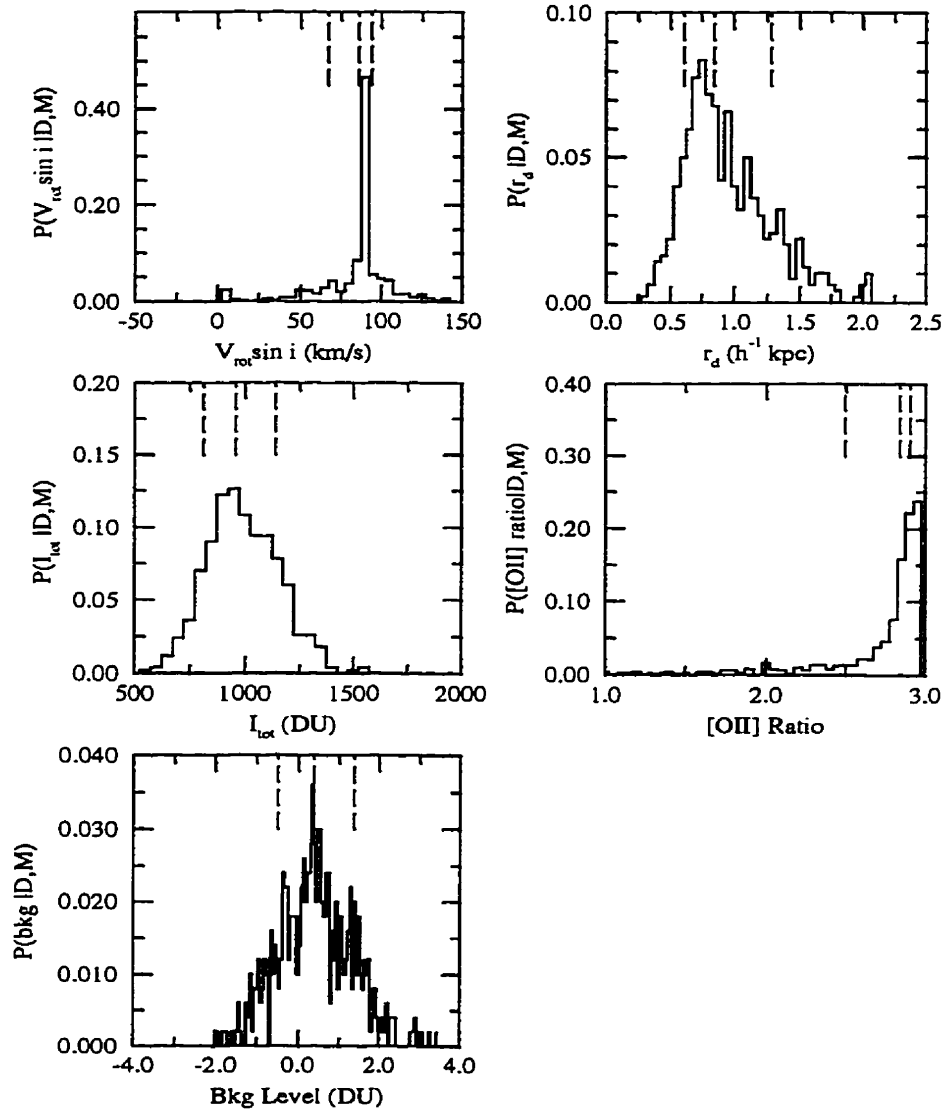


Figure 7.17: Parameter Probability Functions - E1512-301037B. Each distribution is made up of 500 Metropolis selected points. Bin sizes are: $\Delta V \sin i = 5$ km/s, $\Delta r_d = 0.05 h^{-1}$ kpc, $\Delta I = 50$ DU, $\Delta[\text{OII}]$ ratio = 0.05 and $\Delta \text{bkg} = 0.05$ DU. The median value as well as the lower and upper bounds of the 68% confidence interval are marked by vertical dashed lines

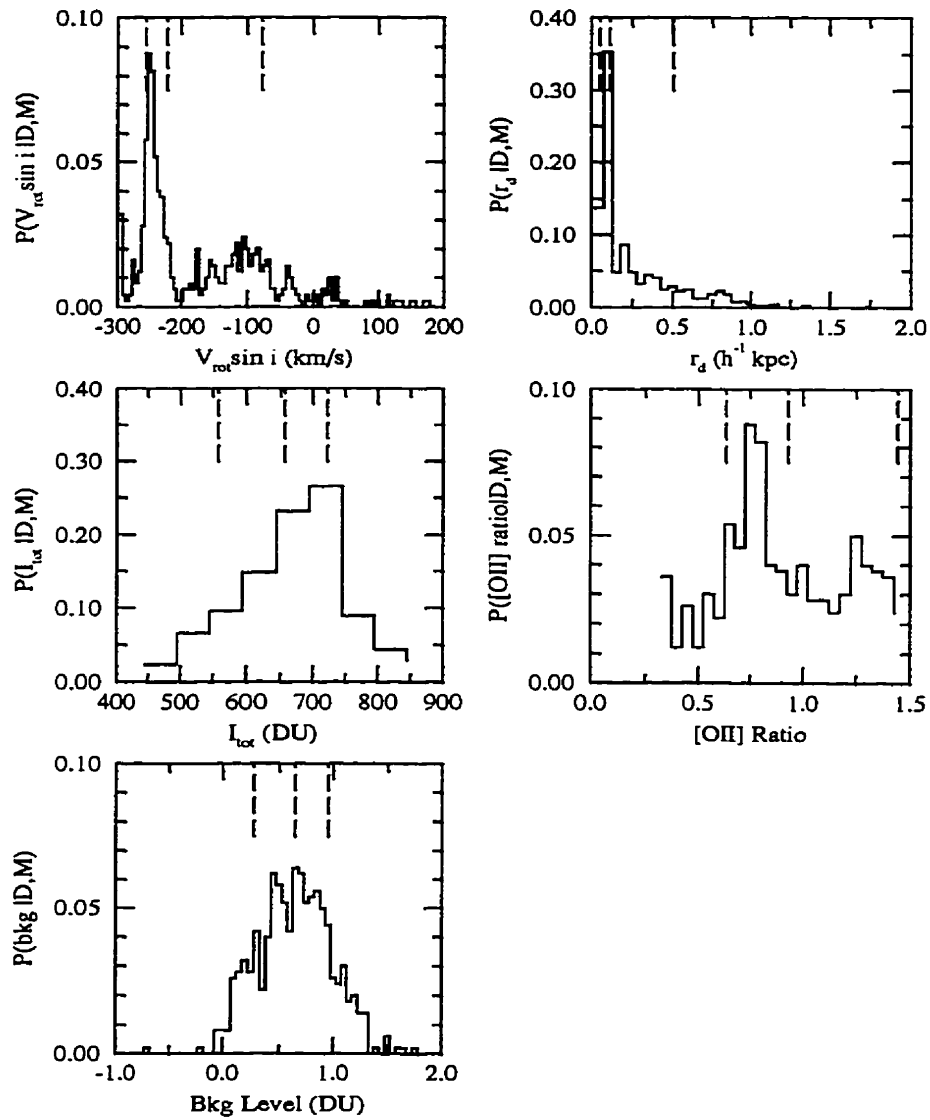


Figure 7.18: Parameter Probability Functions - E1512-101526. Each distribution is made up of 500 Metropolis selected points. Bin sizes are: $\Delta V \sin i = 5 \text{ km/s}$, $\Delta r_d = 0.05 \text{ h}^{-1} \text{ kpc}$, $\Delta I = 50 \text{ DU}$, $\Delta [\text{OII}] \text{ ratio} = 0.05$ and $\Delta \text{bkg} = 0.05 \text{ DU}$. The median value as well as the lower and upper bounds of the 68% confidence interval are marked by vertical dashed lines

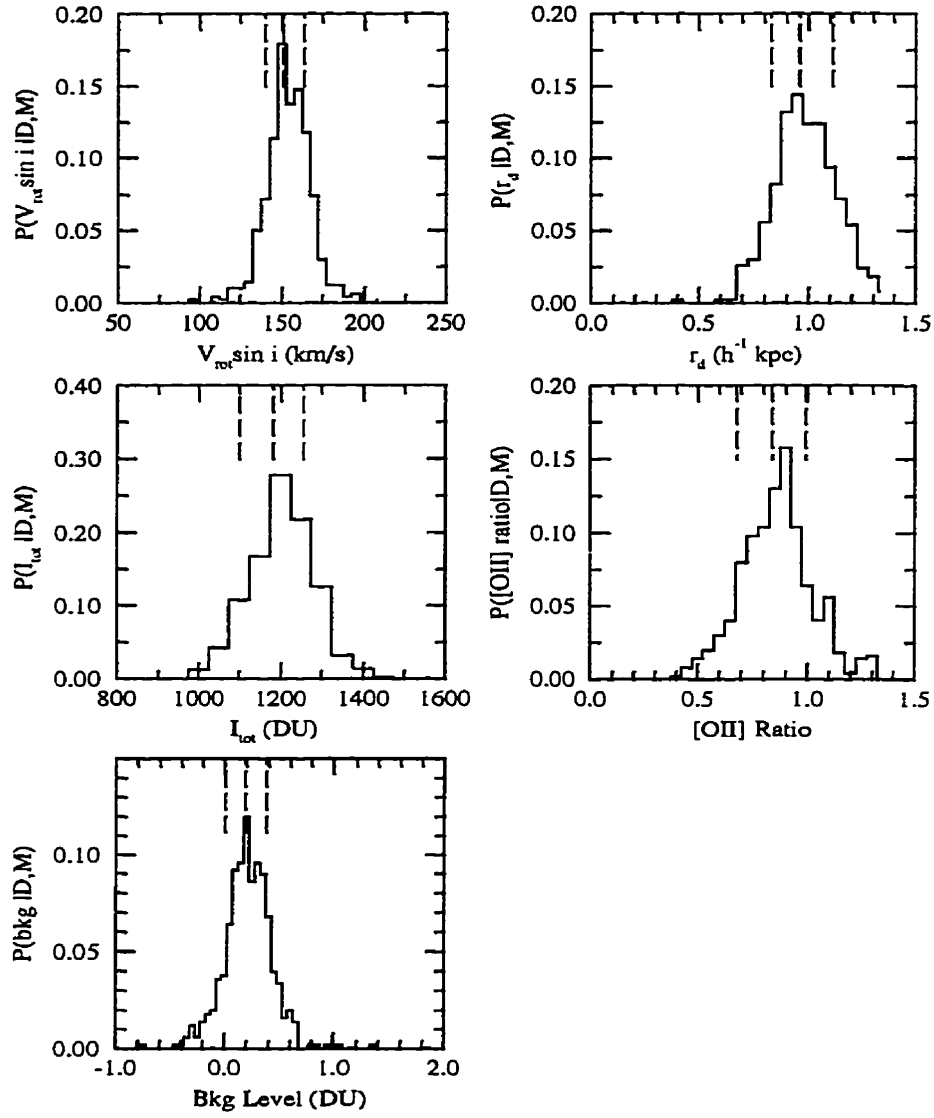


Figure 7.19: Parameter Probability Functions - E1512-201429. Each distribution is made up of 500 Metropolis selected points. Bin sizes are: $\Delta V \sin i = 5$ km/s, $\Delta r_d = 0.05 h^{-1}$ kpc, $\Delta I = 50$ DU, $\Delta[\text{OII}]$ ratio = 0.05 and $\Delta \text{bkg} = 0.05$ DU. The median value as well as the lower and upper bounds of the 68% confidence interval are marked by vertical dashed lines

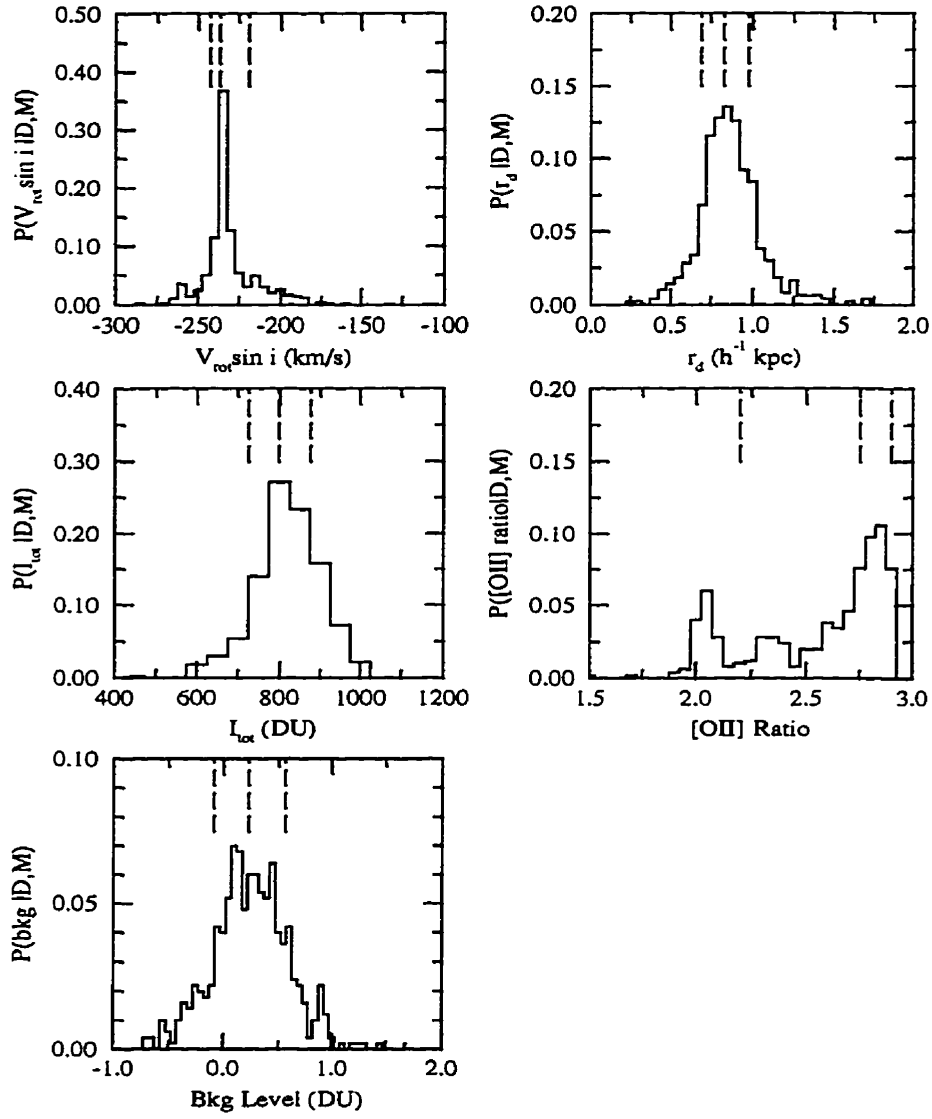


Figure 7.20: Parameter Probability Functions - E1621-100515. Each distribution is made up of 500 Metropolis selected points. Bin sizes are: $\Delta V \sin i = 5$ km/s, $\Delta r_d = 0.05 h^{-1}$ kpc, $\Delta I = 50$ DU, $\Delta[\text{OII}]$ ratio = 0.05 and $\Delta \text{bkg} = 0.05$ DU. The median value as well as the lower and upper bounds of the 68% confidence interval are marked by vertical dashed lines

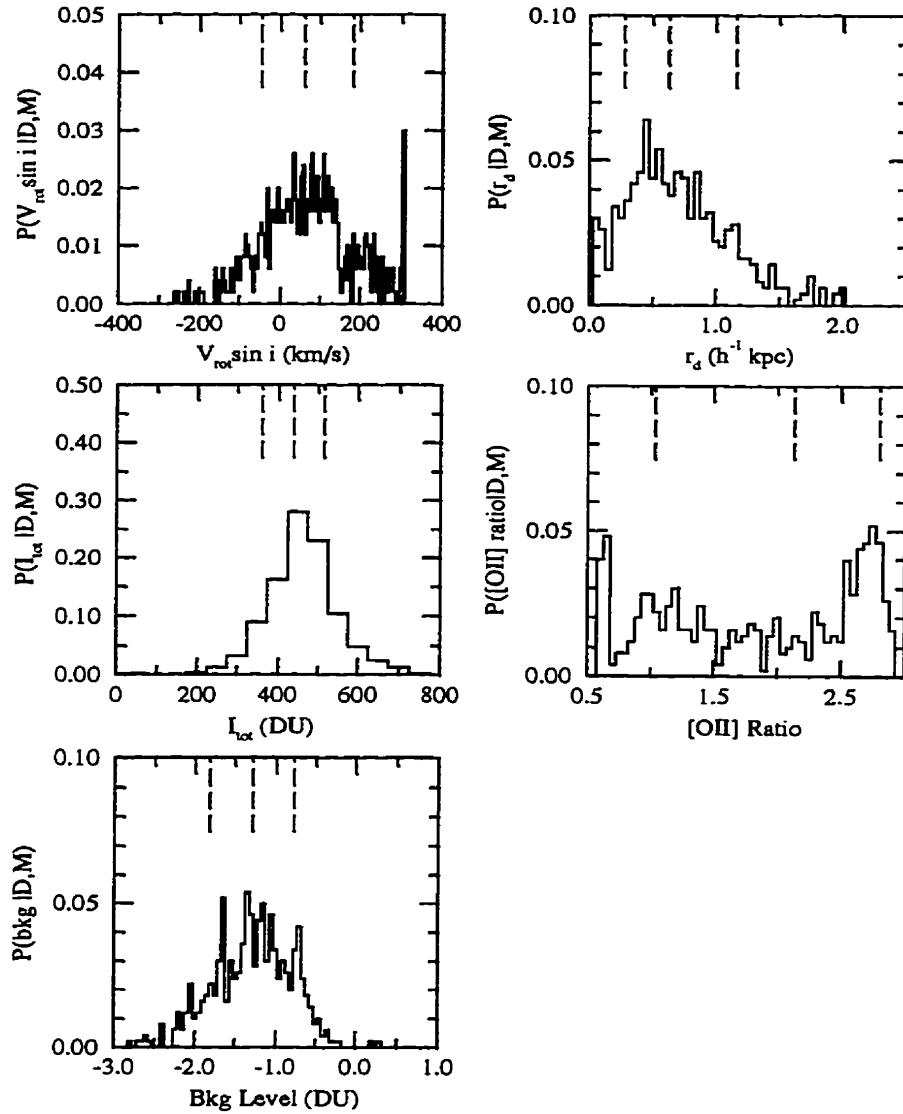


Figure 7.21: Parameter Probability Functions - A2390-100225. Each distribution is made up of 500 Metropolis selected points. Bin sizes are: $\Delta V \sin i = 5$ km/s, $\Delta r_d = 0.05 h^{-1}$ kpc, $\Delta I = 50$ DU, $\Delta[\text{OII}]$ ratio = 0.05 and $\Delta \text{bkg} = 0.05$ DU. The median value as well as the lower and upper bounds of the 68% confidence interval are marked by vertical dashed lines

Table 7.1: Parameter Value Search – Initial Conditions – Part 1

ID	σ_{bkg} (DU)	$V_{rot\,sini}$ (km/s)				r_d (h_{100}^{-1} kpc)			
		I_{tot} (DU)		B_{kg} (DU)		[OII] Ratio			
		init	min	max	T	init	min	max	T
A2390-101033	8.33	-325	-500	150	350	0.5	-1.0	2.0	3.0
		2500	1000	4000	3000	1.75	0.6	2.9	2.3
		0.0	-5.0	5.0	10.0				
A2390-100686	6.61	150	0	300	300	3.0	0.0	6.0	6.0
		600	1	1200	1200	1.75	0.6	2.9	2.3
		0.0	-5.0	5.0	10.0				
A2390-350416	6.56	0	-200	200	400	3.0	0.0	6.0	6.0
		750	1	1500	1500	1.75	0.6	2.9	2.3
		0.0	-5.0	5.0	10.0				
A2390-350471	6.30	250	0	500	500	3.0	0.0	6.0	6.0
		600	1	1200	1200	1.75	0.6	2.9	2.3
		0.0	-5.0	5.0	10.0				
E1512-301037A	7.92	150	0	300	300	1.0	0.0	2.0	2.0
		1000	1	2000	2000	1.75	0.6	2.9	2.3
		0.0	-5.0	5.0	10.0				
E1512-301037B	7.92	150	0	300	300	1.0	0.0	2.0	2.0
		1000	1	2000	2000	1.75	0.6	2.9	2.3
		0.0	-5.0	5.0	10.0				
E1512-101526	6.48	0	-300	300	600	0.5	-1.0	2.0	3.0
		750	1	1500	1500	1.75	0.6	2.9	2.3
		0.0	-5.0	5.0	10.0				
E1512-201429	6.60	150	0	300	300	3.0	0.0	6.0	6.0
		750	1	1500	1500	1.75	0.6	2.9	2.3
		0.0	-5.0	5.0	10.0				
E1621-515	6.38	-150	-300	0	300	2.5	0.0	5.0	5.0
		1000	1	2000	2000	1.75	0.6	2.9	2.3
		0.0	-5.0	5.0	10.0				
A2390-100225	9.46	0	-300	300	600	0.0	-2.0	2.0	4.0
		1000	1	2000	2000	1.75	0.6	2.9	2.3
		0.0	-5.0	5.0	10.0				
A2390-101084	10.1	-400	-600	-200	400	0.5	-1.0	2.0	3.0
		5000	3000	7000	4000	1.75	0.6	2.9	2.3
		0.0	-5.0	5.0	10.0				

Table 7.2: Parameter Value Search – Initial Conditions – Part 2

ID	σ_{bkg} (DU)	$V_{rot} \sin i$ (km/s)				r_d (h_{100}^{-1} kpc) [OII] Ratio			
		I_{tot} (DU)							
		Bkg (DU)							
		init	min	max	T	init	min	max	T
A2390-200928	9.8	300	0	600	600	2.0	0.0	4.0	4.0
		750	1	1500	1500	1.75	0.6	2.9	2.3
		0.0	-5.0	5.0	10.0				
A2390-200802	10.76	-100	-400	200	600	2.0	0.0	4.0	4.0
		1500	1	3000	3000	1.75	0.6	2.9	2.3
		0.0	-5.0	5.0	10.0				
A2390-200372	10.66	0	-200	200	400	3.0	1.0	5.0	4.0
		1000	1	2000	2000	1.75	0.6	2.9	2.3
		0.0	-5.0	5.0	10.0				
E1512-201845	7.89	300	0	600	600	2.0	0.0	4.0	4.0
		1500	500	2500	2000	1.75	0.6	2.9	2.3
		0.0	-5.0	5.0	10.0				
E1512-201773	8.39	-300	-600	0	600	0.5	-1.0	2.0	3.0
		2500	1000	4000	3000	1.75	0.6	2.9	2.3
		0.0	-5.0	5.0	10.0				
E1512-200730	8.18	0	-200	200	400	0.5	-1.0	2.0	3.0
		1000	1	2000	2000	1.75	0.6	2.9	2.3
		0.0	-5.0	5.0	10.0				
E1512-200334	8.92	250	0	500	500	3.0	0.0	6.0	6.0
		1000	1	2000	2000	1.75	0.6	2.9	2.3
		0.0	-5.0	5.0	10.0				
E1512-200672	9.16	50	-200	300	500	-0.5	-2.0	1.0	3.0
		750	1	1500	1500	1.75	0.6	2.9	2.3
		0.0	-5.0	5.0	10.0				
E1512-201268	8.06	0	-300	300	600	2.0	0.0	4.0	4.0
		1000	1	2000	2000	1.75	0.6	2.9	2.3
		0.0	-5.0	5.0	10.0				
E1512-202096	8.50	0	-200	200	400	2.0	0.0	4.0	4.0
		1000	1	2000	2000	1.75	0.6	2.9	2.3
		0.0	-5.0	5.0	10.0				
E1512-201125	8.09	0	-300	300	600	0.0	-2.0	2.0	4.0
		1000	1	2000	2000	1.75	0.6	2.9	2.3
		0.0	-5.0	5.0	10.0				

Table 7.3: Best Parameter Values and Confidence Intervals

ID	$V_{\text{rot}} \sin i$ (km/s)	r_d (h_{100}^{-1} kpc)	I_{tot} (DU)	[OII] Ratio	Bkg (DU)
A2390-101033 ^{nc}	$-212 \pm \begin{smallmatrix} 9 \\ -11 \end{smallmatrix}$	$0.09 \pm \begin{smallmatrix} +0.02 \\ -0.02 \end{smallmatrix}$	$1889 \pm \begin{smallmatrix} 76 \\ -89 \end{smallmatrix}$	$0.9 \pm \begin{smallmatrix} +0.20 \\ -0.30 \end{smallmatrix}$	$2.1 \pm \begin{smallmatrix} +0.3 \\ -0.4 \end{smallmatrix}$
A2390-100686 [†]	$91 \pm \begin{smallmatrix} 21 \\ -39 \end{smallmatrix}$	$2.3 \pm \begin{smallmatrix} +0.50 \\ -0.40 \end{smallmatrix}$	$778 \pm \begin{smallmatrix} 82 \\ -80 \end{smallmatrix}$	$0.7 \pm \begin{smallmatrix} +0.20 \\ -0.20 \end{smallmatrix}$	$0.1 \pm \begin{smallmatrix} +0.2 \\ -0.2 \end{smallmatrix}$
A2390-350416 [†]	$62 \pm \begin{smallmatrix} 18 \\ -21 \end{smallmatrix}$	$1.9 \pm \begin{smallmatrix} +0.40 \\ -0.40 \end{smallmatrix}$	$797 \pm \begin{smallmatrix} 87 \\ -88 \end{smallmatrix}$	$0.6 \pm \begin{smallmatrix} +0.20 \\ -0.10 \end{smallmatrix}$	$0.4 \pm \begin{smallmatrix} +0.3 \\ -0.3 \end{smallmatrix}$
A2390-350471 [†]	$171 \pm \begin{smallmatrix} 26 \\ -29 \end{smallmatrix}$	$2.2 \pm \begin{smallmatrix} +0.70 \\ -0.50 \end{smallmatrix}$	$612 \pm \begin{smallmatrix} 90 \\ -111 \end{smallmatrix}$	$2.2 \pm \begin{smallmatrix} +0.70 \\ -1.00 \end{smallmatrix}$	$0.2 \pm \begin{smallmatrix} +0.2 \\ -0.2 \end{smallmatrix}$
E1512-301037A [†]	$77 \pm \begin{smallmatrix} 22 \\ -24 \end{smallmatrix}$	$1.8 \pm \begin{smallmatrix} +0.20 \\ -0.50 \end{smallmatrix}$	$909 \pm \begin{smallmatrix} +111 \\ -127 \end{smallmatrix}$	$1.0 \pm \begin{smallmatrix} +0.40 \\ -0.30 \end{smallmatrix}$	$1.2 \pm \begin{smallmatrix} +0.6 \\ -0.7 \end{smallmatrix}$
E1512-301037B [†]	$86 \pm \begin{smallmatrix} 8 \\ -18 \end{smallmatrix}$	$0.8 \pm \begin{smallmatrix} +0.40 \\ -0.20 \end{smallmatrix}$	$956 \pm \begin{smallmatrix} +185 \\ -142 \end{smallmatrix}$	$2.8 \pm \begin{smallmatrix} +0.06 \\ -0.40 \end{smallmatrix}$	$0.4 \pm \begin{smallmatrix} +1.0 \\ -0.9 \end{smallmatrix}$
E1512-101526 ⁿ	$-222 \pm \begin{smallmatrix} +143 \\ -33 \end{smallmatrix}$	$0.1 \pm \begin{smallmatrix} +0.40 \\ -0.10 \end{smallmatrix}$	$657 \pm \begin{smallmatrix} 65 \\ -100 \end{smallmatrix}$	$0.9 \pm \begin{smallmatrix} +0.50 \\ -0.30 \end{smallmatrix}$	$0.6 \pm \begin{smallmatrix} +0.3 \\ -0.4 \end{smallmatrix}$
E1512-201429 [†]	$151 \pm \begin{smallmatrix} 13 \\ -11 \end{smallmatrix}$	$1.0 \pm \begin{smallmatrix} +0.20 \\ -0.10 \end{smallmatrix}$	$1181 \pm \begin{smallmatrix} 75 \\ -82 \end{smallmatrix}$	$0.8 \pm \begin{smallmatrix} +0.20 \\ -0.20 \end{smallmatrix}$	$0.2 \pm \begin{smallmatrix} +0.2 \\ -0.2 \end{smallmatrix}$
E1621-100515	$-237 \pm \begin{smallmatrix} 18 \\ -7 \end{smallmatrix}$	$0.8 \pm \begin{smallmatrix} +0.20 \\ -0.10 \end{smallmatrix}$	$798 \pm \begin{smallmatrix} 78 \\ -73 \end{smallmatrix}$	$2.8 \pm \begin{smallmatrix} +0.20 \\ -0.60 \end{smallmatrix}$	$0.2 \pm \begin{smallmatrix} +0.3 \\ -0.3 \end{smallmatrix}$
A2390-100225	$61 \pm \begin{smallmatrix} +121 \\ -107 \end{smallmatrix}$	$0.6 \pm \begin{smallmatrix} +0.50 \\ -0.40 \end{smallmatrix}$	$437 \pm \begin{smallmatrix} 78 \\ -76 \end{smallmatrix}$	$2.1 \pm \begin{smallmatrix} +0.70 \\ -1.10 \end{smallmatrix}$	$-1.3 \pm \begin{smallmatrix} +0.5 \\ -0.5 \end{smallmatrix}$
A2390-101084 ^{nc}	$-271 \pm \begin{smallmatrix} 12 \\ -12 \end{smallmatrix}$	$0.4 \pm \begin{smallmatrix} +0.03 \\ -0.06 \end{smallmatrix}$	$3517 \pm \begin{smallmatrix} +105 \\ -90 \end{smallmatrix}$	$1.8 \pm \begin{smallmatrix} +0.40 \\ -0.20 \end{smallmatrix}$	$1.4 \pm \begin{smallmatrix} +0.4 \\ -0.8 \end{smallmatrix}$
A2390-200928 [†]	$65 \pm \begin{smallmatrix} 13 \\ -15 \end{smallmatrix}$	$0.3 \pm \begin{smallmatrix} +0.20 \\ -0.10 \end{smallmatrix}$	$1031 \pm \begin{smallmatrix} 81 \\ -84 \end{smallmatrix}$	$2.9 \pm \begin{smallmatrix} +0.04 \\ -0.20 \end{smallmatrix}$	$-0.1 \pm \begin{smallmatrix} +0.4 \\ -0.4 \end{smallmatrix}$
A2390-200802 [†]	$-198 \pm \begin{smallmatrix} 76 \\ -65 \end{smallmatrix}$	$1.0 \pm \begin{smallmatrix} +0.40 \\ -0.50 \end{smallmatrix}$	$781 \pm \begin{smallmatrix} +114 \\ -98 \end{smallmatrix}$	$1.6 \pm \begin{smallmatrix} +0.90 \\ -0.70 \end{smallmatrix}$	$0.7 \pm \begin{smallmatrix} +0.6 \\ -0.6 \end{smallmatrix}$
A2390-200372 [†]	$-86 \pm \begin{smallmatrix} 52 \\ -18 \end{smallmatrix}$	$3.2 \pm \begin{smallmatrix} +0.90 \\ -0.60 \end{smallmatrix}$	$1354 \pm \begin{smallmatrix} +159 \\ -174 \end{smallmatrix}$	$1.2 \pm \begin{smallmatrix} +0.60 \\ -0.60 \end{smallmatrix}$	$0.0 \pm \begin{smallmatrix} +0.6 \\ -0.5 \end{smallmatrix}$
E1512-201845 ⁿ	$385 \pm \begin{smallmatrix} 22 \\ -31 \end{smallmatrix}$	$0.4 \pm \begin{smallmatrix} +0.10 \\ -0.10 \end{smallmatrix}$	$1457 \pm \begin{smallmatrix} 76 \\ -70 \end{smallmatrix}$	$1.2 \pm \begin{smallmatrix} +0.80 \\ -0.40 \end{smallmatrix}$	$0.5 \pm \begin{smallmatrix} +0.3 \\ -0.3 \end{smallmatrix}$
E1512-201773	$-116 \pm \begin{smallmatrix} 13 \\ -15 \end{smallmatrix}$	$0.9 \pm \begin{smallmatrix} +0.10 \\ -0.10 \end{smallmatrix}$	$2765 \pm \begin{smallmatrix} 80 \\ -88 \end{smallmatrix}$	$0.5 \pm \begin{smallmatrix} +0.20 \\ -0.10 \end{smallmatrix}$	$1.4 \pm \begin{smallmatrix} +0.3 \\ -0.4 \end{smallmatrix}$
E1512-200730 ⁿ	$-1 \pm \begin{smallmatrix} 7 \\ -5 \end{smallmatrix}$	$0.2 \pm \begin{smallmatrix} +0.10 \\ -0.10 \end{smallmatrix}$	$1702 \pm \begin{smallmatrix} 53 \\ -58 \end{smallmatrix}$	$2.7 \pm \begin{smallmatrix} +0.20 \\ -1.02 \end{smallmatrix}$	$-0.6 \pm \begin{smallmatrix} +0.3 \\ -0.2 \end{smallmatrix}$
E1512-200334 [†]	$60 \pm \begin{smallmatrix} 46 \\ -31 \end{smallmatrix}$	$1.5 \pm \begin{smallmatrix} +0.30 \\ -0.30 \end{smallmatrix}$	$1229 \pm \begin{smallmatrix} +118 \\ -119 \end{smallmatrix}$	$1.8 \pm \begin{smallmatrix} +0.60 \\ -0.40 \end{smallmatrix}$	$0.0 \pm \begin{smallmatrix} +0.4 \\ -0.4 \end{smallmatrix}$
E1512-200672 ⁿ	$44 \pm \begin{smallmatrix} 56 \\ -91 \end{smallmatrix}$	$0.3 \pm \begin{smallmatrix} +0.10 \\ -0.10 \end{smallmatrix}$	$1097 \pm \begin{smallmatrix} 61 \\ -80 \end{smallmatrix}$	$2.8 \pm \begin{smallmatrix} +0.10 \\ -0.40 \end{smallmatrix}$	$0.9 \pm \begin{smallmatrix} +0.6 \\ -0.5 \end{smallmatrix}$
E1512-201268 [†]	$33 \pm \begin{smallmatrix} 45 \\ -84 \end{smallmatrix}$	$1.4 \pm \begin{smallmatrix} +0.30 \\ -0.20 \end{smallmatrix}$	$777 \pm \begin{smallmatrix} 74 \\ -70 \end{smallmatrix}$	$2.8 \pm \begin{smallmatrix} +0.10 \\ -0.40 \end{smallmatrix}$	$-0.3 \pm \begin{smallmatrix} +0.4 \\ -0.4 \end{smallmatrix}$
E1512-202096 [†]	$28 \pm \begin{smallmatrix} 39 \\ -33 \end{smallmatrix}$	$2.0 \pm \begin{smallmatrix} +0.20 \\ -0.30 \end{smallmatrix}$	$1224 \pm \begin{smallmatrix} 95 \\ -91 \end{smallmatrix}$	$2.4 \pm \begin{smallmatrix} +0.50 \\ -0.80 \end{smallmatrix}$	$-0.4 \pm \begin{smallmatrix} +0.3 \\ -0.3 \end{smallmatrix}$
E1512-201125 ⁿ	$59 \pm \begin{smallmatrix} 79 \\ -92 \end{smallmatrix}$	$0.5 \pm \begin{smallmatrix} +0.40 \\ -0.30 \end{smallmatrix}$	$377 \pm \begin{smallmatrix} 78 \\ -62 \end{smallmatrix}$	$2.6 \pm \begin{smallmatrix} +0.30 \\ -0.40 \end{smallmatrix}$	$-0.5 \pm \begin{smallmatrix} +0.5 \\ -0.6 \end{smallmatrix}$

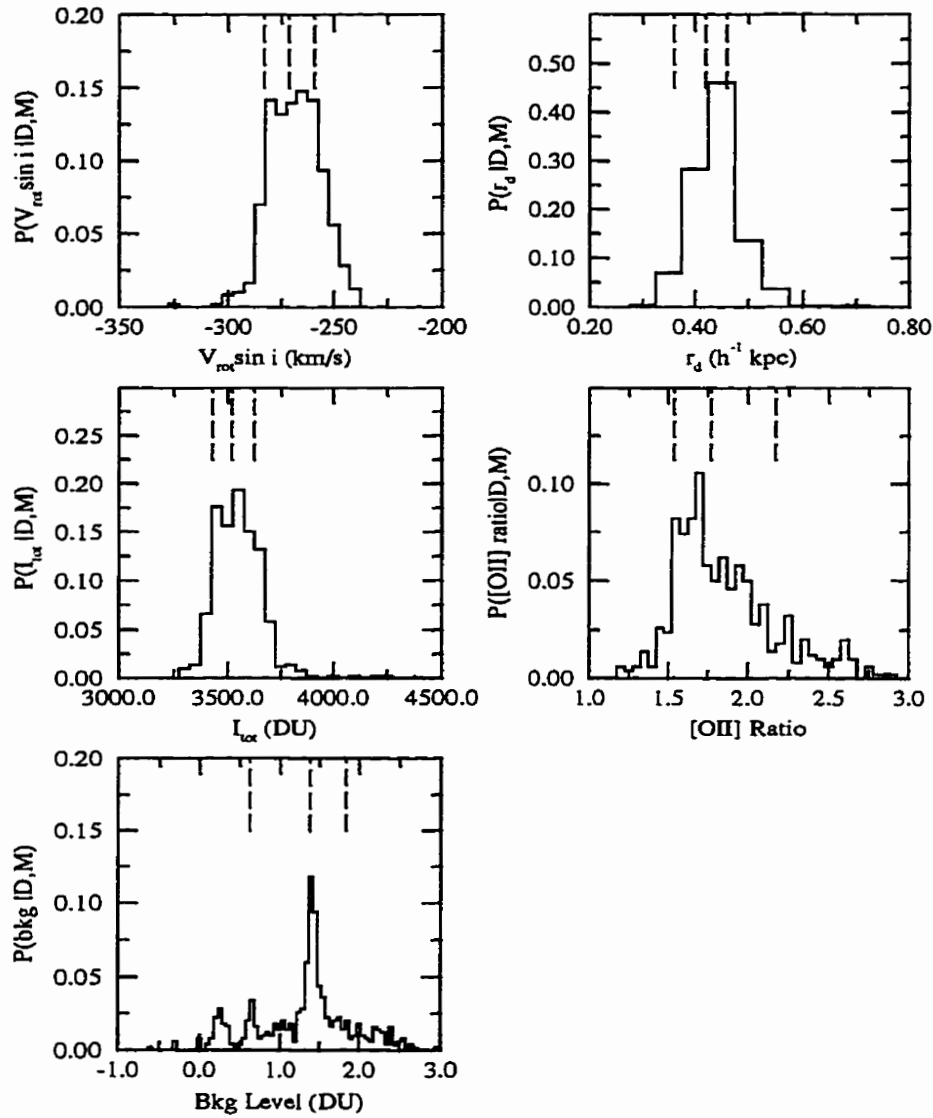


Figure 7.22: Parameter Probability Functions - A2390-101084. Each distribution is made up of 500 Metropolis selected points. Bin sizes are: $\Delta V \sin i = 5$ km/s, $\Delta r_d = 0.05 h^{-1}$ kpc, $\Delta I = 50$ DU, $\Delta[\text{OII}]$ ratio = 0.05 and $\Delta \text{bkg} = 0.05$ DU. The median value as well as the lower and upper bounds of the 68% confidence interval are marked by vertical dashed lines

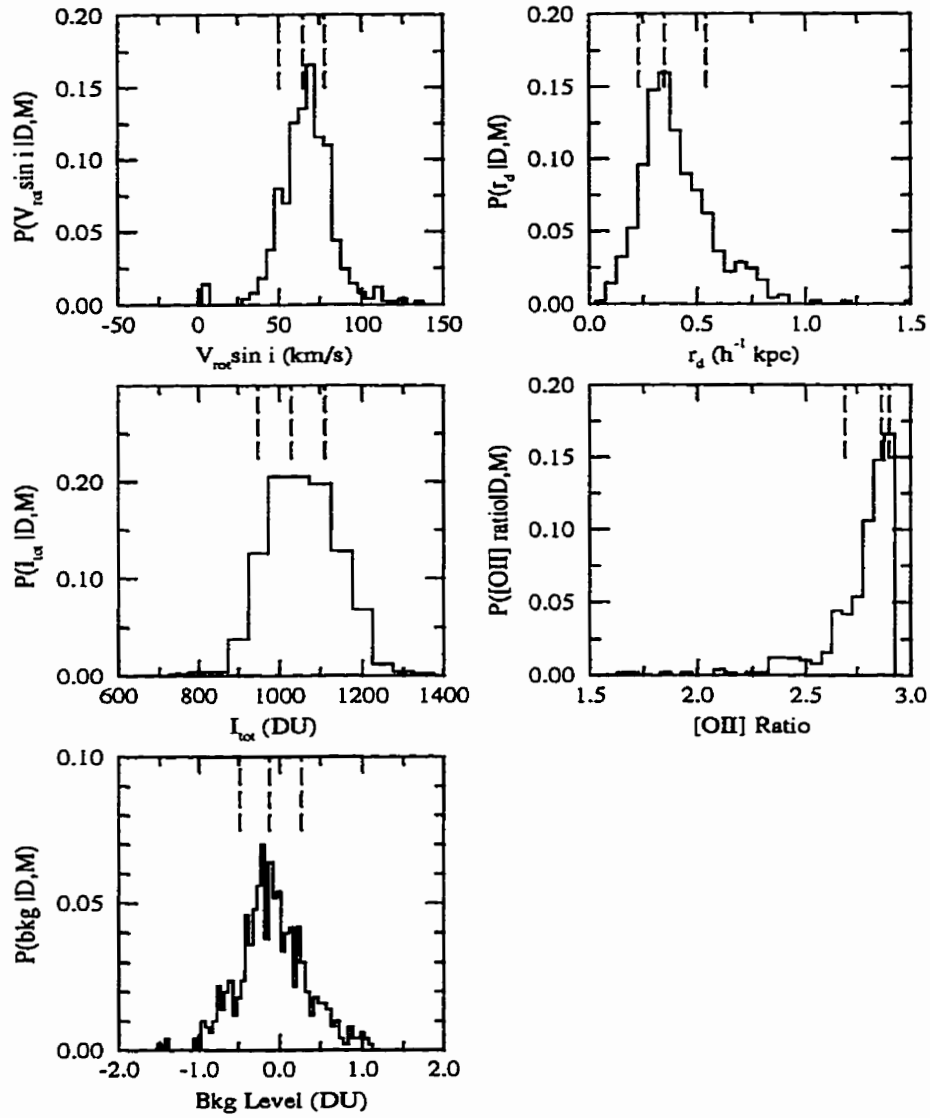


Figure 7.23: Parameter Probability Functions - A2390-200928. Each distribution is made up of 500 Metropolis selected points. Bin sizes are: $\Delta V \sin i = 5$ km/s, $\Delta r_d = 0.05 h^{-1}$ kpc, $\Delta I = 50$ DU, $\Delta[\text{OII}]$ ratio = 0.05 and $\Delta \text{bkg} = 0.05$ DU. The median value as well as the lower and upper bounds of the 68% confidence interval are marked by vertical dashed lines

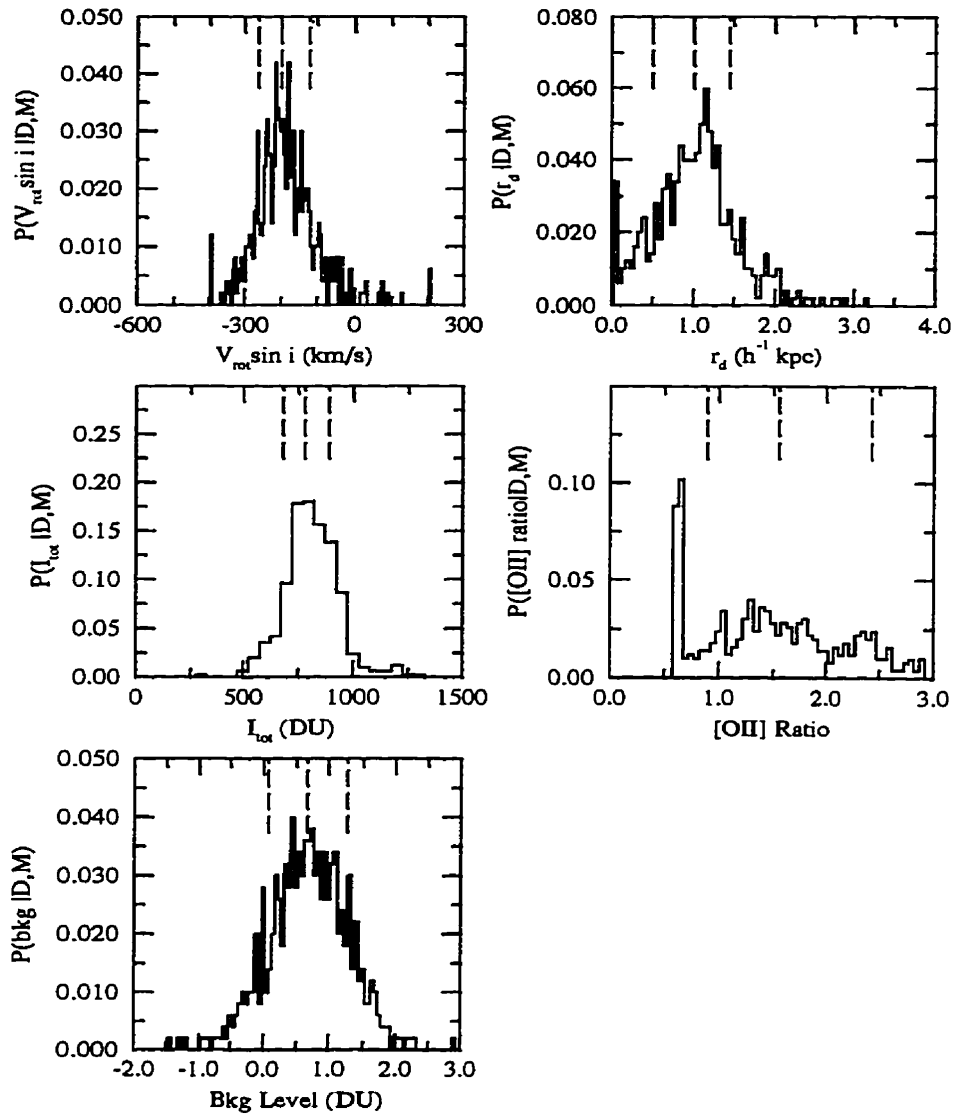


Figure 7.24: Parameter Probability Functions - A2390-200802. Each distribution is made up of 500 Metropolis selected points. Bin sizes are: $\Delta V \sin i = 5$ km/s, $\Delta r_d = 0.05 h^{-1}$ kpc, $\Delta I = 50$ DU, $\Delta [\text{OII}] \text{ ratio} = 0.05$ and $\Delta \text{bkg} = 0.05$ DU. The median value as well as the lower and upper bounds of the 68% confidence interval are marked by vertical dashed lines

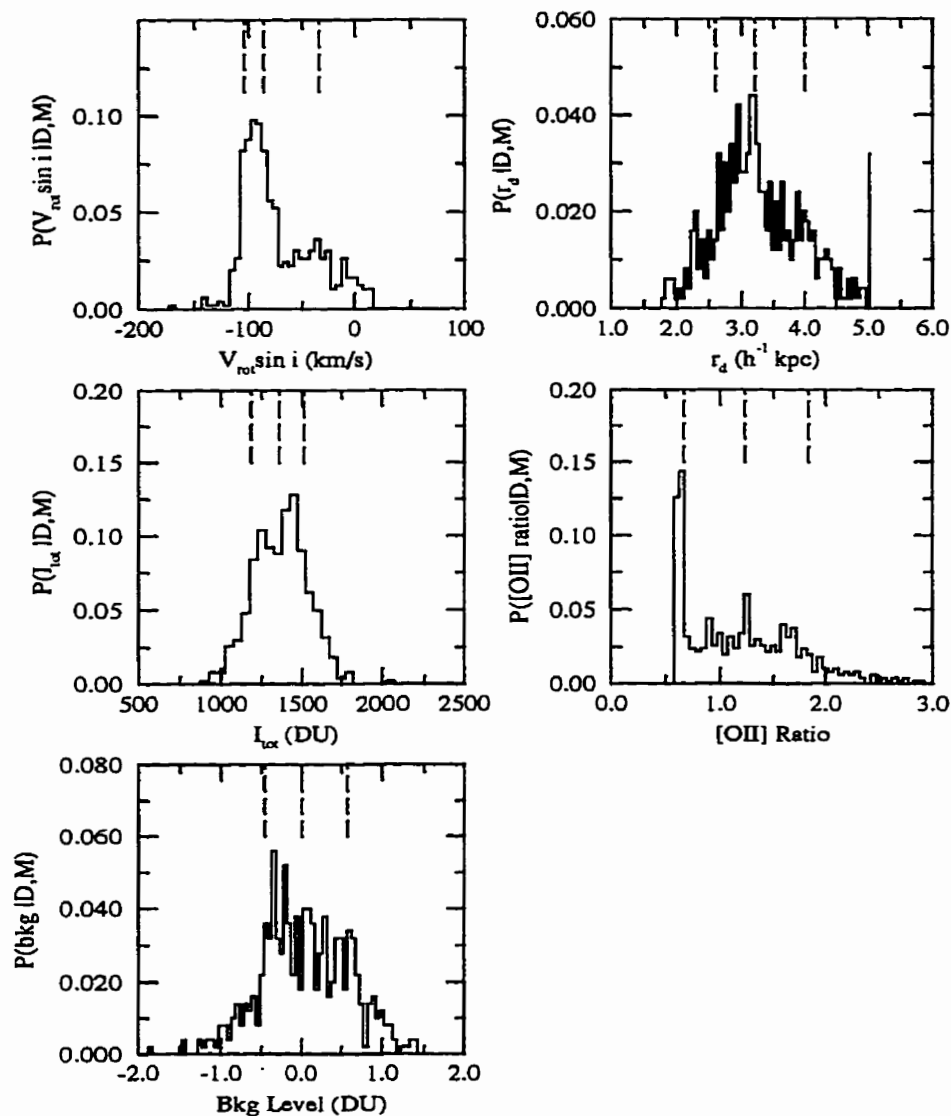


Figure 7.25: Parameter Probability Functions - A2390-200372. Each distribution is made up of 500 Metropolis selected points. Bin sizes are: $\Delta V \sin i = 5$ km/s, $\Delta r_d = 0.05 h^{-1}$ kpc, $\Delta I = 50$ DU, $\Delta[\text{OII}] \text{ ratio} = 0.05$ and $\Delta \text{bkg} = 0.05$ DU. The median value as well as the lower and upper bounds of the 68% confidence interval are marked by vertical dashed lines

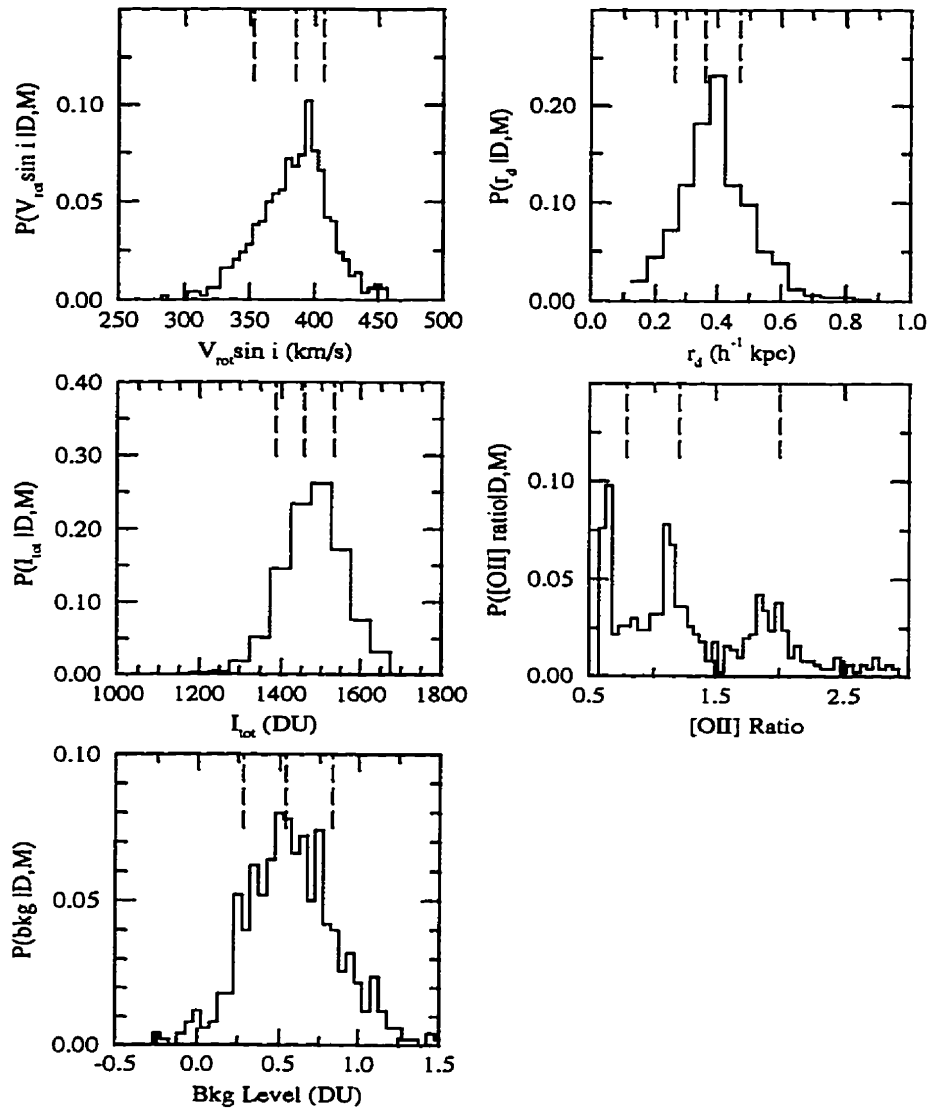


Figure 7.26: Parameter Probability Functions - E1512-201845. Each distribution is made up of 500 Metropolis selected points. Bin sizes are: $\Delta V \sin i = 5$ km/s, $\Delta r_d = 0.05 h^{-1}$ kpc, $\Delta I = 50$ DU, $\Delta [\text{OII}] \text{ ratio} = 0.05$ and $\Delta \text{bkg} = 0.05$ DU. The median value as well as the lower and upper bounds of the 68% confidence interval are marked by vertical dashed lines

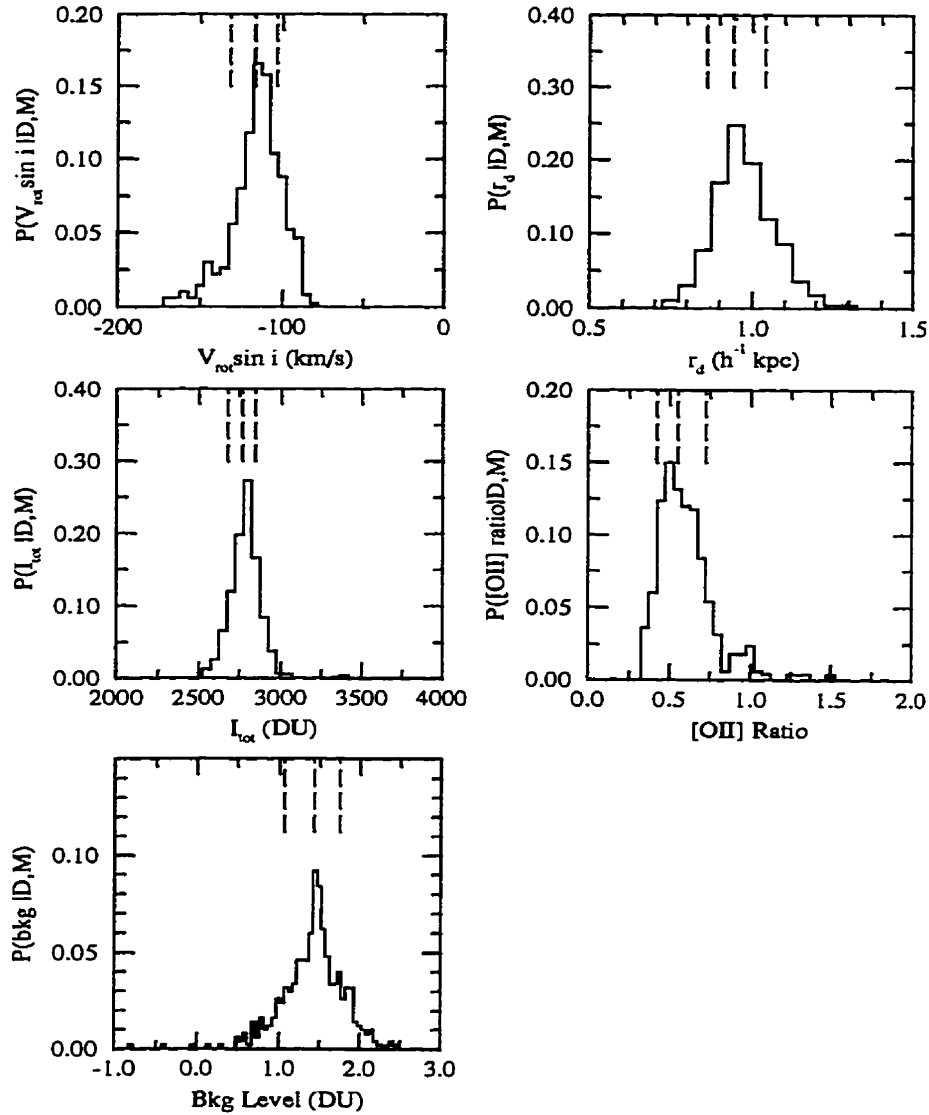


Figure 7.27: Parameter Probability Functions - A2390-201773. Each distribution is made up of 500 Metropolis selected points. Bin sizes are: $\Delta V \sin i = 5$ km/s, $\Delta r_d = 0.05 h^{-1}$ kpc, $\Delta I = 50$ DU, $\Delta[\text{OII}]$ ratio = 0.05 and $\Delta \text{bkg} = 0.05$ DU. The median value as well as the lower and upper bounds of the 68% confidence interval are marked by vertical dashed lines

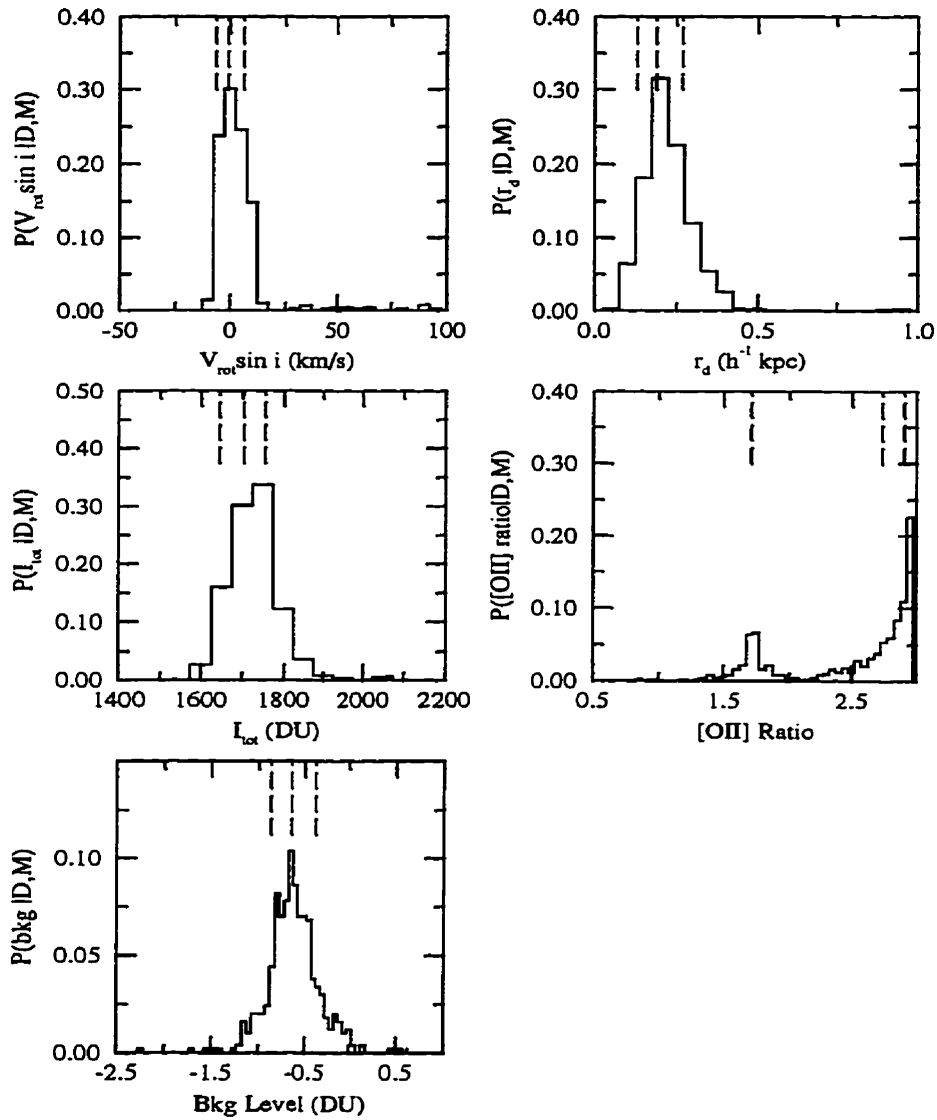


Figure 7.28: Parameter Probability Functions - E1512-200730. Each distribution is made up of 500 Metropolis selected points. Bin sizes are: $\Delta V \sin i = 5$ km/s, $\Delta r_d = 0.05 h^{-1}$ kpc, $\Delta I = 50$ DU, $\Delta[\text{OII}]$ ratio = 0.05 and $\Delta \text{bkg} = 0.05$ DU. The median value as well as the lower and upper bounds of the 68% confidence interval are marked by vertical dashed lines

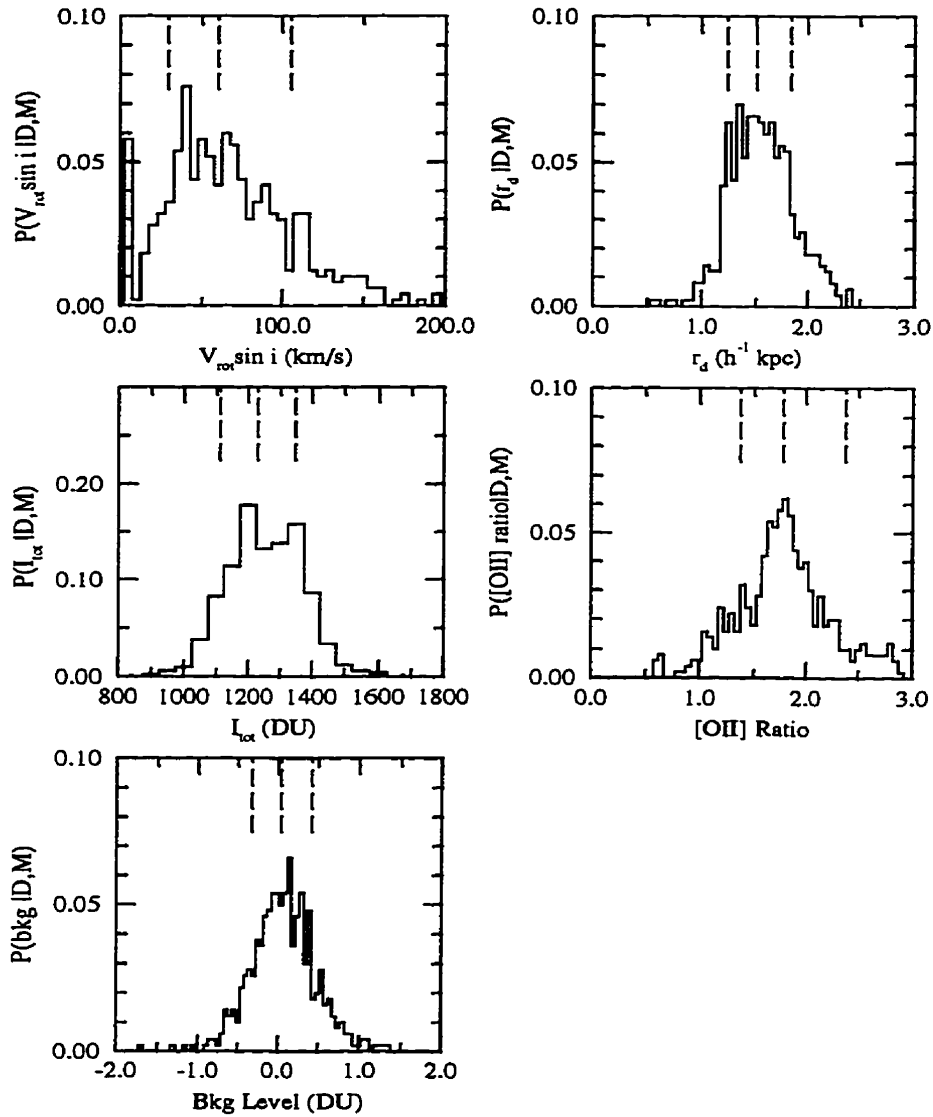


Figure 7.29: Parameter Probability Functions - E1512-200334. Each distribution is made up of 500 Metropolis selected points. Bin sizes are: $\Delta V \sin i = 5$ km/s, $\Delta r_d = 0.05$ h^{-1} kpc, $\Delta I = 50$ DU, $\Delta[\text{OII}]$ ratio = 0.05 and $\Delta \text{bkg} = 0.05$ DU. The median value as well as the lower and upper bounds of the 68% confidence interval are marked by vertical dashed lines

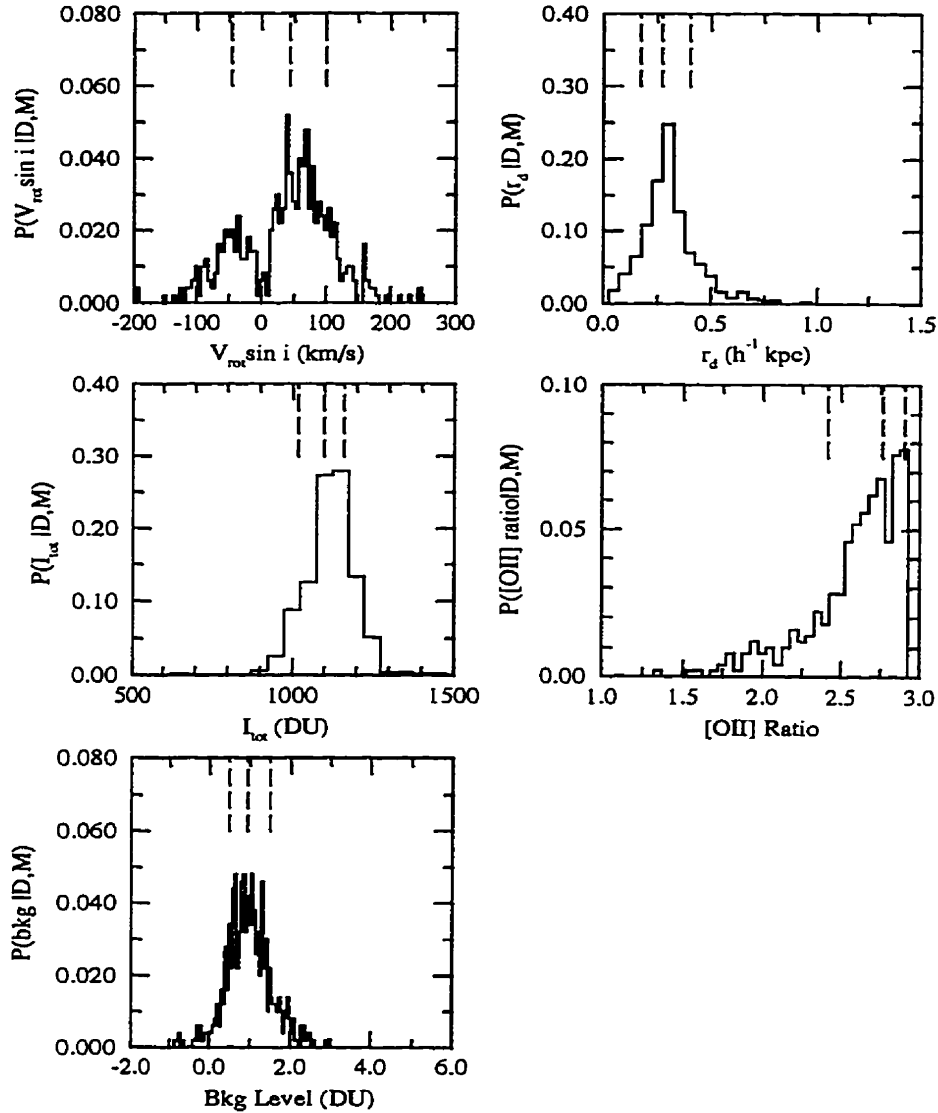


Figure 7.30: Parameter Probability Functions - E1512-200672. Each distribution is made up of 500 Metropolis selected points. Bin sizes are: $\Delta V \sin i = 5$ km/s, $\Delta r_d = 0.05 h^{-1}$ kpc, $\Delta I = 50$ DU, $\Delta [\text{OII}] \text{ ratio} = 0.05$ and $\Delta \text{bkg} = 0.05$ DU. The median value as well as the lower and upper bounds of the 68% confidence interval are marked by vertical dashed lines

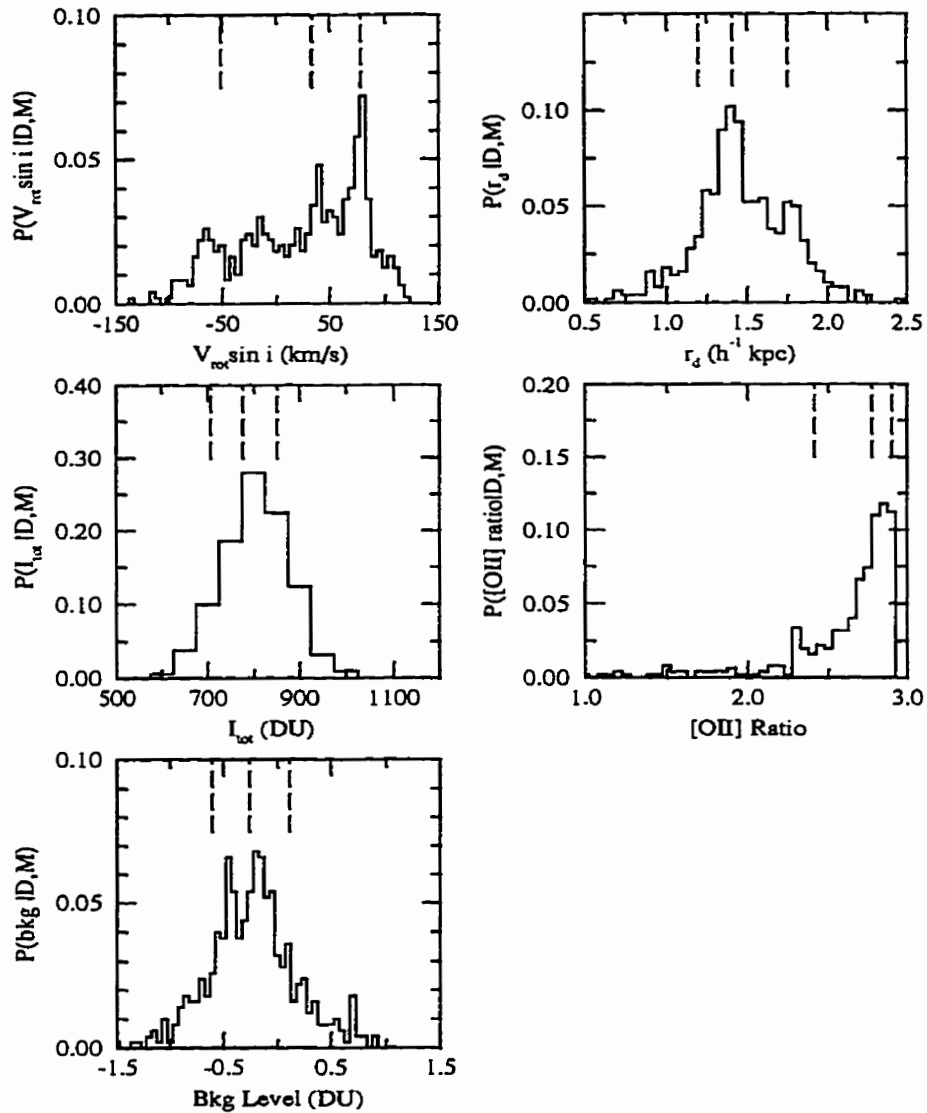


Figure 7.31: Parameter Probability Functions - E1512-201268. Each distribution is made up of 500 Metropolis selected points. Bin sizes are: $\Delta V \sin i = 5$ km/s, $\Delta r_d = 0.05$ h^{-1} kpc, $\Delta I = 50$ DU, $\Delta [\text{OII}] \text{ ratio} = 0.05$ and $\Delta \text{bkg} = 0.05$ DU. The median value as well as the lower and upper bounds of the 68% confidence interval are marked by vertical dashed lines

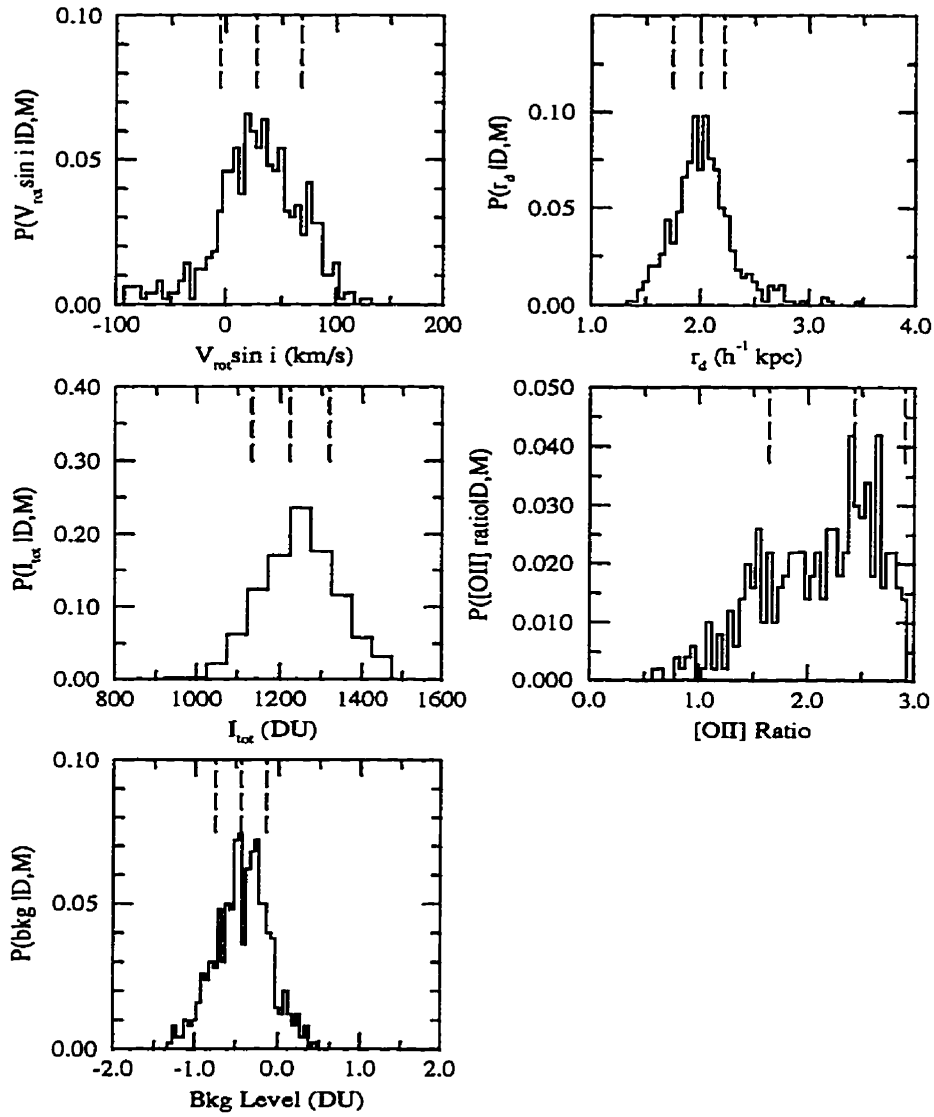


Figure 7.32: Parameter Probability Functions - E1512-202096. Each distribution is made up of 500 Metropolis selected points. Bin sizes are: $\Delta V \sin i = 5$ km/s, $\Delta r_d = 0.05 h^{-1}$ kpc, $\Delta I = 50$ DU, $\Delta [\text{OII}] \text{ ratio} = 0.05$ and $\Delta \text{bkg} = 0.05$ DU. The median value as well as the lower and upper bounds of the 68% confidence interval are marked by vertical dashed lines

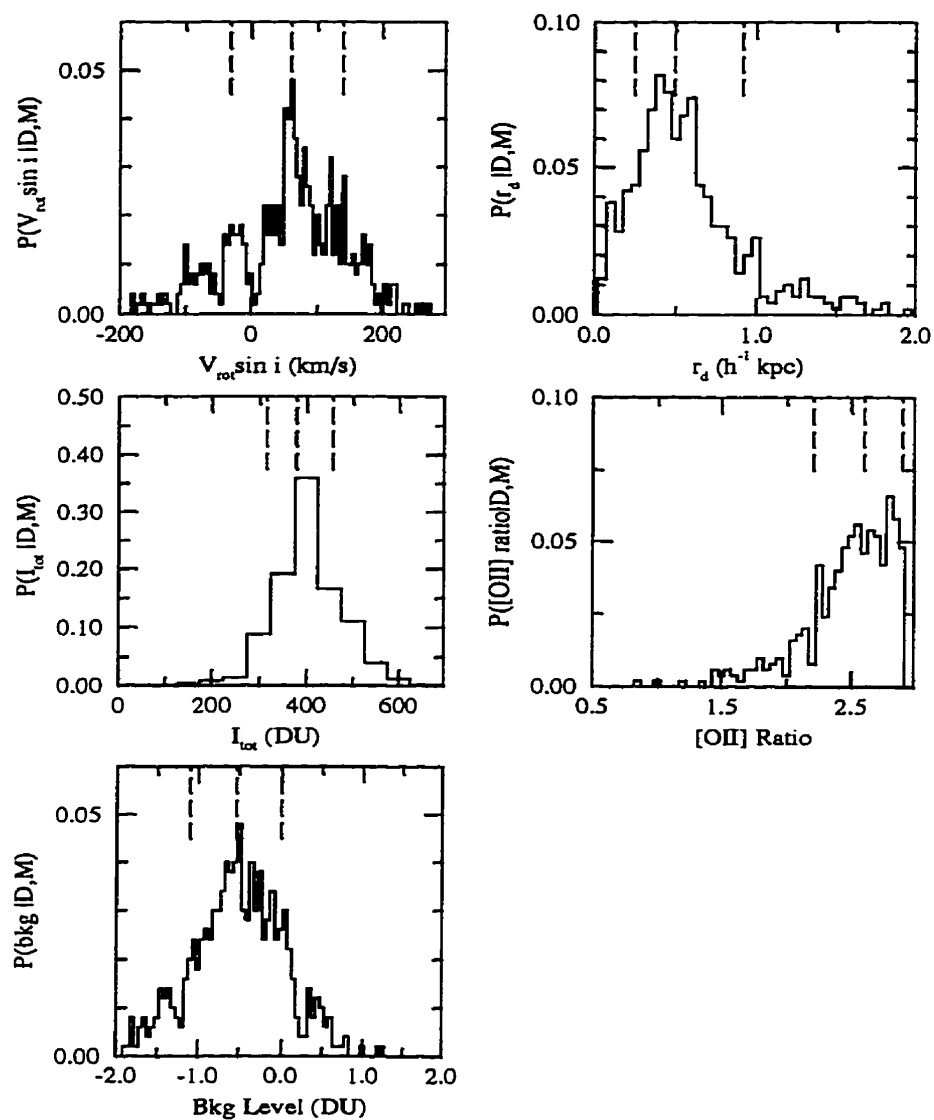


Figure 7.33: Parameter Probability Functions - E1512-201125. Each distribution is made up of 500 Metropolis selected points. Bin sizes are: $\Delta V \sin i = 5$ km/s, $\Delta r_d = 0.05$ h^{-1} kpc, $\Delta I = 50$ DU, $\Delta[\text{OII}]$ ratio = 0.05 and $\Delta \text{bkg} = 0.05$ DU. The median value as well as the lower and upper bounds of the 68% confidence interval are marked by vertical dashed lines

7.3 [OII] Morphologies

The ELFIT2D results presented in Section 7.2 can only be properly interpreted by looking at the morphologies of the [OII] emission. Clearly, $V_{\text{rot}} \sin i$ will not be a measurement of rotation if the [OII] emission is concentrated in the nucleus of the galaxy. This section provides comments on ELFIT2D results, broad-light and [OII] morphologies and broad-band disk scale lengths for each galaxy.

A2390-101033. This galaxy looks completely normal on deep SIS V and R images apart for what appears to be ringing on one side of the disk. The surface brightness profiles are all fitted with an exponential disk scale length of $2.5 \text{ h}^{-1} \text{ kpc}$ (Figures 7.1, 7.5 and 7.11). There is a close companion at an apparent angular distance of $3''.2$ which corresponds to $7.7 \text{ h}^{-1} \text{ kpc}$ at a redshift of 0.2460. The SIS [OII] spectrum is striking (Figure 7.34). It shows a strong [OII] emission superposed over a much fainter continuum. The continuum is extended whereas the [OII] emission is unresolved. All of the emission is concentrated in the nucleus of the galaxy. The [OII] scale length measured by ELFIT2D is $0.09^{+0.02}_{-0.02} \text{ h}^{-1} \text{ kpc}$ which is significantly smaller than the broad-band scale length. Moreover, there is an extension on one side of the [OII] emission. This extension remains when the main unresolved [OII] component is subtracted out. The extension could be the kinematical signature of a small companion galaxy in the process of merging with its host. If so, the extension would be direct evidence that minor mergers are responsible for enhanced star formation activity in some galaxies at intermediate redshifts. This galaxy is the prototype of a “kinematically

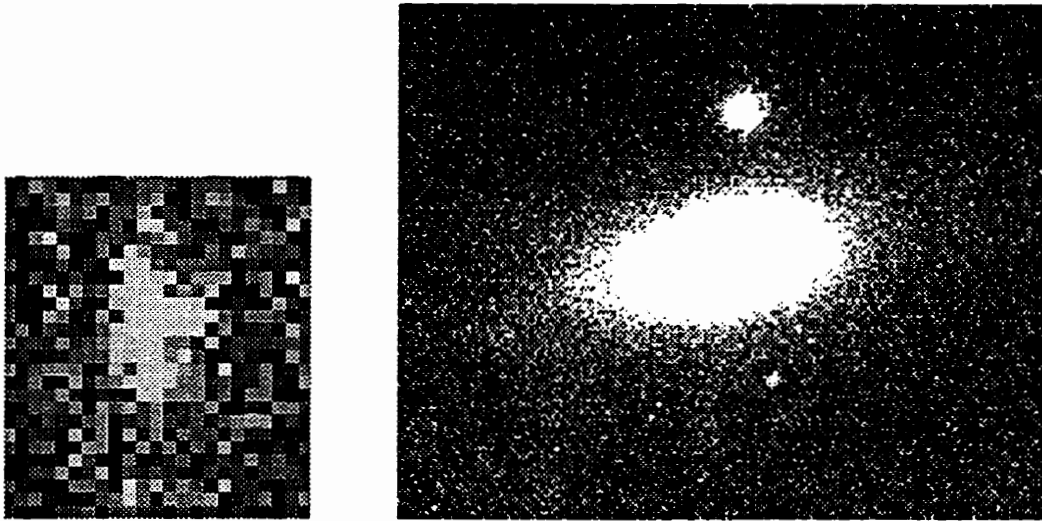


Figure 7.34: Left: Observed SIS 2D spectrum of [OII] nuclear emission in a galaxy at $z = 0.25$ (A2390-101033). The horizontal axis is the spatial axis, and the dispersion is along the vertical axis. [OII] scale length = $0.09^{+0.02}_{-0.02} h^{-1}$ kpc ($q_0 = 0.5$) and R band disk scale length = $2.4 \pm 0.2 h^{-1}$ kpc. The faint, extended continuum of the galaxy can be seen on the original spectrum. The knot of [OII] emission in the right-hand central region of the 2D spectrum could be the signature of a very close companion in the process of merging with its host galaxy. Image scale = $0''.17/\text{pixel}$, dispersion = $0.88 \text{ \AA}/\text{pixel}$, and seeing = $0''.5$ FWHM. Right: 1800 seconds SIS R band direct image with $0''.087/\text{pixel}$ and seeing = $0''.5$ FWHM. The morphology is surprisingly normal apart from a “ringing” on the left-hand side of the disk. This “ringing” may be the result of tidal interactions with the companion at a projected distance of $8 h^{-1}$ kpc

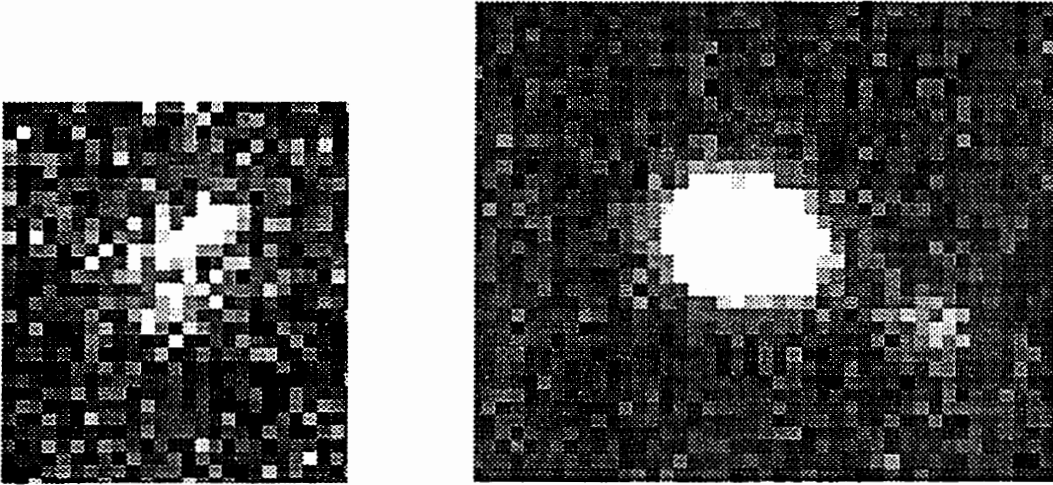


Figure 7.35: Left: Observed SIS 2D rotation curve of a kinematically normal galaxy at $z = 0.42$ (E1512-201429). The horizontal axis is the spatial axis, and the dispersion is along the vertical axis. Total integration time of 4800 seconds with a seeing of $0''.6$ FWHM. The [OII] doublet components are resolved due to the $(1+z)$ increase in spectral resolution. $V_{\text{rot}} \sin i = 151 \pm_{11}^{13}$ km/s, [OII] scale length = $1.0 \pm_{0.10}^{0.20} h^{-1}$ kpc ($q_0 = 0.5$). Image scale = $0''.17/\text{pixel}$ and dispersion = $0.88 \text{ \AA}/\text{pixel}$. Right: MOS 900 seconds R band direct image. Image scale = $0''.32/\text{pixel}$ and broad-band disk scale length = $1.8 \pm 0.2 h^{-1}$ kpc.

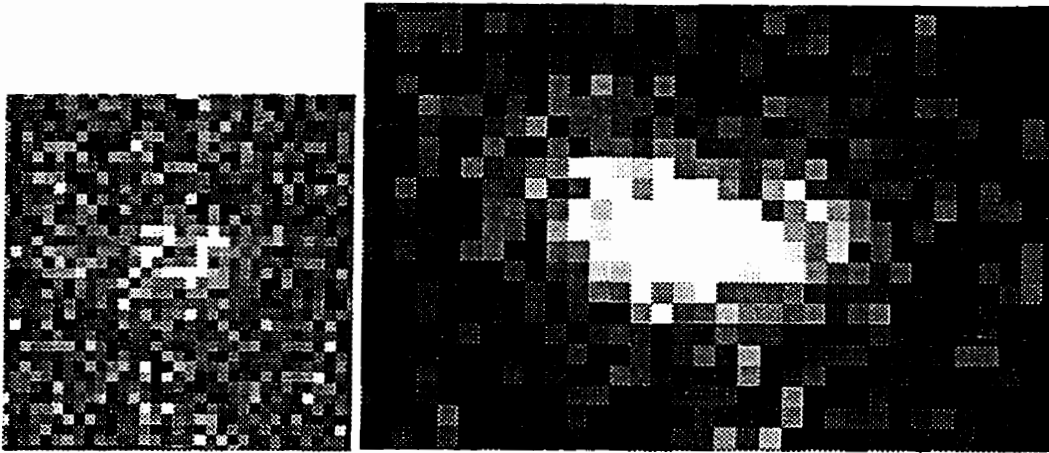


Figure 7.36: **Left:** Observed SIS 2D spectrum of donut-shaped [OII] emission in a galaxy at $z = 0.35$ (E1512-301037). Image scale = $0''.17/\text{pixel}$, dispersion = $0.88 \text{ \AA}/\text{pixel}$ and seeing = $0''.6$ FWHM. This peculiar [OII] morphology could be produced by a pair of very close galaxies or by an expanding galactic supershell. **Right:** Sum of 3 direct SIS 300 seconds I band images. Image scale = $0''.17/\text{pixel}$ and seeing = $0''.7$ FWHM.

anomalous” object. It resembles blue nucleated galaxies described by Schade *et al.* (1995).

A2390-100686. This galaxy looks normal in Gunn r and g and in I. The surface brightness profiles are barely resolved and have a scale length of $1.2 h^{-1}$ kpc (Figures 7.1, 7.5 and 7.9). There are no close companions. The SIS [OII] spectrum shows a tilted, extended emission centered on a faint continuum as extended as the [OII] emission. The tilted emission appears “puffed up”. It is probably a result of seeing the [OII] doublet components almost resolved by wavelength stretching from the cosmological expansion. This object was classified as kinematically normal.

A2390-350416. This galaxy looks normal in all three bandpasses. It is better resolved in Gunn g than in Gunn r as shown by the surface brightness profiles on the CNOC MOS images (Figures 7.5 and 7.1). The Gunn g and Johnson I profiles are fitted with a disk scale length of $1.8 h^{-1}$ kpc. There are no nearby companions. The SIS [OII] spectrum shows a tilted line as extended as the continuum light. The [OII] scale length is $1.9^{+0.40}_{-0.40}$ which is equal to the I and Gunn g scale lengths. The [OII] emission is centered on the continuum. This object was classified as kinematically normal.

A2390-350471. The I image suggests that this galaxy could be distorted, but the Gunn r and g images look smooth. The position angle of its isophotes varies substantially. However, the surface brightness profiles are very well fitted by an exponential profile. The I and Gunn g profiles have a scale length of $1.4 h^{-1}$ kpc (Figures 7.10 and 7.5). There are no close companions. The SIS [OII] spectrum shows a tilted line with no apparent distortion. The [OII] scale length is $2.2^{+0.70}_{-0.50}$. This object was classified as

kinematically normal.

E1512-301037. This galaxy has faint distortions on the Gunn g and r CNOC MOS image. There are at least two faint tails. However, the Gunn r and g profiles are well-fitted by an exponential profile with a scale length of $3.8 h^{-1}$ kpc (Figures 7.1 and 7.5). There are two faint close companions with an apparent angular distance of $5''.4$ ($16.1 h^{-1}$ kpc at $z = 0.3457$). The SIS [OII] spectrum is by far the most intriguing one in the sample. It shows a very faint continuum, and the [OII] line is *donut-shaped* (Figure 7.36). This line shape can be interpreted in two ways: either (1) the line is made of two rotation curves from two galaxies very close together, or (2) the line arises from an expanding supershell presumably driven by supernova winds from a massive starburst. Unfortunately, no deep SIS images are available for this object. If option (1) is true, then the separation between the two galaxies would be $0''.8$ which corresponds to $2.5 h^{-1}$ kpc at a redshift of 0.3457. Option (1) was retained for the ELFIT2D analysis. This is why there are two entries in Table 7.3. However, there is a problem with option (1). If this object is in fact a very close pair, then there should be a systematic offset in wavelength between the two rotation curves due to the relative velocities of the pair members. No such offset is observed. If option (2) is true, then the supershell has a diameter of $2.5 h^{-1}$ kpc and an expansion velocity of about 80 km/s. These characteristics are amazingly similar to those of supershells observed in local dwarf irregular galaxies (Marlowe et al., 1995; Martin, 1995). It is likely that this object is a so-called Doppler ellipse, the first one found at intermediate redshifts. This object was of course classified as kinematically anomalous.

E1512-101526. The Gunn r image shows the galaxy has a close companion at an apparent distance of $2''.1$ ($6.8 h^{-1}$ kpc at $z = 0.4026$). Gunn r and g profiles are well fitted with an exponential disk scale length of $3.1 h^{-1}$ kpc (Figures 7.1 and 7.5). The SIS [OII] spectrum has a faint continuum, and the [OII] emission shows no sign of rotation and appears unresolved. The [OII] scale length measured by ELFIT2D is $0.1^{+0.40}_{-0.10} h^{-1}$ kpc which is significantly smaller than the broad-band scale lengths. This object was therefore classified as kinematically anomalous.

E1512-201429. This galaxy looks normal in all three bandpasses. It is resolved on the CNOC Gunn g and the SIS I band images. The profiles can be fitted with a scale length of $1.8 h^{-1}$ kpc. (Figure 7.2, 7.6 and 7.9) The Gunn r image is not well resolved. The nearest companion is at an apparent angular distance of $5''.0$ ($16.4 h^{-1}$ kpc at $z = 0.4231$). The SIS spectrum shows an extended continuum with a double tilted [OII] emission line (Figure 7.35). The double line is in fact the two components of the [OII] doublet resolved as a result of wavelength stretching by the cosmological expansion. The blue component of the doublet clearly has a different brightness from the red component as a function of galactocentric radius. This indicates that the electron density in the interstellar medium of this galaxy varies as a function of distance from its center. This object was classified as kinematically normal.

E1621-100515. This galaxy looks normal in all three bandpasses. The profiles are all very well fitted by an exponential disk scale length of $1.5 h^{-1}$ kpc (Figures 7.2, 7.6 and 7.10). There are no close companions. The SIS spectrum shows a tilted line with a faint, extended continuum. Unfortunately, the line received a string of cosmic rays hits which seem to have

affected the ELFIT2D fit. This object was classified as kinematically normal, but it was not included in the final Tully-Fisher sample because of the effect of so many cosmic rays in the ELFIT2D fit.

A2390-100225. This galaxy looks normal in I and Gunn r and g . It is resolved on the SIS I and CNOC MOS Gunn r images. The exponential profiles are well fitted with a scale length of $1.2 h^{-1}$ kpc (Figures 7.2, 7.6 and 7.10). There are no close companions. The MOS spectrum shows a very faint, concentrated [OII] emission. ELFIT2D was not able to achieve a good fit of this [OII] distribution. The MOS ELFIT2D simulation (Figure 6.33) shows that the [OII] flux received from this galaxy was simply too low for ELFIT2D to find meaningful parameter values.

A2390-101084. Deep SIS V and R images show that this distorted galaxy has at least four close companions within a radius of $4''.2$ ($9.8 h^{-1}$ kpc). The Gunn images also show many faint companions. This galaxy is in fact the central cD galaxy of the cluster Abell 2390. This galaxy was observed serendipitously as part of one of the MOS multi-object exposures. The V and R surface profiles have a scale length of $2.5 h^{-1}$ kpc (Figure 7.11). The MOS spectrum shows a strong, unresolved [OII] emission line. The [OII] scale length is $0.4^{+0.03}_{-0.06} h^{-1}$ kpc which is significantly smaller than the broadband scale length. This object was classified as kinematically anomalous. Since cD galaxies are believed to be the result of galaxy cannibalism, this suggests that kinematically anomalous galaxies may be related to merging events. The MOS ELFIT2D simulation (Figure 6.33) shows no biases.

A2390-200928. This galaxy is not clearly resolved on the CNOC MOS images. There is no sign of distortions, and there are no close companions.

The MOS spectrum shows a fairly concentrated [OII] emission. The [OII] scale length is $0.3^{+0.20}_{-0.10} \text{ h}^{-1} \text{ kpc}$. This object was classified as kinematically normal. However, if the broad-band scale length has been seriously underestimated due to seeing effects, then this galaxy should have been classified as kinematically anomalous. The MOS ELFIT2D simulation (Figure 6.33) shows no biases.

A2390-200802. This galaxy is barely resolved on the CNOC MOS images, and it looks more elongated in g than in r . The exponential profiles can be fitted with a scale length of about $1.2 \text{ h}^{-1} \text{ kpc}$ (Figures 7.2, 7.6). There are no signs of distortions, and there are no close companions. The MOS spectrum shows a compact, tilted line. The [OII] scale length is $1.0^{+0.40}_{-0.50} \text{ h}^{-1} \text{ kpc}$ which is identical to the broad-band scale length. This object was classified as kinematically normal. The MOS ELFIT2D simulation (Figure 6.34) shows no r_d bias, but $V_{\text{rot}} \sin i$ appears to slightly *overestimated*. It is therefore not surprising to find this galaxy *above* the Tully-Fisher relation in Figure 7.37 with a large error bar.

A2390-200372. The galaxy is fully resolved on the CNOC MOS Gunn r and g images, and it looks normal on both images. The exponential profiles are well fitted with a scale length of $1.7 \text{ h}^{-1} \text{ kpc}$ (Figures 7.3 and 7.7). The nearest object is at an apparent angular distance of $5''.8$ ($17 \text{ h}^{-1} \text{ kpc}$ at $z = 0.3485$). The MOS spectrum shows a nice tilted line over a faint, less extended continuum. The [OII] emission, which is centered on the continuum emission, has a scale length of $3.2^{+0.90}_{-0.60} \text{ h}^{-1} \text{ kpc}$. This object was classified as kinematically normal. The MOS ELFIT2D simulation (Figure 6.34) shows no biases.

E1512-201845. The galaxy is fully resolved on the CNOC MOS Gunn r and g images, and it has a distorted morphology. There are two close companions within a radius of $4''.2$ ($12 \text{ h}^{-1} \text{ kpc}$ at $z = 0.3387$). The profiles are not well fitted by an exponential. In fact, the profiles have the shape expected from a de Vaucouleurs profile in $\log \Sigma - r$ space. If an exponential is used to fit the profiles, the resulting scale length is $4.8 \text{ h}^{-1} \text{ kpc}$ (figures 7.3 and 7.7). The MOS spectrum shows a strong and slightly tilted [OII] line centered on a faint continuum. The [OII] scale length was $0.4^{+0.10}_{-0.10} \text{ h}^{-1} \text{ kpc}$ which is much smaller than the broad-band scale length. This early-type galaxy was classified as kinematically anomalous. The MOS ELFIT2D simulation (Figure 6.34) shows no biases.

E1512-201773. This galaxy looks distorted on the SIS I band and MOS Gunn r images. There is a large extension on the west side. It may be a close pair in the process of merging. The surface brightness profiles on the CNOC MOS images are very well fitted with an exponential scale length of about $1.6 \text{ h}^{-1} \text{ kpc}$ (Figures 7.3 and 7.7) whereas the SIS I band image yields a scale length of $1.2 \text{ h}^{-1} \text{ kpc}$ (Figure 7.9). The MOS spectrum shows a very strong, tilted line, but this line appears to be significantly distorted with respect to a pure rotation curve. This object was not included in the final Tully-Fisher sample. The MOS ELFIT2D simulation (Figure 6.35) shows no biases.

E1512-200730. The galaxy is fully resolved on the CNOC MOS Gunn r and g images, and it looks smoother on the r image. There are no close companions. The exponential profiles are well fitted with a scale length of $1.5 \text{ h}^{-1} \text{ kpc}$ (Figure 7.3 and 7.7). The MOS spectrum shows an unresolved [OII] emission. The [OII] scale length was $0.2^{+0.10}_{-0.10} \text{ h}^{-1} \text{ kpc}$. This object

was classified as kinematically anomalous. The MOS ELFIT2D simulation (Figure 6.35) shows no biases.

E1512-200334. The galaxy has a fully resolved exponential profile in Gunn g with a scale length of $2.0 \text{ h}^{-1} \text{ kpc}$ (Figure 7.7), but it is not resolved in Gunn r . The Gunn g looks elongated, and there are no close companions. The MOS spectrum shows a tilted [OII] centered on a faint continuum. The [OII] scale length was $1.5^{+0.30}_{-0.30} \text{ h}^{-1} \text{ kpc}$, and this object was classified as kinematically normal. The MOS ELFIT2D simulation (Figure 6.35) shows no biases.

E1512-200672. The galaxy has a fully resolved exponential profile in Gunn g (scale length = $1.5 \text{ h}^{-1} \text{ kpc}$, Figure 7.7), but it is not well resolved in Gunn r . The Gunn g image has a very strong nucleus. There are no close companions. The MOS spectrum shows a strong, unresolved [OII] emission centered on a faint continuum. The [OII] scale length was $0.3^{+0.10}_{-0.10} \text{ h}^{-1} \text{ kpc}$, and this object was classified as kinematically anomalous. Considering the fact that many kinematically anomalous galaxies have close companions, it is somewhat surprising that this galaxy is isolated. The MOS ELFIT2D simulation (Figure 6.36) shows no biases.

E1512-201268. The galaxy is not well resolved in Gunn g and r , so the scale length of $1.4 \text{ h}^{-1} \text{ kpc}$ (Figures 7.4 and 7.8) is probably a lower limit. There are no close companions. The r and g images are both elongated. The MOS spectrum shows an extended and tilted [OII] line centered on a more compact continuum. The [OII] scale length was $1.4^{+0.30}_{-0.20} \text{ h}^{-1} \text{ kpc}$, and this object was classified as kinematically normal. This galaxy has low [OII] flux, so its $V_{\text{rot}} \sin i$ has a fairly large error bar in Figure 7.37, and the MOS

ELFIT2D simulation (Figure 6.36) shows that $V_{\text{rot}} \sin i$ may be slightly underestimated.

E1512-202096. This galaxy looks normal in all three bandpasses. The galaxy is best resolved in Gunn r . It is best fitted with a scale length of $2.1 \text{ h}^{-1} \text{ kpc}$ (Figure 7.4). There are no close companions. The MOS spectrum shows a very interesting [OII] morphology. There is a faint rotational component symmetric about the faint continuum. Atop this rotational component, there is a relatively strong source about $0''.8$ ($2.6 \text{ h}^{-1} \text{ kpc}$ at a redshift of 0.4252) away from the center of the continuum. This source, which is unresolved spatially and spectrally, could be a giant HII region. The [OII] scale length measured with ELFIT2D was $2.0^{+0.20}_{-0.30} \text{ h}^{-1} \text{ kpc}$, which is identical to the broad-band scale length. Based upon its faint rotational component, this object was classified as kinematically normal. The MOS ELFIT2D simulation (Figure 6.36) shows no biases.

E1512-201125. This galaxy is resolved in Gunn r (scale length = $1.6 \text{ h}^{-1} \text{ kpc}$, Figure 7.4), but it is not resolved in Gunn g . The r image looks distorted. There is an small extension on one side which could be a very close companion. The MOS spectrum shows a faint [OII] line which is not resolved. The [OII] scale length was $0.5^{+0.40}_{-0.30} \text{ h}^{-1} \text{ kpc}$, and this object was classified as kinematically anomalous. Despite the very low [OII] flux, the MOS ELFIT2D simulation (Figure 6.36) shows no systematic biases, but the scatter in $V_{\text{rot}} \sin i$ is large.

Seven galaxies (identified by the superscript n in Table 7.3) have [OII] scale lengths significantly smaller (and consistent with being unresolved) than their broad-band scale lengths. Two of these galaxies (identified by

the superscript *c* in Table 7.3) are serendipitously observed cluster galaxies. Such discrepancies indicate that the [OII] gas kinematics is decoupled from galaxy rotation in some galaxies. Two properties of kinematically anomalous galaxies have emerged so far: (1) All but one have close companions. This suggests that enhanced star formation activity may be the result of merger events; and (2) Some of these galaxies appears to be of early-types. Kinematically “anomalous” field galaxies make up 25% of the field sample. This percentage is similar to the fraction (20%) of field galaxies up to $z = 0.3$ with properties between Seyfert 2 galaxies and LINERs (Tresse et al., 1994). Unfortunately, the study of kinematical anomalies is not suited to long-slit or multi-object spectrographs. Slits provide spatial information along their axis. Only integral field spectrographs such as Fabry-Pérot interferometers and fibre bundles can fully uncover the complex kinematics expected in those cases.

7.4 Intermediate Redshift Tully-Fisher Relation

In order to construct an intermediate redshift Tully–Fisher relation, we used galaxies satisfying the following two selection criteria: (1) a difference between the position angle of the slitlet and the position angle of the major axis of the galaxy less than 45° , and (2) consistent [OII] and broad-band scale lengths. Criterion (1) was applied only to the MOS data, since a misalignment between the major axis of a galaxy and the position angle of the slitlet artificially decreases the magnitude of $V_{\text{rot}} \sin i$. Figure 7.37 shows $V_{\text{rot}} \sin i$

versus k -corrected absolute B magnitude for the 12 remaining kinematically “normal” galaxies. $V_{\text{rot}} \sin i$'s and B magnitudes were taken from Tables 7.3 and 5.1 respectively.

The solid line is the expected H_{α} rotation velocity as derived from the absolute calibration of the B-band inclination-corrected TF relation for local galaxies (Pierce and Tully, 1992; Jacoby et al., 1992) and a linear fit to the HI velocity width- H_{α} rotation velocity data of 204 galaxies (Mathewson et al., 1992). See section 8.1 for details. Also shown is the H_{α} TF relation expected for randomly oriented disks (dashed line) based on the fact that $\langle V_{\text{obs}} \rangle = 0.7854 \langle V_{\text{edge-on}} \rangle$ for randomly oriented disks.

Since we selected relatively elongated galaxies on CNOC images, and seeing tends to make galaxy images rounder, it is likely that the observed galaxies were on average much more inclined than a randomly inclined sample. The solid line should therefore be closer to the local TF locus of our sample. The implications of Figure 7.37 for galaxy evolution are discussed in section 8.3.

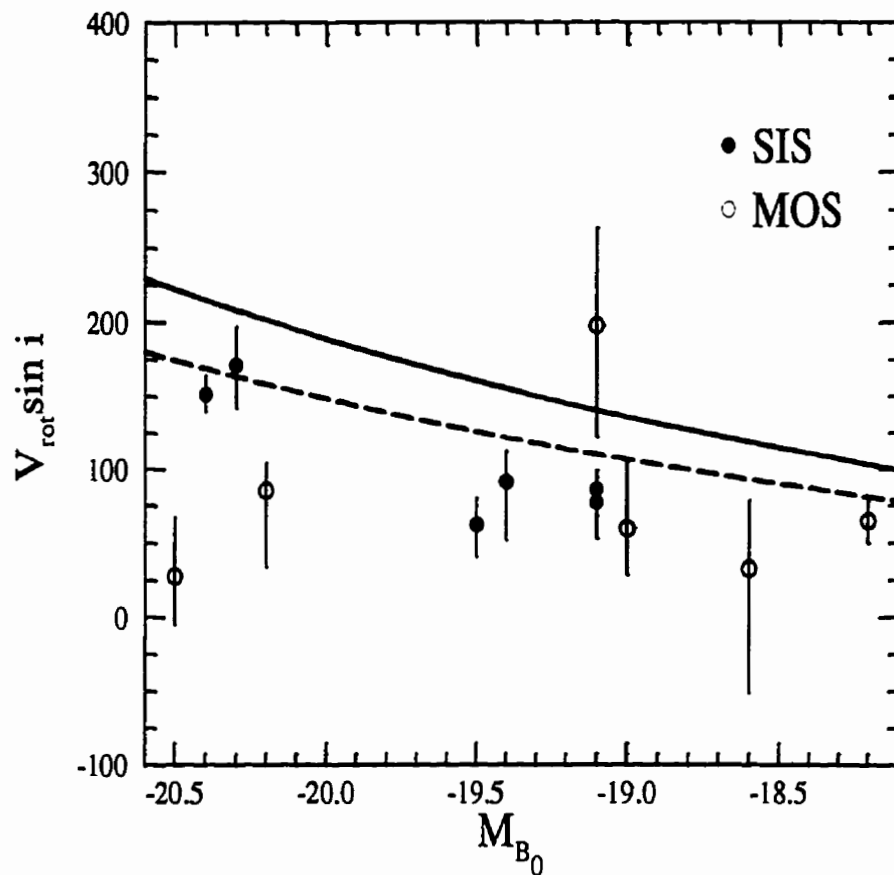


Figure 7.37: $V_{\text{rot}} \sin i$ versus rest-frame absolute B magnitude for kinematically normal galaxies observed with SIS (filled circles) and MOS (open circles). The error bars are 68% confidence levels. The solid line is the expected H_{α} rotation velocity as derived from the absolute calibration of the B-band inclination-corrected TF relation for local galaxies and a linear fit to the HI velocity width- H_{α} rotation velocity data of 204 galaxies. The dashed line is the same H_{α} TF relation corrected for randomly oriented disks using $\langle V_{\text{obs}} \rangle = 0.7854 V_{\text{TF}}(\text{edge-on})$.

Chapter 8

Discussion

8.1 The Local Tully-Fisher Relation

The Tully-Fisher relation is an empirical relationship between the luminosity of a spiral/irregular galaxy and its rotational velocity. It is interesting to note that even though a variant of the Tully-Fisher relation was first used by Öpik (1922) to find the distance to the Andromeda galaxy (Messier 31), it took 55 years to fully realize its potential as a major component of the extragalactic distance scale (Tully and Fisher, 1977). The global neutral hydrogen 21cm linewidth corrected for inclination and receiver broadening is usually used as a measure of a galaxy's rotational velocity while CCD detectors are used to measure the galaxy's total light and inclination.

The physical basis of the relation is not understood because the process of galaxy formation remains for the most part a mystery. Simple “back-of-the-envelope” arguments (Jacoby et al., 1992) based on too many assumptions (spherical symmetry, constant surface brightness and constant mass-to-light ratio) can be used as a plausibility argument for the relation, but a thorough

explanation will have to wait for better models of galaxy formation. The Tully-Fisher relation highlights two remarkable properties of galaxies. First, the mass-to-light ratio of galaxies must remain constant over a broad range in luminosity since the relation remains tight over at least 7 magnitudes (a factor of 600 in luminosity!). The dispersions for the Tully-Fisher relations in the B, R and I bands are 0.37, 0.31 and 0.28 mag respectively. Second, there must be a conspiracy between the disks (luminous matter) and halos (dark matter) of galaxies such that both components “know” exactly how much each one should contribute to the mass within a characteristic optical radius as a function of total galaxy mass.

Since there is a good correlation between HI linewidth and galaxy luminosity, it is reasonable (and important!) to ask whether rotation velocities measured from optical emission lines follow a similar relationship. After all, since the HI distribution in disk galaxies typically extends twice as far in galactocentric distance as the optical emission, optical emission might not sample the full velocity width of disk galaxies. Moreover, rotational and turbulent motions both contribute to the intrinsic HI 21cm linewidth. High luminosity galaxies are rotationally-supported whereas low luminosity dwarf galaxies are supported by turbulence. A major advantage of optical rotation curves is the possibility of isolating the rotational component based on its characteristic “S” shape which eliminates the need for a turbulence correction to the velocity width. Figure 8.1 shows that rotation velocities measured using the H_α optical emission line ($\lambda = 6562 \text{ \AA}$) are very well-correlated with HI linewidths and that internal kinematics measured from optical emission lines should follow the same Tully-Fisher relation. Recent simultaneous ob-

servations of [OII] and H_α (Vogt et al., 1993) indicate that both lines yield the same rotation velocities.

In order to determine whether the internal kinematics of intermediate redshift galaxies deviate significantly from the local Tully-Fisher relation, it is important to define the local locus of that relation in the best way possible. Two methods were used to do so. The first method is based on the absolute calibration of the B-band Tully-Fisher relation (Pierce and Tully, 1992; Jacoby et al., 1992). This calibration based on 15 local galaxies is given by

$$M_B^{b,i} = -7.48(\log W_R^i - 2.50) - 19.55 \quad (8.1)$$

where $M_B^{b,i}$ is the total B magnitude corrected to a face-on inclination and for internal absorption. W_R^i is the HI linewidth corrected for inclination and turbulence according to the prescription of (Tully and Fouqué, 1985):

$$W_R^2 = W_{20}^2 + W_t^2 - 2W_{20}W_t(1 - e^{(W_{20}/W_c)^2}) - 2W_t^2 e^{(W_{20}/W_c)^2} \quad (8.2)$$

where $W_R = W_R^i \sin i$, W_{20} is the measured HI width at 20% of peak intensity, W_t is the expected 20% width due to turbulence (38 km s^{-1}) and W_c is the characteristic transition width from “horned” to Gaussian-shaped profiles (120 km s^{-1}). Thus, for a given absolute magnitude, W_{20} was obtained by finding the roots of eqs. 8.1 and 8.2 with RTSAFE (Press et al., 1986), and W_{20} was then converted to H_α using a linear regression fit (solid line, Figure 8.1) to ΔV_{20} ($\equiv W_{20}/2$) versus ΔV_{H_α} for 204 galaxies (Mathewson et al., 1992).

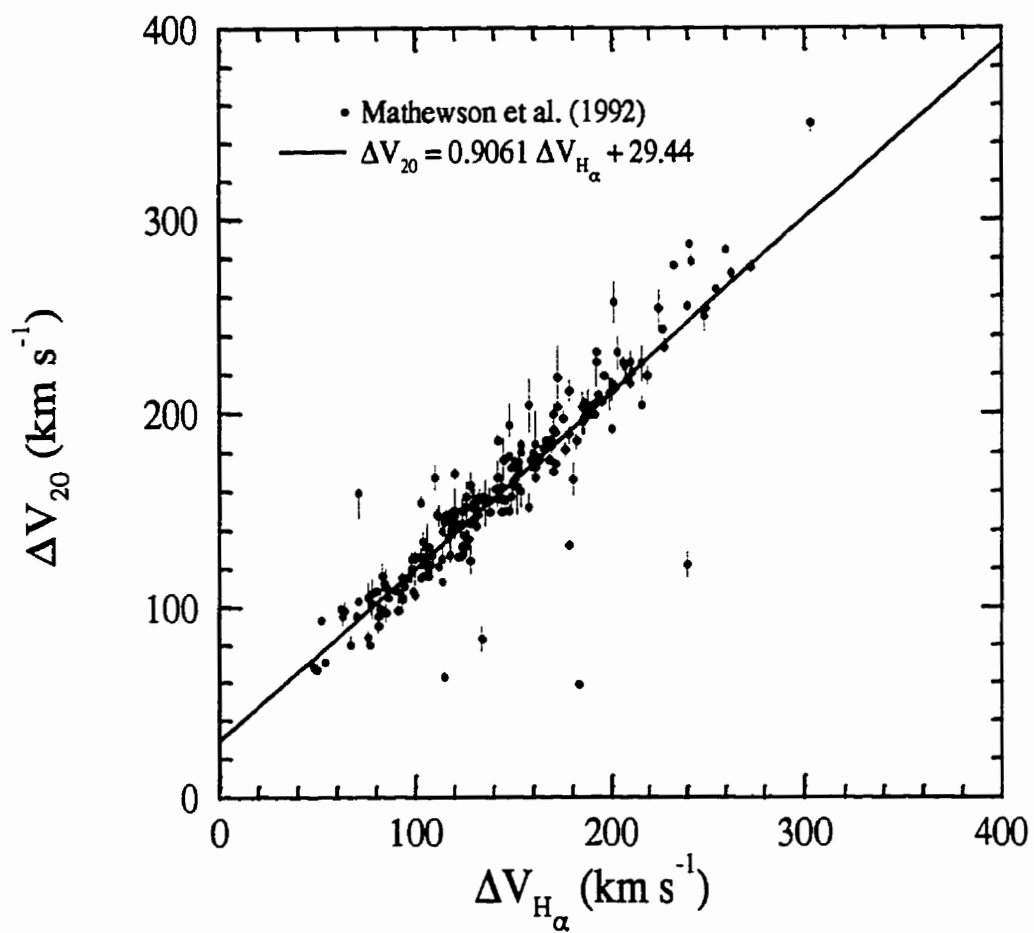


Figure 8.1: HI half-linewidth versus H α rotation velocity for a sample of 204 nearby galaxies. Data taken from Mathewson *et al.* (1992)

The above method suffers from two drawbacks: (1) it is indirect, and (2) it does not give any information on the dispersion of the local relation. These drawbacks are eliminated by using the H_α rotation velocities and total magnitudes of 1355 local galaxies observed by Mathewson *et al.* (1992) to define the locus of the local Tully-Fisher relation as described in the next section. This approach allows one to tackle a possible morphological dependence of the Tully-Fisher relation and the wide range of properties of local galaxies.

8.2 Morphological Dependence of the Tully-Fisher Relation

The question of a possible dependence of the Tully-Fisher relation on morphology expressed as a Hubble type has been first raised by Roberts (1975). It received drastic support from Rubin *et al.* (1980; 1982; 1985) who measured H_α rotation velocities in a magnitude-limited sample of 21 Sc, 23 Sb and 16 Sa galaxies. At a fixed rotation velocity V_{max} , Rubin *et al.* (1985) claimed that Sc galaxies were 2 magnitudes brighter in absolute B magnitude than Sa's and 0.5 magnitude brighter than Sb's and that the Tully-Fisher relation had a slope of 10 nearly independent of Hubble Type. This result deserves considerable attention as such a strong morphological dependence could be used to argue that any systematic deviation from the local Tully-Fisher relation seen at intermediate redshifts might be due to a wide range of local galaxy properties and strong selection effects.

De Vaucouleurs *et al.* (1982) used a sample of 173 galaxies with revised morphological type T between -2 and 10 and heliocentric recession veloci-

ties V_0 between 500 and 2000 km s⁻¹ to find least-squares solutions to the equation

$$-M_T^0 = a_0 + a_1(T - 4) + b_1X \quad (8.3)$$

where M_T^0 is the total absolute magnitude corrected to face-on, $X = \log V_{max} - 2.20$ and T is the revised morphological type. They obtained three types of solutions: (1) all free parameters, (2) fixed slope $b_1 = 5$ and (3) fixed slope $b_1 = 10$. The free parameter solutions yielded a b_1 value of 3 and a value of a_1 of zero (within the mean error). A fixed slope of 10 introduced a morphological type dependence with values of b_1 significantly different from zero and as high as 0.377 (with a mean error = 0.056).

Aaronson and Mould (1983) in their study of 300 nearby ($V_0 < 3000$ km s⁻¹) galaxies raised a number of important issues. They pointed out that treating magnitude as the independent variable guarantees the same width at fixed magnitude for a volume- or magnitude-limited sample, but it does not guarantee the correct slope. For example, they found that regressing on magnitude for each individual type produced steeper slopes which caused an artificial spread in velocity width at a fixed magnitude – i.e. a false type dependence. They obtained the best slope representation of their sample in a least squares sense by weighting the fit according to the distribution spread in each coordinate (in addition to measurement errors) and not by treating either absolute magnitude or velocity width as an independent variable. In the B band, they found no dependence of the slope on morphological type and a slight dependence of the zero point (~ 0.4 mag going from Sa to Sc

with the Sc zero point being fainter) on morphological type.

Many other studies (Fouqué et al., 1990; Ichikawa and Fukugita, 1992; Bothun et al., 1984; Pierce and Tully, 1988) argued against a strong morphological dependence of the Tully-Fisher relation. Bothun *et al.* (1984) found that the mean line width of their sample of 20 Sc I galaxies ($2 < V_{max} > = 467 \pm 20 \text{ km s}^{-1}$) was virtually identical to the value obtained for the Sb sample of Rubin *et al.* (1982). Pierce and Tully (1988) found a slight type dependence of at most 0.4 mag in volume-limited samples in the Virgo and Ursa Major galaxy clusters.

How can one reconcile the Rubin *et al.* (1985) result with the above works? The source of the discrepancy may reside in the internal absorption corrections applied to different samples. Internal absorption corrections are very important and poorly-understood in the B band, and this is why much recent work has been devoted to an infrared Tully-Fisher relation. Rubin *et al.* (1985) applied the same internal absorption correction ($\Delta m_i = \log a/b$ where a/b is the axial ratio of the galaxy image) to *all* morphological types. However, Kodaira and Watanabe (1988) conducted a statistical study of internal absorption in a sample of 184 disk galaxies and found that internal absorption was more important in late-type (Sc) galaxies because they contained more dust. Any error in the internal absorption correction should therefore have more of an impact on late-type galaxies. It is interesting to note that, in the sample of Rubin *et al.* (1985), the dispersion in absolute B magnitude increases going from Sa to Sb galaxies and is thus correlated with the amount of internal absorption given by Kodaira and Watanabe (1988). Since the different subsamples have different intrinsic dispersions and the Ru-

bin sample is magnitude-limited, it is conceivable that they may have been differentially affected by the Malmquist bias. Since Malmquist bias would lead to steeper slopes, one would expect the slope of the linear regression for the Sc subsample to be larger than for the Sa and Sb subsamples. The slopes obtained by Rubin *et al.* (1985) for their Sa, Sb and Sc subsamples are 9.95, 10.2 and 11.0 respectively. As mentioned previously, an overestimate of the slope will introduce an artificial type dependence (Vaucouleurs *et al.*, 1982; Aaronson and Mould, 1983).

Small sample sizes preclude one from settling the issue of morphological dependence and the Tully-Fisher relation. The discrepancy between the Rubin result and other studies may only be symptomatic of large variations in local galaxy properties. These variations can be brought to light with a truly large local sample. Mathewson *et al.* (1992) measured total I magnitude and H_α rotation velocity for a sample of 1355 local galaxies with morphological classification. Figure 8.2 shows $\log V_{max}$ versus absolute I magnitude for galaxies with morphological types between $T = 1$ (Sa) and $T = 8$ (Sdm). Although Mathewson *et al.* provided total I apparent magnitudes corrected for internal absorption, their uncorrected I magnitudes were used to derive absolute magnitudes. This is to insure that the Mathewson *et al.* data can be later compared with the CFHT internal kinematics data for which CNOC provided uncorrected apparent magnitudes. Figure 8.2 is a beautiful illustration of the local Tully-Fisher locus and its dispersion. There are no systematic shifts between loci of different morphological types, but it is obvious that certain types (e.g. $T = 6$) display larger dispersions. Since galaxy heliocentric velocities were used to calculate absolute I band magni-

tudes, some of the scatter in Figure 8.2 actually comes from galaxy peculiar velocities. It should therefore be kept in mind that this scatter will lead to conservative luminosity evolution estimates whenever the Mathewson *et al.* relation is used as a reference.

The absence of a type dependence in the I band does not necessarily apply to the B band since galaxies have different B–I colors. We can convert Figure 8.2 to the B band using the B–I colors of local galaxies. Frei and Gunn (1994) have generated tables of colors and k-corrections for different Hubble types. Their local ($z = 0$) B–I colors are 1.72 (Sbc, $T = 3-4$), 1.32 (Scd, $T = 6-7$) and 1.16 (Im, $T = 8-9$). These color correction were applied to the data shown in Figure 8.2 to build Figure 8.3. Rubin *et al.* (1985)'s Sa and Sb Tully-Fisher relations are also plotted for comparison. There are no systematic shifts between loci of different morphological types at the ~ 2.0 mag level as claimed by Rubin *et al.* (1985).

Figures 8.3 and 8.4 shed some much needed light on the Rubin *et al.* (1985) result. First, the Rubin relations have the wrong slope. They are too steep (in the magnitude versus $\log V_{max}$ sense). The Rubin sample is biased against fast rotating Sc galaxies or alternatively, it is biased against faint Sc galaxies at a fixed rotation velocity. There is a significant number of Sb and Sc galaxies in the Mathewson *et al.* (1992) sample lying right on the Rubin Sa relation even though there is only one Sa galaxy in the Mathewson *et al.* (1992) sample. The key here is the larger dispersion displayed by Sc galaxies. This dispersion coupled to small sample size and selection effects probably lead to an artificial type dependence of the Tully-Fisher relation. However, the absence of type dependence should not obscure the fact that local late-

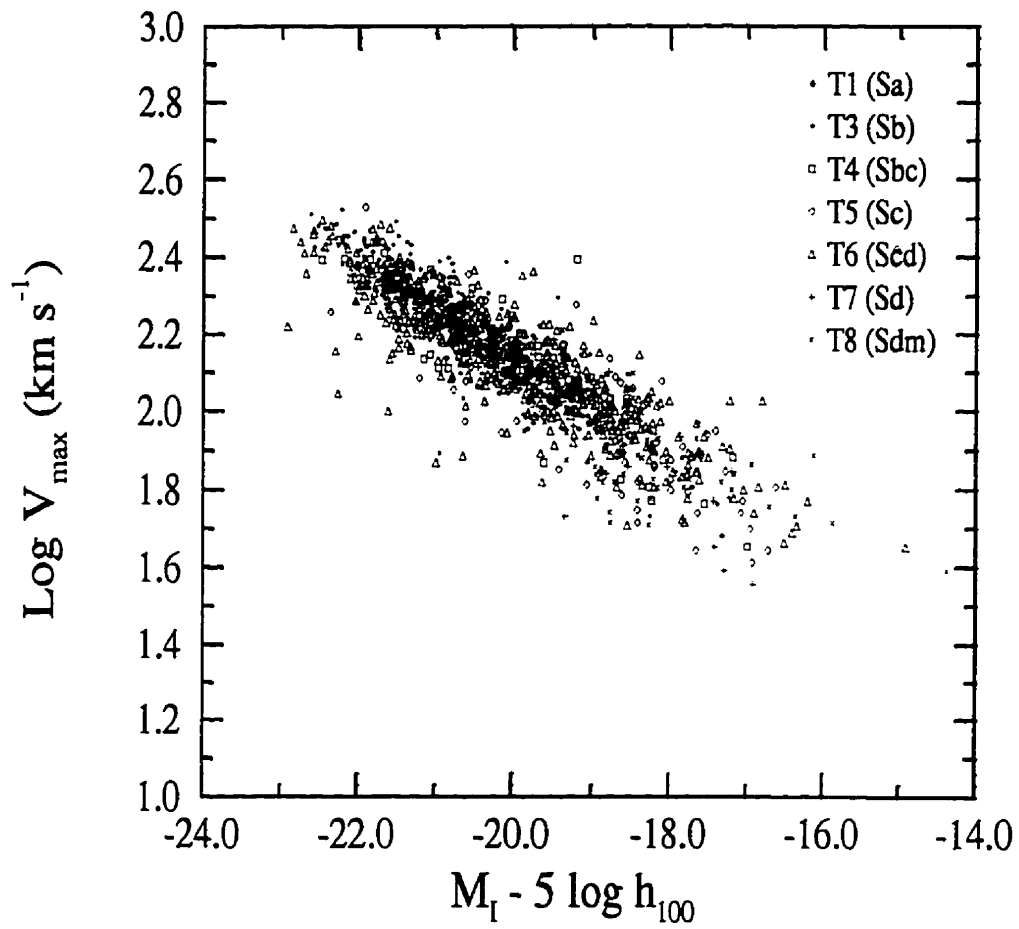


Figure 8.2: The locus of the local H_α -I band Tully-Fisher relation and its dispersion. Data taken from Mathewson *et al.* (1992)

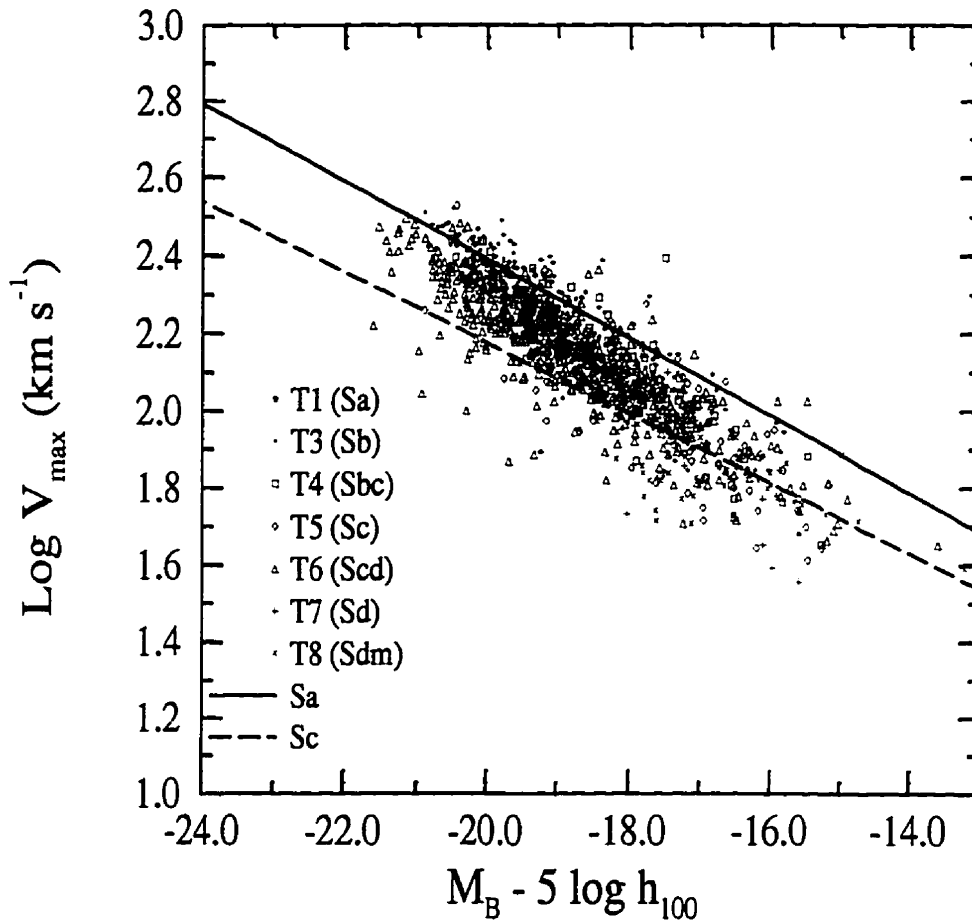


Figure 8.3: The locus of the local H_α -B band Tully-Fisher relation and its dispersion. Data taken from Mathewson *et al.* (1992). B-I colors of Frei and Gunn (1994) were used to convert I to B. The solid and dashed lines are the Sa and Sb Tully-Fisher local relations respectively according to Rubin *et al.* (1985).

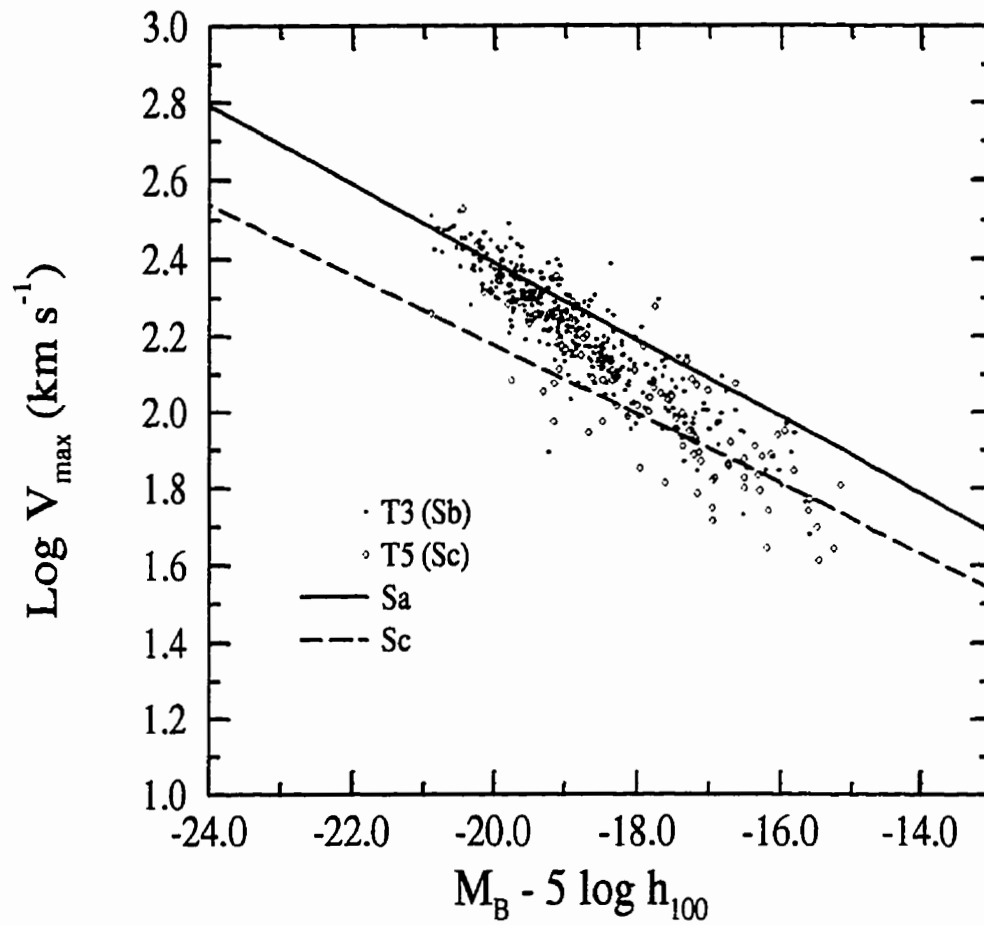


Figure 8.4: The locus of the local H_{α} -B band Tully-Fisher relation for Hubble types Sb and Sc only. Data taken from Mathewson *et al.* (1992) and B-I colors of Frei and Gunn (1994) were used to convert I to B. The solid and dashed lines are the Sa and Sc Tully-Fisher local relations respectively according to Rubin *et al.* (1985).

type galaxies do show a large scatter and that this scatter should be carefully considered in claims of luminosity evolution at intermediate redshifts. This issue is the topic of the next section.

8.3 Kinematical Evidence for Luminosity Evolution

As discussed in section 4.1, one can compare the internal kinematics of intermediate redshift galaxies with the local Tully-Fisher to look for kinematical evidence for luminosity evolution. Figure 7.37 shows the CFHT internal kinematics results with respect to the absolute calibration of the Tully-Fisher relation (Pierce and Tully, 1992) converted to H_α velocities as explained in section 8.1. All data points except one appear to lie systematically below the local TF relation for edge-on galaxies. 9 out of 12 galaxies lie below the expected relation for randomly oriented disks. The relation would have to be shifted to brighter magnitudes to lie on top of the internal kinematics measurements. The target galaxies are too bright for their mass, as one would expect from luminosity-dependent luminosity evolution. Number counts and redshift studies are unable to differentiate between density and luminosity evolution to explain the increase in the Schechter normalization ϕ^* , since to increase ϕ^* , one can either increase the number of galaxies or increase the luminosity of existing galaxies to L^* . Figure 7.37 is clear evidence that luminosity is the evolving variable in these intermediate redshift galaxies.

Table 8.1 lists the change in absolute magnitude ΔM_{B_0} for each of the 12 kinematically normal galaxies plotted in Figure 7.37. Column 3 gives the H_α

rotation velocity expected for a galaxy with M_{B_0} given in Column 2 based on the Pierce and Tully (1992) TF calibration. Column 5 gives the absolute B magnitude M'_{B_0} of a galaxy with $V_{\text{rot}} \sin i$ given in Column 4 based on the same TF calibration. Column 6 gives the change in absolute magnitude $\Delta M_{B_0} = M_{B_0} - M'_{B_0}$. There is a wide range of ΔM_{B_0} , but ΔM_{B_0} appears to be ~ 1.8 mag on average. Interestingly enough, the luminosity evolution scenario of Broadhurst *et al.* (1988) needed $\Delta M_{B_0} = +2.2$ mag of fading to explain the excess of field galaxies seen at $z \sim 0.4$ over no-evolution number counts based on the Loveday *et al.* (1992) LF.

Another aspect of the Broadhurst *et al.* (1988) was the dependence of ΔM_{B_0} on the gas content of galaxies (Section 3.1). Low-luminosity (i.e. low mass), gas-rich galaxies underwent more luminosity evolution than brighter, relatively gas-poor ones. This led to a non-uniform brightening of the dwarf component of the galaxy population. This non-uniformity would have a direct influence on the slope of the TF relation at intermediate redshifts as massive galaxies would have smaller ΔM_{B_0} 's. Although the current sample is quite small, Figure 7.37 offers tantalizing hints that such a non-uniform luminosity evolution is indeed occurring. The two galaxies with $V_{\text{rot}} \sin i \sim 175$ km/s and $M_{B_0} \sim -20.4$ are at least near the dashed line. Galaxies with $V_{\text{rot}} \sin i < 100$ km/s have larger and more spread out ΔM_{B_0} values even though these galaxies roughly have the same mass. It therefore seems that low-mass galaxies are more affected by whatever process is causing luminosity evolution at those redshifts (see Section 8.4 for further discussion). A larger sample is needed to study $\langle \Delta M_{B_0} \rangle$ and $\sigma(\Delta M_{B_0})$ as function of redshift and galaxy mass.

Table 8.1: Luminosity Evolution from Absolute TF relation

Galaxy ID (1)	M_{B_0} (2)	V_{rot}^{TF} (3)	$V_{rot} \sin i$ (4)	M'_{B_0} (5)	ΔM_{B_0} (6)
A2390-100686	-19.4	155	91^{+21}_{-39}	$-17.9^{+2.0}_{-0.5}$	$-1.5^{+0.5}_{-2.0}$
A2390-350416	-19.5	160	62^{+18}_{-21}	$-16.9^{+0.9}_{-0.6}$	$-2.6^{+0.6}_{-0.9}$
A2390-350471	-20.3	208	171^{+26}_{-29}	$-19.7^{+0.6}_{-0.4}$	$-0.6^{+0.4}_{-0.6}$
E1512-301037A	-19.1	140	77^{+22}_{-24}	$-17.4^{+0.9}_{-0.6}$	$-1.7^{+0.6}_{-0.9}$
E1512-301037B	-19.1	140	86^{+8}_{-18}	$-17.7^{+0.6}_{-0.2}$	$-1.4^{+0.7}_{-0.6}$
E1512-201429	-20.4	215	151^{+13}_{-11}	$-19.3^{+0.2}_{-0.3}$	$-1.1^{+0.3}_{-0.2}$
A2390-200928	-18.2	103	65^{+13}_{-15}	$-17.0^{+0.6}_{-0.4}$	$-1.2^{+0.4}_{-0.6}$
A2390-200802	-19.1	140	-198^{+76}_{-65}	$-20.1^{+1.4}_{-0.9}$	$+1.0^{+0.9}_{-1.4}$
A2390-200372	-20.2	202	-86^{+52}_{-18}	$-17.7^{+2.1}_{-0.5}$	$-2.5^{+0.5}_{-2.1}$
E1512-200334	-19.0	136	60^{+46}_{-31}	$-16.8^{+1.4}_{-1.5}$	$-2.2^{+1.5}_{-1.4}$
E1512-201268	-18.6	119	33^{+45}_{-84}	$-15.7^{--}_{-1.7}$	$-2.9^{+1.7}_{--}$
E1512-202096	-20.5	222	28^{+39}_{-33}	$-15.3^{--}_{-1.7}$	$-5.2^{+1.7}_{--}$

It is impossible to tell from Figure 7.37 how much the scatter in the local TF relation might contribute to ΔM_{B_0} . To solve this problem, the CFHT internal kinematics data were plotted against the Mathewson *et al.* (1992) TF relation shown in Figure 8.3. The result is shown in Figure 8.5. $V_{rot} \sin i$'s were taken from Table 7.3, and M_{B_0} magnitudes were taken from Table 5.1. Since these magnitudes had been computed using $H_0 = 75$, they were shifted by +0.62 mag before they were plotted on Figure 8.5. The internal kinematics

data clearly lie below the centroid of the Mathewson *et al.* relation. Part of the difference comes from the fact that the rotation velocities V_{max} given by Mathewson *et al.* are for edge-on galaxies whereas the internal kinematics data have not been inclination-corrected. For randomly-oriented disks, the Mathewson *et al.* relation would shift downwards by 0.1 in $\log V_{max}$ ($\langle V_{obs} \rangle = 0.7854 \langle V_{edge-on} \rangle$). The correction to the Mathewson *et al.* relation is likely to be smaller since target galaxies with elongated CNOC MOS images have been preferentially selected.

Even if the Mathewson *et al.* relation is shifted downwards by a full 0.1 in $\log V_{max}$, the internal kinematics data points still lie below the centroid of the relation. To illustrate the size of the discrepancy, an unweighted linear fit was made to the data for all morphological types in the Mathewson *et al.* relation. After three 3σ -clipping rejection iterations, the fit converged to

$$\log V_{max} = -0.12(\pm 0.02)M_{B_0} - 0.17(\pm 0.42) \quad (8.4)$$

The uncertainty on the coefficients are formal 1σ errors. This fit was then shifted in M_{B_0} by -1.0 and -2.0 mag. The result are the three dashed lines shown in Figure 8.6. The $\Delta M_{B_0} = -2.0$ mag line appears to be closer to the data points in agreement with the amount of luminosity evolution estimated using Pierce and Tully (1992) TF calibration. However, it is immediately obvious that the TF envelope of local late-type galaxies (Scd-Sm) reaches down as far as most of the internal kinematics data points. According to Frei and Gunn (1994)'s tables, the target galaxies have colors typical of Scd-Sdm galaxies, so a comparison with a subset of the Mathewson *et al.* sample comprising only late-type (T6-T8) might be more appropriate. The

result is shown in Figure 8.7. After three 3σ -clipping rejection iterations, an unweighted linear fit converged to

$$\log V_{max} = -0.12(\pm 0.03)M_{B_0} - 0.02(\pm 0.56) \quad (8.5)$$

The TF late-type relation is not systematically different from the global one since Equations 8.4 and 8.5 have the same slopes and the same intercepts (within the uncertainty).

The scatter in the Tully-Fisher shown in Figures 8.6 and 8.7 comes from three sources: internal absorption, galaxy peculiar velocities and variations in star formation rates. The Mathewson *et al.* catalog does list total magnitudes corrected for internal absorption. These magnitudes were not used because the absolute magnitudes of the galaxies in the CFHT sample were not corrected for internal absorption. The effect of galaxy peculiar velocities is minor. Peculiar velocities lead to $\sim 10\%$ errors on galaxy distances. The major unknown is star formation. The existing body of local Tully-Fisher data is insufficient to ascertain the dependence of local galaxy luminosity on the strengths of emission lines indicative of star formation. In order to accurately measure magnitude offsets from the Tully-Fisher relation, each galaxy in the CFHT sample (or any other sample for that matter) should be compared to the local Tully-Fisher relation for galaxies with similar [OII] emission line strengths. This is not possible for now. A large, homogeneous sample of local emission-line strengths, rotation velocities, morphologies and absolute magnitudes is required to settle this issue. This will remain a major limitation of internal kinematics studies at high redshifts as long as technical

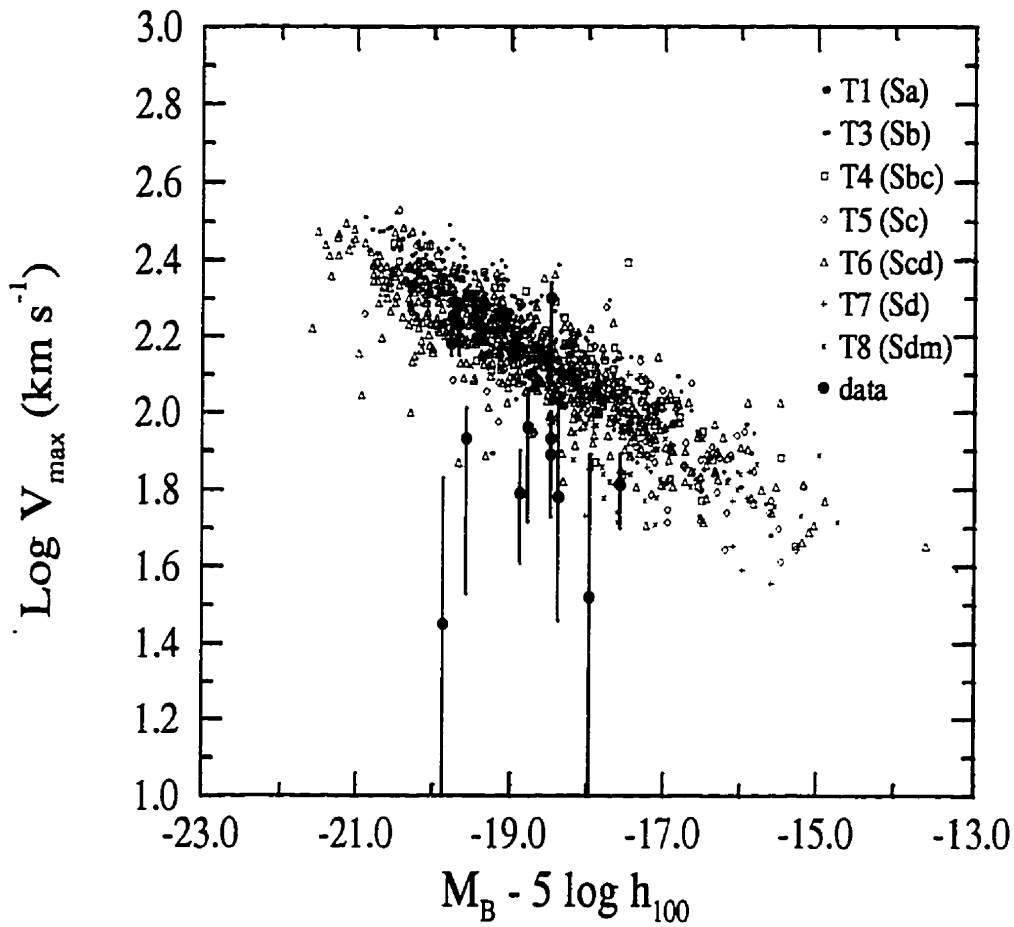


Figure 8.5: The locus of the local H_{α} -B band Tully-Fisher relation and its dispersion. Data taken from Mathewson *et al.* (1992). B-I colors of Frei and Gunn (1994) were used to convert I to B. Solid circles are the $V_{\text{rot}} \sin i$'s versus rest-frame B magnitude of the CFHT internal kinematics data

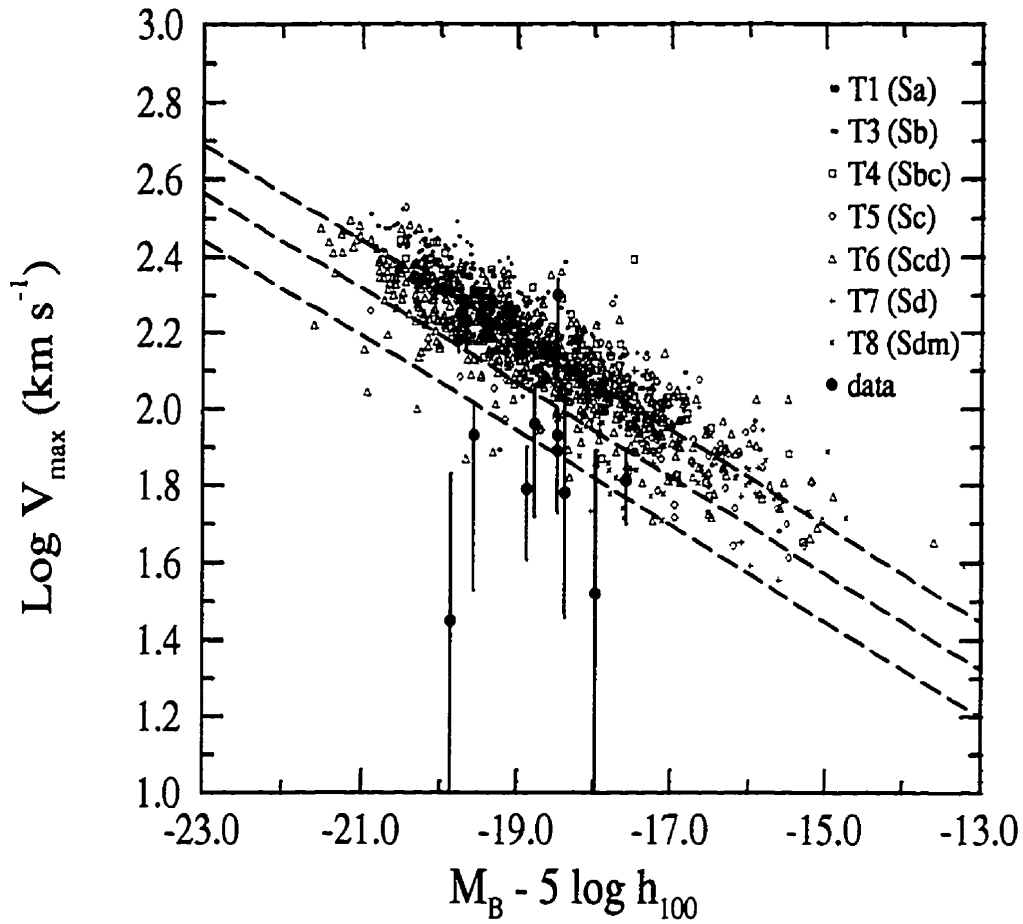


Figure 8.6: Kinematical evidence for luminosity evolution at intermediate redshifts. The locus of the local H_α -B band Tully-Fisher relation for all morphological types as defined by data taken from Mathewson *et al.* (1992) is used as a reference. Solid circles are the $V_{\text{rot}} \sin i$'s versus rest-frame B magnitude of the CFHT internal kinematics data. The upper long dashed line is an unweighted linear fit to all the local morphological types. This linear fit was then shifted by $\Delta M_{B_0} = 1.0$ mag (middle dashed line) and $\Delta M_{B_0} = 2.0$ mag (lower dashed line) to represent various degrees of luminosity evolution.

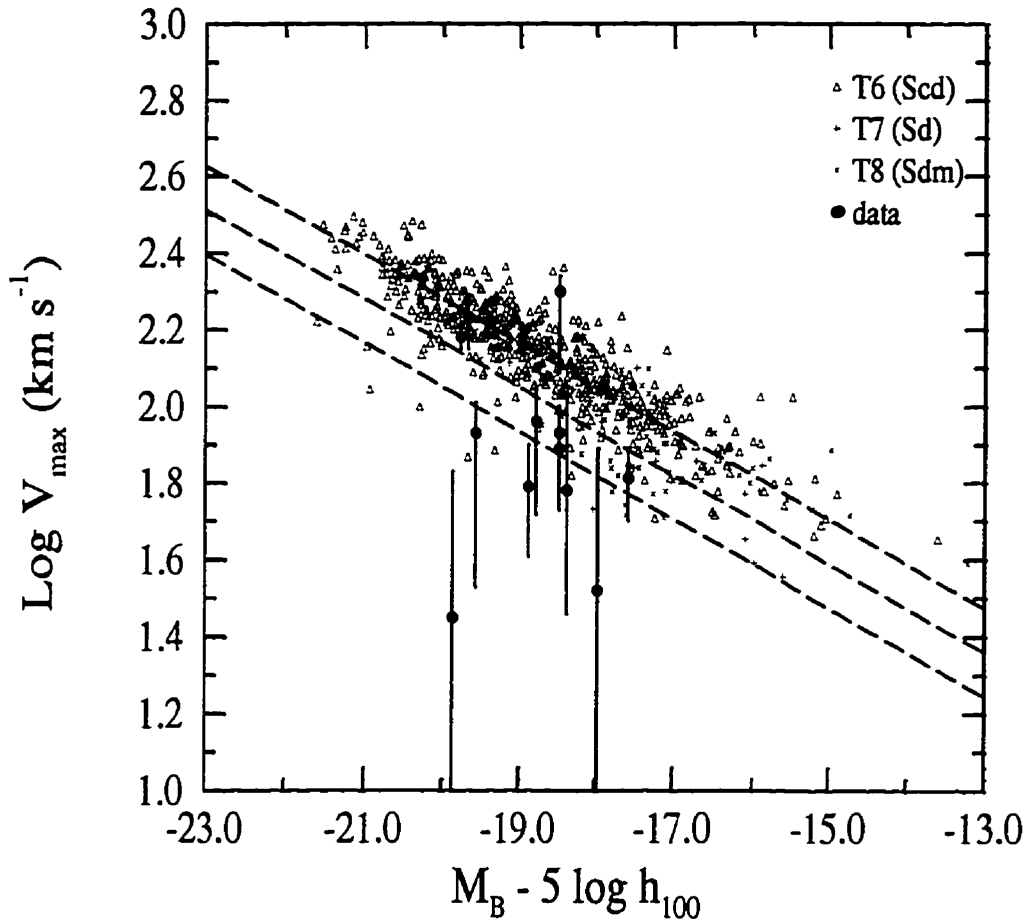


Figure 8.7: Kinematical evidence for luminosity evolution at intermediate redshifts. The locus of the local H_α -B band Tully-Fisher relation for late morphological types (T6–T8) as defined by data taken from Mathewson *et al.* (1992) is used as a reference. Solid circles are the $V_{\text{rot}} \sin i$'s versus rest-frame B magnitude of the CFHT internal kinematics data. The upper long dashed line is an unweighted linear fit to local late morphological types (T6–T8). This linear fit was then shifted by $\Delta M_{B_0} = 1.0$ mag (middle dashed line) and $\Delta M_{B_0} = 2.0$ mag (lower dashed line) to represent various degrees of luminosity evolution.

requirements restrict them to strong emission-line objects.

8.4 Comparison with Other Works

This section discusses all available evidence to give a picture of galaxy evolution at high redshift consistent with luminosity-dependent luminosity evolution. This scenario neatly reconciles the various amounts of luminosity evolution seen in the surface brightness and internal kinematics studies.

Starting with internal kinematics, there are three studies which appear to be at odds with one another: Koo *et al.* (1995), Vogt *et al.* (1996) and the CFHT sample presented in this thesis. At the low end of the galaxy mass spectrum, Koo *et al.* (1995) looked at compact, unresolved galaxies with narrow emission line widths. They found that the line widths of these galaxies were $2-3\times$ lower than expected from the luminosity-linewidth relation of normal spiral galaxies. Those low-mass galaxies were identified with local HII galaxies on the basis that they fell on the luminosity-linewidth relation of local HII galaxies given by Telles and Terlevich (1993). At a fixed velocity width, the Koo *et al.* galaxies were 4 magnitudes brighter than expected from the local Tully-Fisher relation. At the high end of the galaxy mass spectrum, there is the Keck study of Vogt *et al.* (1996). The galaxies in this study were intrinsically large ($r_d \geq 3.0$ kpc) and bright ($M_B \leq -20.7$). They were also intrinsically massive with typical rotation velocities of 200 km/s. Their rotation curves were similar to those of local normal galaxies, and the increase in luminosity with respect to the local Tully-Fisher was less than 0.6 magnitude in the B band.

The CFHT sample occupies a niche in size and mass right in between the above two Keck samples. The CFHT galaxies were typically a full magnitude fainter than the objects in the Vogt *et al.* study. They were also intrinsically smaller with typical disk scale lengths less than 2.0 kpc, and some of them were barely resolved. They were also less massive with rotation velocities ~ 100 km/s, but they were nonetheless more massive than the galaxies observed by Koo *et al.* The CFHT galaxies exhibited a diversity of internal kinematics not seen in the Keck study but consistent with local peculiar phenomena such as galactic supershells. The kinematically normal galaxies showed an increase in luminosity of ~ 1.5 mag with respect with the local Tully-Fisher relation defined by the Mathewson *et al.* sample. If mass is taken as an indicator of the luminosity all the galaxies would have had in a quiescent phase, then all three internal kinematics studies can be understood with luminosity-dependent luminosity evolution. Low-mass galaxies are more susceptible to processes such as interactions/mergers which trigger star formation because they have a higher gas fraction. Supernova-driven winds and nuclear outflows will also be more damaging to the normal (i.e. rotational) kinematics of low-mass galaxies, so their internal kinematics should be more varied.

HII galaxies at high redshifts remain an unknown. There is no doubt that some galaxies in the Koo *et al.* sample are indeed HII galaxies with linewidths dominated by low velocity, ionized gas from a small number of star forming complexes; they lie too neatly on the luminosity-linewidth relation for HII galaxies. On the other hand, it is not inconceivable that some of the galaxies are low-mass, disk galaxies which may have been brightened up by 4.0 mag or less. These galaxies may have been lumped with HII galax-

ies due to the lack of spatial resolution. As far as the CFHT galaxies are concerned, their linewidths are clearly not dominated by a few star forming regions. First, [OII] follows the continuum light profile, and [OII] is symmetrically distributed about the galaxian centers. Smooth exponential [OII] distributions are unlikely to be produced by a small number of star forming complexes. Second, although some of our galaxies have a spatially-resolved spectrum with a rotation velocity consistent with zero, others clearly show a systematic rotation. Evidence for a giant HII region has been detected in one of the CFHT galaxies, but the rotational component could nonetheless be isolated and analyzed. An important question must be answered in order to accept that HII galaxies play as significant a role as Koo *et al.* claim over the redshift range 0.1–0.7 they observed. The timescale for a star burst is typically shorter than 1 Gyr. The redshift range 0.1–0.7 corresponds to a time interval of 3.5 Gyrs ($H_0=75$ and $q_0 = 0.5$). If HII galaxies are present in great numbers at all redshifts, then they must be forming at all redshifts, so that the newborn galaxies may replace the fading ones to keep them in sufficient numbers over many Gyrs.

The B-band surface brightness $\mu_0(B)$ of field disk galaxies undergoes a strong evolution over the redshift range $0.1 < z < 0.6$ compared to a local $z=0.06$ relation and the Freeman law (Schade *et al.*, 1996a). At redshifts of 0.43 and 0.55, $\Delta\mu_0(B)$ is equal to -1.22 and -0.97 respectively. This is consistent with or slightly less than the evolution seen in the CFHT sample, and it is certainly more than the amount of evolution seen in the Keck sample of Vogt *et al.* Looking at Figure 1 of Schade *et al.* (1996a), there is a hint that surface brightness evolution depends on the disk scale length. Smaller

galaxies evolve more drastically than large galaxies. The effect is particularly noticeable in the highest redshift bin where the $\log r_d - M_B$ relation at that redshift clearly curves “down”. Taking $M_B \simeq -21$ and $\langle r_d \rangle = 4.3$ kpc ($H_0 = 75$), one can see on the Schade diagram for $0.45 < z < 0.65$ that a large number of galaxies at (\log scale length = 0.8, -21) show little or no evolution as observed in the Keck sample.

Of course, the best way to reconcile the evolution seen in surface brightness and internal kinematics will be to study both in the same galaxies. For now, luminosity-dependent luminosity evolution is an elegant way to explain the available data.

Chapter 9

Conclusion and Future Work

[O II] internal kinematics has been measured in a sample of 22 intermediate redshift galaxies. A number of conclusions can be drawn from this survey:

- The synthetic rotation curve method provides a way to optimally extract the best parameter values allowed by the noise from low S/N data. With bigger telescopes and more efficient CCD detectors, this method will be invaluable to study high redshift objects which are not as [OII] strong and hence more representative of the local normal galaxy population.
- [OII] kinematics at intermediate redshifts is varied. 25% of the field galaxies in the sample had anomalous kinematics. In some of these galaxies, all of the [OII] emission was confined to the nucleus (as in local galaxies harboring active galactic nuclei), and the [OII] linewidth had no relation to galaxy rotation. In one kinematically anomalous galaxy, the [OII] emission may be coming from a galactic super shell which bears a striking resemblance to shells observed in local dwarf irregular galaxies. It is interesting that peculiarities in internal kinematics have local counterparts. Anomalous galaxies appear to be associated with minor

merger events, and at least two galaxies appear to be early-types.

- Based on the absolute calibration of the Tully-Fisher relation, galaxies in the sample are ~ 1.5 – 2.0 magnitudes brighter than expected for their rotation velocity. Relatively low-mass galaxies with V_{rot} of ~ 100 km/s exhibit a wider range of offsets from the Tully-Fisher relation. This is against arguments for uniform luminosity evolution.
- There is considerable scatter in the local Tully-Fisher relation especially for late-type spiral galaxies. There is insufficient local data (e.g. equivalent widths for a truly large and homogeneous sample) to determine whether most of this scatter comes from variations in star formation rates. Since local star-forming galaxies may be systematically brighter than expected from the local TF relation for normal galaxies, the magnitude of the magnitude offset seen in [OII] strong galaxies at intermediate redshifts may be reduced.
- A comparison with other works, notably spectroscopy obtained with the Keck telescope and CNOC surface brightness measurements, indicates the available evidence is best explained by luminosity-dependent luminosity evolution. Large, bright galaxies have rotation curves similar to local normal galaxies and show no evidence of an offset from the Tully-Fisher. On the other hand, the internal kinematics of small, low-mass objects are more varied and display a significant Tully-Fisher offset.

The future prospects for internal kinematics are very exciting. On the local front, the dependence of the local Tully-Fisher relation on variations in star formation rates must be investigated. The conclusions of all internal kinematics studies at high redshifts will critically depend on that aspect of the

local TF relation as long as technical requirements restrict them to strong emission-line objects.

Properties of kinematically anomalous galaxies such as color, surface brightness profiles, [OII] equivalent widths and diagnostic emission line ratios need to be studied for a larger sample to confirm that merger events in early and late type galaxies may be triggering star formation in the nuclei of some intermediate redshift galaxies.

Current samples cannot be used to determine how the Tully-Fisher zero-point shifts as a function of redshift. The samples are small, and they are spread over a wide range of redshifts. However, it does appear that the TF slope does not remain constant under the effect of luminosity-dependent luminosity evolution, and larger samples are needed to measure luminosity changes as a function of redshift *and* galaxy mass. The dispersion in ΔL at a given mass could be used to look for correlations with other parameters such as star formation rate.

Galaxies with [OII] substructures should be imaged with very high spatial resolution with the Hubble Space Telescope and ground-based adaptive optics systems such as the CFHT Adaptive Bonnette to find out what kind of morphological distortions are associated with those [OII] substructures.

It would also be possible with integral field spectrographs such as Fabry-Perot interferometers and fibre bundles to measure the electron density and [O/H] abundance using diagnostic line ratios (e.g. McGaugh (1991)) as a function of position *within* intermediate redshift galaxies. Maps of N_e and [O/H] would be extremely valuable to understanding ionization processes and ISM enrichment mechanisms at work in distant galaxies.

Bibliography

- Aaronson, M. and Mould, J.: 1983, *Astrophys. J.* **265**, 1
- Babul, A. and Rees, M. J.: 1992, *M.N.R.A.S.* **255**, 364
- Bernstein, G., Tyson, J., and Jarvis, J.: 1994, *Astrophys. J.* **426**, 516
- Bothun, G. D., Aaronson, M., Schommer, B., Huchra, J., and Mould, J.:
1984, *Astrophys. J.* **278**, 475
- Broadhurst, T. J., Ellis, R. S., and Glazebrook, K.: 1992, *Nature* **355**, 55
- Broadhurst, T. J., Ellis, R. S., and Shanks, T.: 1988, *M.N.R.A.S.* **235**, 827
- Carlberg, R. G. and Charlot, S.: 1992, *Astrophys. J.* **397**, 5
- Carlberg, R. G., Yee, H. K. C., and Ellingson, E.: 1994, *Journal of the Royal
Astron. Soc. of Canada* **88**, 39
- Colless, M.: 1994, in S. Maddox and A. Aragon-Salamanca (eds.), *35th Herst-
monceux Conference: Wide Field Spectroscopy and the Distant Universe*,
World Scientific Publishing Company, Singapore
- Colless, M. M., Ellis, R. S., Broadhurst, T. J., and Peterson, B. A.: 1993,
M.N.R.A.S. **244**, 408
- Colless, M. M., Ellis, R. S., Taylor, K., and Hook, R. N.: 1990, *M.N.R.A.S.*
244, 408
- Cowie, L. L., Songaila, A., and Hu, E. M.: 1991, *Nature* **354**, 460

- Dalcanton, J. J.: 1993, *Astrophys. J.* **415**, L87
- Dekel, A. and Silk, J.: 1986, *Astrophys. J.* **303**, 39
- Driver, S. P., Windhorst, R. A., Ostrander, E. J., Keel, W. C., Griffiths, R. E., and Ratnatunga, K. U.: 1995, *Astrophys. J.* **449**, 23
- Efstathiou, G., Bernstein, G., Katz, N., Tyson, J. A., and Guhathakurta, P.: 1991, *Astrophys. J.* **380**, L47
- Ellis, R. S., Colless, M., Broadhurst, T., Heyl, J., and Glazebrook, K.: 1996, *M.N.R.A.S.* **280**, 235
- Forbes, D. A., Phillips, A. C., Koo, D. C., and Illingworth, G. D.: 1995, *Astrophys. J.* **462**, 89
- Fouqué, P., Bottinelli, L., Gouguenheim, L., and Paturel, G.: 1990, *Astrophys. J.* **349**, 1
- Franx, M.: 1993, *Publ. Astron. Soc. Pacific* **105**, 1058
- Frei, Z. and Gunn, J. E.: 1994, *Astron. J.* **108**(4), 1476
- Gardner, J. P., Cowie, L. L., and Wainscoat, R. J.: 1993, *Astrophys. J.* **415**, L9
- Glazebrook, K., Ellis, R., Colless, M., Broadhurst, T., Allington-Smith, J., and Tanvir, N.: 1995a, *M.N.R.A.S.* **273**, 157
- Glazebrook, K., Ellis, R., Santiago, B., and Griffiths, R.: 1995b, *M.N.R.A.S.* p. Astroph
- Glazebrook, K., Peacock, J., Miller, L., and Collins, C.: 1995c, *M.N.R.A.S.* **275**, 169
- Huang, S. and Carlberg, R. G.: 1996, *Astrophys. J.* Submitted, Astroph9511076
- Hubble, E. and Tolman, R. C.: 1935, *Astrophys. J.* **82**, 302

- Ichikawa, T. and Fukugita, M.: 1992, *Astrophys. J.* **394**, 61
- Im, M., Ratnatunga, K. U., Griffiths, R. E., and Casertano, S.: 1995, *Astrophys. J.* **445**, L15
- Infante, L. and Pritchett, C.: 1995, *Astrophys. J.* **439**, 565
- Jacoby, G. H., Branch, D., Ciardullo, R., Davies, R. L., Harris, W. E., Pierce, M. J., Pritchett, C. J., Tonry, J. L., and Welch, D. L.: 1992, *Publ. Astron. Soc. Pacific* **104**, 599
- Jedrzejewski, R. I.: 1987, *M.N.R.A.S.* **226**, 747
- Kennicutt, R. C.: 1992, *Astrophys. J.* **388**, 310
- King, C. R. and Ellis, R. S.: 1985, *Astrophys. J.* **288**, 456
- Kodaira, K. and Watanabe, M.: 1988, *Astron. J.* **96**, 1593
- Koo, D. C.: 1986, *Astrophys. J.* **311**, 651
- Koo, D. C., Guzman, R., Faber, S. M., Illingworth, G. D., Bershad, M. A., Kron, R. G., and Takamiya, M.: 1995, *Astrophys. J.* **440**, L49
- LeFèvre, O., Crampton, D., Felenbok, P., and Monnet, G.: 1994, *Astron. & Astrophys.* **282**, 325
- Lilly, S. J.: 1993, *Astrophys. J.* **411**, 501
- Lilly, S. J., Tresse, L., Hammer, F., Crampton, D., and Fèvre, O. L.: 1995, *Astrophys. J.* **455**, 108
- Lin, H., Kirshner, R. P., Shethman, S. A., Landy, S. D., Oemler, A., Tucker, D. L., and Schechter, P. L.: 1996, *Astrophys. J.* **464**, 60
- Loveday, J., Peterson, B. A., Efstathiou, G., and Maddox, S. J.: 1992, *Astrophys. J.* **390**, 338
- Marlowe, A. T., Heckman, T. M., Wyse, R. F. G., and Schommer, R.: 1995, *Astrophys. J.* **438**, 563

- Martin, C. L.: 1995, *Bull. American Astron. Soc.* 187(65)
- Marzke, R. O., Geller, M. J., Huchra, J. P., and Corwin, H. G. J.: 1994a, *Astron. J.* 108, 437
- Marzke, R. O., Huchra, J. P., and Geller, M. J.: 1994b, *Astrophys. J.* 428, 43
- Mathewson, D. S., Ford, V. L., and Buchhorn, M.: 1992, *Astrophys. J. Supp.* 81, 413
- McGaugh, S. S.: 1991, *Astrophys. J.* 380, 140
- Metcalf, N., Shanks, T., Fong, R., and Jones, L. R.: 1991, *M.N.R.A.S.* 249, 498
- Opik, E.: 1922, *Astrophys. J.* 55, 406
- Osterbrock, D. E.: 1974, *Astrophysics of Gaseous Nebulae*, W.H. Freeman and Company
- Peterson, B. A., Ellis, R. S., Efstathiou, G., Shanks, T., Bean, A. J., Fong, R., and Zen-Long, Z.: 1986, *M.N.R.A.S.* 221, 233
- Phillipps, S. and Driver, S. P.: 1995, *M.N.R.A.S.* 274, 832
- Pierce, M. J. and Tully, R. B.: 1988, *Astrophys. J.* 330, 579
- Pierce, M. J. and Tully, R. B.: 1992, *Astrophys. J.* 387, 47
- Press, W. H., Flannery, B. P., Teukolsky, S. A., and Vetterling, W. T.: 1986, *Numerical Recipes in C: The Art of Scientific Computing, 2nd Edition*, Cambridge University Press
- Roberts, M. S.: 1975, in A. Sandage, M. Sandage, and J. Kristian (eds.), *Stars and Stellar Systems*, Vol. 9 of *Galaxies and the Universe*, p. 309, University of Chicago Press
- Rocca-Volmerange, B. and Guiderdoni, B.: 1990, *M.N.R.A.S.* 247, 166

- Rubin, V. C., Burstein, D., Ford, W. K. J., and Thonnard, N.: 1985, *Astrophys. J.* **289**, 81
- Rubin, V. C., Thonnard, N., and Ford, W. K. J.: 1980, *Astrophys. J.* **238**, 471
- Rubin, V. C., Thonnard, N., Ford, W. K. J., and Burstein, D.: 1982, *Astrophys. J.* **261**, 439
- Saha, P. and Williams, T. B.: 1994, *Astron. J.* **107**, 1295
- Schade, D., Carlberg, R. G., Yee, H. K. C., López-Cruz, O., and Ellingson, E.: 1996b, *Astrophys. J.* **464**, L63
- Schade, D., Carlberg, R. G., Yee, H. K. C., López-Cruz, O., and Ellingson, E.: 1996a, *Astrophys. J.* **465**, L103
- Schade, D., Lilly, S. J., Crampton, D., Hammer, F., LeFèvre, O., and Tresse, L.: 1995, *Astrophys. J.* **451**, L1
- Schechter, P. L.: 1976, *Astrophys. J.* **203**, 297
- Shanks, T., Stevenson, P. R. F., Fong, R., and MacGillivray, H. T.: 1984, *M.N.R.A.S.* **206**, 767
- Smecker-Hane, T. A., Stetson, P. B., Hesser, J. E., and Lehnert, M. D.: 1994, *Astron. J.* **108**, 507
- Telles, E. and Terlevich, R.: 1993, *Astron. & Astrophys. Supp.* **205**, 49
- Tòth, G. and Ostriker, J. P.: 1992, *Astrophys. J.* **389**, 5
- Tresse, L., Rola, C., Hammer, F., and Stasinska, G.: 1994, in S. Maddox and A. Aragon-Salamanca (eds.), *35th Herstmonceux Conference: Wide Field Spectroscopy and the Distant Universe*, World Scientific Publishing Company, Singapore
- Tully, R. B. and Fisher, J. R.: 1977, *Astron. & Astrophys.* **54**, 661

- Tully, R. B. and Fouqué, P.: 1985, *Astrophys. J. Supp.* **58**, 67
- Tyson, J. A.: 1988, *Astron. J.* **96**, 1
- Vaucouleurs, G. D., Buta, R., Bottinelli, L., Gouguenheim, L., and Paturel, G.: 1982, *Astrophys. J.* **254**, 8
- Vogt, N., Herter, T., Haynes, M., and Courteau, S.: 1993, *Astrophys. J.* **415**, 95
- Vogt, N. P., Forbes, D. A., Phillips, A. C., Gronwall, C., Faber, S. M., Illingworth, G. D., and Koo, D. C.: 1996, *Astrophys. J.* **465**, L15
- Windhorst, R. A., Burstein, D., Mathis, D. F., Neuschaefer, L. W., Bertola, F., Buson, L. M., Koo, D. C., Matthews, K., Barthel, P. D., and Chambers, K. C.: 1991, *Astrophys. J.* **380**, 362
- Windhorst, R. A., Franklin, B. E., and Neuschaefer, L. W.: 1994, *Publ. Astron. Soc. Pacific* **106**, 798
- Yee, H. K. C., Ellingson, E., and Carlberg, R. G.: 1996, *Astrophys. J. Supp.* **102**, 269

Glossary

CCD: Charge Coupled Device. A two dimensional photometric detector.

CFHT: Canada France Hawaii Telescope.

E/S0/Sa/Sb/Sc/Irr: Different galaxy morphologies from elliptical (E) through the different kinds of spiral (Sa/Sb/Sc) to irregular (Irr).

Gyr: One Giga-year. A common notation in the astronomical literature.

IRAF: Image Reduction and Analysis Facility. The most commonly used image analysis program in optical astronomy.

MOS: Multi-Object Spectrograph at CFHT.

Parsec: A unit distance equal to 3.26 light-years. It is the distance at which 1 astronomical unit would subtend an angle of 1'' on the sky.

SIS: Subarcsecond Imaging Spectrograph at CFHT.

SNR: Signal to Noise Ratio.

TF: Tully-Fisher. The Tully-Fisher relation links the intrinsic luminosity of galaxies to their rotation velocity.

VITA

Surname: Simard

Given Name: Luc

Place of Birth: Québec City, Québec, Canada

Educational Institutions Attended:

University of Victoria	1990 – 1995
Queen's University	1987 – 1990

Degrees Awarded:

B.Sc. (Honours) Queen's University	1990
------------------------------------	------

Honours and Awards:

President's Scholarship (Victoria)	1994 – 1995
Petrie Scholarship (Victoria)	1994 – 1995
Petch Research Scholarship (Victoria)	1993 – 1994
President's Scholarship (Victoria)	1992 – 1993
NSERC Postgraduate Scholarship (Victoria)	1992 – 1994
MacDonell Graduate Award in Physics (Victoria)	1990 – 1991
Frank Carrel Upper Year Scholarship (Queen's)	1989 – 1990
Carl Reinhardt Scholarship in Physics (Queen's)	1989 – 1990
Susan Near Prize in Physics (Queen's)	1989
Edna McGill and Susan Near Prizes in Physics (Queen's)	1988
Frank Carrel Merit Scholarship (Queen's)	1987 – 1990